Contents

List of Figures

List of Tables

Frequently Used Acronyms

AC	Analysis Center
AIUB	Astronomical Institute of the University of Bern, Switzerland
CHAMP	CHAllenging Minisatellite Payload
CODE	Center for Orbit Determination in Europe, Bern, Switzerland
CNES	Centre National d'Etudes Spatiales
CSR	Center for Space Research, Austin, Texas
DD	Double Difference
DEOS	Department of Earth Observation and Satellite systems, Delft, The Netherlands
DOY	Day of Year
EIGEN	European Improved Gravity field model of the Earth by New techniques
ERP	Earth rotation parameters
ESA	European Space Agency
GFZ	GeoForschungsZentrum, Potsdam, Germany
GNSS	Global Navigation Satellite System
GOCE	Gravity field and steady-state Ocean Circulation Explorer
GPS	Global Positioning System
GRACE	Gravity Recovery And Climate Experiment
GRGS	Groupe de Recherches de Géodésie Spatiale
HPF	High-level Processing Facility
HRD	Higly Reduced-Dynamic (orbit)
IAPG	Institute for Astronomical and Physical Geodesy, Munich, Germany
IGS	International GNSS Service
ILRS	International Laser Ranging Service
JPL	Jet Propulsion Laboratory, Pasadena, California
KBR	K/Ka-Band Ranging
L_1	L_1 carrier (1575.42 MHz)
L_2	L_2 carrier (1227.60 MHz)
LC	Linear Combination
LEO	Low Earth Orbit(er)
MRD	Maximum Reduced-Dynamic (orbit)
NASA	National Aeronautics and Space Administration
O–C	Observed-minus-Computed
P-code	Precision code
PODAAC	Physical Oceanography Distributed Active Archive Center
PRN	Pseudo-random noise
RINEX	Receiver-INdependent EXchange format
RMS	Root-Mean-Square (error)

SF	Satellite-fixed
SH	Spherical harmonic
SLR	Satellite Laser Ranging
SST	Satellite-to-satellite tracking
STAR	Space Triaxial Accelerometer for Research missions
TUM	Technical University of Munich
UCAR	University Corporation for Atmospheric Research
ZD	Zero Difference

1. Introduction

The orbit modeling of low Earth satellites in the presence of various perturbations is a complex matter. Whereas a dynamic modeling of a satellite trajectory requires careful consideration of the impact of all the various perturbing forces, the Global Positioning System (GPS) has become a unique tool for deriving very precise orbits of Low Earth satellites equipped with onboard GPS receivers. The uninterrupted three-dimensional GPS tracking makes it possible to relax the strength of the dynamic laws for a most precise orbit determination, which is the subject of this work.

Low Earth Orbiters (LEOs) equipped with onboard GPS receivers (will) cover the region between approximately 250 and 1500 kilometers above the Earth's surface and serve dedicated mission purposes such as gravity field recovery, atmosphere sounding, and radar and laser altimetry. They are equipped with space-qualified geodetic-type receivers, which collect the GPS microwave signals traveling from the GPS satellites to the spaceborne GPS receiver on two carriers. The basic GPS observables for positioning are the so-called pseudo-range and the carrier phase, which may both be viewed as biased measurements of the slant range between the spaceborne GPS receiver and a GPS satellite. Due to the dispersive nature of the ionosphere, the ionospheric refraction can be almost completely eliminated by forming the so-called ionosphere-free linear combination of the original dual-frequency measurements. The analysis of ionosphere-free carrier phase observations (accuracies of a few millimeters) from all in view GPS satellites makes it possible to derive very precise information on the location of the spaceborne receiver, provided that the GPS satellite positions are known. This work introduces in a first, theoretical part several methods to derive orbital information from the ionosphere-free GPS observations.

Since a long time uncertainties in the dynamic models have been considered as the main limiting factor to model tracking data of low Earth satellites. In the time period of the first LEOs equipped with GPS receivers, it was important to derive very precise orbit solutions despite the presence of deficient gravitational and non-gravitational models, [*Yunck et al.*, 1990] and [*Wu et al.*, 1991]. Later on it became obvious that valuable information about the Earth's gravity field could be extracted from GPS data, if the non-gravitational accelerations are measured along the satellite trajectory [*Reigber et al.*, 2002b]. This was the advent of a decade with new geopotential models of unprecedented accuracy.

Efficient orbit determination was the main topic of the work performed by [*Bock*, 2003]. She could show that orbits of LEOs equipped with dual-frequency GPS receivers can be determined efficiently with decimeter accuracy. H. Bock used early GPS observations from the GPS receivers aboard CHAMP and SAC-C and gained valuable experience for the processing of spaceborne GPS data at the Astronomical Institute of the University of Bern (AIUB). Her methods made full use of the highly accurate GPS ephemerides, Earth rotation parameters, and GPS satellite clock corrections from the Center for Orbit Determination in Europe (CODE), located at AIUB. CODE is one of the ten analysis centers of the International GNSS Service (IGS). It was originally a joint venture of four European institutions [*Hugentobler et al.*, 2004b].

The core products from CODE are the backbone for the present work as well. In [*Jäggi et al.*, 2005b]

we could show that by analyzing undifferenced ionosphere-free CHAMP GPS data – instead of the so far analyzed time differenced data – and by setting up pseudo-stochastic parameters, it is possible to reconstruct the CHAMP trajectory with an accuracy at the few centimeter level. To do so, we revised the pseudo-stochastic orbit modeling part by a more refined representation based on acceleration parameters to effectively compensate for deficiencies in the dynamic models. In this context, we may mention that we contributed with our orbit solutions to the CHAMP orbit comparison campaign organized by the IGS.

After implementing more refined pseudo-stochastic orbit representations into a development environment of the Bernese GPS software [*Dach et al.*, 2007], we focused on the analysis of longer series of undifferenced GPS observations from CHAMP and from the GRACE twin satellites. All three satellites orbit the Earth at altitudes below 500 km, which poses a challenge to precise orbit determination. In order to assess the quality of the computed orbits, we used other observation techniques such as Satellite Laser Ranging (SLR), on-board accelerometry, and inter-satellite K/Ka-band ranging for an independent validation. The corresponding time series are presented and discussed in the second part of this work.

It is well known that interferometric data processing techniques are beneficial for high-precision applications of the GPS system. We processed doubly differenced carrier phase measurements from the GRACE satellites and from globally distributed IGS sites to compare the resulting orbits with solutions from undifferenced GPS data, and to assess the impact of resolving the doubly differenced carrier phase ambiguities to their integer values [*Mervart*, 1995]. It is striking that the space baseline between the GRACE twin satellites can be determined with millimeter precision when fully exploiting the processing of doubly differenced GPS data (whereas the precision of the individual positions is on the few cm level).

A most precise knowledge of satellite trajectories from a post-processing analysis of GPS data is useful for many spaceborne applications. Formation flying Synthetic Aperture Radar (SAR) satellite missions require precise relative orbit information for the generation of highly accurate digital elevation models when they are operated in a bistatic mode. Altimetry missions may profit from small radial orbit errors which facilitates a correct interpretation of the measured altimeter heights, and gravity field recovery missions may profit from most precise orbits to properly geolocate their sensor readings in an Earth-fixed reference frame. In this context, we may mention that the orbit determination methods presented in this work will be used in the framework of the High-level Processing Facility (HPF) to determine the precise science orbit of ESA's upcoming GOCE mission at AIUB [*Bock et al.*, 2007].

It may be necessary to adjust not only a few hundred but a few thousand pseudo-stochastic parameters when analyzing GPS data from very low Earth satellites. In order to still enable a most efficient processing, a revision of the algorithmic part of the orbit determination procedures was inevitable. The full exploitation of the structure of the underlying least-squares adjustment made it possible to set up pseudo-stochastic parameters with the highest possible frequency, the GPS observation sampling rate. It could be shown that such a "heavy" parametrization yields orbit positions which are identical with positions obtained from a precise point positioning at the GPS measurement epochs.

It is a well established fact that positions of low Earth satellites from a precise point positioning, which yields not the most precise positions, but positions that are independent from information about LEO dynamics, are a valuable product for the recovery of the Earth's gravity field [*Gerlach et al.*, 2003c]. In the last part of this work, we use simulated data to relax the strength of the dynamic laws by pseudo-stochastic orbit modeling to an extent interesting for gravity field determination, and we analyze the trade-off between the reduction of noise and the introduction of dynamic model information.

The present work has to be seen as a continuation of the research work about LEO orbit determination using GPS performed at AIUB. New aspects with respect to [*Bock*, 2003] are:

- zero and double difference orbit determination,
- extended pseudo-stochastic orbit modeling,
- independent validation of orbit results,
- continuous transition to precise point positioning, and
- pre-analysis of orbits for subsequent gravity field recovery.

Let us conclude with an outline of the subsequent chapters:

Chapter 2, *Low Earth Orbiters Using GPS,* gives an overview of satellites equipped with geodetic-type receivers, recapitulates their mission purposes, and presents their instruments. The CHAMP and GRACE satellites, which are relevant to this work, are described in more detail.

Chapter 3, *Gravity Field Models from Satellite Tracking,* gives a short overview of the different concepts for gravity field recovery from satellite tracking and lists the most recent gravity field models available.

Chapter 4, *Fundamentals of the GPS Data Analysis,* recapitulates the GPS principle, introduces the GPS institutions relevant to this work, and describes the most important aspects in modeling the GPS observables. A "pocket guide" of least-squares adjustment is provided as well.

Chapter 5, *Modeling Satellite Motion,* focuses on the derivation of orbit parameters, introduces the primary and variational equations, describes various types of pseudo-stochastic orbit modeling techniques, and presents efficient methods for the solution of the associated variational equations.

Chapter 6, *Efficient Normal Equation Handling,* analyzes the structure of the underlying normal equation systems, develops alternative procedures for an efficient orbit determination, and analyzes the resulting performance for zero and double difference orbit determination.

Chapter 7, *CHAMP and GRACE Orbit Determination Using Undifferenced GPS Data,* describes the external sources needed for orbit determination, sketches the orbit determination scheme, lists the available observations for an independent orbit validation, and presents and discusses selected results from orbit determination with undifferenced CHAMP and GRACE data. In addition, a combination study with accelerometer data is performed with simulated data.

Chapter 8, *GRACE Orbit Determination Using Doubly Differenced GPS Data,* deals with orbit determination using doubly differenced GPS data between the GRACE satellites and IGS tracking sites, determination of the flying baseline, ambiguity resolution, and the validation and comparison of the results.

Chapter 9, *Analyzing Pseudo-Stochastic Parameters,* is based on simulated data and discusses the interpretation of the pseudo-stochastic parameters and the associated orbits, analyzes spectra of orbit positions and velocities with respect to noise and dynamic model content, and compares the performance of reduced-dynamic and kinematic orbits for a recovery of gravity field parameters.

Chapter 10, *Summary, Conclusions, and Outlook,* summarizes the essential results and conclusions of this work and presents the continuation in the context of the GOCE HPF activities at AIUB.

2. Low Earth Orbiters Using GPS

Satellites in the Low Earth Orbit (LEO) are defined as Earth orbiting satellites at heights below 1600 km or below 2000 km (depending on the source) above the Earth's surface [*AIAA*, 1999]. Since the beginning of the space flight era, this belt has been of particular interest for a large variety of scientific satellites, e.g., for Earth observation, but also for many commercial satellites, e.g., for mobile telephone communication. The idea to make use of the upcoming constellation of the Global Positioning System (GPS) for validation and calibration of LEO positioning dates back to the late seventies [*Hoffman and Birmingham*, 1978], and was further promoted with the successful launch of the first GPS satellite on February 22, 1978. Only for years later, the GPSPAC (GPS receiver and processor package) onboard LANDSAT-4 was successfully launched on July 16, 1982, which was the first operating spaceborne GPS receiver in history. The lifetime of the receiver, however, ended shortly after launch [*Birmingham et al.*, 1983]. Another GPSPAC was launched onboard LANDSAT-5 on March 1, 1984, which eventually demonstrated that clock synchronization and orbit determination based on pseudo-range tracking data is feasible with navigational accuracies below 50 m for short arcs [*Heuberger*, 1984].

Since those early days, many GPS receivers have been used on all kinds of LEOs. Whereas the first ones mainly aimed at verifying and improving the concept of the satellite-to-satellite tracking (SST) with GPS, a significant milestone was set by the launch of the radar altimeter mission TOPEX/Poseidon [*Fu et al.*, 1994] on August 10, 1992, which was equipped with an onboard GPS demonstration receiver. For the first time, extensive use was made of both the GPS pseudo-range and the carrier phase. The inclusion of the very accurate phase observables showed that radial orbit accuracies of about 3 cm are feasible in the post-processing mode. This result was not only a strong and impressive demonstration for the potential of GPS precise orbit determination (POD) as a navigation tool in an operational satellite environment, it also showed the potential of GPS precise orbit determination as a backbone for further scientific applications, such as the determination of the ocean topography in the case of TOPEX/Poseidon. The prospect to continuously track satellites with sub-decimeter accuracy on a low cost basis encouraged many satellite mission designers to install GPS receivers on their LEOs in the following years. Table 2.1 gives an overview of selected LEOs equipped with spaceborne geodetic-type GPS receivers since the launch of TOPEX/Poseidon.

The following sections briefly describe the main mission objectives and orbital characteristics of the LEOs in Table 2.1. They give an impression of the wide range of GPS-supported scientific applications covered in the past, in the present, and, with utmost certainty, also in the future.

2.1 TOPEX/Poseidon

TOPEX/Poseidon [*Fu et al.*, 1994] was the first mission specifically designed and conducted to study the world's ocean circulation. It was launched on August 10, 1992 with a planned minimum operation time of three years, which was eventually exceeded by more than 10 years; operations were closed

Table 2.1: Initial elements of LEOs using geodetic-type GPS receivers (source: DISCOS database).

Satellite	Apogee (km)	Perigee (km)	Inclination (°)	Launch date
TOPEX/Poseidon	1331	1317	66.1	10 Aug. 1992
MicroLab-1	749	733	70.0	3 Apr. 1995
CHAMP	477	416	87.3	15 Jul. 2000
SAC-C	707	687	98.2	21 Nov. 2000
JASON-1	1333	1318	66.1	7 Dec. 2001
GRACE 1,2	506/507	483/483	89.0	17 Mar. 2002
ICESat	598	595	94.0	13 Jan. 2003
Formosat 3A,B,D-F	524-543	496-508	72.0	15 Apr. 2006
Formosat 3C	828	776	72.0	15 Apr. 2006
GOCE	270	270	96.5	Mar. 2008

on January 18, 2006. The mission purpose was to measure the ocean topography with a state-of-the-art radar altimeter (ALT). This primary instrument was the first spaceborne altimeter which made use of dual-frequency measurements to minimize the errors caused by the free electrons in the ionosphere [*Zieger et al.*, 1991], allowing it to measure heights with an accuracy of 2–2.5 cm. In addition to the radar instruments ALT, SALT (single-frequency solid state radar altimeter), and the TOPEX microwave radiometer (TMR), the satellite is equipped with a laser retro-reflector array for Satellite Laser Ranging (SLR), a receiver for Doppler Orbitographie et Radio-positionnement Intégrés par Satellite (DORIS), and a GPS demonstration receiver (GPSDR). Figure 2.1 shows the locations of the scientific instruments onboard the satellite. The three independent tracking systems are perfectly suited for POD and orbit validation. Thanks to the GPSDR and its antenna (on top of the 4.3 m mast) radial orbit accuracies of better than 3 cm could be achieved with the reduced-dynamic orbit determination technique [*Bertiger et al.*, 1994], which was much better than the pre-launch requirements. The high accuracy of the different tracking techniques made them perfectly suited for the external calibration of the measured altimeter heights, which is essential for a correct analysis of sea-level data [*Christensen et al.*, 1994].

2.2 Microlab-1

For a long time the meteorological community had been aware of the potential of LEOs to extract information about the Earth's atmosphere by analyzing satellite transmitted radio signals propagating through the Earth's atmosphere before reception onboard of the LEO [*Lusignan et al.*, 1969]. To achieve a global coverage of measurements, however, multiple orbiting transmitters and receivers are required. In this respect, the GPS constellation is perfectly well-suited to realize the transmitter side. Microlab-1 was the first satellite mission to demonstrate the GPS radio occultation technique in the framework of the GPS/MET experiment [*Rocken et al.*, 1997], which consisted of a space-qualified TurboRogue GPS receiver with a GPS receiving antenna. For an optimal mode of operation, the antenna boresight was pointed in the negative velocity direction, which is, of course, far from being ideal for other purposes like POD (because of an unfavorable coverage of trackable GPS satellites). Approximately, 100–150 globally distributed atmospheric profiles per day could be extracted from the GPS signals with the best accuracies obtained for atmospheric layers between 5 and 30 km, e.g., 0.2 to 0.4 K for temperature profiles. For more detailed and specific information on the technique of atmosphere sounding with GPS we refer to [*Kursinski et al.*, 1997].

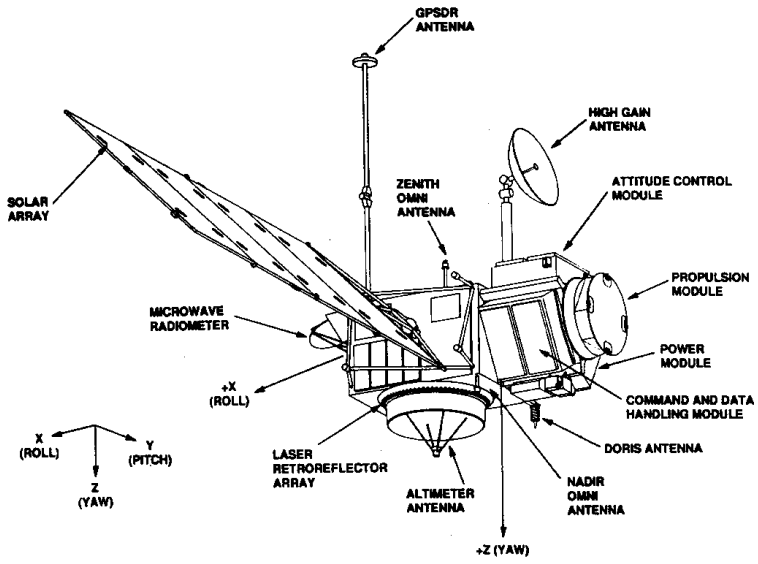

Figure 2.1: TOPEX/Poseidon satellite (courtesy by CNES/AVISO).

2.3 CHAMP

The CHAllenging Minisatellite Payload (CHAMP) [*Reigber et al.*, 1998] is a German mission specifically designed to study the Earth's gravity and magnetic fields. It was launched on July 15, 2000 with a planned operation time of five years, but thanks to two orbital maneuvers performed in June and December 2002 (see Fig. 2.4), the CHAMP spacecraft is still in use today and will probe the Earth's gravity field for at least one more year. One of the main mission purposes was the determination of the Earth's gravity field with unprecedented accuracy from continuously collected GPS measurements by the onboard receiver and non-gravitational accelerations measured by the onboard accelerometer. Apart from these primary instruments for gravity field recovery, the satellite carries a laser retro-reflector array for SLR tracking, star cameras for attitude determination, an ion drift meter, and magnetometers for magnetosphere science.

2.3.1 Orbit

CHAMP was launched into an almost circular, near-polar orbit with an initial height of 454 km and an inclination of 87° from the launch site at Plesetsk, Russia. A close to global coverage of the Earth with orbit and magnetometer data and local time variations at sub-satellite points ruled out other orbit configurations such as sun-synchronous orbits. The initial height of 454 km was chosen to meet the requirements of the different mission goals in the best possible way, and to guarantee a multi-year mission duration despite the presence of atmospheric drag which continuously lowers the satellite orbit. The atmosphere and ionosphere sounding experiments favor orbits at higher altitudes to scan the different atmospheric layers from the outside, whereas the gravity field recovery experiment asks for lower orbits to avoid a strong attenuation of the gravity field induced orbit perturbations. The initial height was thus ideal in the best case for the determination of the magnetic field.

Figure 2.4 shows the decaying orbit altitude over the first five years of the CHAMP mission. The slope of

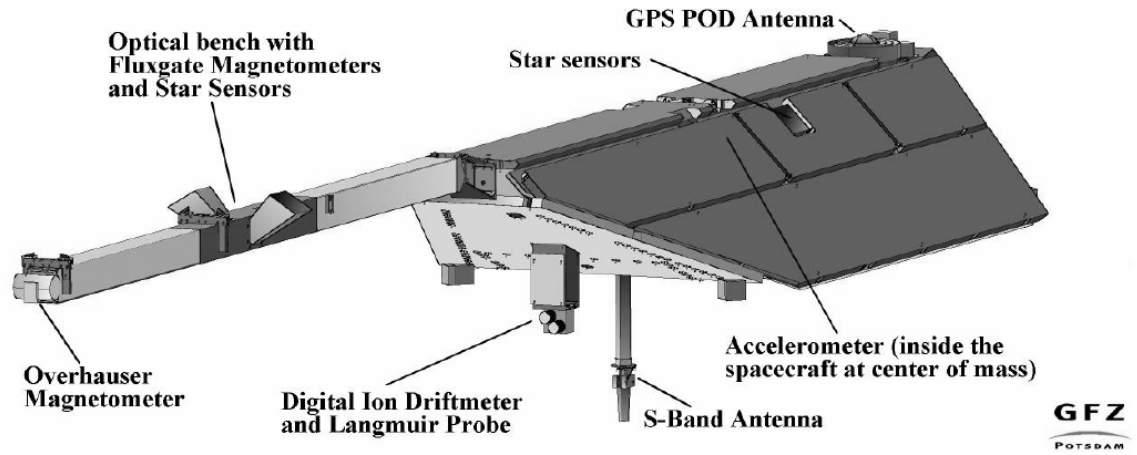

Figure 2.2: CHAMP satellite: front side (courtesy by GFZ Potsdam).

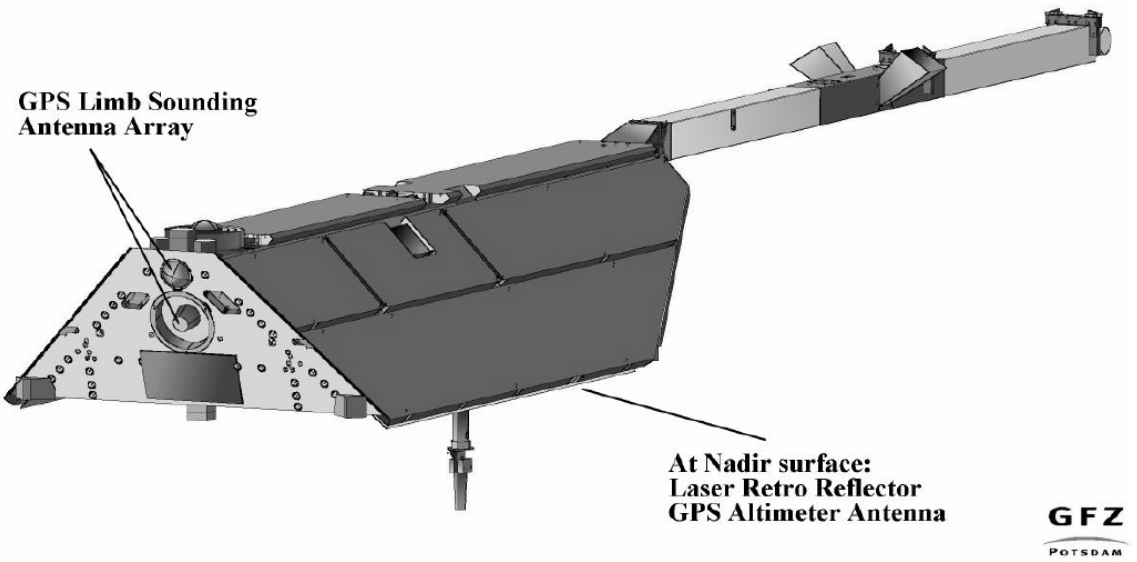

Figure 2.3: CHAMP satellite: rear side (courtesy by GFZ Potsdam).

the decay is correlated with the solar activity, e.g., showing large decay rates of more than one hundred meters per day around the solar maximum at the beginning of the year 2002. Therefore, two orbital maneuvers have been performed in 2002 to raise the altitude and to correct for orbit injection errors.

Attitude maneuvers are performed regularly (between 70 and 200 times per day) by small thruster pulses of the cold gas propulsion system to keep the orientation of the satellite within a few degrees with respect to the nominal orientation (see also Sect. 7.3.2). Nominally, the boresight vector of the GPS POD antenna coincides with the radial direction and the magnetometry boom (see Fig. 2.2) is oriented in flight direction.

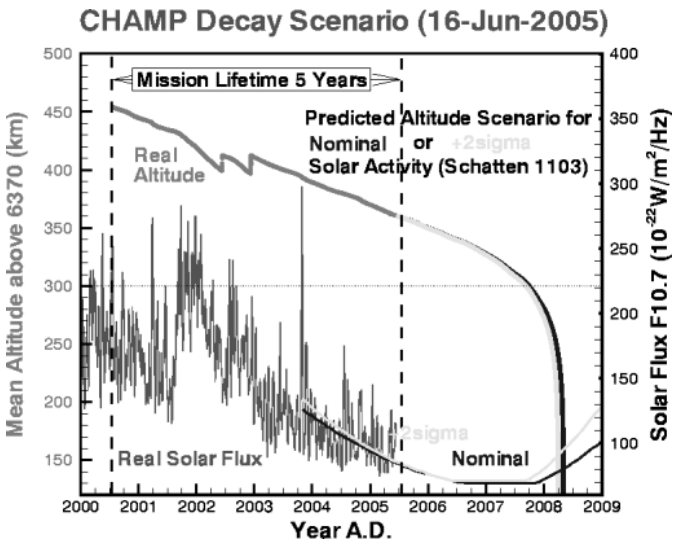

Figure 2.4: CHAMP orbit altitude over 5 years (courtesy by GFZ Potsdam).

2.3.2 Science Instruments

Figures 2.2 and 2.3 show the front and the rear side of the CHAMP satellite with its payload. Without exaggeration, the 8.333 m $\times$ 1.621 m $\times$ 0.750 m spacecraft itself must be considered as the main scientific instrument for the purpose of gravity field recovery from orbit perturbations, because it would represent a 522 kg free falling proof-mass in the absence of non-conservative forces. To support the gravity field estimation, a number of additional instruments such as the JPL BlackJack GPS receiver, the STAR accelerometer, and autonomous star sensors are part of the scientific payload.

The GPS BlackJack receiver is a 2nd generation TurboRogue Space Receiver (TRSR-2) manufactured at the Jet Propulsion Laboratory [*Kuang et al.*, 2001]. It collects dual-frequency phase and pseudo-range measurements on sixteen channels and serves four GPS antennas: one zenith-viewing POD antenna equipped with a choke ring, two limb-viewing atmosphere sounding helix antennas, and one nadir-viewing experimental helix altimeter antenna. The receiver firmware allows for tracking of up to twelve GPS satellites for POD, but was set to no more than seven from the day of activation on July, 17, 2000 until March 22, 2001, and to no more than eight until March 5, 2002 to keep the number of resets low [*Grunwaldt and Meehan*, 2003]. Since then the receiver was allowed to track up to ten GPS satellites.

The STAR (Space Triaxial Accelerometer for Research missions) instrument is manufactured by the Office National d'Etudes et de Recherches Aerospatials (ONERA) [*Touboul et al.*, 1998]. It uses electrostatic forces to keep a proof-mass at the center of an electrode-equipped cage, which provide a measure of the total (non-gravitational) acceleration acting on the cage, which is hardmounted to the satellite body and located within 2 mm to the vicinity of the center of mass. A total of six pairs of electrodes is used to control the three translational and the three rotational degrees of freedom and to serve the accelerometer sensor unit (SU) with electrode voltages for a final delivery of linear and angular accelerations as output voltages. Due to the design of the accelerometer SU, the specifications of the measured linear accelerations are not the same for the three axes; namely $3 \cdot 10^{-9}$ m/s^2 for the along-track and the cross-track axes and $3 \cdot 10^{-8}$ m/s^2 for the radial axis within a measurement bandwidth of 10^{-4} to 10^{-1} Hz [*Grunwaldt and Meehan*, 2003].

The ASC (Advanced Stellar Compass) instruments [*Jorgensen,* 1999] provide the precise orientation (attitude) of the satellite with respect to the stars in form of quaternions. The Danish University of Technology manufactured two ASCs for CHAMP, one being mounted on the boom to support magnetometry and another one being fixed on the spacecraft main body. Each instrument consists of two camera head units and a common data processing unit to match the obtained star centroids from the CCD arrays with computed star positions from an on-board HIPPARCOS catalogue [*ESA*, 1997]. The ASCs provide attitude data with a precision of about 4 arcsec, which are primarily needed for the magnetic field vector measurements and the ion flux direction measurements, but they are useful as auxiliary data for a proper modeling of the GPS and SLR phase center offsets as well. Note that an in-flight GPS navigation solution is needed to correct the attitude data for the effect of aberration [*Bock and Lühr,* 2001].

2.4 SAC-C

The "Satelite de Aplicanciones Cientificas-C" (SAC-C) is an Earth observing satellite which was launched on November 21, 2000 into a sun-synchronous orbit at an altitude of about 700 km. Among eleven scientific instruments, the satellite carries a BlackJack GPS receiver which serves four GPS antennas: one zenith-viewing POD antenna, one fore- and one aft-viewing antenna for atmosphere sounding, and one nadir-viewing antenna for GPS altimetry. Apart from the BlackJack receiver, the satellite is also equipped with a Lagrange GPS/GLONASS demonstration receiver. The spacecraft is not equipped with any other instrumentation for satellite tracking such as a laser retro-reflector array for SLR.

2.5 JASON-1

JASON-1 is the follow-on mission of TOPEX/Poseidon, see Sect. 2.1, and was launched on December 7, 2001. The satellite is smaller than its predecessor, but uses the same orbit and the same instrumentation. The primary instrument is the Poseidon-2 dual-frequency radar altimeter. In addition, the satellite is equipped with a JASON-1 microwave radiometer (JMR), a laser retro-reflector array for SLR, a DORIS receiver, and a GPS BlackJack receiver. The GPS antenna is mounted at the side of the spacecraft body and is tilted with respect to the axes of the satellite. Due to the altitude of about 1300 km of the satellite, orbit determination with GPS allows it to reconstruct the satellite trajectory with 1 cm radial accuracy, see [*Luthcke et al.,* 2003] and [*Haines et al.,* 2004].

2.6 GRACE

The Gravity Recovery And Climate Experiment (GRACE) [*Tapley and Reigber,* 2001] is a joint US-German partnership mission within NASA's Earth System Science Pathfinder (ESSP) program and may be viewed as the follow-on mission of CHAMP. GRACE was launched on March 17, 2002 with a planned operation time of five years with two identical formation flying satellites following each other in a nominal distance of 220 km on the same orbital trajectory. One of the main mission purposes is to map the time varying changes in the Earth's gravity field [*Tapley et al.,* 2004b] with unprecedented accuracy from continuously collected inter-satellite measurements by the K/Ka-Band Ranging (KBR) system, as well as from continuously collected GPS measurements by the onboard receivers and non-gravitational accelerations measured by the onboard accelerometers. Apart from these primary instruments for gravity field recovery, both GRACE satellites carry laser retro-reflector arrays for SLR tracking and star cameras for attitude determination.

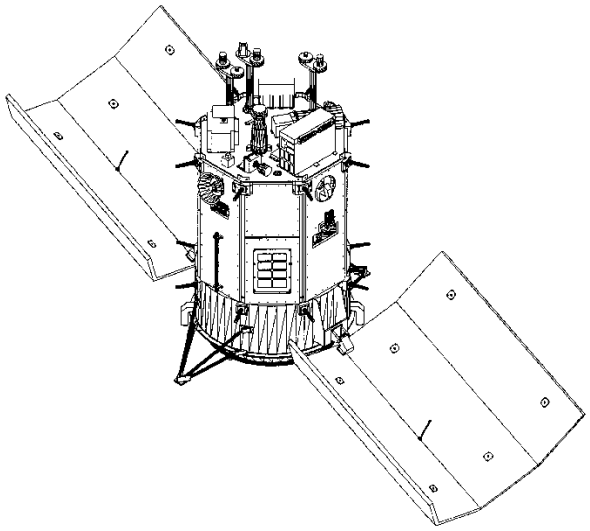

Figure 2.5: SAC-C satellite (courtesy by CONAE).

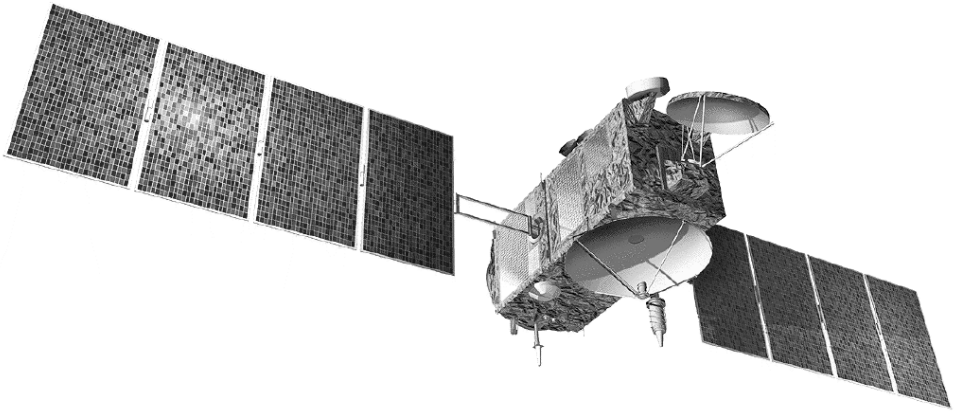

Figure 2.6: JASON-1 satellite (courtesy by CNES/AVISO).

2.6.1 Orbit

GRACE was launched into an almost circular, near-polar orbit with an initial height of 500 km and an inclination of 89° from the launch site at Plesetsk, Russia. As in the case of CHAMP, a close to global coverage of the Earth with orbit data ruled out other orbit configurations. The separation between the two satellites has to be actively controlled in order to stay within 170 and 270 km. This is accomplished by orbital maneuvers taking place about every 50 days. Note that GRACE A was the leading satellite from launch until the switch maneuver on December 10, 2005 at 03:47 UTC to limit the surface erosion of the K-band horns [*Montenbruck et al.*, 2006].

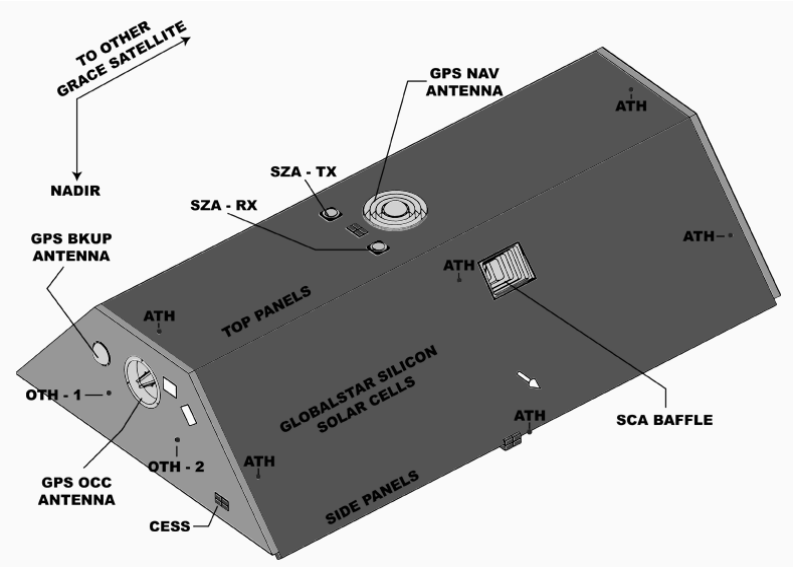

Figure 2.7: GRACE satellite: external view (courtesy by Astrium GmbH).

2.6.2 Science Instruments

Figure 2.7 shows the top side of one GRACE satellite with its payload. In essence, both GRACE satellites are identical in construction and resemble the CHAMP satellite (apart from the missing boom, which is unnecessary for the GRACE mission). Again, the 3.122 m $\times$ 1.942 m $\times$ 0.720 m spacecrafts themselves must be considered as the main scientific instruments to recover the temporal changes of the gravity field from the differential perturbations between both orbits. To meet the challenging mission requirements, a number of additional instruments such as the JPL BlackJack GPS receivers, the SuperSTAR accelerometers, autonomous star sensors, and last but not least, the K/Ka-Band Ranging system are part of the scientific payload.

The GPS BlackJack receiver is an advanced codeless dual-frequency space receiver manufactured at NASA's Jet Propulsion Laboratories [*Dunn et al.*, 2003]. It collects dual-frequency phase and pseudo-range measurements on sixteen channels and serves three GPS antennas: one zenith-viewing crossed dipole POD (GPS NAV) antenna equipped with a choke ring, and two limb-viewing antennas: a backup crossed dipole POD (GPS BKUP) antenna and a helix (GPS OCC) antenna for atmosphere sounding. The receiver firmware allows for tracking of up to twelve GPS satellites for POD, but was set to no more than ten to keep the number of resets low [*Dunn et al.*, 2003]. Note that the GPS BlackJack receiver is capable as well to collect the dual-frequency phase measurements from the K/Ka-Band Ranging system, to time tag the accelerometer data, and to read out the two CCD-based star cameras. It is therefore also referred to as the Instrument Processing Unit (IPU).

The SuperSTAR instrument [*Touboul et al.*, 1999] is a modified three-axis capacitive accelerometer, which is similar to the STAR instrument aboard CHAMP (see Sect. 2.3.2). The sensitive axes, however, point into the along-track and into the radial direction, the less sensitive axis points into the cross-track direction. According to the specifications, the accuracies are improved by about one order of magnitude with respect to the STAR instrument, i.e., to 10^{-10} m/s^2 and 10^{-9} m/s^2, respectively, within a measurement bandwidth of 10^{-4} to 10^{-1} Hz.

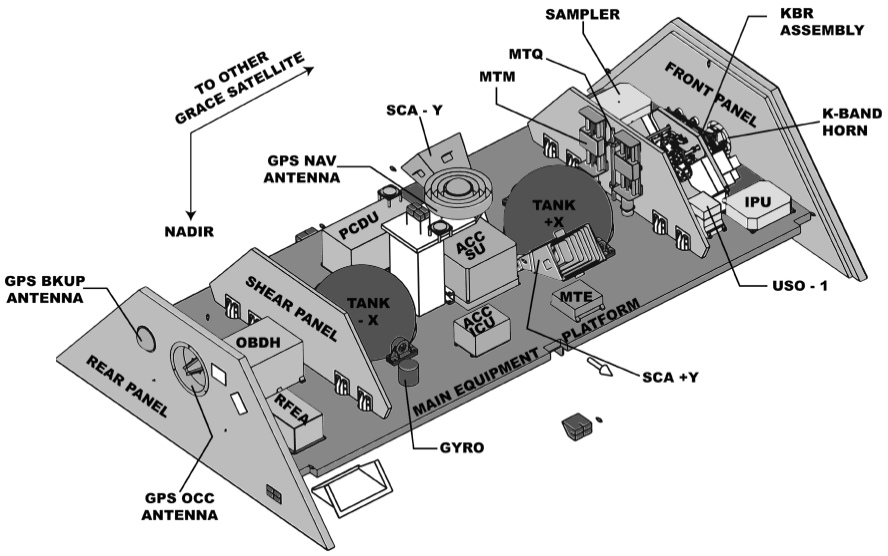

Figure 2.8: GRACE satellite: internal view (courtesy by Astrium GmbH).

The star camera assembly (SCA) provides the precise orientation (attitude) of the satellite with respect to the stars. As for CHAMP, one instrument was manufactured by the Danish University of Technology. Note that only one SCA consisting of two camera head units is mounted on the spacecraft body, which provides attitude data with a precision of about 25 arcsec [*Dunn et al.*, 2003]. The requirements are less stringent than for CHAMP due to the absence of precision vector measurements for magnetosphere science.

The K/Ka-Band Ranging (KBR) system manufactured at NASA's Jet Propulsion Laboratories is the key science instrument of the GRACE mission [*Dunn et al.*, 2003]. The hardware on each satellite consists of a single horn antenna for the transmission and reception of the K- and Ka-band microwave signals at 24.5 GHz and 32.7 GHz, respectively, an ultra-stable oscillator (USO) serving as a frequency reference, a KBR assembly for amplifying and mixing the received and the reference carrier phase, and an Instrument Processing Unit (IPU) for digital signal processing. The KBR system provides ultra-precise measurements of the biased range between both satellites on the K/Ka-Band links with systematic phase variations being as low as 10 μm (diameter of a human blood cell) or better [*Dunn et al.*, 2003]. Note that a GPS solution is used to determine the absolute time tags of the KBR measurements since the ultra-stable oscillator drives both the GPS receiver and the KBR system.

2.7 ICESat

The Ice, Cloud and land Elevation Satellite (ICESat) [*Schutz et al.*, 2005] was designed for cryosphere applications and was launched on January 13, 2003 into a 600 km altitude orbit with a 94° inclination. The mission purpose was to measure for the first time the inter-annual and long-term changes in polar ice-sheet volume with a state-of-the-art Geoscience Laser Altimeter System (GLAS), and to assess their impact on global sea level change [*Zwally et al.*, 2002]. The GLAS is used to derive the surface elevation

Figure 2.9: ICESat satellite (courtesy by Ball Aerospace & Technologies Corp.).

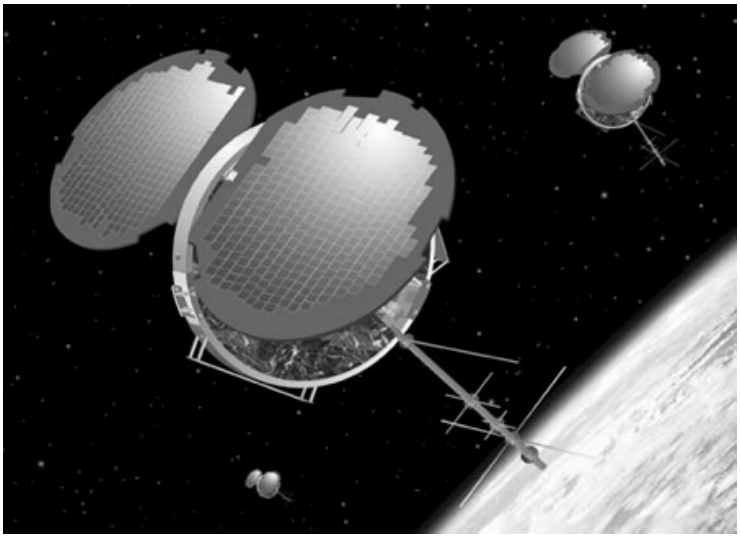

Figure 2.10: COSMIC constellation (courtesy by Orbital Sciences Corp.).

with a noise level of about 3 cm from echo pulses captured by a 1 m onboard telescope [*Abshire et al.*, 2005]. In addition to this primary instrumentation, the satellite is equipped with autonomous star sensors, a laser retro-reflector array for SLR, and two JPL BlackJack GPS receiver/antenna combinations (one spare). Precise reduced-dynamic orbit determination has been shown to exhibit radial accuracies of 2 cm [*Rim et al.*, 2005], which is a prerequisite for a correct analysis of the measured altimeter heights.

2.8 FORMOSAT-3

The Constellation Observing System for Meteorology, Ionosphere, and Climate (COSMIC) [*Wu et al.*, 2005] is a collaborative Taiwan-USA mission consisting of six microsatellites. It was launched on April 14, 2006 with a minimum designed operation time of two years. The main mission purpose is to collect GPS signals to study the atmosphere, the ionosphere, and geodesy. Therefore, the primary instrument of each microsatellite is the GPS occultation experiment (GOX). It consists of one GPS BlackJack receiver and four patch antennas: two fore/aft high-gain occultation limb antennas for atmosphere sounding and two fore/aft POD antennas for orbit determination. The POD antennas are mounted at the spacecraft's front and back side with a boresight of about 75° off the zenith in the satellite-fixed coordinate system. The GPS data from the POD antennas are collected at 1 Hz because they are also intended to be used for studying time variations in the Earth's gravity field [*Hwang and Kao*, 2003]. Apart from this primary instrumentation, each microsatellite is equipped with a tiny ionospheric photometer (TIP) and a tri-band beacon (TBB) for ionospheric research.

2.9 GOCE

The Gravity field and steady-state Ocean Circulation Explorer (GOCE) [*ESA*, 1999] is the first core mission within ESA's "Living Planet" program and may be viewed as a complementary mission to CHAMP and GRACE. It shall be launched in September, 2007 with a planned operation time of 20 months to probe the Earth's gravity field. The main mission purpose is the determination of the stationary part of the Earth's gravity field and geoid with the highest possible spatial accuracy and resolution from continuously collected gravity gradiometer and GPS measurements. Apart from the gravity gradiometer and the GPS receiver, the GOCE satellite will carry a laser retro-reflector array for SLR tracking and star cameras for attitude determination. The derived gravity and geoid model will serve solid Earth physics, oceanography, geodesy, and glaciology, see [*Rummel et al.*, 2002] and [*Johanessen et al.*, 2003].

2.9.1 Orbit

GOCE will be launched into an almost circular orbit with an inclination of 96.5° and an initial height of 270 km, which will be left to decay in the commissioning phase to the nominal altitude of 250 km. In order to simplify the spacecraft configuration, and to minimize the duration of eclipses, a sun-facing, sun-synchronous orbit ruled out other orbit configurations as they are in use for CHAMP and GRACE. For the planned launch date in September, a dusk-dawn orbit at a mean altitude of 250 km will be used during the first half of the mission, which will be lowered after the eclipse season to approximately 240 km for the second half of the mission. The very low altitude is necessary to meet the mission requirements to determine the mean gravity field and geoid with a precision of 1 mgal (one millionth of the surface gravity acceleration) and 1 to 2 cm, respectively, with a spatial resolution of better than 200 km full wavelength. In order to maintain the low orbital height, the satellite will be actively kept drag-free by an ion propulsion system.

2.9.2 Science Instruments

Figure 2.11 shows the top side of the GOCE satellite. The satellite envelope is a long and slender prism, with a cross-section of 0.8 m^2 and a length of 4 m. As Opposed to CHAMP and GRACE, the satellite body itself is no longer the main scientific instrument to recover the high-resolution gravity field, which

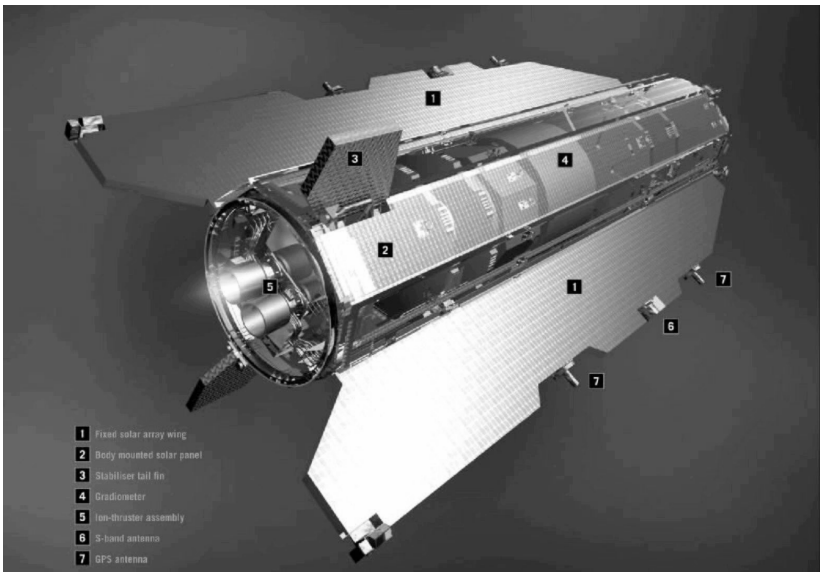

Figure 2.11: GOCE satellite (courtesy by ESA Publications Division).

will be mainly derived from the gravity gradiometer measurements. To meet the challenging mission requirements, a few additional instruments such as the Lagrange GPS receiver and autonomous star sensors are part of the scientific payload.

The GPS LAGRANGE receiver is a dual-frequency space-qualified receiver, see [*Zin et al.*, 2006], manufactured by Alcatel Alenia Space (formerly Laben). It will collect dual-frequency pseudo-range and phase measurements on twelve channels at 1 Hz frequency, and serves one active GPS helix antenna [*Dilssner et al.*, 2006]. As opposed to CHAMP and GRACE, it is planned that the receiver firmware will actually allow for tracking twelve GPS satellites at maximum. The GPS data will be used for precise orbit determination, but also for the recovery of the long to medium wavelength part of the gravity field, which is outside of the measurement bandwidth of the gravity gradiometer.

The three-axis gravity gradiometer is the core instrument of the GOCE mission and consists of three pairs of orthogonally mounted accelerometers. Each pair is separated by about 50 cm on the gradiometer baseline. The difference between accelerations measured by each of the two accelerometer pairs, in the direction joining them, is the basic gradiometer observable, while half of the sum is proportional to the externally induced perturbing accelerations (common mode measurement). According to the specifications, the accelerometer precision is 10^{-12} m/s$^2/\sqrt{\text{Hz}}$ for the sensitive axes. The individual accelerometers will be arranged in a way to recover the diagonal gravity gradient components and the centrifugal acceleration around the axis perpendicular to the orbit with the highest accuracy [*ESA*, 1999]. The gradiometer measurements are furthermore used as control signals for angular and thruster control of the spacecraft.

2.9.3 High-level Processing Facility

The High-level Processing Facility (HPF) is a distributed system which is developed and operated by the European GOCE Gravity Consortium (EGG-C). The tasks of the HPF are the generation of orbits and gravity field models (Level 2 products) from nominal and calibrated data from the gradiometer and the

GPS receiver (Level 1B products), and the generation of the GOCE calibration and validation products.

The Astronomical Institute of the University of Bern (AIUB) is member of the HPF and will be in charge of the generation of the Precise Science Orbit product (SST_PSO_2), one of five Level 2 products generated by the HPF. The PSO product will consist of reduced-dynamic and kinematic science GOCE orbits, rotation matrices between the inertial and the Earth-fixed reference frames, and a quality report for the precise orbits. The orbit determination will be based on the methodologies presented in this work, and will be performed by AIUB, and validated by the Institute of Astronomical and Physical Geodesy (IAPG) at the Technical University of Munich (TUM). The challenging 1-D accuracy requirement to achieve will be 2 cm for the reduced-dynamic orbit with a latency of two weeks (with an ultimate goal of 1 cm). For more information about the ongoing preparation and implementation of the GOCE procedures at AIUB the reader is referred to [*Bock et al.*, 2007].

3. Gravity Field Models from Satellite Tracking

Satellite motion is governed by the sum of all forces acting on the satellite. This includes gravitational signals of the Earth's irregular gravity field at the satellite's altitude, third body perturbations due to the attraction by the Moon and the Sun, and non-gravitational perturbations arising from air drag (for low altitudes) and direct and indirect solar radiation pressure. Like a fingerprint, the resulting orbit perturbations (deviations from an ellipse) contain valuable information about the different constituents.

In order to get access to the orbit perturbations, a precise restitution of the satellite's trajectory by one or more satellite tracking techniques has to be performed. Only then it is possible to extract the orbit perturbations, and to subtract the non-gravitational constituents, either by taking into account air density and radiation pressure models or precise measurements from on-board accelerometers. Finally, the purely gravitational orbit signal is available for the aimed-at gravity field recovery.

This chapter briefly introduces the parametrization of the Earth's gravity field, gives a short overview of available state-of-the-art global gravity field models obtained from different satellite tracking techniques, and shows the change from the classical orbit perturbation methods to the most recent methodologies for gravity field recovery. For a more detailed overview, the reader is referred to, e.g., [*Johanessen et al.*, 2003] or [*Ilk et al.*, 2005].

3.1 Global Representation of the Earth's Gravitational Potential

The stationary part of the Earth's gravitational potential at any point above the Earth's surface is conveniently expressed on a global scale as a spherical harmonic (SH) expansion [*Heiskanen and Moritz*, 1967], which reads as

$$V(r,\beta,\lambda) = \frac{G\,M}{R}\sum_{n=0}^{n_{max}}\left(\frac{R}{r}\right)^{n+1}\sum_{m=0}^{n}\bar{P}_{n,m}(\sin\beta)\;\left(\bar{C}_{n,m}\,\cos(m\,\lambda)+\bar{S}_{n,m}\,\sin(m\,\lambda)\right)\;, \qquad (3.1)$$

where

r, β, λ are the spherical geocentric coordinates,

$G\,M$ is the gravitational constant times mass of the Earth,

R is the mean semi-major axis of the Earth,

n, m are the degree and order of the SH expansion,

n_{max} is the maximum degree of the SH expansion,

$\bar{P}_{n,m}$ is the normalized associated Legendre function of degree n and order m,

$\bar{C}_{n,m}, \bar{S}_{n,m}$ are the normalized SH coefficients and global gravity field model parameters, respectively.

The SH coefficients $\bar{S}_{n,0}$ are zero by definition. The term $\bar{C}_{0,0}$ is close to unity and scales $G\,M$. The degree 1 SH coefficients, $\bar{C}_{1,0}$, $\bar{C}_{1,1}$, and $\bar{S}_{1,1}$, are related to the geocenter coordinates, and the coefficients $\bar{C}_{2,1}$, $\bar{S}_{2,1}$, and $\bar{S}_{2,2}$ are connected to the principal axes of inertia. The SH coefficients represent the global structure and irregularities of the Earth's gravitational potential.

The number of coefficients $\bar{C}_{n,m}$ and $\bar{S}_{n,m}$ in the SH expansion (3.1) is given by

$$u_V = (n_{max} + 1)^2 \,. \tag{3.2}$$

The maximum degree n_{max} also dictates the spatial resolution of the truncated SH expansion (3.1) as

$$\Delta L = \frac{2\,\pi\,R}{n_{max}} \,, \tag{3.3}$$

where ΔL is the (full wavelength) resolution on the Earth surface.

3.2 Classical Gravity Field Mapping

The analysis of accumulated orbit perturbations from precise tracking data of some tens of satellites at different altitudes and inclinations has gradually improved the knowledge of the Earth's gravity field over the last three decades. These conventional methods have provided accurate models on the large scale structures of the gravity field, but are limited in the spatial resolution due to the sparse tracking coverage, mainly relying on Satellite Laser Ranging (SLR) and Doppler data. Further difficulties are related to a strong attenuation of high-degree gravitational signals with satellite altitude, and to the challenge to accurately model non-gravitational accelerations for satellites with a complex shape.

One of the latest pre-CHAMP satellite-only models, GRIM5-S1, has got full power up to about degree 32, and thus resolves all wavelengths down to 1200 km full wavelength [*Biancale et al.*, 2000]. The high flying laser satellites LAGEOS-1/2 and ETALON-1/2 strengthen the very long wavelength part of this gravity field solution, whereas the very low orbit of GFZ-1 at only 400 km exhibits among all 21 contributing satellites the most pronounced and broadest spectrum of gravitationally induced perturbations [*König et al.*, 1999]. The combined solution, GRIM5-C1, resolves all wavelengths down to 330 km (full wavelength) thanks to the incorporation of surface data from gravimetry and satellite altimetry [*Gruber et al.*, 2000].

The GRIM5-S1/C1 gravity field models were created to provide a most precise basis for initial orbit determination of the CHAMP satellite, and for a combination with the new observations from the CHAMP GPS receiver.

3.3 Gravity Field Mapping from High-Low SST Data

The analysis of orbit perturbations from continuously collected precise high-low satellite-to-satellite tracking (SST) data between the GPS constellation and the CHAMP spacecraft opened, together with precisely measured non-gravitational accelerations, a new era for gravity field mapping. For the first time it was possible to derive a high-quality long-wavelength gravity field model using only one satellite and from only a few months' worth of data [*Reigber et al.*, 2003b].

Figure 3.1 illustrates the concept of the high-low SST with GPS data. A very low Earth orbiting spacecraft (CHAMP) is continuously tracked by up to ten GPS satellites in three spatial directions, which

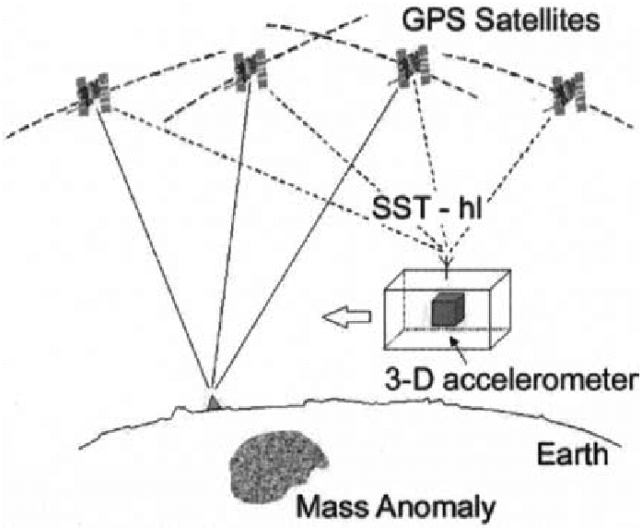

Figure 3.1: Satellite-to-satellite tracking in the high-low mode. A low Earth orbiter is tracked by the high orbiting GPS satellites relative to a network of GPS ground stations. Non-gravitational accelerations are measured by on-board accelerometry (courtesy by [*Johanessen et al.*, 2003]).

allows for almost "in-situ" 3-D position, velocity, and acceleration determination. The up-to-then unique combination of the satellite's low altitude (below 450 km), the near-polar orbit, the continuously collected dual-frequency pseudo-range and carrier phase observations by the GPS receiver, as well as the precise measurements of the non-gravitational accelerations by the STAR accelerometer proved to be very well suited to map the Earth's gravity field with unprecedented accuracy from orbit perturbations. Due to the almost "in-situ" character of the measurements, long satellite orbit arcs were no longer required as in the case of the classical gravity field mapping.

3.3.1 The EIGEN Gravity Field Models

The success of the proof-of-concept mission CHAMP is well documented by the series of gravity field models released by GFZ, called European Improved Gravity field model of the Earth by New techniques (EIGEN). Table 3.1 (top) gives an overview of the EIGEN models, all relying on different CHAMP data sets, but not on GRACE data. Note that the models need not to be necessarily complete up to the maximum degree n_{max}. Depending on the analyzed time period, bands of selected orders were extended to higher degrees in order to profit from an increased sensitivity in the recovery due to near-resonant orbit perturbations.

Shortly after the launch of CHAMP, a very first CHAMP-only gravity field model, EIGEN-1 (EIGEN-1S also includes other data), was computed from a very limited data base covering 88 days. In contrast, the most recent model, EIGEN-CHAMP03S, is derived from a total of 33 months of CHAMP data, which significantly improved the recovery. The accuracy of EIGEN-CHAMP03S is estimated to be about 5 cm in terms of geoid heights at a full wavelength of 800 km [*Reigber et al.*, 2004b].

The EIGEN solutions from Table 3.1 (top) are based on the so-called "brute-force" or direct approach,

Table 3.1: EIGEN (top) and alternative (bottom) gravity field models based on CHAMP data.

Model	Year	n_{max}	Reference
EIGEN-1S	2002	119	[*Reigber et al.*, 2002b]
EIGEN-1	2002	119	[*Reigber et al.*, 2003a]
EIGEN-2	2003	140	[*Reigber et al.*, 2003b]
EIGEN-CHAMP03S	2003	140	[*Reigber et al.*, 2004b]
TUM-1S	2003	60	[*Gerlach et al.*, 2003c]
TUM-2Sp	2003	60	[*Földváry et al.*, 2004]
TUM-2S	2004	70	[*Wermuth et al.*, 2004]
ITG-CHAMP01	2003	90	[*Mayer-Gürr et al.*, 2005]
DEOS_CHAMP-01C_70	2004	70	[*Ditmar et al.*, 2006]

implying that unknown gravity field coefficients are directly estimated from the GPS data together with all arc-specific parameters. The acronym is explained by the large number of unknown parameters that contribute to the individual, daily normal equation systems. According to (3.2), the coefficients $\bar{C}_{n,m}$, $\bar{S}_{n,m}$ alone represent more than ten thousand unknowns for $n_{max} > 100$.

3.3.2 Alternative Methods for Gravity Field Recovery

Since the beginning of the space flight era, other methods than the "brute-force" computation have been developed for the determination of the Earth's gravity field from satellite data. The so-called "energy balance" approach, e.g., was proposed by [*O'Keefe*, 1957] already in the late fifties, and relies on the balance between gravity potential and kinetic energy to determine the gravitational potential of the Earth by measuring the velocity of a satellite. Due to a lack of precise orbital data in the past, the feasibility of this method with real data could not be proved before the advent of the CHAMP era.

The time for the energy balance approach seemed to have come with the possibility to precisely restitute the CHAMP orbit positions and velocities from the multi-directional GPS high-low SST data, see [*Gerlach et al.*, 2003a], [*Howe and Tscherning*, 2003], and [*Gerlach et al.*, 2003b]. It turned out, however, that the recovered gravity field parameters were biased towards the a priori gravity field models used for the CHAMP orbit determination. At the same time it was shown by [*Švehla and Rothacher*, 2003c] that GPS high-low SST data are strong enough to determine precise CHAMP orbit positions (not velocities) by geometric means only, i.e., without using any a priori information on satellite dynamics, which finally paved the way for an unbiased gravity field recovery with the energy balance approach [*Gerlach et al.*, 2003c]. The use of the same kinematic positions had also a stimulating impact on other research groups to perform gravity field determination with alternative methods as well, e.g., with the short-arc method [*Mayer-Gürr et al.*, 2005] or with the acceleration method [*Ditmar et al.*, 2006], due to less demanding computational resources than in the case of classical numerical integration techniques [*Visser et al.*, 2003]. It is a drawback of the energy balance approach and the acceleration method, however, that they both require numerical differentiation to derive orbital velocities and accelerations, respectively, from the kinematic positions.

The success of the alternative methods can be judged from the models listed in Table 3.1 (bottom). They are all based on precise kinematic orbit positions computed by [*Švehla and Rothacher*, 2003c] and [*Švehla and Rothacher*, 2004a]. Note that they are complete up to the maximum degree n_{max}. For an assessment of the quality of the individual models we refer to the references given in Table 3.1 (bottom).

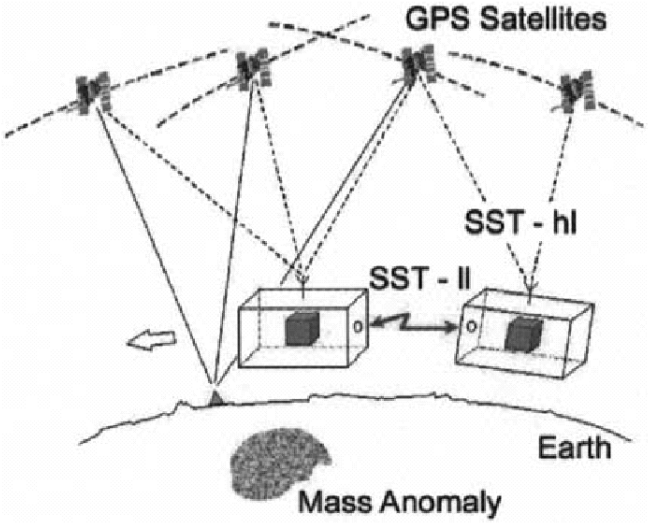

Figure 3.2: Satellite-to-satellite tracking in the low-low mode. The relative motion between two low Earth orbiters is measured by an inter-satellite link. High-low SST with GPS and onboard accelerometry are used as complementary measurements (courtesy by [*Johanessen et al.*, 2003]).

3.4 Gravity Field Mapping from Low-Low SST Data

It was noted already in the late sixties by [*Wolff*, 1969] that the inter-satellite signal between a pair of satellites orbiting the Earth in the same orbital plane contains significant information on the medium and short wavelength components of the Earth's gravity field. The analysis of the ultra-precise K-band microwave observations between the two GRACE spacecrafts, together with high-low GPS SST data and the measured non-gravitational accelerations, drastically improved the performance of the gravity field recovery in both accuracy and resolution. For the first time, it was possible to derive high-quality monthly gravity field solutions, and to determine the non-tidal temporal gravitational field variations, e.g., due to seasonal variations from continental water storage [*Tapley et al.*, 2004b].

Figure 3.2 illustrates the concept of the low-low SST for GRACE. The line-of-sight biased range between two low Earth orbiters is continuously measured by the ultra-precise K-band microwave observations, which enables an in-situ determination of the line-of-sight acceleration difference between the two spacecrafts. In combination with the very low altitude below 500 km, the near-polar orbit, the continuously collected dual-frequency pseudo-range and carrier phase observations by the GPS receiver, as well as the precise measurements of the non-gravitational accelerations by the SuperSTAR accelerometers, the configuration proved to be very well suited to set a new milestone for gravity field mapping.

3.4.1 GRACE Gravity Field Models

Table 3.2 gives an impression of the large number of GRACE mean gravity field models already released by CSR and GFZ (state October 2006). The maximum degrees are much higher for the GRACE-only models than for the CHAMP-only models, e.g., typically around 140, and the accuracies are improved by more than one order of magnitude, e.g., [*Reigber et al.*, 2005]. For details concerning methodologies,

Table 3.2: Gravity field models based on GRACE data.

GRACE Model	Combined Model	Year	Reference (Comb. Model)
GGM01S	GGM01C	2003	[*Tapley et al.*, 2004a]
EIGEN-GRACE01S		2003	-
EIGEN-GRACE02S	EIGEN-CG01C	2004	[*Reigber et al.*, 2006]
GGM02S	GGM02C	2004	[*Tapley et al.*, 2005]
EIGEN-GRACE03S	EIGEN-CG03C	2005	[*Förste*, 2005]
EIGEN-GRACE04S	EIGEN-GL04C	2005	[*Förste*, 2006]
ITG-GRACE02S		2006	-

specialties, and accuracies of the individual models we refer to the references in Table 3.2 for the combined models. Note that a first GRACE gravity field model, ITG-GRACE02S, has recently been released by a third institution (in addition to the GFZ and the CSR), see [*Mayer-Gürr et al.*, 2006].

3.5 Gravity Field Mapping from Satellite Gradiometry

Satellite gradiometry measures acceleration differences, ideally in three spatial directions, between the test masses of an ensemble of accelerometers inside one satellite. This measurement principle will be applied for the first time aboard of the upcoming GOCE mission [*ESA*, 1999].

Figure 3.3 illustrates the concept of satellite gradiometry. The measured signals correspond to the gradients of the gravitational acceleration, which is an in-situ determination of the second derivatives of the gravitational potential. It should be pointed out that the measurements contain the complete spectral band of the gravity field, but are limited by the measurement bandwidth of the accelerometers. Therefore, a combination with the GPS high-low SST data or with CHAMP/GRACE gravity field models will be needed to recover the long wavelength part of the gravity field.

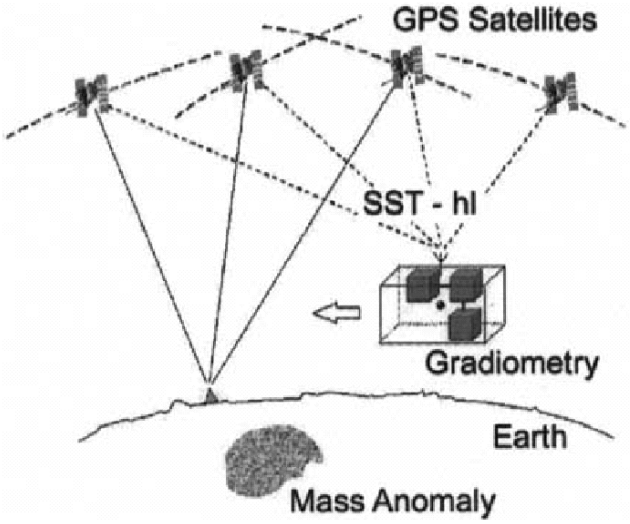

Figure 3.3: Satellite gravity gradiometry. The second-order derivative of the gravitational potential of the Earth is measured in a low Earth orbiter by differential accelerometry. High-low SST with GPS and common-mode accelerometry are used as complementary measurements (courtesy by [*Johanessen et al.*, 2003]).

4. Fundamentals of the GPS Data Analysis

4.1 The Global Positioning System (GPS)

In the early sixties, the U.S. Department of Defense began pursuing the idea of developing an all-weather, space-based radio navigation system. Stimulated by the experience gained with TRANSIT and TIMATION, forerunner systems of the Global Positioning System (GPS), the first GPS satellite, PRN 4, was successfully launched on 22 February, 1978. PRN 4 was the first of a series of eleven so-called Block-I satellites that were used to build up the constellation and to validate the concept for positioning.

GPS satellites of the Block-II type were used later on to complement the constellation gradually. The first Block-II satellite, PRN 14, was successfully launched on 14 February, 1989. It was the first of a series of nine Block-II satellites, followed by a total of nineteen Block-IIA satellites. A major milestone in the development of the GPS constellation was December 8, 1993, when 24 satellites, 3 of them active spares, were successfully operating. The full constellation guarantees that at least four satellites are simultaneously visible at any time and for any location in the vicinity of the Earth's surface.

The successful launch of the first Block-IIR satellite, PRN 13, on 23 July, 1997 initiated an ongoing process of maintaining and renewing the GPS constellation. At present (2006), a first modernized GPS satellite, PRN 17, even broadcasts a second civilian signal (L_{2C}).

4.1.1 GPS Satellite Orbits

The Block-II satellites are arranged in six orbital planes which are inclined by about 55° with respect to the Earth's equator and equally separated by 60° on the equator. Figure 4.1 (left) gives an impression of the GPS satellite orbits around the Earth as seen in inertial space from a latitude of 35°. The satellite orbits are close to circular, with a semi-major axis of about 26 600 km.

The orbital revolution period is about 11 hours 58 minutes, which is almost precisely half a sidereal day. Therefore, the satellites complete two orbital revolutions while the Earth rotates once by 360° with respect to inertial space. Consequently, the satellites' trajectories in an Earth-fixed coordinate system repeat themselves daily. Figure 4.1 (right) illustrates the shape of the resulting tracks for three individual GPS satellites.

4.1.2 GPS Frequencies and Codes

Each GPS satellite is equipped with an ensemble of rubidium and cesium atomic clocks to generate two coherent carriers, L_1 and L_2, in the microwave L-band. The two carrier frequencies, ν_1 and ν_2, are derived from the fundamental frequency $\nu_0 = 10.23\,\text{MHz}$ as

$$\begin{array}{rclcrcl} \nu_1 & = & 154\,\nu_0 & = & 1575.42\,\text{MHz} & \text{with} & \lambda_1 = \frac{c}{\nu_1} \approx 19.0\,\text{cm} \\ \nu_2 & = & 120\,\nu_0 & = & 1227.60\,\text{MHz} & \text{with} & \lambda_2 = \frac{c}{\nu_2} \approx 24.4\,\text{cm} \end{array} \quad , \tag{4.1}$$

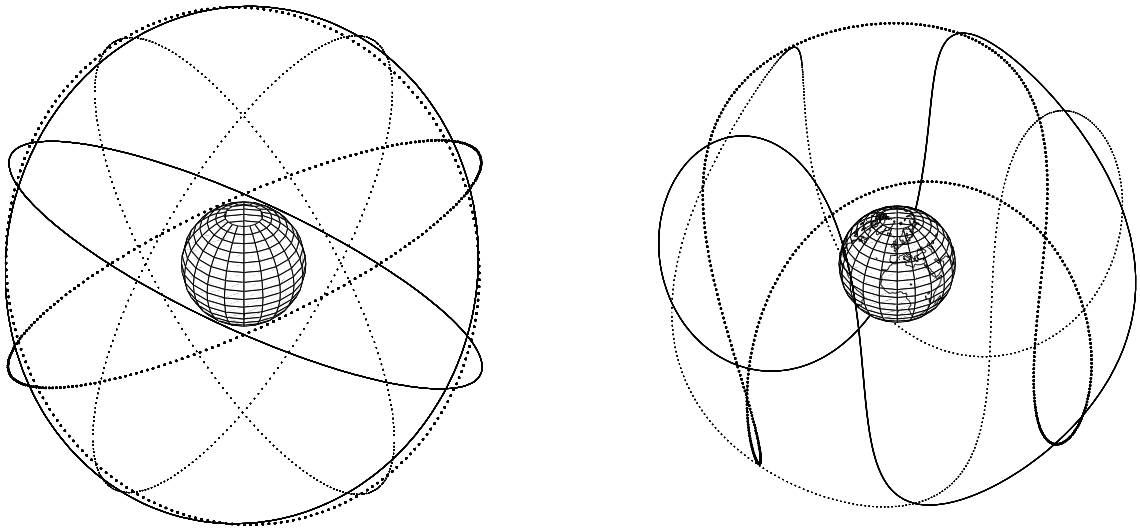

Figure 4.1: GPS satellite orbits viewed from inertial space (left) and shape of the tracks in an Earth-fixed system for three individual GPS satellites (right).

where

λ_1, λ_2 denote the corresponding wavelengths and

c is the speed of light.

Two pseudo-random noise (PRN) codes are generated and modulated on the carriers. The so-called coarse/acquisition (C/A) code is modulated with a chip rate of 1.023 Mbps on the L_1 carrier only. Its length per chip is about 293 m. The principal code for positioning is, however, the precision (P) code or its encrypted version, the Y-code, which is modulated with a chip rate of 10.23 Mbps on both carriers L_1 and L_2. Its length per chip is about 29.3 m. Note that "anti-spoofing" (AS), the artificial encryption of the P-code, is usually activated.

4.2 The International GNSS Service (IGS)

By the late 1980s, many organizations had recognized the potential of GPS for geodesy and geodynamics. A test campaign, conducted in the summer of 1992, involved the deployment and operation of a global GPS tracking network, the fast acquisition of observational data and transfer to global data centers (DCs), and the rapid data analysis by several analysis centers (ACs). Thanks to the successful operation and to the continuing effort of the large majority of participating organizations, the IGS became an official service of the International Association of Geodesy (IAG) on January 1, 1994 [*Beutler et al.*, 1994b], entitled at that time as the International GPS Service for Geodynamics. Since then, more than 200 organizations, agencies, and universities have shared their resources to define international standards and to establish an independent ground segment, which generates high-accuracy products on a best efforts basis with reliability through redundancy. The IGS name was shortened in 1999 to International GPS Service as it had become clear that the IGS was serving many applications other than geodynamics. At present (2006), ten ACs produce the IGS products, which are

- precise ephemerides and clocks of all active GPS satellites with a delay of 13 to 20 days for the final products, a delay of 17 h for the rapid products, and a delay of 3 h for the ultra-rapid products,
- Earth rotation parameters (ERP's), as polar motion and length of day,
- IGS tracking station coordinates, velocities, and clock corrections,
- global ionosphere maps, and
- IGS tracking station troposphere zenith path delays.

After more than 10 years as an official IAG service [*Dow et al.*, 2005], the IGS replaced the term GPS in its name by GNSS in 2005, paving the way for the integration of other global navigation satellite systems like the upcoming Galileo system. At present, three ACs are already producing orbits and other products for the functioning satellites of the Russian GLONASS (Global Navigation Satellite System), which is a first step towards a fully combined processing of data from multiple global navigation satellite systems.

The IGS consists of components like network stations, data centers, analysis centers (ACs), analysis center coordinator, central bureau, governing board, and users. At present ten ACs contribute to the IGS:

- Center for Orbit Determination in Europe, AIUB, Bern, Switzerland,
- Energy, Mines and Resources, NRCan, Ottawa, Canada,
- European Space Agency, ESOC, Darmstadt, Germany,
- GeoForschungsZentrum Potsdam, Germany,
- Jet Propulsion Laboratory, Pasadena, California, USA,
- Massachusetts Institute of Technology, Cambridge, Massachusetts, USA,
- National Geodetic Survey, NOAA, Silver Spring, Maryland, USA,
- Scripps Institution of Oceanography, San Diego, California, USA,
- U.S. Naval Observatory, Washington D.C., USA, and
- Geodetic Observatory Pecny, Czech Republic.

For more information about the IGS and its products, we refer, e.g., to [*Meindl*, 2005].

4.2.1 The Center for Orbit Determination in Europe

CODE, the Center for Orbit Determination in Europe, is one of the ten ACs of the IGS. It is a joint venture of the following three institutions:

- the Astronomical Institute of the University of Bern (AIUB), Bern, Switzerland,
- the Federal Office of Topography (swisstopo), Wabern, Switzerland, and
- the Federal Agency of Cartography and Geodesy (BKG), Frankfurt a.M., Germany.

CODE is located at the AIUB. Since 21 June, 1992, the start of the IGS test campaign, CODE has significantly contributed to the IGS with a wide range of products, which are generated with the latest version of the Bernese GPS Software, at present development version 5.1. Full use of the various products is made in this work whenever possible. For further information about the different CODE products and the applied processing strategies, the reader is referred, e.g., to [*Hugentobler et al.*, 2004b].

4.3 Modeling the GPS Observables

In this section, we discuss the GPS observation equations, the relevant linear combinations for LEO POD, and the ambiguity resolution techniques applicable to spaceborne GPS measurements. For a thorough derivation and a more detailed discussion, the reader is referred to [*Teunissen and Kleusberg*, 1998a].

In general, there are three types of GPS code observations, the C/A-, P_1-, and P_2-code observations, or their encrypted versions, the Y_1- and Y_2-code observations, which can be collected by a terrestrial or spaceborne GPS receiver. However, not every receiver type supports (or reports) all of them. It is worth mentioning that the BlackJack receivers aboard the CHAMP and GRACE satellites support the tracking of all code and accompanying carrier phase observations of all GPS satellites in view. The accompanying carrier phase observations are denoted as L_A, L_1, and L_2.

4.3.1 Code Observation Equation

The C/A-, P-, or Y-code, transmitted by the satellite k at time T^k and registered by the receiver i at time T_i, is defined as

$$P_i^k \doteq c\,(T_i - T^k)\;, \tag{4.2}$$

where

P_i^k is the code observation (or pseudo-range), expressed in units of length,

c is the speed of light,

T_i is the arrival (or observation) time of the signal, as measured by the clock of the receiver i, and

T^k is the transmission time of the signal, as measured by the clock of the satellite k.

GPS positioning is primarily based on one-way measurements of the signal traveling time. Therefore, a common reference time, the so-called GPS system time [*Rockwell*, 1984], has been defined, which is aligned to the international atomic time (TAI) with a constant offset of -19 s. Although the GPS satellites are equipped with redundant atomic clocks of either Cesium- or Rubidium-type, they are subject to an offset between their internal clocks and the GPS system time. The same holds for GPS receivers which are usually only equipped with temperature compensated crystal oscillators. Due to the lack of receiver clock synchronization, one cannot directly derive ranges from the code measurements, which therefore are called pseudo-ranges. Modern GPS receivers, such as the BlackJack receivers aboard the CHAMP and GRACE satellites, at least keep their clocks roughly synchronized with respect to GPS time within about one millisecond. As satellite and receiver clocks are usually affected by a drift, both clock offsets are only valid on a certain epoch.

The pseudo-range P_i^k may be related to the slant range ρ_i^k, the geometric distance between the receiver i at signal reception (GPS time t_i) and the satellite k at signal transmission (GPS time t^k), and to the delays due to the Earth's atmosphere as

$$P_i^k = \rho_i^k - c \cdot \Delta t^k + c \cdot \Delta t_i + \Delta\rho_{i,trop}^k + \Delta\rho_{i,ion}^k + \epsilon_i^k\;, \tag{4.3}$$

where

Δt^k is the clock offset $T^k - t^k$ of the satellite k w.r.t. the GPS system time,

Δt_i is the clock offset $T_i - t_i$ of the receiver i w.r.t. the GPS system time,

$\Delta\rho^k_{i,trop}$ is the signal delay due to the troposphere, expressed in units of length,

$\Delta\rho^k_{i,ion}$ is the signal delay due to the ionosphere, expressed in units of length, and

ϵ^k_i is the residual.

Equation (4.3) actually contains additional terms like satellite and receiver specific hardware delays. They are not explicitly listed in the single frequency observation equation because they cannot be separated from the clock offsets Δt^k and Δt_i, which implicitly compensate for them. Code multipath, other systematic errors, and the measurement thermal noise of the code observations are all part of the unmodeled residual term ϵ^k_i.

Note that antenna phase center offsets (and variations) of the emitting and receiving antenna have to be included in the term ρ^k_i to ensure a correct modeling. The same holds for relativistic corrections.

4.3.2 Phase Observation Equation

The accompanying accumulated carrier (beat) phase observation L_A, L_1, or L_2 of the corresponding code observation is defined as

$$L^k_i \doteq \lambda\,(\phi_i - \phi^k + N^k_i)\,, \tag{4.4}$$

where

L^k_i is the accumulated carrier phase observation, expressed in units of length,

λ is the corresponding wavelength,

ϕ_i is the carrier phase of the reference signal generated by the receiver i at arrival time T_i,

ϕ^k is the carrier phase of the transmitted signal at transmission time T^k, and

N^k_i is the constant initial carrier phase ambiguity, expressed in integer cycles of λ.

The carrier phase observation equation may be formulated in analogy to the observation equation (4.3) as

$$L^k_i = \rho^k_i - c\cdot\Delta t^k + c\cdot\Delta t_i + \Delta\rho^k_{i,trop} - \Delta\rho^k_{i,ion} + \lambda\cdot B^k_i + \epsilon^k_i\,, \tag{4.5}$$

where

B^k_i denotes a constant bias related to the initial carrier phase ambiguity, expressed in cycles.

The major difference to (4.3) is the bias term B^k_i, which consists of the integer-valued initial carrier phase ambiguity N^k_i, the real-valued non-zero phase difference between ϕ_i and ϕ^k at any common epoch, and the real-valued satellite and receiver specific hardware delays. As it is not possible to separate these constituents in undifferenced GPS data, only the total effect per satellite pass, receiver, and frequency can be determined by the real-valued bias term B^k_i. If the receiver loses lock of the signal, an additional bias term has to be set up due to the discontinuity (cycle slip) in the accumulated carrier phase observations. In addition, carrier phase observations are subject to a polarization induced phase wind-up [*Wu et al.*, 1993]. A further difference to the code observation equation (4.3) is the opposite sign of the ionospheric refraction $\Delta\rho^k_{i,ion}$ due to a phase advance instead of a group delay.

In essence, we may distinguish between two types of terms in the fundamental GPS observation equations (4.3) and (4.5):

- The slant range ρ_i^k, which contains the information about the "observation geometry". This term will be in the focus of this work as it allows to retrieve LEO receiver positions, and thus LEO orbits. The content of information is, however, not restricted to different positioning tasks as it contains as well information related to the GPS satellite orbits, Earth orientation, antenna locations, etc.
- The remaining, "non-geometry" terms, which contain information related to satellite and receiver clocks, Δt^k and Δt_i, to the tropospheric delay, $\Delta\rho_{i,trop}^k$, and to the ionospheric delay $\Delta\rho_{i,ion}^k$. They illustrate the wide range of scientific applications accessible by GPS, e.g., time and frequency transfer [*Dach et al.*, 2003], ionosphere mapping [*Schaer*, 1999], etc.

For LEO positioning, the last mentioned terms are merely a nuisance, in particular the ionospheric delay (the troposphere is non-existent at LEO altitudes). Fortunately, the ionosphere is a dispersive medium for the L-band carrier waves broadcasted by the GPS satellites, which in turn makes the ionospheric refraction to be proportional to $1/\nu^2$ in first order approximation, where ν is the carrier frequency. The observation equations for the set of observations provided by a dual-frequency, geodetic-type GPS receiver may therefore be written in a simplified notation as

$$\begin{aligned} P_{i,1}^k &= \tilde{\rho}_i^k + I_i^k \\ P_{i,2}^k &= \tilde{\rho}_i^k + \xi \cdot I_i^k \\ L_{i,1}^k &= \tilde{\rho}_i^k - I_i^k + \lambda_1 \cdot B_{i,1}^k \\ L_{i,2}^k &= \tilde{\rho}_i^k - \xi \cdot I_i^k + \lambda_2 \cdot B_{i,2}^k \,, \end{aligned} \tag{4.6}$$

where

$P_{i,1}^k$, $P_{i,2}^k$ are the P-code observations on both frequencies,

$L_{i,1}^k$, $L_{i,2}^k$ are the accumulated carrier phase observations on both frequencies,

$\tilde{\rho}_i^k$ is the geometric distance between the receiver i and the satellite k including the clock offsets and the tropospheric refraction,

I_i^k is the L_1-related ionospheric refraction,

ξ is the conversion factor $\nu_1^2/\nu_2^2 \approx 1.6469$ to obtain the L_2-related ionospheric refraction, and

$B_{i,1}^k$, $B_{i,2}^k$ are the carrier phase bias parameters on both frequencies.

It is important to mention that throughout this work the individual observations (4.6) will always be assumed to be completely uncorrelated in the time domain, as well as uncorrelated in-between different measurement types and frequencies. Furthermore, equal a priori variances (or weights) will be assumed for the code observables on both frequencies, and for the phase observables on both frequencies.

In principle, the set of dual-frequency code and carrier phase observations provides sufficient information for deriving the unknown quantities on the right-hand sides of equation (4.6). However, the code observations are two to three orders of magnitude less accurate than the phase observations, which exhibit a thermal noise at the level of mm's only and multipath errors that are confined to a quarter of the signal wavelength [*Braasch*, 1995]. Therefore, the carrier phase observables are primarily used for high-precision geodetic applications. In order to minimize or eliminate specific error sources, such as the ionospheric refraction on the right-hand sides of equation (4.6), it is common practice to form differences between the original measurements with GPS observations from other receivers, or to form linear

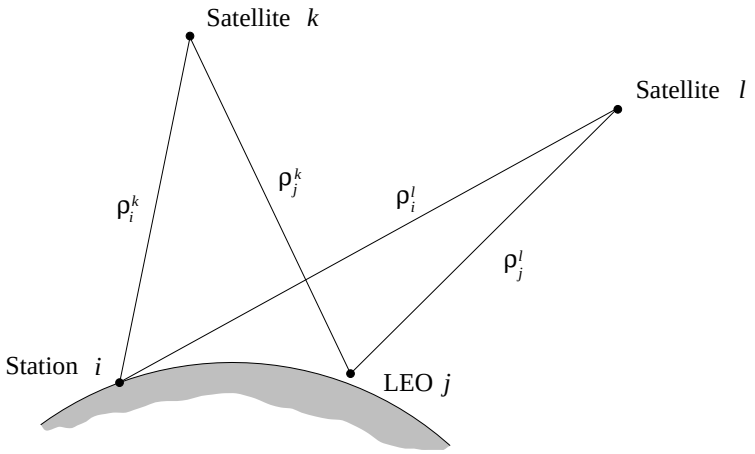

Figure 4.2: Double difference formed out of four one-way observations.

combinations of the original dual-frequency measurements, or to combine both techniques, respectively.

4.3.3 Observation Differences

Differences

$$L_{ij}^k \doteq L_i^k - L_j^k \tag{4.7}$$

of carrier phase (or code) observations that are acquired quasi-simultaneously by two receivers i and j (ground stations or LEOs) on the same frequency to the satellite k are called single differences. They are very sensitive to the relative position (baseline vector) between both receivers and thus of particular interest for formation flying spacecrafts [*Kroes*, 2006]. The satellite hardware delay and the satellite non-zero initial phase are completely eliminated by forming a single difference. In addition, the satellite clock offset Δt^k is almost completely eliminated and any spatially correlated errors, e.g., unmodeled ionospheric disturbances, are considerably reduced on short baselines as well. Multipath and other systematic errors are, however, still present since they generally have a different pattern for the individual antennas and antennas environments. Note that the individual single difference observations remain uncorrelated, but experience an increase of $\sqrt{2}$ in the noise level if the noise of the observations from both receivers is assumed to be equal.

Differences between two quasi-simultaneous carrier phase (or code) single differences to the satellites k and l

$$L_{ij}^{kl} \doteq L_{ij}^k - L_{ij}^l = (L_i^k - L_j^k) - (L_i^l - L_j^l) \tag{4.8}$$

are called double differences and are related to a satellite pair and a receiver pair. Figure 4.2 illustrates the forming of this new observable out of four undifferenced observations, also called zero difference observations, or two single difference observations. The double difference observable does no longer contain the receiver clock offsets Δt_i and Δt_j, the receiver non-zero initial phases, and almost no receiver hardware delays. The doubly differenced carrier phase bias parameter can thus be identified with the doubly differenced initial carrier phase ambiguity, which is of integer nature. Multipath and other systematic errors are, however, still present in (4.8). Note that the receiver clock offsets, obtained, e.g.,

from a code solution, must be applied with an accuracy of better than one microsecond prior to differentiation due to the GPS satellite motion.

In close analogy to equation (4.6), the dual-frequency code and carrier phase observation equations read as

$$\begin{aligned} P_{ij,1}^{kl} &= \tilde{\rho}_{ij}^{kl} + I_{ij}^{kl} \\ P_{ij,2}^{kl} &= \tilde{\rho}_{ij}^{kl} + \xi \cdot I_{ij}^{kl} \\ L_{ij,1}^{kl} &= \tilde{\rho}_{ij}^{kl} - I_{ij}^{kl} + \lambda_1 \cdot N_{ij,1}^{kl} \\ L_{ij,2}^{kl} &= \tilde{\rho}_{ij}^{kl} - \xi \cdot I_{ij}^{kl} + \lambda_2 \cdot N_{ij,2}^{kl} \,, \end{aligned} \tag{4.9}$$

where

$\tilde{\rho}_{ij}^{kl}$ is the doubly differenced geometric term including the tropospheric refraction and

$N_{ij,1}^{kl}$, $N_{ij,2}^{kl}$ are the integer-valued double difference carrier phase ambiguity parameters of both frequencies.

Note that the removal of the relative GPS receiver clock offset from (4.7) to (4.8) is done at the expense of one observation and the introduction of a correlation between observations of the same measurement type and frequency.

The difference of two double differences referring to different epochs yields a triple difference, which is unambiguous as the doubly differenced initial carrier phase ambiguities cancel out. The same is also true for epoch differences of undifferenced carrier phase observations [*Bock*, 2003]. Both types of observables are useful for screening the double and the zero difference carrier phase observations, respectively.

4.3.4 Linear Combinations

Linear combinations of dual-frequency carrier phase (or code) observations may be formed at each level of differentiation, e.g., at the level of double differences, by

$$L_{ij,n}^{kl} \doteq \kappa_{1,n} \cdot L_{ij,1}^{kl} + \kappa_{2,n} \cdot L_{ij,2}^{kl} \,, \tag{4.10}$$

where the coefficients $\kappa_{1,n}$ and $\kappa_{2,n}$ define the characteristics of the linear combination. Subsequently, we briefly review the relevant linear combinations for this work on the basis of double difference observations, and state the associated observation equations. For more detailed information, also about other linear combinations, the reader is referred to [*Schaer*, 1999].

Ionosphere-Free Linear Combination

The linear combination (LC) with the coefficients

$$\kappa_{1,3} \doteq \frac{\nu_1^2}{\nu_1^2 - \nu_2^2} \approx 2.5457 \qquad \text{and} \qquad \kappa_{2,3} \doteq \frac{-\nu_2^2}{\nu_1^2 - \nu_2^2} \approx -1.5457 \tag{4.11}$$

eliminates the ionospheric refraction terms quoted in equation (4.9), and is therefore called ionosphere-free. The double difference code and carrier phase observation equations thus read as

$$\begin{aligned} P_{ij,3}^{kl} &= \tilde{\rho}_{ij}^{kl} \\ L_{ij,3}^{kl} &= \tilde{\rho}_{ij}^{kl} + \lambda_3 \cdot B_{ij,3}^{kl} \,, \end{aligned} \tag{4.12}$$

where

λ_3 is the narrow-lane wavelength (to be defined in (4.16)) and

$B_{ij,3}^{kl}$ is a real-valued ambiguity parameter, expressed in narrow-lane cycles.

The ionosphere-free or L_3 LC is definitely the most frequently used observable for GPS analysis. This also applies for the applications which are in the focus of this work. Only for the task of ambiguity resolution, other LCs than the ionosphere-free LC have to be used.

Wide-Lane Linear Combination

The coefficients

$$\kappa_{1,5} \doteq \frac{\nu_1}{\nu_1 - \nu_2} \approx 4.5294 \qquad \text{and} \qquad \kappa_{2,5} \doteq \frac{-\nu_2}{\nu_1 - \nu_2} \approx -3.5294 \tag{4.13}$$

define the wide-lane LC, which is useful for ambiguity resolution. The wide-lane double difference carrier phase observation equation reads as

$$L_{ij,5}^{kl} = \tilde{\rho}_{ij}^{kl} - \xi_5 \cdot I_{ij}^{kl} + \lambda_5 \cdot N_{ij,5}^{kl} \,, \tag{4.14}$$

where

ξ_5 is the ionospheric conversion factor $-\nu_1/\nu_2 \approx -1.2833$,

λ_5 is the wide-lane wavelength $c/(\nu_1 - \nu_2) \approx 86.2$ cm, and

$N_{ij,5}^{kl}$ is an integer-valued ambiguity parameter, expressed in wide-lane cycles.

The ionospheric errors I_{ij}^{kl} and $\xi\, I_{ij}^{kl}$ expressed in L_1- and L_2-cycles, respectively, are considerably larger than the ionospheric error $\xi_5\, I_{ij}^{kl}$ expressed in L_5-cycles, e.g., an ionospheric error of 1.000 L_1- and 1.283 L_2-cycles results only in an ionosphere-induced error of -0.283 L_5-cycles. Resolving wide-lane ambiguities $N_{ij,5}^{kl}$ to integer values is therefore less sensitive to unmodeled ionospheric errors than resolving original L_1- and L_2-ambiguities, because of the relatively long wavelength $\lambda_5 \approx 86.2$ cm.

The wide-lane ambiguity $N_{ij,5}^{kl}$ is related to the doubly differenced L_1- and L_2-ambiguities as

$$N_{ij,5}^{kl} = N_{ij,1}^{kl} - N_{ij,2}^{kl} \,. \tag{4.15}$$

If the wide-lane ambiguity $N_{ij,5}^{kl}$ is known, it may be used to resolve the doubly differenced L_1- and L_2-ambiguities with the ionosphere-free LC. Introducing (4.15) in (4.12), the ionosphere-free phase observation equation reads as

$$L_{ij,3}^{kl} = \tilde{\rho}_{ij}^{kl} + \lambda_3 \cdot N_{ij,1}^{kl} - \kappa_{2,3} \cdot \lambda_2 \cdot N_{ij,5}^{kl} \,, \tag{4.16}$$

where

λ_3 is the narrow-lane wavelength $\kappa_{1,3} \cdot \lambda_1 + \kappa_{2,3} \cdot \lambda_2 = c/(\nu_1 + \nu_2) \approx 10.7$ cm (see (4.12)),

$N_{ij,1}^{kl}$ is the integer-valued L_1- or narrow-lane ambiguity, expressed in narrow-lane cycles, and

$\kappa_{2,3} \cdot \lambda_2 \cdot N_{ij,5}^{kl}$ is the known bias from the wide-lane ambiguity resolution.

The integer nature of the original, dual-band ambiguities $N_{ij,1}^{kl}$ and $N_{ij,2}^{kl}$ may thus be recovered via the previously resolved wide-lane ambiguity $N_{ij,5}^{kl}$. However, the narrow-lane ambiguity resolution is considerably more difficult than the wide-lane ambiguity resolution due to the relatively short wavelength $\lambda_3 \approx 10.7$ cm. Therefore, it is essential to properly model the doubly differenced geometric term $\tilde{\rho}_{ij}^{kl}$ including the tropospheric refraction. It might be seen as a slight advantage for purely spaceborne applications that the troposphere is non-existent at LEO altitudes.

Melbourne-Wübbena Linear Combination

[*Melbourne,* 1985] and [*Wübbena,* 1985] independently proposed a LC of dual-band phase and code measurements which yields an observation equation for the wide-lane ambiguity $N_{ij,5}^{kl}$ only. At the level of double differences, this LC is formed according to

$$L_{ij,MW}^{kl} \doteq \kappa_{1,5} \cdot L_{ij,1}^{kl} + \kappa_{2,5} \cdot L_{ij,2}^{kl} + \kappa_{3,5} \cdot P_{ij,1}^{kl} + \kappa_{4,5} \cdot P_{ij,2}^{kl} \,, \tag{4.17}$$

with the code multipliers

$$\kappa_{3,5} \doteq \frac{-\nu_1}{\nu_1 + \nu_2} \approx -0.5620 \qquad \text{and} \qquad \kappa_{4,5} \doteq \frac{-\nu_2}{\nu_1 + \nu_2} \approx -0.4380 \tag{4.18}$$

and the phase multipliers being defined by (4.13). The Melbourne-Wübbena LC eliminates the geometry, the troposphere, and the clock offsets due to

$$\kappa_{1,5} + \kappa_{2,5} + \kappa_{3,5} + \kappa_{4,5} = 0 \,, \tag{4.19}$$

and the ionosphere due to

$$-\kappa_{1,5} - \xi \cdot \kappa_{2,5} + \kappa_{3,5} + \xi \cdot \kappa_{4,5} = 0 \,, \tag{4.20}$$

keeping only the wide-lane ambiguity term $\lambda_5 \cdot N_{ij,5}^{kl}$. Therefore, this LC may be used for wide-lane ambiguity fixing even on long baselines due to the eliminated ionospheric refraction. However, P-code measurements $P_{ij,1}^{kl}$ and $P_{ij,2}^{kl}$ of good quality are a prerequisite, because (4.17) is dominated by the noise of the code observations.

4.4 Pocket Guide of Least-Squares Adjustment

Least-squares adjustment is the mathematical method uniquely used in this work to derive LEO orbits from GPS data. We refer to [*Tapley et al.*, 2004c] for a discussion of other parameter estimation algorithms in the context of orbit determination.

Let us assume that each observation may be expressed as a function of the parameters of a given mathematical model. Based on the model function $\boldsymbol{F}$, we may write the system of observation equations in the presence of observation errors as

$$\boldsymbol{L}' + \boldsymbol{\epsilon} = \boldsymbol{F}(\boldsymbol{X}) \,, \tag{4.21}$$

or, if $\boldsymbol{F}$ is a non-linear function of the parameters, in its linearized form as

$$\boldsymbol{L}' + \boldsymbol{\epsilon} = \boldsymbol{F}(\boldsymbol{X}_0) + \boldsymbol{A}\,\boldsymbol{x} \,, \tag{4.22}$$

with the column arrays

$\boldsymbol{L}'$ of the actual observations,

$\boldsymbol{\epsilon}$ of the observation corrections (or residuals),

$\bar{\boldsymbol{L}} = \boldsymbol{L}' + \boldsymbol{\epsilon}$ of the adjusted observations,

$\boldsymbol{X} = \boldsymbol{X}_0 + \boldsymbol{x}$ of the adjusted model parameters,

$\boldsymbol{X}_0$ of the approximate (or a priori) model parameters,

$\boldsymbol{x}$ of the model parameter corrections w.r.t. $\boldsymbol{X}_0$ (solution vector), and

$\boldsymbol{A}$, which denotes the first design (or Jacobi) matrix.

The first design matrix is defined by

$$\boldsymbol{A} \doteq \left.\frac{\partial \boldsymbol{F}(\boldsymbol{X})}{\partial \boldsymbol{X}}\right|_{\boldsymbol{X}=\boldsymbol{X}_0} \tag{4.23}$$

Rearranging the linearized observation equations yields the system of correction equations

$$\boldsymbol{\epsilon} = \boldsymbol{A}\,\boldsymbol{x} - \left(\boldsymbol{L}' - \boldsymbol{F}(\boldsymbol{X}_0)\right) = \boldsymbol{A}\,\boldsymbol{x} - \boldsymbol{l}\,, \tag{4.24}$$

where the term $\boldsymbol{l} \doteq \boldsymbol{L}' - \boldsymbol{F}(\boldsymbol{X}_0)$ is often referred to as "observed-minus-computed" (O–C).

The nature of the observation errors is taken into account by a stochastic model, which is described by

$$\boldsymbol{P} = \boldsymbol{Q}_{ll}^{-1} = \sigma_0^2\,\boldsymbol{C}_{ll}^{-1}\,, \tag{4.25}$$

where

$\boldsymbol{P}$ is the weight matrix of the observations,

$\boldsymbol{Q}_{ll}$ is the cofactor matrix of the observations,

σ_0 is the a priori standard deviation of unit weight, and

$\boldsymbol{C}_{ll}$ is the covariance matrix of the observations.

Observe that the weight matrix $\boldsymbol{P}$ is diagonal, if the observations are uncorrelated. In this case, the diagonal elements are given by $P_{ll} = \sigma_0^2/\sigma_l^2$, where σ_l^2 is the a priori variance of the corresponding observation.

In least-squares adjustment, the solution of the correction equation (4.24) is obtained by minimizing the quadratic form $\boldsymbol{\epsilon}^T\,P\,\boldsymbol{\epsilon}$. The underlying variation problem can be solved by Lagrange multipliers, which yield the normal equation system

$$\left(\boldsymbol{A}^T\,\boldsymbol{P}\,\boldsymbol{A}\right)\,\boldsymbol{x} - \boldsymbol{A}^T\,\boldsymbol{P}\,\boldsymbol{l} = \boldsymbol{N}\,\boldsymbol{x} - \boldsymbol{b} = \boldsymbol{0}\,, \tag{4.26}$$

where

$\boldsymbol{N} \doteq \boldsymbol{A}^T\,\boldsymbol{P}\,\boldsymbol{A}$ is the normal equation matrix and

$\boldsymbol{b} \doteq \boldsymbol{A}^T\,\boldsymbol{P}\,\boldsymbol{l}$ is the right-hand side of the normal equation system.

$\boldsymbol{N}$ is by definition a quadratic and symmetric matrix. If it is regular, the solution vector follows as

$$\boldsymbol{x} = \left(\boldsymbol{A}^T\,\boldsymbol{P}\,\boldsymbol{A}\right)^{-1}\,\boldsymbol{A}^T\,\boldsymbol{P}\,\boldsymbol{l} = \boldsymbol{N}^{-1}\,\boldsymbol{b}\,, \tag{4.27}$$

where

$\boldsymbol{N}^{-1}$ is the inverse normal equation matrix.

The estimated (a posteriori) standard deviation of unit weight is computed as

$$m_0 = \sqrt{\frac{\boldsymbol{\epsilon}^T \, P \, \boldsymbol{\epsilon}}{f}} \tag{4.28}$$

for $f > 0$, where

$f \doteq n - u$ is the degree of freedom (DOF) of the least-squares adjustment,

n is the number of observations, and

u is the number of adjusted model parameters.

Note that the quadratic form (sum of the weighted residual squares) may be computed either using (4.24), which makes it necessary to evaluate the first design matrix $\boldsymbol{A}$, or, alternatively, by the more efficient but numerically less stable formula

$$\boldsymbol{\epsilon}^T \, P \, \boldsymbol{\epsilon} = \boldsymbol{l}^T \, P \, \boldsymbol{l} - \boldsymbol{x}^T \, \boldsymbol{b} \, . \tag{4.29}$$

The covariance matrix of the adjusted model parameters is given by

$$\boldsymbol{C_{xx}} = m_0^2 \, \boldsymbol{Q_{xx}} = m_0^2 \, \boldsymbol{N}^{-1} \, , \tag{4.30}$$

where

$\boldsymbol{Q_{xx}}$ is the cofactor matrix of the adjusted model parameters.

The (a posteriori) standard deviations of the adjusted model parameters are given by

$$m_x = \sqrt{C_{xx}} = m_0 \, \sqrt{Q_{xx}} \, , \tag{4.31}$$

where C_{xx} and Q_{xx} are diagonal elements of the covariance and cofactor matrices, respectively.

The covariance matrix of a particular function $\boldsymbol{y} = \boldsymbol{B} \, \boldsymbol{x} + \boldsymbol{y}_0$ of the adjusted model parameters is given by the general law of error propagation

$$\boldsymbol{C_{yy}} = \boldsymbol{B} \, \boldsymbol{C_{xx}} \, \boldsymbol{B}^T \tag{4.32}$$

4.4.1 Parameter Pre-Elimination

The parameter pre-elimination technique is useful to handle a large number of model parameters efficiently, e.g., epoch-specific receiver clock offsets and pseudo-stochastic orbit parameters in the context of LEO orbit determination, as it will be outlined in Sects. 6.1 and 6.3, respectively. Let us subdivide the system of normal equations (4.26) into two parts

$$\begin{pmatrix} \boldsymbol{N_{11}} & \boldsymbol{N_{12}} \\ \boldsymbol{N_{21}} & \boldsymbol{N_{22}} \end{pmatrix} \cdot \begin{pmatrix} \boldsymbol{x_1} \\ \boldsymbol{x_2} \end{pmatrix} = \begin{pmatrix} \boldsymbol{b_1} \\ \boldsymbol{b_2} \end{pmatrix} \tag{4.33}$$

and assume that we are not interested in the actual values of the solution sub-vector $\boldsymbol{x_2}$. In this case, we may reduce the normal equation system (4.33) by pre-eliminating the model parameters $\boldsymbol{x_2}$, which yields the modified system of normal equations as

$$\boldsymbol{N_{11}^*} \, \boldsymbol{x_1} = \boldsymbol{b_1^*} \, , \tag{4.34}$$

where

$\boldsymbol{N_{11}^*} = \boldsymbol{N_{11}} - \boldsymbol{N_{12}}\,\boldsymbol{N_{22}^{-1}}\,\boldsymbol{N_{21}}$ is the normal equation matrix of the model parameters $\boldsymbol{x_1}$ and

$\boldsymbol{b_1^*} = \boldsymbol{b_1} - \boldsymbol{N_{12}}\,\boldsymbol{N_{22}^{-1}}\,\boldsymbol{b_2}$ is the corresponding right-hand side of the normal equation system.

It must be underlined that the pre-eliminated model parameters $\boldsymbol{x_2}$ were correctly taken into account in the normal equation system (4.34) although their estimates are no longer available. One must be aware, however, that the parameter pre-elimination step cannot be performed at any arbitrary time; it can be performed only if additional observations do no longer contribute directly to the elements related to the solution sub-vector $\boldsymbol{x_2}$ of the normal equation system (4.33).

The quadratic form $\boldsymbol{\epsilon}^T\,P\,\boldsymbol{\epsilon}$ may be computed for the modified normal equation system (4.34) by formula (4.29) as

$$\boldsymbol{\epsilon}^T\,P\,\boldsymbol{\epsilon} = \boldsymbol{l}^{*T}\,P\,\boldsymbol{l}^* - \boldsymbol{x_1}^T\,\boldsymbol{b_1^*}\,, \tag{4.35}$$

where

$\boldsymbol{l}^{*T}\,P\,\boldsymbol{l}^* = \boldsymbol{l}^T\,P\,\boldsymbol{l} - \boldsymbol{b_2}^T\,\boldsymbol{N_{22}^{-1}}\,\boldsymbol{b_2}$ is the modified quadratic form of the terms O–C.

4.4.2 Parameter Constraining

It is common practice to constrain selected model parameters to their a priori values (“absolute constraints”) or to other parameters (“relative constraints”). This may be done to suppress large excursions of weakly determined model parameters from their a priori values or from neighboring parameter values, which is frequently done with pseudo-stochastic orbit parameters in the context of LEO orbit determination. One must be aware, however, that a priori information is introduced by this process into the system of normal equations, which may or may not be desired for certain applications.

Absolute Constraining

Parameter constraints may be introduced by artificial observations with a user-specified variance σ_{abs}^2. These observations have to be appended to the system of observation equations (4.22). If the change with respect to the a priori value is used as the actual parameter in the artificial observation equation, the weight

$$W = \frac{\sigma_0^2}{\sigma_{abs}^2} \tag{4.36}$$

has to be only added to the corresponding diagonal element of the normal equation matrix $\boldsymbol{N}$, because the value O–C is zero in this special case. Observe that the DOF counter has to be incremented by 1, as well.

Relative Constraining

In order to constrain the difference of two particular model parameters with respect to each other, the weight matrix

$$\boldsymbol{W} = \begin{pmatrix} W & -W \\ -W & W \end{pmatrix} \qquad \text{with} \qquad W = \frac{\sigma_0^2}{\sigma_{rel}^2} \tag{4.37}$$

has to be added to the normal equation matrix $\boldsymbol{N}$, i.e., the values W and $-W$ have to be added to the diagonal and off-diagonal elements corresponding to the two parameters involved. Note that the DOF counter has to be incremented by 1, again.

5. Modeling Satellite Motion

Artificial Earth satellites are generally extended objects of considerable size, consisting of several components of complex shape such as antennas, thrusters, and solar panels. Satellite motion thus comprises the motion of its center of mass around the Earth, and the orientation of a satellite-fixed coordinate system in inertial space, which is addressed as the attitude of the satellite. Whereas the attitude of a passive satellite is uniquely defined by the Euler equations, see e.g., [*Beutler*, 2005], active satellites have to be correctly oriented at any time according to the instrument specifications. Therefore, the satellite's attitude has to be actively maintained and controlled, e.g., by momentum wheels or by frequent thruster firings, which makes attitude modeling difficult for certain satellites. In order to still guarantee a proper interpretation of the instrument readings, star cameras are installed on scientific satellites with stringent accuracy requirements, and measure the orientation of the satellite with high precision at any time with respect to the stars. Since the CHAMP and GRACE satellites considered here are equipped with such cameras, see Sects. 2.3.2 and 2.6.2, we may assume their attitude motion as known (see Sect. 7.3.2).

The satellite's center of mass motion around the Earth is governed by the sum of all forces acting on the satellite body. Since the satellite mass may always be neglected with respect to the masses of the Earth, Moon, Sun, and planets, their orbits and orientation may be assumed as known. Opposed to the third body perturbations, see Chapter 3, a very detailed description of the stationary part of the Earth's gravitational potential including thousands of terms is needed for an accurate modeling of the motion of the satellites considered here due to their very low altitudes above the Earth's surface. Moreover, tidal deformations of the Earth, the so-called solid Earth and ocean tides, as well as non-gravitational forces like air drag due to the Earth's upper atmosphere and solar radiation pressure effects have to be taken into account. It is unnecessary to say that the modeling of non-conservative forces is difficult for satellites with a complex shape.

In view of the fact that the most complex of the above mentioned models, i.e., the Earth gravitational potential models and the upper atmosphere density models, still heavily rely on the assimilation of data from very low Earth orbiting satellites, it may be understood that they are still not perfect and can be improved steadily. Therefore, it is of utmost importance that a most precise restitution of a satellite's trajectory from very accurate tracking data can be performed even in the presence of deficient dynamic models, e.g., during the initial phase of a new satellite mission before improved models are available.

This chapter introduces different orbit determination techniques applicable to high-low GPS SST data from LEO receivers. It starts with a short discussion of the underlying GPS observation equations with regard to orbit determination, introduces dynamic and kinematic orbit parameters, and subsequently focuses on the development of the mathematical equipment for a so-called pseudo-stochastic modeling of satellite orbits. Although these developments are applicable to any type of satellite and to any type of tracking data, pseudo-stochastic orbit modeling is mainly intended for LEO orbit determination based on high-low GPS SST data. Summaries of the presented algebra may be found in [*Jäggi et al.*, 2005b] and [*Jäggi et al.*, 2006a].

5.1 Extracting LEO Positions from GPS Data

According to Chapter 4, the slant range ρ_i^k contains the relevant information for positioning receiver i with respect to GPS satellite k. In order to rewrite the observation equations (4.6) or (4.9) for the determination of the position of a LEO receiver, the tropospheric refraction, $\Delta\rho_{i,trop}^k$, has to be omitted and the geometric term ρ_i^k has to be replaced by

$$\rho_{leo}^k = |\boldsymbol{r}_{leo}(t_{leo}) - \boldsymbol{r}^k(t_{leo} - \tau_{leo}^k)| \ , \tag{5.1}$$

where

$\boldsymbol{r}_{leo}$ is the inertial position of the LEO antenna phase center at GPS time t_{leo},

$\boldsymbol{r}^k$ is the inertial position of the antenna phase center of GPS satellite k at GPS time $t_{leo} - \tau_{leo}^k$, and

τ_{leo}^k is the signal traveling time between the two phase center positions.

Note that for the sake of simplicity the quasi-inertial International Celestial Reference Frame ICRF (see Sect. 7.3.1) is addressed as inertial frame. In order to extract the inertial center of mass position of the LEO spacecraft at time t_{leo}, additional information on the orientation of a satellite-fixed coordinate system has to be available, as well as the location and orientation of the receiving GPS antenna in this coordinate system (see Sect. 7.3.2). If both conditions are fulfilled, the LEO center of mass position may be modeled in (5.1) either by a dynamic or a kinematic orbit representation.

5.1.1 Dynamic Orbit Representation

A dynamic orbit representation seems to be natural for modeling satellite trajectories, because they are always particular solutions of an equation of motion. In a dynamic representation, the antenna phase center position $\boldsymbol{r}_{leo}$ is expressed in the inertial frame as

$$\boldsymbol{r}_{leo}(t_{leo}) = \boldsymbol{r}_{leo,0}(t_{leo}; a, e, i, \Omega, \omega, u_0; Q_1, ..., Q_d) + \delta\boldsymbol{r}_{leo,ant}(t_{leo}) \ , \tag{5.2}$$

where

$\boldsymbol{r}_{leo,0}$ is the LEO center of mass position, expressed in the inertial frame,

$\delta\boldsymbol{r}_{leo,ant}$ is the antenna phase center offset, expressed in the inertial frame,

$a, e, i, \Omega, \omega, u_0$ are six (unknown) LEO orbital elements O_j, $j = 1, ..., 6$, and

$Q_1, ..., Q_d$ are d (unknown) LEO dynamical parameters.

$\delta\boldsymbol{r}_{leo,ant}$ is introduced as known, and follows in the inertial frame from the antenna offsets, the phase center offsets (and variations), and the actual LEO attitude. The unknown parameters are the LEO orbital elements O_j, $j = 1, ..., 6$, and additional dynamical parameters.

Figure 5.1 gives an illustration of an orbit representation by the six initial osculating elements a, e, i, Ω, ω, and u_0 at time t_0. The semi-major axis a and the numerical eccentricity e describe the orbital shape, the inclination i and the right ascension Ω of the ascending node describe the orbital plane with respect to the Earth's equator, the argument ω of the perigee Π describes the orbital orientation, and the argument of latitude u_0 describes the satellite's position at time t_0. These six initial osculating elements are equivalent to initial conditions for position and velocity at time t_0, see, e.g., [*Beutler*, 2005].

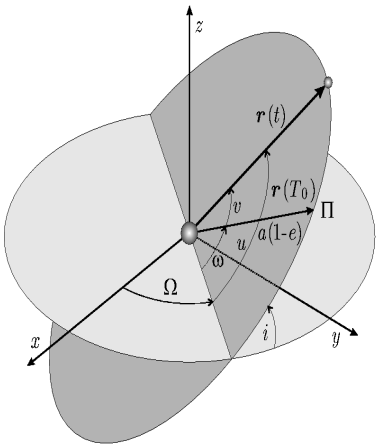

Figure 5.1: Initial osculating elements a, e, i, Ω, ω, and the argument of latitude u.

5.1.2 Kinematic Orbit Representation

Opposed to a dynamic representation which is restricted to objects that obey an equation of motion, the kinematic representation can be applied to all different kinds of moving objects, e.g., cars, ships, aircrafts, and satellites. Also for a LEO, the inertial phase center position $\boldsymbol{r}_{leo}$ is related to the center of mass as

$$\boldsymbol{r}_{leo}(t_{leo}) = \boldsymbol{R}(t_{leo}) \cdot (\boldsymbol{r}_{leo,e,0}(t_{leo}) + \delta\boldsymbol{r}_{leo,e,ant}(t_{leo})) \ , \tag{5.3}$$

where

$\boldsymbol{R}$ is the transformation matrix from the Earth-fixed to the inertial frame (see Sect. 7.3.1),

$\boldsymbol{r}_{leo,e,0}$ is the LEO center of mass position, expressed in the Earth-fixed frame, and

$\delta\boldsymbol{r}_{leo,e,ant}$ is the antenna phase center offset, expressed in the Earth-fixed frame.

In analogy to equation (5.2), $\delta\boldsymbol{r}_{leo,e,ant}$ is introduced as known. The unknown parameters are the epoch-wise kinematic coordinates, which are conventionally expressed in the Earth-fixed system because there exist more terrestrial than spaceborne applications. Note that kinematic positions of the LEO receiving antenna phase center could be established without the knowledge of antenna offsets and satellite attitude, but not the center of mass positions.

5.2 Dynamic LEO Orbit Determination

As mentioned in Sect. 5.1.2, kinematic positioning can be applied to a wide range of scenarios because no constraints are imposed on the receiver motion. However, kinematic positioning is very sensitive to bad measurements, unfavorable viewing geometry of GPS satellites, and data outages, which sometimes restricts its value in practice. Dynamic orbit determination, in contrast, makes use of physical models of the satellite motion to determine a best fitting trajectory to the measurements in the least-squares sense. This allows for some sort of “averaging” measurements from different epochs, which makes the resulting position estimates much less sensitive to bad measurements and data outages. To some extent, a satellite trajectory can even be propagated across data gaps, if good dynamic models are available.

This section briefly introduces the primary and variational equations needed for a mathematical description of satellite motion.

5.2.1 Primary Equations

Dynamic force models are used to propagate the satellite's center of mass position and velocity over time by means of numerical integration techniques [*Beutler*, 2005]. The equation of motion of an Earth-orbiting satellite including all perturbations reads in the inertial frame as

$$\ddot{\boldsymbol{r}} = -GM\frac{\boldsymbol{r}}{r^3} + \boldsymbol{f}_1(t, \boldsymbol{r}, \dot{\boldsymbol{r}}, Q_1, ..., Q_d) \doteq \boldsymbol{f} \tag{5.4}$$

with the initial conditions

$$\boldsymbol{r}(t_0) = \boldsymbol{r}(a, e, i, \Omega, \omega, u_0; t_0) \qquad \text{and} \qquad \dot{\boldsymbol{r}}(t_0) = \dot{\boldsymbol{r}}(a, e, i, \Omega, \omega, u_0; t_0)\ , \tag{5.5}$$

where

GM is the gravity constant times the mass of the Earth,

$\boldsymbol{r}$ is the geocentric position of the satellite, expressed in the inertial frame,

$\boldsymbol{f}_1$ is the perturbing acceleration acting on the satellite, expressed in the inertial frame, and

$\boldsymbol{f}$ is the total acceleration.

The acceleration $\boldsymbol{f}_1$ consists of all gravitational and non-gravitational accelerations taken into account to model the orbit perturbations. More specifically, dynamic force models are used to compute the gravitational and non-gravitational perturbations acting on the spacecraft, which may depend on the time t, the position $\boldsymbol{r}$, and the velocity $\dot{\boldsymbol{r}}$ of the satellite, as well as on additional force model parameters $Q_1, ..., Q_d$ to be adjusted.

Often, the perturbation model consists of a known part with accelerations given by analytical models, and of a part which includes force model parameters to be adjusted. Following the naming convention in [*Bertiger et al.*, 1994], we address the equation of motion (5.4) as deterministic if $\boldsymbol{f}_1$ only consists of (deterministic) accelerations given by analytical models. This implies that initial conditions, e.g., given by six Keplerian elements $a, e, i, \Omega, \omega, u_0$ at time t_0, and scaling factors $Q_1, ..., Q_d$ of analytically known accelerations (dynamical parameters) may be addressed as deterministic orbit parameters.

We always assume that an a priori orbit $\boldsymbol{r}_0(t)$ is available, e.g., realized by a dynamical fit of LEO positions obtained from a GPS code single point positioning solution (see Sect. 7.5). Therefore, orbit determination discussed in this work should be understood as an orbit improvement process, i.e., the actual orbit $\boldsymbol{r}(t)$ is expressed as a truncated Taylor series with respect to the unknown orbit parameters P_i about the a priori orbit, which is represented by the (a priori) parameter values $P_{0,i}$:

$$\boldsymbol{r}(t) = \boldsymbol{r}_0(t) + \sum_{i=1}^{n} \frac{\partial \boldsymbol{r}_0}{\partial P_i}(t) \cdot (P_i - P_{0,i})\ , \tag{5.6}$$

where

n denotes the total number $(6 + d)$ of orbit parameters and

$\frac{\partial \boldsymbol{r}_0}{\partial P_i}(t)$ describes the orbital change due to a change in the parameter P_i.

Equation (5.6) allows us to improve the a priori orbit provided that the orbit parameter corrections $p_i = P_i - P_{0,i}$ and the partial derivatives of the a priori orbit with respect to the orbit parameters are known. The trajectory (5.6) should be addressed as the "linearized" solution of the original (non-linear) orbit determination problem. Alternatively, it is also possible to again use the dynamic models together with the improved dynamical parameters to propagate the improved initial state vector by numerical integration. Usually the latter method is used in this work.

If $P_i, i = 1, ..., n$ are deterministic orbit parameters, we also speak of dynamic orbit determination. If additional pseudo-stochastic parameters (see Sect. 5.3) occur in the equation of motion (5.4), we speak of a special kind of reduced-dynamic orbit determination.

5.2.2 Variational Equations

Because initial conditions and force model parameters are estimated as part of the orbit determination process, knowledge of the partial derivatives of the a priori orbit with respect to the estimated parameters as a function of time is required for modeling the GPS observations.

Let us assume that P_i is one of the parameters defining the initial conditions or the dynamics in the equation of motion (5.4), and that the partial derivative of the a priori orbit $\boldsymbol{r}_0(t)$ with respect to this parameter is designated by the function

$$\boldsymbol{z}_{P_i}(t) \doteq \frac{\partial \boldsymbol{r}_0}{\partial P_i}(t) \; . \tag{5.7}$$

The initial value problem associated with (5.7) is obtained from the dynamic force models by taking the partial derivative of the equation of motion (5.4). The result is subsequently referred to as the variational equation of parameter P_i, which reads as

$$\ddot{\boldsymbol{z}}_{P_i} = \boldsymbol{A}_0 \cdot \boldsymbol{z}_{P_i} + \boldsymbol{A}_1 \cdot \dot{\boldsymbol{z}}_{P_i} + \frac{\partial \boldsymbol{f}_1}{\partial P_i} \; , \tag{5.8}$$

with the 3×3 (Jacobian) matrices defined by

$$A_{0[i;k]} \doteq \frac{\partial f_i}{\partial r_{0,k}} \qquad \text{and} \qquad A_{1[i;k]} \doteq \frac{\partial f_i}{\partial \dot{r}_{0,k}} \; , \tag{5.9}$$

where

f_i denotes the component i of the total acceleration $\boldsymbol{f}$ from (5.4) and

$r_{0,k}$ denotes the component k of the geocentric position from (5.4).

The variational equation (5.8) is a linear, homogeneous differential equation system of second order in time with initial values $\boldsymbol{z}_{P_i}(t_0) \neq \boldsymbol{0}$ and $\dot{\boldsymbol{z}}_{P_i}(t_0) \neq \boldsymbol{0}$ for $P_i \in \{a, e, i, \Omega, \omega, u_0\}$. For $P_i \in \{Q_1, ..., Q_d\}$ (5.8) is inhomogeneous, but has zero initial values since the initial satellite state does not depend on the force model parameters. It is important to mention that the homogeneous part of (5.8) is the same for dynamical parameters and for parameters defining the initial conditions, which allows for the implementation of an efficient integration process [*Beutler*, 2005].

As already mentioned, the solutions of the n variational equations related to the orbit parameters $P_i, i = 1, ..., n$ are needed to set up the first design matrix (4.23), which allows us to eventually solve for the improvements of the orbit parameters in a standard least-squares adjustment process (see Sect. 4.4) of GPS

observations together with all other relevant parameters, and to finally improve the orbit using equation (5.6). Although each variational equation (5.8) represents a different initial value problem, it is not necessary to solve n differential equation systems as their solutions can be represented by definite integrals [*Beutler*, 2005].

Let us assume that the functions $\boldsymbol{z}_{O_j}(t), j = 1, ..., 6$ are the partial derivatives of the a priori orbit $\boldsymbol{r}_0(t)$ with respect to the six parameters $O_j, j = 1, ..., 6$ defining the initial conditions at time t_0. The ensemble of these six functions forms one complete system of solutions of the homogeneous part of the variational equation (5.8), which allows us to obtain the solution of the inhomogeneous system by the method of "variation of constants". The solution and its first time derivative may thus be written as a function of the homogeneous solutions $\boldsymbol{z}_{O_j}(t)$ as

$$\boldsymbol{z}_{P_i}^{(k)}(t) = \sum_{j=1}^{6} \alpha_{O_j P_i}(t) \cdot \boldsymbol{z}_{O_j}^{(k)}(t) \; ; \quad k = 0, 1 \; , \tag{5.10}$$

with the coefficient functions defined by

$$\boldsymbol{\alpha}_{P_i}(t) \doteq \int_{t_0}^{t} \boldsymbol{Z}^{-1}(t') \cdot \boldsymbol{h}_{P_i}(t') \cdot dt' \; , \tag{5.11}$$

where

$\boldsymbol{\alpha}_{P_i}$ denotes the column array $(\alpha_{O_1 P_i}, ..., \alpha_{O_6 P_i})^T$,

$\boldsymbol{Z}$ denotes the 6×6 matrix defined by $\boldsymbol{Z}_{[1,...,3;j]} \doteq \boldsymbol{z}_{O_j}$, $\boldsymbol{Z}_{[4,...,6;j]} \doteq \dot{\boldsymbol{z}}_{O_j}$, and

$\boldsymbol{h}_{P_i}$ denotes the column array $(\boldsymbol{0}^T, \; \partial \boldsymbol{f}_1^T / \partial P_i)^T$.

Observe that the solution $\boldsymbol{z}_{P_i}(t)$ of the variational equation (5.8) and its first time derivative may be expressed with the same functions $\alpha_{O_j P_i}(t)$ as a linear combination with the homogeneous solutions $\boldsymbol{z}_{O_j}(t)$ and $\dot{\boldsymbol{z}}_{O_j}(t)$, respectively. Due to this representation, only the six initial value problems associated with the initial conditions have to be actually treated as differential equation systems; their solutions have to be obtained either approximately [*Beutler et al.*, 1994a] or, preferably, by numerical integration techniques, e.g., by collocation methods [*Beutler*, 2005]. All variational equations related to dynamical orbit parameters, however, may be reduced to definite integrals, which can be efficiently solved numerically, e.g., with a Gaussian quadrature technique [*Beutler*, 2005].

Despite the numerical efficiency of available quadrature techniques, it must be emphasized that each additional orbit parameter requires an additional numerical solution of the definite integral (5.11) – an issue that might be relevant when setting up a large number of dynamical orbit parameters such as gravity field coefficients, see Chapter 9. Only for selected parameter types, e.g., pseudo-stochastic orbit parameters (see Sect. 5.3), an explicit numerical quadrature of the corresponding definite integrals can be avoided.

The accuracy requirements for the numerical integration of the variational equations are in general not as stringent as for the primary equations, because many terms are small and do not harm the parameter adjustment process (which could be iterated on request) when being neglected. Therefore, the partial derivatives (5.9) with respect to the satellite position are modeled in this work by only the central term GM and by the lowest zonal term $C_{2,0}$ of the Earth's static gravity field. The partial derivatives (5.9) with respect to the satellite velocity are ignored at all in this work.

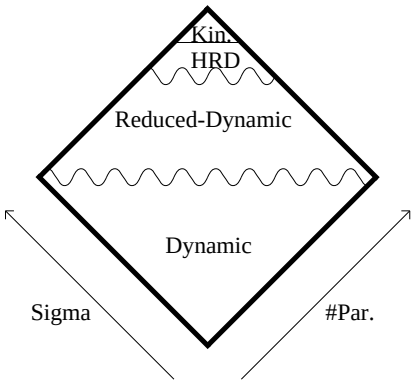

Figure 5.2: Dynamic, reduced-dynamic, highly reduced-dynamic (HRD), and kinematic (Kin.) orbit determination as a function of the number (# Par.) and a priori standard deviation (Sigma) of the estimated pseudo-stochastic orbit parameters (qualitative illustration).

5.3 Pseudo-Stochastic Orbit Modeling

The real-world LEO dynamics are hardly known to a level which is comparable to highly accurate tracking data such as high-low GPS carrier phase measurements or low-low K-band observations. This insufficient knowledge has to be mainly attributed to aerodynamic forces which are not well predictable at altitudes of 300–600 km due to limitations in the upper atmosphere density models [*Bruinsma et al.*, 2004], and due to complicated interactions of neutral gases and charged particles with the satellite surface. Therefore, the concept of reduced-dynamic orbit determination, see [*Yunck et al.*, 1990] and [*Wu et al.*, 1991], has been introduced decades ago to fully exploit the accuracy of the GPS measurements. This has been accomplished by complementing the deterministic model of the spacecraft dynamics by additional stochastic parameters that were adjusted together with the deterministic orbit parameters.

Pseudo-stochastic orbit modeling performed in this work may be considered as a particular realization of the reduced-dynamic orbit determination technique, which makes use of both the geometric strength of the GPS observations and the fact that satellite trajectories are particular solutions of a deterministic equation of motion. The attribute "pseudo" distinguishes this method from stochastic orbit modeling where a satellite trajectory is modeled as a solution of a stochastic differential equation [*Jazwinski*, 1970]. Pseudo-stochastic orbit modeling, in contrast, introduces additional empirical parameters $P_1, ..., P_s$, subsequently referred to as pseudo-stochastic orbit parameters, to the deterministic equation of motion (5.4), which then reads as

$$\ddot{\boldsymbol{r}} = -GM\frac{\boldsymbol{r}}{r^3} + \boldsymbol{f}_1(t, \boldsymbol{r}, \dot{\boldsymbol{r}}, Q_1, ..., Q_d, P_1, ..., P_s) \doteq \boldsymbol{f} \ . \tag{5.12}$$

The attribute "stochastic" arises from the practice to optionally characterize these additional parameters by a priori known statistical properties like, e.g., expectation values and a priori weights, which constrain the estimated parameters to user-specified expectation values (see Sect. 4.4.2).

Figure 5.2 illustrates qualitatively that reduced-dynamic orbit determination may be placed "somewhere" in-between dynamic and kinematic orbit determination. Depending on the number and a priori weights of the solved for pseudo-stochastic parameters, the satellite dynamics can be relaxed accordingly. On the one hand, it is thus obvious that one still obtains an almost dynamic orbit if only a very small number of pseudo-stochastic parameters, or alternatively, pseudo-stochastic parameters with very tight constraints

are introduced into the equation of motion (5.12). On the other hand, it is possible to obtain a kinematic orbit if the maximum number of unconstrained pseudo-stochastic parameters is solved for (see Chapter 9), which means that any type of orbit can be approximated by pseudo-stochastic modeling. The most precise orbits of CHAMP and GRACE as determined in Chapters 7 and 8 are located, e.g., in the region designated as "Reduced-Dynamic", whereas the Highly Reduced-Dynamic (HRD) orbits as discussed in Chapter 9 are located in the region which lies just in front of the kinematic point at the top of the square.

It should be emphasized that each additional (empirical) parameter introduced into the orbit determination weakens the solution for the other (non-empirical) parameters. Nevertheless, it is often necessary to solve for pseudo-stochastic parameters to compensate for deficiencies in the dynamic models. Because continuously improving models of the Earth's static gravity field have been made available during the last few years (see Chapter 3), the limiting factor for dynamic LEO POD has to be attributed today to the non-gravitational force models. Provided that dense GPS SST tracking data of good quality are available, LEO POD with additional pseudo-stochastic parameters is thus an attractive and simple method to determine highly accurate satellite trajectories without taking into account sophisticated models of surface forces. If enough pseudo-stochastic parameters are set up, it is even possible to neglect the physical modeling of the non-gravitational forces at all. Depending on the applied constraints, the estimates reflect mainly the unmodeled non-gravitational accelerations acting on the LEO (see Sect. 7.8.3) , which are dominated either by air drag in the case of very low Earth orbiting satellites or by radiation pressure for higher orbiting satellites.

The following sections develop efficient methods for the solution of the variational equations related to different types of pseudo-stochastic orbit parameters, such as piecewise constant accelerations, instantaneous velocity changes, and piecewise linear accelerations. All three types of empirical parameters are well suited to compensate for any modeling deficiencies in the employed spacecraft dynamics, and might easily be used for the construction of more refined pseudo-stochastic orbit parametrizations as briefly discussed at the end of this chapter.

5.3.1 Piecewise Constant Accelerations

Let us assume that piecewise constant accelerations are set up as the only orbit parameters apart from the six initial conditions. The parametrization subsequently used for the residual acceleration $\boldsymbol{A}(t)$ in the inertial system shall read as the sum of at maximum three accelerations acting in three predefined directions, e.g., in the radial, along-track, and cross-track directions in the satellite co-rotating system or, alternatively, in other predefined directions that seem to be useful for a particular orbit determination problem:

$$\boldsymbol{A}(t) \doteq \boldsymbol{A}_1(t) + \boldsymbol{A}_2(t) + \boldsymbol{A}_3(t) \; . \tag{5.13}$$

Each acceleration $\boldsymbol{A}_d(t)$, $d \in \{1,2,3\}$ shall be represented by m constant pieces in direction d, being active only between the predefined epochs t_{i-1} and t_i, i.e.,

$$\boldsymbol{A}_d(t) \;\; = \;\; \left(A_{0,d} + \sum_{i=1}^{m} A_{i,d} \cdot \xi(t, t_{i-1}, t_i) \right) \cdot \boldsymbol{e}_d(t) \; , \tag{5.14}$$

where $\boldsymbol{e}_d(t)$, $d \in \{1,2,3\}$ denotes, e.g., the unit vector

$$\boldsymbol{e}_1 = \frac{\boldsymbol{r}_0}{|\boldsymbol{r}_0|} \quad , \quad \boldsymbol{e}_2 = \boldsymbol{e}_3 \times \boldsymbol{e}_1 \quad , \quad \boldsymbol{e}_3 = \frac{\boldsymbol{r}_0 \times \dot{\boldsymbol{r}}_0}{|\boldsymbol{r}_0 \times \dot{\boldsymbol{r}}_0|} \tag{5.15}$$

in the radial, along-track, and cross-track direction, and where

$$\xi(t, t_{i-1}, t_i) \doteq \begin{cases} 1 & ; \quad t_{i-1} \le t < t_i \\ 0 & ; \quad \text{otherwise} \end{cases} . \tag{5.16}$$

Altogether a total number of $6 + 3(m + 1)$ orbit parameters are set up including $3m$ pseudo-stochastic parameters. Note that it makes sense to solve as well for constant accelerations $A_{0,d}$ acting over the whole arc in (5.14), provided that the piecewise constant accelerations are actually characterized by a priori standard deviations. In the absence of a priori weights, however, these three parameters become singular and must be omitted.

Variational Equations

Let us now develop the mathematical background for estimating m constant accelerations $A_{i,d}$ in the predetermined direction $\boldsymbol{e}_d(t)$ for $t_{i-1} \le t < t_i, i = 1, ..., m$. For the sake of simplicity, we drop the index d in the following and focus on one acceleration A_i. The contribution of this parameter $P_i = A_i$ to $\boldsymbol{f}_1$ in (5.12) is of the form $A_i \cdot \boldsymbol{e}(t)$ for $t_{i-1} \le t < t_i$. The corresponding variational equation reads as

$$\ddot{\boldsymbol{z}}_{A_i} = \boldsymbol{A}_0 \cdot \boldsymbol{z}_{A_i} + \boldsymbol{A}_1 \cdot \dot{\boldsymbol{z}}_{A_i} + \begin{cases} \boldsymbol{e}(t) & ; \quad t_{i-1} \le t < t_i \\ \boldsymbol{0} & ; \quad \text{otherwise} \end{cases} . \tag{5.17}$$

The variational equation (5.17) may be easily solved thanks to the general mathematical properties of variational equations, see Sect. 5.2.2. Equation (5.11) reads for the special case of a piecewise constant acceleration as

$$\boldsymbol{\alpha}_{A_i}(t) \doteq \int_{t_0}^{t} \boldsymbol{Z}^{-1}(t') \cdot \boldsymbol{h}_{A_i}(t') \cdot dt' = \int_{t_{i-1}}^{t^*} \boldsymbol{Z}^{-1}(t') \cdot \boldsymbol{h}_{A_i}(t') \cdot dt' , \tag{5.18}$$

where the upper integration limit is given by

$$t^* \doteq \begin{cases} t_{i-1} & ; \quad t < t_{i-1} \\ t & ; \quad t_{i-1} \le t < t_i \\ t_i & ; \quad t \ge t_i \end{cases} . \tag{5.19}$$

The solution $\boldsymbol{z}_{A_i}(t)$ and its first time derivative for the parameter A_i follow from (5.10), and may be written as

$$\boldsymbol{z}_{A_i}^{(k)}(t) = \begin{cases} \boldsymbol{0} & ; \quad t < t_{i-1} \\ \sum_{j=1}^{6} \alpha_{O_j A_i}(t) \cdot \boldsymbol{z}_{O_j}^{(k)}(t) & ; \quad t_{i-1} \le t < t_i \\ \sum_{j=1}^{6} \alpha_{O_j A_i}(t_i) \cdot \boldsymbol{z}_{O_j}^{(k)}(t) & ; \quad t \ge t_i \end{cases} . \tag{5.20}$$

Note that $\boldsymbol{z}_{A_i}(t)$ is a once (continuously) differentiable function of time for the entire arc. The non-zero coefficients $\alpha_{O_j A_i}(t)$ are constant in time for the case $t \ge t_i$. This implies that a change in the parameter A_i does not only affect the orbit in the interval $[t_{i-1}, t_i)$ where it is active, but it affects all positions (and velocities) for $t \ge t_{i-1}$ as well.

For the case $t_{i-1} \le t < t_i$ the coefficients are time-dependent and require, in principle, a quadrature of (5.18). The following two paragraphs demonstrate an efficient alternative solution based on linear combinations relying on a small set of partial derivatives.

Efficient Solution for $t_{i-1} \leq t < t_i$

Let us introduce an auxiliary problem and write the solution $\boldsymbol{z}_{A_i}(t)$ as a function of the solution of this auxiliary problem. The parameter underlying our auxiliary problem shall be a constant acceleration $\bar{A}$ acting in the corresponding direction over the entire arc. The corresponding variational equation is closely related to the variational equation (5.17) and reads as

$$\ddot{\boldsymbol{z}}_{\bar{A}} = \boldsymbol{A}_0 \cdot \boldsymbol{z}_{\bar{A}} + \boldsymbol{A}_1 \cdot \dot{\boldsymbol{z}}_{\bar{A}} + \boldsymbol{e}(t) \quad \forall t \,. \tag{5.21}$$

Observe that $\bar{A}$ can be identified with $A_{0,d}$ in (5.14), implying that the solution of its variational equation would be needed anyway if the parameter should be solved for.

The difference $\boldsymbol{\Delta}_i \doteq \boldsymbol{z}_{\bar{A}} - \boldsymbol{z}_{A_i}$ solves the homogeneous differential equation system $\ddot{\boldsymbol{\Delta}}_i = \boldsymbol{A}_0 \cdot \boldsymbol{\Delta}_i + \boldsymbol{A}_1 \cdot \dot{\boldsymbol{\Delta}}_i$ in the time interval $[t_{i-1}, t_i)$. Therefore, its solution can be written as a linear combination with constant coefficients $\beta_{O_j A_i}$ of the functions $\boldsymbol{z}_{O_j}(t)$. As a consequence, the solution $\boldsymbol{z}_{A_i}(t)$ follows as

$$\boldsymbol{z}^{(k)}_{A_i}(t) = \boldsymbol{z}^{(k)}_{\bar{A}}(t) - \sum_{j=1}^{6} \beta_{O_j A_i} \cdot \boldsymbol{z}^{(k)}_{O_j}(t) \,; \quad k = 0, 1 \,, \tag{5.22}$$

Evaluating the above equation at time t_{i-1} and taking (5.20) into account yields a linear system of six scalar and algebraic equations

$$\begin{aligned} \sum_{j=1}^{6} \beta_{O_j A_i} \cdot \boldsymbol{z}_{O_j}(t_{i-1}) &= \boldsymbol{z}_{\bar{A}}(t_{i-1}) \\ \sum_{j=1}^{6} \beta_{O_j A_i} \cdot \dot{\boldsymbol{z}}_{O_j}(t_{i-1}) &= \dot{\boldsymbol{z}}_{\bar{A}}(t_{i-1}) \,, \end{aligned} \tag{5.23}$$

which can be solved for the unknown coefficients $\beta_{O_j A_i}$. Equations (5.22) and (5.23) thus show that the partial derivative $\boldsymbol{z}_{A_i}(t)$ may be written in the interval $t_{i-1} \leq t < t_i$ as a function of the six partial derivatives $\boldsymbol{z}_{O_j}(t)$ of the a priori orbit w.r.t. the parameters defining the initial conditions at time t_0, and the partial derivative $\boldsymbol{z}_{\bar{A}}(t)$ of the a priori orbit w.r.t. a constant acceleration acting in the same direction over the entire arc. The solutions of the mentioned $6 + 1$ partial derivatives have to be available from a numerical integration in order to make use of the representation (5.22).

Efficient Solution for $t \geq t_i$

From equation (5.20) we conclude that $\boldsymbol{z}_{A_i}(t)$ is continuous and differentiable at time t_i, which implies that $\boldsymbol{z}^{(k)}_{A_i}(t_i)$ may be computed by evaluating (5.22) at time t_i. The coefficients $\alpha_{O_j A_i}(t_i)$ in (5.20) may therefore be obtained as a solution of the following linear system of algebraic equations:

$$\begin{aligned} \sum_{j=1}^{6} \alpha_{O_j A_i}(t_i) \cdot \boldsymbol{z}_{O_j}(t_i) &= \boldsymbol{z}_{A_i}(t_i) \\ \sum_{j=1}^{6} \alpha_{O_j A_i}(t_i) \cdot \dot{\boldsymbol{z}}_{O_j}(t_i) &= \dot{\boldsymbol{z}}_{A_i}(t_i) \,. \end{aligned} \tag{5.24}$$

As the above equations form, in close analogy to (5.23), a linear system of six scalar equations for the six unknowns $\alpha_{O_j A_i}(t_i)$, it is possible to write the partial derivative $\boldsymbol{z}_{A_i}(t)$ in the interval $t \geq t_i$ as a linear combination with constant coefficients of only the six partial derivatives $\boldsymbol{z}_{O_j}(t)$ of the a priori orbit w.r.t. the parameters defining the initial conditions at time t_0. This expresses the fact that the

accumulated orbital change in the interval $[t_{i-1}, t_i)$ can be represented for times $t \geq t_i$ by a new set of initial conditions at time t_0.

In conclusion, the small number of $6+3$ numerically integrated partial derivatives is sufficient to compute all the partial derivatives of the a priori orbit w.r.t. piecewise constant accelerations over the entire arc. The proposed parametrization yields a continuous position vector $\boldsymbol{r}(t)$ and a continuous velocity vector $\dot{\boldsymbol{r}}(t)$ of the improved orbit over the entire arc.

5.3.2 Instantaneous Velocity Changes (Pulses)

Let us briefly mention the special case of instantaneous velocity changes $V_{i,d}$ at times t_i in predetermined directions $\boldsymbol{e}_d(t_i)$, see [*Beutler et al.*, 1994a], and outline how it fits into the formalism presented so far. For the sake of simplicity, we drop the index d in the following and focus on one pulse V_i. The contribution of this parameter $P_i = V_i$ to $\boldsymbol{f}_1$ in (5.12) may formally be written as $V_i \cdot \delta(t - t_i) \cdot \boldsymbol{e}(t)$, where $\delta(t)$ represents Dirac's delta function. The corresponding variational equation reads as

$$\ddot{\boldsymbol{z}}_{V_i} = \boldsymbol{A}_0 \cdot \boldsymbol{z}_{V_i} + \boldsymbol{A}_1 \cdot \dot{\boldsymbol{z}}_{V_i} + \delta(t - t_i) \cdot \boldsymbol{e}(t) \; . \tag{5.25}$$

Using the notation from Sect. 5.3.1, but identifying $\boldsymbol{h}_{V_i}$ with $\boldsymbol{h}_{A_i}$ in (5.18), the definite integral (5.18) may be simplified for $t \geq t_i$ as

$$\boldsymbol{\alpha}_{V_i}(t) \doteq \int_{t_0}^{t} \delta(t' - t_i) \cdot \boldsymbol{Z}^{-1}(t') \cdot \boldsymbol{h}_{V_i}(t') \cdot dt' = \boldsymbol{Z}^{-1}(t_i) \cdot \boldsymbol{h}_{V_i}(t_i) \; . \tag{5.26}$$

Obviously, $\alpha_{O_j V_i}(t)$ is zero for $t < t_i$ and non-zero but constant for $t \geq t_i$. Therefore, the partial derivatives $\boldsymbol{z}_{V_i}(t)$ may be written as a linear combination of only the six partial derivatives $\boldsymbol{z}_{O_j}(t)$ of the a priori orbit w.r.t. the parameters defining the initial conditions at time t_0. The parametrization yields a continuous position vector $\boldsymbol{r}(t)$ but, as opposed to the parametrization from Sect. 5.3.1, a discontinuous velocity vector $\dot{\boldsymbol{r}}(t)$ of the improved orbit. The discontinuities lie at the pulse epochs t_i.

This parametrization may be viewed as a special case of the short-arc representation (see Sect. 5.3.4) of the entire arc, where the individual short-arcs are forced to be continuous at the arc boundaries.

5.3.3 Piecewise Linear Accelerations

Let us develop the mathematical background for a more refined LEO orbit parametrization. It seems to be natural to improve the piecewise constant acceleration model with a model that represents each of the residual accelerations in (5.13) by m linear pieces acting between predefined epochs t_{i-1} and t_i. From the technical point of view, there exist basically two different possibilities to realize such a piecewise linear parametrization. Either each of the accelerations $\boldsymbol{A}_d(t)$, $d \in \{1, 2, 3\}$ in (5.13) is represented by

$$\boldsymbol{A}_d(t) = A_{i-1} \cdot \boldsymbol{e}_d(t) + B_i \cdot (t - t_{i-1}) \cdot \boldsymbol{e}_d(t) \; , \tag{5.27}$$

where

A_{i-1} is a parameter describing the (pointwise) acceleration at time t_{i-1} of the interval $[t_{i-1}, t_i)$ and

B_i is a second parameter describing the slope of the linear acceleration in the interval $[t_{i-1}, t_i)$,

or each of the accelerations $\boldsymbol{A}_d(t)$ is represented by

$$\boldsymbol{A}_d(t) = \frac{t - t_{i-1}}{t_i - t_{i-1}} \cdot A_i \cdot \boldsymbol{e}_d(t) + \frac{t_i - t}{t_i - t_{i-1}} \cdot A_{i-1} \cdot \boldsymbol{e}_d(t) \ , \tag{5.28}$$

where

A_{i-1} describes the pointwise acceleration at time t_{i-1} of the interval $[t_{i-1}, t_i]$ and

A_i describes the pointwise acceleration at time t_i of the interval $[t_{i-1}, t_i]$.

From the mathematical point of view the parametrizations (5.27) and (5.28) are equivalent (if (5.27) is continuous) and can be conveyed into each other by the transformation

$$\begin{pmatrix} A_{i-1} \\ B_i \end{pmatrix} = \begin{pmatrix} 1 & 0 \\ \frac{-1}{t_i - t_{i-1}} & \frac{1}{t_i - t_{i-1}} \end{pmatrix} \cdot \begin{pmatrix} A_{i-1} \\ A_i \end{pmatrix} \ . \tag{5.29}$$

For two reasons the parametrization (5.28) is preferable: first, it consists only of $m + 1$ parameters per direction, i.e., only one more parameter per direction than in the case of piecewise constant accelerations, secondly, the continuity at the interval boundaries t_i is imposed by construction. The parametrization (5.27) consists of $2m$ parameters per direction, i.e., doubles the amount of parameters to be solved for, and yields a discontinuous acceleration at the interval boundaries t_i. When asking for continuity in connection with the parametrization (5.27), constraints have to be imposed at the interval boundaries.

Variational Equations

Let us now develop the mathematical background for estimating $m + 1$ pointwise accelerations $A_{i,d}$ in predetermined directions $\boldsymbol{e}_d(t)$ at epochs t_i that define a continuous acceleration over the entire arc consisting of m linear pieces between subsequent epochs t_i. For the sake of simplicity we drop the index d in the following and focus on one acceleration A_i. The corresponding variational equation follows from the parametrization (5.28) and reads as

$$\ddot{\boldsymbol{z}}_{A_i} = \boldsymbol{A}_0 \cdot \boldsymbol{z}_{A_i} + \boldsymbol{A}_1 \cdot \dot{\boldsymbol{z}}_{A_i} + \begin{cases} \left(\frac{t - t_{i-1}}{T_{i,i-1}}\right) \cdot \boldsymbol{e}(t) & ; \quad t_{i-1} \le t < t_i \quad ; \quad i > 0 \\ \left(\frac{t_{i+1} - t}{T_{i+1,i}}\right) \cdot \boldsymbol{e}(t) & ; \quad t_i \le t < t_{i+1} \quad ; \quad i < m \\ \boldsymbol{0} & ; \quad \text{otherwise} \end{cases} \ , \tag{5.30}$$

where

$T_{i,j}$ is the time interval $t_i - t_j$ between two pointwise accelerations A_i and A_j.

Equation (5.30) is closely related to the variational equation (5.17) with an additional term proportional to t occurring in the inhomogeneous part. In addition, it is necessary to distinguish between four different regimes in time due to a strong coupling between subsequent accelerations, i.e., one more regime in time than for the case of piecewise constant accelerations. Observe that the variational equations related to the accelerations A_0 and A_m referring to the beginning and the end of the orbital arc, respectively, are of simpler structure than the rest of the variational equations related to accelerations referring to in-between epochs.

The variational equation (5.30) may be solved in analogy to Sect. 5.3.1. Equation (5.11) reads for the special case of a pointwise acceleration as

$$\boldsymbol{\alpha}_{A_i}(t) \doteq \int_{t_0}^{t} \boldsymbol{Z}^{-1}(t') \cdot \boldsymbol{h}_{A_i}(t') \cdot dt' = \int_{t_{i-1}}^{t^*} \boldsymbol{Z}^{-1}(t') \cdot \boldsymbol{h}_{A_i}(t') \cdot dt' \ , \tag{5.31}$$

where the upper integration limit is given by

$$t^* \doteq \begin{cases} t_{i-1} & ; \quad t < t_{i-1} \\ t & ; \quad t_{i-1} \leq t < t_{i+1} \\ t_{i+1} & ; \quad t \geq t_{i+1} \end{cases} . \tag{5.32}$$

The solution $\boldsymbol{z}_{A_i}(t)$ and its first time derivative for the parameter A_i follow from (5.10) and may be written as

$$\boldsymbol{z}^{(k)}_{A_i}(t) = \begin{cases} \boldsymbol{0} & ; \quad t < t_{i-1} \\ \sum\limits_{j=1}^{6} \alpha_{O_j A_i}(t) \cdot \boldsymbol{z}^{(k)}_{O_j}(t) & ; \quad t_{i-1} \leq t < t_{i+1} \\ \sum\limits_{j=1}^{6} \alpha_{O_j A_i}(t_{i+1}) \cdot \boldsymbol{z}^{(k)}_{O_j}(t) & ; \quad t \geq t_{i+1} \end{cases} . \tag{5.33}$$

Note that $\boldsymbol{z}_{A_i}(t)$ is a twice (continuously) differentiable function of time for the entire arc. The non-zero coefficients $\alpha_{O_j A_i}(t)$ are constant in time for the case $t \geq t_{i+1}$.

For the case $t_{i-1} \leq t < t_{i+1}$ the coefficients are time-dependent and require, in principle, a quadrature of (5.31). The following three paragraphs introduce an efficient alternative, which makes use of linear combinations in analogy to Sect. 5.3.1 for piecewise constant accelerations.

Efficient Solution for $t_{i-1} \leq t < t_i$

Let us introduce two auxiliary problems and write the solution $\boldsymbol{z}_{A_i}(t)$ as a function of the solution of these auxiliary problems. In analogy to Sect. 5.3.1, the parameters underlying our auxiliary problems shall be a constant acceleration $\bar{A}$ acting in the corresponding direction over the entire arc, and the slope $\bar{B}$ of a linearly changing acceleration in the same direction over the entire orbital arc. The two corresponding variational equations read for the entire arc as

$$\ddot{\boldsymbol{z}}_{\bar{A}} = \boldsymbol{A}_0 \cdot \boldsymbol{z}_{\bar{A}} + \boldsymbol{A}_1 \cdot \dot{\boldsymbol{z}}_{\bar{A}} + \boldsymbol{e}(t) \qquad \text{and} \qquad \ddot{\boldsymbol{z}}_{\bar{B}} = \boldsymbol{A}_0 \cdot \boldsymbol{z}_{\bar{B}} + \boldsymbol{A}_1 \cdot \dot{\boldsymbol{z}}_{\bar{B}} + t \cdot \boldsymbol{e}(t) \; . \tag{5.34}$$

Observe that the solution method outlined in the following relies on the solution $\boldsymbol{z}_{\bar{B}}(t)$, i.e., it requires one more variational equation per direction than for piecewise constant accelerations.

In close analogy to Sect. 5.3.1, we form the difference

$$\boldsymbol{\Delta}_i \doteq \frac{\boldsymbol{z}_{\bar{B}} - t_{i-1} \cdot \boldsymbol{z}_{\bar{A}}}{T_{i,i-1}} - \boldsymbol{z}_{A_i} \tag{5.35}$$

which solves the homogeneous differential equation system $\ddot{\boldsymbol{\Delta}}_i = \boldsymbol{A}_0 \cdot \boldsymbol{\Delta}_i + \boldsymbol{A}_1 \cdot \dot{\boldsymbol{\Delta}}_i$ in the time interval $[t_{i-1}, t_i)$. Therefore, its solution can be written as a linear combination with constant coefficients $\beta_{O_j A_i}$ of the functions $\boldsymbol{z}_{O_j}(t)$. As a consequence, the solution $\boldsymbol{z}_{A_i}(t)$ follows as

$$\boldsymbol{z}^{(k)}_{A_i}(t) = \frac{1}{T_{i,i-1}} \cdot \boldsymbol{z}^{(k)}_{\bar{B}}(t) - \frac{t_{i-1}}{T_{i,i-1}} \cdot \boldsymbol{z}^{(k)}_{\bar{A}}(t) - \sum_{j=1}^{6} \beta_{O_j A_i} \cdot \boldsymbol{z}^{(k)}_{O_j}(t) \; ; \quad k = 0, 1 \; . \tag{5.36}$$

Evaluating the above equation at time t_{i-1} and taking (5.33) into account yields a linear system of six scalar and algebraic equations

$$\begin{aligned} \sum_{j=1}^{6} \beta_{O_j A_i} \cdot \boldsymbol{z}_{O_j}(t_{i-1}) &= \tfrac{1}{T_{i,i-1}} \cdot \boldsymbol{z}_{\bar{B}}(t_{i-1}) - \tfrac{t_{i-1}}{T_{i,i-1}} \cdot \boldsymbol{z}_{\bar{A}}(t_{i-1}) \\ \sum_{j=1}^{6} \beta_{O_j A_i} \cdot \dot{\boldsymbol{z}}_{O_j}(t_{i-1}) &= \tfrac{1}{T_{i,i-1}} \cdot \dot{\boldsymbol{z}}_{\bar{B}}(t_{i-1}) - \tfrac{t_{i-1}}{T_{i,i-1}} \cdot \dot{\boldsymbol{z}}_{\bar{A}}(t_{i-1}) \; , \end{aligned} \tag{5.37}$$

which can be solved for the unknown coefficients $\beta_{O_j A_i}$. The equations (5.36) and (5.37) thus show that the partial derivative $\boldsymbol{z}_{A_i}(t)$ may be written in the interval $t_{i-1} \le t < t_i$ as a function of the six partial derivatives $\boldsymbol{z}_{O_j}(t)$ of the a priori orbit w.r.t. the parameters defining the initial conditions at time t_0, the partial derivative $\boldsymbol{z}_{\bar{A}}(t)$ of the a priori orbit w.r.t. a constant acceleration acting in the same direction over the entire arc, and the partial derivative $\boldsymbol{z}_{\bar{B}}(t)$ of the a priori orbit w.r.t. a linearly changing acceleration acting in the same direction over the entire arc.

Efficient Solution for $t_i \le t < t_{i+1}$

In close analogy to the previous paragraph, we form the difference

$$\boldsymbol{\Delta}_i^* \doteq \frac{t_{i+1} \cdot \boldsymbol{z}_{\bar{A}} - \boldsymbol{z}_{\bar{B}}}{T_{i+1,i}} - \boldsymbol{z}_{A_i} \tag{5.38}$$

which solves the homogeneous differential equation system $\ddot{\boldsymbol{\Delta}}_i^* = \boldsymbol{A}_0 \cdot \boldsymbol{\Delta}_i^* + \boldsymbol{A}_1 \cdot \dot{\boldsymbol{\Delta}}_i^*$ in the time interval $[t_i, t_{i+1})$. Therefore, its solution can be written as a linear combination with constant coefficients $\beta^*_{O_j A_i}$ of the functions $\boldsymbol{z}_{O_j}(t)$. As a consequence, the solution $\boldsymbol{z}_{A_i}(t)$ follows as

$$\boldsymbol{z}_{A_i}^{(k)}(t) = \frac{t_{i+1}}{T_{i+1,i}} \cdot \boldsymbol{z}_{\bar{A}}^{(k)}(t) - \frac{1}{T_{i+1,i}} \cdot \boldsymbol{z}_{\bar{B}}^{(k)}(t) - \sum_{j=1}^{6} \beta^*_{O_j A_i} \cdot \boldsymbol{z}_{O_j}^{(k)}(t) \; ; \quad k = 0, 1 \; . \tag{5.39}$$

From (5.33) we conclude that $\boldsymbol{z}_{A_i}(t)$ is continuous and differentiable at time t_i, which implies that $\boldsymbol{z}_{A_i}^{(k)}(t_i)$ may be computed by evaluating (5.36) at time t_i. Evaluating (5.39) at time t_i as well, and taking $\boldsymbol{z}_{A_i}^{(k)}(t_i)$ from (5.36) into account yields a linear system of six scalar and algebraic equations

$$\begin{aligned} \sum_{j=1}^{6} \beta^*_{O_j A_i} \cdot \boldsymbol{z}_{O_j}(t_i) &= \tfrac{t_{i+1}}{T_{i+1,i}} \cdot \boldsymbol{z}_{\bar{A}}(t_i) - \tfrac{1}{T_{i+1,i}} \cdot \boldsymbol{z}_{\bar{B}}(t_i) - \boldsymbol{z}_{A_i}(t_i) \\ \sum_{j=1}^{6} \beta^*_{O_j A_i} \cdot \dot{\boldsymbol{z}}_{O_j}(t_i) &= \tfrac{t_{i+1}}{T_{i+1,i}} \cdot \dot{\boldsymbol{z}}_{\bar{A}}(t_i) - \tfrac{1}{T_{i+1,i}} \cdot \dot{\boldsymbol{z}}_{\bar{B}}(t_i) - \dot{\boldsymbol{z}}_{A_i}(t_i) \; , \end{aligned} \tag{5.40}$$

which can be solved for the unknown coefficients $\beta^*_{O_j A_i}$. The equations (5.39) and (5.40) show, in combination with the equations (5.36) and (5.37), that the partial derivative $\boldsymbol{z}_{A_i}(t)$ may be written in the interval $t_i \le t < t_{i+1}$ as a function of the six partial derivatives $\boldsymbol{z}_{O_j}(t)$, and the partial derivatives $\boldsymbol{z}_{\bar{A}}(t)$ and $\boldsymbol{z}_{\bar{B}}(t)$.

Efficient Solution for $t \ge t_{i+1}$

From (5.33) we conclude that $\boldsymbol{z}_{A_i}(t)$ is continuous and differentiable at time t_{i+1}, which implies that $\boldsymbol{z}_{A_i}^{(k)}(t_{i+1})$ may be computed by evaluating (5.39) at time t_{i+1}. The coefficients $\alpha_{O_j A_i}(t_{i+1})$ in (5.33) may therefore be obtained as a solution of the following linear system of algebraic equations:

$$\begin{aligned} \sum_{j=1}^{6} \alpha_{O_j A_i}(t_{i+1}) \cdot \boldsymbol{z}_{O_j}(t_{i+1}) &= \boldsymbol{z}_{A_i}(t_{i+1}) \\ \sum_{j=1}^{6} \alpha_{O_j A_i}(t_{i+1}) \cdot \dot{\boldsymbol{z}}_{O_j}(t_{i+1}) &= \dot{\boldsymbol{z}}_{A_i}(t_{i+1}) \; . \end{aligned} \tag{5.41}$$

As the above equations form a linear system of six scalar equations for the six unknowns $\alpha_{O_j A_i}(t_{i+1})$, it is possible to write the partial derivative $\boldsymbol{z}_{A_i}(t)$ in the interval $t \ge t_{i+1}$ as a linear combination of only

the six partial derivatives $\boldsymbol{z}_{O_j}(t)$ of the a priori orbit w.r.t. the parameters defining the initial conditions at time t_0.

The small number of $6 + 3 + 3$ numerically integrated partial derivatives are thus sufficient to compute all the partial derivatives of the a priori orbit w.r.t. pointwise accelerations defining a piecewise linear acceleration over the entire arc. The parametrization yields a continuous position vector $\boldsymbol{r}(t)$, a continuous velocity vector $\dot{\boldsymbol{r}}(t)$, and a continuous acceleration vector $\ddot{\boldsymbol{r}}(t)$ of the improved orbit over the entire arc.

From the conceptual point of view, the piecewise linear acceleration model does not introduce any additional difficulties with respect to the piecewise constant acceleration model except for the slightly more complicated formulas to be evaluated, but this does not significantly harm the computational efficiency. From the technical point of view, the "absolute" times in the expressions (5.36), (5.37), (5.39), and (5.40) are preferably referred to the beginning of the orbital arc in order to keep the numerical values small.

5.3.4 Other Orbit Modeling Techniques

For the sake of completeness, we include two other widely-used orbit modeling techniques, which are, from the conceptual point of view, related to the technique of pseudo-stochastic orbit modeling.

Short-Arc Method

The short-arc parametrization represents the solution within each subinterval by a new set of six initial osculating elements. The resulting trajectory is thus characterized by a discontinuous velocity vector and a discontinuous position vector as well. Obviously, it is not only possible to obtain such a trajectory by splitting the original orbital arc into several short-arcs by setting up new initial conditions at the beginning of each short-arc, but it is also possible to solve for one set of initial osculating elements and for instantaneous velocity changes V_i (see Sect. 5.3.2) in conjunction with instantaneous position changes X_i at times t_i in predetermined directions $\boldsymbol{e}(t_i)$. Using the notation from Sect. 5.3.1, but identifying $\boldsymbol{h}_{X_i}$ with $(\boldsymbol{e}^T(t_i),\ \boldsymbol{0}^T)$, the coefficients of the partial derivatives $\boldsymbol{z}_{X_i}(t)$ may be obtained in close analogy to Sect. 5.3.2 by

$$\boldsymbol{\alpha}_{X_i}(t) \doteq \int_{t_0}^{t} \delta(t' - t_i) \cdot \boldsymbol{Z}^{-1}(t') \cdot \boldsymbol{h}_{X_i}(t') \cdot dt' = \boldsymbol{Z}^{-1}(t_i) \cdot \boldsymbol{h}_{X_i}(t_i) \tag{5.42}$$

for $t \geq t_i$.

For the sake of completeness and clarity, the two linear systems of algebraic equations to be solved for the coefficients $\alpha_{O_j X_i}(t_i)$ and $\alpha_{O_j V_i}(t_i)$ of the partial derivatives $\boldsymbol{z}_{X_i}(t)$ and $\boldsymbol{z}_{V_i}(t)$, respectively, may be explicitly written as

$$\begin{aligned}
\sum_{j=1}^{6} \alpha_{O_j X_i}(t_i) \cdot \boldsymbol{z}_{O_j}(t_i) &= \boldsymbol{e}(t_i) \\
\sum_{j=1}^{6} \alpha_{O_j X_i}(t_i) \cdot \dot{\boldsymbol{z}}_{O_j}(t_i) &= \boldsymbol{0} \\
&\quad , \\
\sum_{j=1}^{6} \alpha_{O_j V_i}(t_i) \cdot \boldsymbol{z}_{O_j}(t_i) &= \boldsymbol{0} \\
\sum_{j=1}^{6} \alpha_{O_j V_i}(t_i) \cdot \dot{\boldsymbol{z}}_{O_j}(t_i) &= \boldsymbol{e}(t_i)
\end{aligned} \tag{5.43}$$

which shows that the parameter X_i is "allowed" to change only the orbital position at time t_i in direction $\boldsymbol{e}(t_i)$, but not the orbital velocity at time t_i. The opposite statement is valid for the parameter V_i.

The advantage of this alternative formulation is that the original arclength remains formally unchanged, i.e., it is easily possible to solve for deterministic orbit parameters still referring to the original arclength. This might be of "technical" importance if the deterministic orbit parameters are identified with geopotential coefficients (see Chapter 9). Instead of saving many (large) normal equation systems referring to the short arclength, a reduced number of normal equation systems may be generated, e.g., on a daily basis.

Periodic Accelerations

Orbital errors are often periodic in nature with the orbital revolution being the main period, see, e.g., Sect. 7.9.1. This is certainly a motivation to solve for other empirical orbit parameters than pseudo-stochastic orbit parameters, in order to constrain orbital errors more specifically, e.g., by coefficients of a truncated Fourier series of periodic accelerations. Such empirical parametrizations are of advantage if the satellite orbit is indeed mainly governed by orbital errors of the modeled characteristics, because they may not so easily absorb other unmodeled systematic effects and harm other parameters as pseudo-stochastic orbit parameters can do. Therefore, once-per-revolution empirical parameters are often solved for when modeling mid- to high-altitude satellites such as Earth observing satellites and navigation satellites, see [*Beutler et al.,* 1994a]. The argument of latitude is often used to define the main period, but it may be easily modified for specific applications, e.g., when modeling solar radiation pressure, to the satellite's argument of latitude with respect to the sun's argument of latitude.

Fourier coefficients of periodic accelerations are also suited to model the trajectory of LEOs. However, the expansion in the Fourier series cannot be truncated after the first few terms, but must be usually extended to a number which is comparable to the number of pseudo-stochastic parameters that are typically estimated. Unfortunately, the coefficients of a truncated Fourier series cannot be set up efficiently by simple linear combinations as it is the case for all types of pseudo-stochastic parameters, because the base functions in the Fourier series expansion are all linearly independent. The problem of solving the associated variational equations can thus be reduced only to numerical quadrature as equation (5.11) still holds.

The developments from Sect. 5.3.1 imply that the concept of estimating piecewise constant accelerations may be easily extended, e.g., to the estimation of piecewise once-per-revolution accelerations, which is attractive, as well, for modeling LEO trajectories. Let us therefore briefly summarize the mathematical background for estimating m periodic accelerations a_i in predetermined directions $\boldsymbol{e}(t)$ for $t_{i-1} \le t < t_i, i = 1, ..., m$. The contribution of one parameter $P_i = A_i$ to $\boldsymbol{f}_1$ in (5.12) is of the form $A_i \cdot g(t) \cdot \boldsymbol{e}(t)$ for $t_{i-1} \le t < t_i$, where $g(t)$ describes, e.g., the once-per-revolution periodicity. The corresponding variational equation reads as

$$\ddot{\boldsymbol{z}}_{A_i} = \boldsymbol{A}_0 \cdot \boldsymbol{z}_{A_i} + \boldsymbol{A}_1 \cdot \dot{\boldsymbol{z}}_{A_i} + \begin{cases} g(t) \cdot \boldsymbol{e}(t) & ; \quad t_{i-1} \le t < t_i \\ \boldsymbol{0} & ; \quad \text{otherwise} \end{cases} . \tag{5.44}$$

In close analogy to the case of piecewise constant accelerations discussed in Sect. 5.3.1, the solution of the variational equation (5.44) may be efficiently obtained as a linear combination of a small set of numerically integrated partial derivatives. The only difference resides in the auxiliary problem (5.21) which has to be replaced by

$$\ddot{\boldsymbol{z}}_{\bar{A}} = \boldsymbol{A}_0 \cdot \boldsymbol{z}_{\bar{A}} + \boldsymbol{A}_1 \cdot \dot{\boldsymbol{z}}_{\bar{A}} + g(t) \cdot \boldsymbol{e}(t) \quad \forall t \, . \tag{5.45}$$

6. Efficient Normal Equation Handling

Setting up the first design matrix $\boldsymbol{A}$ and the associated construction of the system of normal equations are essential steps in every least-squares procedure, followed by the inversion of the normal equation matrix $\boldsymbol{N}$ and, eventually, the computation of the model parameter corrections with their standard deviations. Unfortunately, the involved matrix operations tend to be time consuming for least-squares problems governed by large numbers of model parameters. The purpose of this chapter is, therefore, to analyze the structure of the system of normal equations associated with reduced-dynamic LEO orbit determination problems, and to develop different algorithms for an efficient handling of the large matrices.

First, we present the general structure of the system of normal equations of reduced-dynamic LEO orbit determination. We then focus on a simplified orbit determination problem where pulses are set up as the only parameters apart from the six initial conditions. The structure of this particular system of normal equations will be exploited to the extent possible, with the goal to develop different methods for an efficient handling of the large matrices. Finally, the presented methods are extended and applied to more general orbit determination problems that occur in practice, e.g., problems which are governed by additional parameters like carrier phase biases, or problems which are based on other pseudo-stochastic orbit parameters, such as piecewise constant accelerations. A comprehensive summary of the presented algebra may be found in [*Beutler et al.*, 2006].

6.1 Conventional Least-Squares Adjustment – An Overview

The orbit determination problems treated in this work are all based on a least-squares adjustment of the underlying system of observation equations (4.22). The model function $\boldsymbol{F}$ is specific for the actual type of observations used for the adjustment, e.g., the observation equations (4.3) and (4.5) have to be used for undifferenced GPS code and GPS carrier phase observations, respectively, or corresponding observation equations would have to be used for other observation types such as range, Doppler, or direction observations. As a consequence, the first design matrix $\boldsymbol{A}$ and the resulting normal equation matrix $\boldsymbol{N}$ depend on the observation type to be processed. The underlying GPS-specific structures for reduced-dynamic LEO orbit determination are illustrated in the following for the processing of undifferenced ionosphere-free GPS carrier phase observations.

6.1.1 Partial Derivatives w.r.t. GPS-Specific Parameters

GPS pseudo-range and GPS carrier phase observations have to be parametrized with the receiver clock offset, $C_l = c \cdot \Delta t_{leo}$, which has to be determined at every measurement epoch t_l. In the absence of data gaps, a 24 h data arc thus requires $n_c = 2880$ offsets if the measurements are processed at 30 s intervals. In addition, the GPS carrier phase observations require an additional ionosphere-free phase bias parameter, $B_m = \lambda_3 \cdot B^k_{leo}$, for each continuous tracking pass. Due to the rapid motion of a LEO, see Sect. 7.4, the GPS satellites are observed for a maximum of about 40 min which typically results in

14 to 15 passes with constant ambiguities for a single GPS satellite. Most of the time the total number of carrier phase bias parameters is thus in the order of $n_b \approx 450 - 500$ for 24 h data arcs.

The partial derivatives of the modeled r-th GPS observation $F_r = h_l^k$ of GPS satellite k at epoch t_l with respect to the clock offset vector,

$$\frac{\partial h_l^k}{\partial \boldsymbol{C}} = \left(0_{(1)} \ \ldots \ 0_{(l-1)} \ 1_{(l)} \ 0_{(l+1)} \ \ldots \ 0_{(n_c)}\right) , \tag{6.1}$$

are very simple and only set for the epoch the measurement was taken. The same is also true for the carrier phase observations, where only the partial derivative with respect to the involved bias parameter is non-zero, i.e.,

$$\frac{\partial h_l^k}{\partial \boldsymbol{B}} = \left(0_{(1)} \ \ldots \ 0_{(m-1)} \ 1_{(m)} \ 0_{(m+1)} \ \ldots \ 0_{(n_b)}\right) . \tag{6.2}$$

Despite the similar shape of (6.1) and (6.2), one has to keep in mind that carrier phase bias parameters are generally valid for many observation epochs, which makes them fundamentally different from epoch-specific parameters such as the receiver clock offsets.

6.1.2 Partial Derivatives w.r.t. LEO Orbit Parameters

It makes sense to express the partial derivatives (4.23) related to the r-th observation and the orbit parameter P_i with the functions $\boldsymbol{z}_{P_i}$ defined by (5.7) as

$$\frac{\partial F_r(\boldsymbol{X})}{\partial P_i} = \left(\boldsymbol{\nabla}\left(F_r(\boldsymbol{X})\right)\right)^T \cdot \boldsymbol{z}_{P_i} , \tag{6.3}$$

where F_r denotes the r-th component of the model function $\boldsymbol{F}$. Its gradient is given by

$$\left(\boldsymbol{\nabla}\left(F_r(\boldsymbol{X})\right)\right)^T = \left(\frac{\partial F_r(\boldsymbol{X})}{\partial r_{0,1}} \ \frac{\partial F_r(\boldsymbol{X})}{\partial r_{0,2}} \ \frac{\partial F_r(\boldsymbol{X})}{\partial r_{0,3}}\right) . \tag{6.4}$$

Observe that slightly more complicated relations (6.3) would result if the observations depend not only on the geocentric position vector, but also on the geocentric velocity vector, or if they were referring to more than one epoch. The advantage of a formulation of type (6.3) is that only the gradient depends on the type of the observations, e.g., it yields the "leocentric" unit vector pointing to the corresponding GPS satellite with a negative sign for a LEO-station baseline and with a positive sign for a station-LEO baseline, respectively. The functions $\boldsymbol{z}_{P_i}$, however, are completely independent of the observation type, which separates the observation-specific (geometric) part from the dynamic part, which, in essence, is the "interesting" part for orbit determination. The formulation (6.3) demonstrates the impact of the equation of motion (5.12) on the system of observation equations by the solutions $\boldsymbol{z}_{P_i}$ of its associated variational equations (5.8).

Let us assume that three pulses $V_{i,j}$ are set up in the three predetermined directions $\boldsymbol{e}_j(t_i)$, $j = 1, 2, 3$ at the epochs t_i, $i = 1, ..., n-1$ as the only orbit parameters, apart from the six initial conditions referring to t_0. According to Sect. 5.3.2, the partial derivative $\boldsymbol{z}_{V_{i,j}}$ of the a priori orbit $\boldsymbol{r}_0(t)$ w.r.t. the parameter $V_{i,j}$ reads as

$$\boldsymbol{z}_{V_{i,j}}(t) = \begin{cases} \boldsymbol{0} & ; \quad t < t_i \\ \sum\limits_{k=1}^{6} \beta_{O_k V_{i,j}} \cdot \boldsymbol{z}_{O_k}(t) & ; \quad t \geq t_i \end{cases} , \tag{6.5}$$

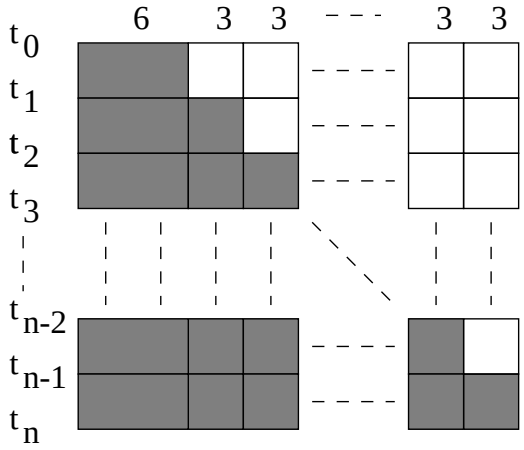

Figure 6.1: Non-zero (grey) and zero (white) occupation of the first design matrix in the presence of six initial conditions and three pulses set up at the epochs t_i, $i = 1, ..., n-1$.

where $\boldsymbol{z}_{O_k}(t)$ are the partial derivatives w.r.t. the initial conditions O_k, $k = 1, ..., 6$. Equation (6.5) shows that $\boldsymbol{z}_{V_{i,j}}$, and as a consequence of (6.3) also $\frac{\partial F_r}{\partial V_{i,j}}$ in the first design matrix (see Fig. 6.1 for the orbit related part), is generally non-zero for all observation times $t_l \geq t_i$. Therefore, the partial derivatives of the modeled GPS observation $F_r = h_l^k$ of GPS satellite k at epoch t_l with respect to the orbit parameter vector read as

$$\frac{\partial h_l^k}{\partial \boldsymbol{P}} = \left(\frac{\partial h_l^k}{\partial \boldsymbol{O}} \; \frac{\partial h_l^k}{\partial \boldsymbol{V}_1} \; \cdots \; \frac{\partial h_l^k}{\partial \boldsymbol{V}_{i-1}} \; \frac{\partial h_l^k}{\partial \boldsymbol{V}_i} \; \mathbf{0}_{(i+1)} \; \cdots \; \mathbf{0}_{(n-1)} \right) , \tag{6.6}$$

where it is assumed that the observation time t_l is part of the subinterval $[t_i, t_{i+1})$. The fact that the pulses in the past contribute to the trajectory shape in the present implies that the number of active parameters grows by 3 after each epoch t_i, $i = 1, ..., n-1$, i.e., from originally only 6 Keplerian elements in the subinterval $[t_0, t_1)$ the number grows to a total $6 + 3\ (n-1)$ active parameters in the last subinterval $[t_{n-1}, t_n)$. The storage requirements are growing about quadratically with the number of active pulses, the CPU requirements even grow with the approximately third power of the number of active pulses.

Finally and for a later use, it should be mentioned that the coefficients $\beta_{O_k V_{i,j}}$ can be identified with the partial derivatives of the initial osculating elements O_k w.r.t. the pulses $V_{i,j}$. Thus, a change in the initial osculating element O_k induced by a change in the pulse $V_{i,j}$ can be computed as

$$\Delta O_k = \frac{\partial O_k}{\partial V_{i,j}} \cdot \Delta V_{i,j} = \beta_{O_k V_{i,j}} \cdot \Delta V_{i,j} \, . \tag{6.7}$$

6.1.3 Structure of the Normal Equation Matrix

The first design matrix (4.23) of reduced-dynamic orbit determination is constructed from the individual contributions (6.1), (6.6), and (6.2) as

$$\boldsymbol{A} \doteq \frac{\partial \boldsymbol{F}(\boldsymbol{X})}{\partial \boldsymbol{X}} = \left(\frac{\partial \boldsymbol{h}}{\partial \boldsymbol{C}} \; \frac{\partial \boldsymbol{h}}{\partial \boldsymbol{P}} \; \frac{\partial \boldsymbol{h}}{\partial \boldsymbol{B}} \right) , \tag{6.8}$$

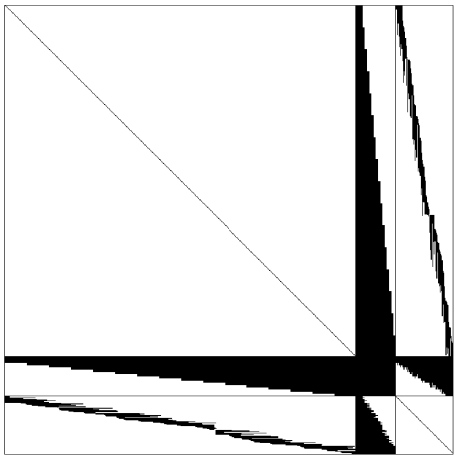

Figure 6.2: Non-zero (black) and zero (white) elements of the normal equation matrix of the system (6.9). The nine sub-matrices are separated with black lines.

which eventually yields the complete system of normal equations (4.26) for the parameter corrections as

$$\begin{pmatrix} \boldsymbol{N_{cc}} & \boldsymbol{N_{cp}} & \boldsymbol{N_{cb}} \\ \boldsymbol{N_{pc}} & \boldsymbol{N_{pp}} & \boldsymbol{N_{pb}} \\ \boldsymbol{N_{bc}} & \boldsymbol{N_{bp}} & \boldsymbol{N_{bb}} \end{pmatrix} \cdot \begin{pmatrix} \boldsymbol{c} \\ \boldsymbol{p} \\ \boldsymbol{b} \end{pmatrix} = \begin{pmatrix} \boldsymbol{b_c} \\ \boldsymbol{b_p} \\ \boldsymbol{b_b} \end{pmatrix} . \tag{6.9}$$

The structure of the partitioned normal equation matrix of (6.9) is visualized in Fig. 6.2 for a 4 h data arc of 30 s CHAMP data collected on DOY 201, 2002. $\boldsymbol{N_{cc}}$ thus consists of 480 clock parameters, $\boldsymbol{N_{pp}}$ of 54 orbit parameters (6 Keplerian elements, 3 constant accelerations acting over the whole arc, and a total of 45 pulses set up at 6-minute intervals), and $\boldsymbol{N_{bb}}$ of 80 bias parameters. Note that the bias parameters are ordered in Fig. 6.2 according to their appearance in time, and that new bias parameters had to be set up at one particular epoch for all GPS satellites, see the middle of the sub-matrix $\boldsymbol{N_{cb}}$.

It can be recognized that the sub-matrix $\boldsymbol{N_{pp}}$ is fully populated. Therefore, it is not immediately obvious how to efficiently handle the orbit-related part in the normal equation system (6.9), although the specific structures of the sub-matrices $\boldsymbol{N_{cp}}$ and $\boldsymbol{N_{pb}}$ indicate as well a particular structure of the sub-matrix $\boldsymbol{N_{pp}}$ due to the activity intervals of the pseudo-stochastic pulses. In contrast, the very simple structures of the diagonal sub-matrices $\boldsymbol{N_{cc}}$ and $\boldsymbol{N_{bb}}$ can be easily exploited as their inverses are readily computed. In order to illustrate this, we group the orbit and the carrier phase bias parameter corrections (small letters) into

$$\boldsymbol{x} = \begin{pmatrix} \boldsymbol{p} \\ \boldsymbol{b} \end{pmatrix} . \tag{6.10}$$

and rewrite the system of normal equations (6.9) as

$$\begin{pmatrix} \boldsymbol{N_{cc}} & \boldsymbol{N_{cx}} \\ \boldsymbol{N_{xc}} & \boldsymbol{N_{xx}} \end{pmatrix} \cdot \begin{pmatrix} \boldsymbol{c} \\ \boldsymbol{x} \end{pmatrix} = \begin{pmatrix} \boldsymbol{b_c} \\ \boldsymbol{b_x} \end{pmatrix} . \tag{6.11}$$

According to (4.33) and (4.34), the receiver clock offset parameters may be pre-eliminated, which yields the updates of the orbit and carrier phase bias parameters as

$$\boldsymbol{x} = \left(\boldsymbol{N_{xx}} - \boldsymbol{N_{xc}}\,\boldsymbol{N_{cc}^{-1}}\,\boldsymbol{N_{cx}}\right)^{-1} \left(\boldsymbol{b_x} - \boldsymbol{N_{xc}}\,\boldsymbol{N_{cc}^{-1}}\,\boldsymbol{b_c}\right) . \tag{6.12}$$

After having processed all observations, $\boldsymbol{x}$ may be back-substituted to obtain the updates for the clock offsets as

$$\boldsymbol{c} = \boldsymbol{N}_{\boldsymbol{cc}}^{-1} \left(\boldsymbol{b}_{\boldsymbol{c}} - \boldsymbol{N}_{\boldsymbol{cx}} \, \boldsymbol{x} \right) \ . \tag{6.13}$$

Note that the clock offsets are pre-eliminated epoch-wise in the Bernese GPS Software Version 5.0 [*Dach et al.*, 2007], i.e., it is usually not necessary to set up (and store) the entire sub-matrix $\boldsymbol{N}_{\boldsymbol{xc}}$. Therefore, the back-substitution is actually not performed with (6.13), but by inserting the updates $\boldsymbol{x}$ of the orbit and carrier phase bias parameters back into the observation equations, which are successively solved for each epoch. For this purpose, parts of the observation equation are stored in a scratch file.

Carrier phase bias parameters may be pre-eliminated as well, e.g., before the inversion of the normal equation matrix or at each time when a multiple bias parameter has to be set up, but the back-substitution process can then no longer be easily achieved to obtain the estimated updates of the bias and clock parameters without saving large matrices.

According to (4.30), the cofactor matrix of the orbit and carrier phase bias parameters follows as

$$\boldsymbol{Q}_{\boldsymbol{xx}} = \left(\boldsymbol{N}_{\boldsymbol{xx}} - \boldsymbol{N}_{\boldsymbol{xc}} \, \boldsymbol{N}_{\boldsymbol{cc}}^{-1} \, \boldsymbol{N}_{\boldsymbol{cx}} \right)^{-1} \ , \tag{6.14}$$

which allows to finally recover the cofactor matrix of the receiver clock offsets by

$$\boldsymbol{Q}_{\boldsymbol{cc}} = \boldsymbol{N}_{\boldsymbol{cc}}^{-1} + \boldsymbol{N}_{\boldsymbol{cc}}^{-1} \, \boldsymbol{N}_{\boldsymbol{cx}} \, \boldsymbol{Q}_{\boldsymbol{xx}} \, \boldsymbol{N}_{\boldsymbol{xc}} \, \boldsymbol{N}_{\boldsymbol{cc}}^{-1} \ . \tag{6.15}$$

Note that the second term in (6.15) accounts for the errors of the non-epoch parameters. If one does not care (too much) about too optimistic estimates of the receiver clock formal errors, this second term can be neglected as its computation may be CPU time- and memory-intensive.

6.2 Structure of Normal Equations related to Orbit Parameters

The structure of the orbit-related parts $\boldsymbol{N}_{\boldsymbol{pp}}$ and $\boldsymbol{b}_{\boldsymbol{p}}$ in the normal equation system (6.9) is important for the understanding of the efficient methods to be discussed in this chapter. Because it is only the gradient (6.4) that depends on the type of the observations in the partial derivatives (6.3), the structure of $\boldsymbol{N}_{\boldsymbol{pp}}$ and $\boldsymbol{b}_{\boldsymbol{p}}$ does not change if reduced-dynamic orbit determination is performed with other observations than undifferenced GPS carrier phase measurements. In the following, we therefore derive the underlying structure for a simplified orbit determination problem with initial conditions and pulses being the only parameters.

The correction equation (4.24) of the r-th observation of this orbit determination problem reads as

$$\epsilon_r = \sum_{k=1}^{6} \frac{\partial F_r}{\partial O_k} \cdot o_k + \sum_{m=1}^{i} \sum_{j=1}^{3} \frac{\partial F_r}{\partial V_{m,j}} \cdot v_{m,j} - l_r \ , \tag{6.16}$$

where o_k, $k = 1, ..., 6$ and $v_{i,j}$, $j = 1, ..., 3$ denote the corrections to six initial conditions and three pulses at each epoch t_i, $i = 1, ..., n-1$, respectively, and where it is assumed that the observation time t_l is part of the subinterval $[t_i, t_{i+1})$. The relations (6.3) and (6.5) yield

$$\frac{\partial F_r}{\partial V_{m,j}} = \left(\boldsymbol{\nabla} F_r \right)^T \cdot \boldsymbol{z}_{V_{m,j}} = \left(\boldsymbol{\nabla} F_r \right)^T \cdot \sum_{k=1}^{6} \beta_{O_k V_{m,j}} \cdot \boldsymbol{z}_{O_k}(t) \ , \tag{6.17}$$

thus the correction equation (6.16) can be rearranged as

$$\epsilon_r = \sum_{k=1}^{6} (\boldsymbol{\nabla} F_r)^T \cdot \boldsymbol{z}_{O_k} \cdot \left(o_k + \sum_{m=1}^{i} \sum_{j=1}^{3} \beta_{O_k V_{m,j}} \cdot v_{m,j} \right) - l_r \ . \tag{6.18}$$

The term in parentheses has an important meaning for a later use: it does not represent the "initially" solved for correction to the osculating element O_k at t_0, which would fully characterize the solution of this particular orbit determination problem in the subinterval $[t_0, t_1)$; it represents, according to (6.7), the correction $o_{i,k}$ to a different initial osculating element $O_{i,k}$ at t_0 which fully characterizes the solution in the subinterval $[t_i, t_{i+1})$ after the occurrence of the $3\,i$ pulses. The correction equation (6.18) illustrates that orbit determination based on pulses may also be understood as a special case of the short-arc parametrization from Sect. 5.3.4 when asking for continuity at the short-arc boundaries. The properties of the newly defined osculating elements $O_{i,k}$ at t_0 will be exploited in Sect. 6.3.

Since the pulse epochs divide the orbital arc into n subintervals, it is advisable to write all n_{o_i} correction equations of the subinterval $I_i = [t_i, t_{i+1})$ in a convenient matrix notation

$$\boldsymbol{\epsilon}_i = \boldsymbol{A}_i\, \boldsymbol{o} + \boldsymbol{A}_i \sum_{m=1}^{i} \boldsymbol{B}_m\, \boldsymbol{v}_m - \boldsymbol{l}_i \ , \tag{6.19}$$

with the column arrays

$\boldsymbol{\epsilon}_i$ of the residuals of subinterval I_i,

$\boldsymbol{l}_i$ of the terms O–C of subinterval I_i,

$\boldsymbol{o}$ of the corrections to the initial osculating elements, and

$\boldsymbol{v}_i$ of the pulse corrections at epoch t_i.

The matrix

$\boldsymbol{A}_i$ denotes the $n_{o_i} \times 6$ first design matrix of the subinterval I_i related to the six initial osculating elements and

$\boldsymbol{B}_m$ denotes the 6×3 coefficient matrix defined by $B_{m[k;j]} \doteq \beta_{O_k V_{m,j}}$.

Taking the correction equations of all subintervals I_i, $i = 0, ..., n-1$ into account, the complete system of normal equations (4.26) reads in the above matrix notation as

$$\begin{pmatrix} \boldsymbol{N} & \sum\limits_{i=1}^{n-1} \boldsymbol{N}_i\, \boldsymbol{B}_1 & \cdots & \sum\limits_{i=n-1}^{n-1} \boldsymbol{N}_i\, \boldsymbol{B}_{n-1} \\ . & \boldsymbol{B}_1^T \sum\limits_{i=1}^{n-1} \boldsymbol{N}_i\, \boldsymbol{B}_1 & \cdots & \boldsymbol{B}_1^T \sum\limits_{i=n-1}^{n-1} \boldsymbol{N}_i\, \boldsymbol{B}_{n-1} \\ . & . & \ddots & \vdots \\ . & . & . & \boldsymbol{B}_{n-1}^T \sum\limits_{i=n-1}^{n-1} \boldsymbol{N}_i\, \boldsymbol{B}_{n-1} \end{pmatrix} \cdot \begin{pmatrix} \boldsymbol{o} \\ \boldsymbol{v}_1 \\ \vdots \\ \boldsymbol{v}_{n-1} \end{pmatrix} = \begin{pmatrix} \boldsymbol{A}^T\, \boldsymbol{P}\, \boldsymbol{l} \\ \boldsymbol{B}_1^T \sum\limits_{i=1}^{n-1} \boldsymbol{A}_i^T\, \boldsymbol{P}_i\, \boldsymbol{l}_i \\ \vdots \\ \boldsymbol{B}_{n-1}^T \sum\limits_{i=n-1}^{n-1} \boldsymbol{A}_i^T\, \boldsymbol{P}_i\, \boldsymbol{l}_i \end{pmatrix} , \tag{6.20}$$

where $\boldsymbol{N}_i \doteq \boldsymbol{A}_i^T\, \boldsymbol{P}_i\, \boldsymbol{A}_i$ is that part associated with the observation interval I_i of the normal equation matrix related to the six initial osculating elements. In analogy, $\boldsymbol{A}_i^T\, \boldsymbol{P}_i\, \boldsymbol{l}_i$ is the contribution of the

same subinterval to the right-hand side of the normal equation system related to the six initial osculating elements. Observe that

$$\boldsymbol{N} = \sum_{i=0}^{n-1} \boldsymbol{A}_i^T \, \boldsymbol{P}_i \, \boldsymbol{A}_i \qquad \text{and} \qquad \boldsymbol{A}^T \, \boldsymbol{P} \, \boldsymbol{l} = \sum_{i=0}^{n-1} \boldsymbol{A}_i^T \, \boldsymbol{P}_i \, \boldsymbol{l}_i \tag{6.21}$$

are the normal equation matrix and the right-hand side of the normal equation system of the deterministic problem, respectively. They would result if no pulses would have been set up. Obviously, the contributions $\boldsymbol{N}_i$ and $\boldsymbol{A}_i^T \, \boldsymbol{P}_i \, \boldsymbol{l}_i$, $i = 0, ..., n-1$ do not only form the complete system of normal equations for dynamic POD according to (6.21), they are together with the matrices $\boldsymbol{B}_i$ also the building blocks of the complete system of normal equations (6.20) for reduced-dynamic POD based on pulses. This implies that the entire system (6.20) may be set up efficiently, because all matrices are of small dimensions. In order to minimize CPU time, it is recommended to set up the normal equation matrix of (6.20) as follows:

- the basic building blocks are the partial sums $\sum_{l=i}^{n-1} \boldsymbol{A}_l^T \, \boldsymbol{P}_l \, \boldsymbol{A}_l$, $i = n-1, ..., 0$. As indicated by this sequence, these sums are best formed starting with $i = n-1$ and ending with $i = 0$, which eventually also yields the contribution (6.21),
- the sub-matrices in the first row are then simply formed for the columns $i > 0$ by multiplying the partial sums $\sum_{l=i}^{n-1} \boldsymbol{A}_l^T \, \boldsymbol{P}_l \, \boldsymbol{A}_l$ from the previous step from the right with the matrices $\boldsymbol{B}_i$, and
- the sub-matrices in columns $i > 0$ and rows $0 < k \leq i$ are finally obtained by multiplying the matrices $\sum_{l=i}^{n-1} \boldsymbol{N}_l \, \boldsymbol{B}_i$ from the previous step from the left with the matrices $\boldsymbol{B}_k^T$.

Similar rules hold for an efficient set up of the right-hand side of the normal equation system (6.20).

Equation (6.20) illustrates that the normal equation matrix has a simple structure. However, its dimension is linearly growing with the number of subintervals, which makes the processing CPU time-intensive for large numbers of pseudo-stochastic parameters, mainly due to the inversion. Unfortunately, it is not possible to apply the parameter pre-elimination technique (see Sect. 4.4.1) to any of the pseudo-stochastic parameters before the very last observation is incorporated into the system of normal equations. This can be seen from the upper summation limits in (6.20) which all include the very last subinterval. A rapid solution strategy based on the presented structure is thus required.

6.3 Rapid Solution Strategy

The correction equation (6.18) implicitly introduced the transformation

$$\boldsymbol{o}_i \doteq \boldsymbol{o} + \sum_{m=1}^{i} \boldsymbol{B}_m \, \boldsymbol{v}_m \tag{6.22}$$

between the "initially" solved for corrections $\boldsymbol{o}$ to the a priori values of the initial osculating elements $\boldsymbol{O}$ at t_0 (subsequently denoted as $\boldsymbol{o}_0$) and the corrections $\boldsymbol{o}_i$ to the a priori values of the initial osculating elements $\boldsymbol{O}_i$ at t_0 which define the solution in the subinterval $[t_i, t_{i+1})$. For the following algebra, it is convenient to define the transformation (6.22) recursively, and in reverse order, between subsequent subintervals as

$$\begin{aligned} \boldsymbol{o}_0 &\doteq \boldsymbol{o} && ; \quad i = 0 \\ \boldsymbol{o}_{i-1} &\doteq \boldsymbol{o}_i - \boldsymbol{B}_i \, \boldsymbol{v}_i = (\boldsymbol{I}_6 \;\; -\boldsymbol{B}_i) \cdot \begin{pmatrix} \boldsymbol{o}_i \\ \boldsymbol{v}_i \end{pmatrix} && ; \quad i \geq 1 \end{aligned} \quad , \tag{6.23}$$

where $\boldsymbol{I}_6$ denotes the identity matrix of dimension 6.

6.3.1 Collection of Observations

First, we consider the system of normal equations in the presence of initial conditions and pulses in its initial stages during the collection of the GPS observations. Let us assume that we already have incorporated all observations for times $t_l \leq t_i$ and that the system may be written in a reduced form as

$$\overline{\boldsymbol{N}}_{i-1}\,\boldsymbol{o}_{i-1} = \overline{\boldsymbol{b}}_{i-1}\;. \tag{6.24}$$

The normal equation matrix $\overline{\boldsymbol{N}}_{i-1}$ and the right-hand side $\overline{\boldsymbol{b}}_{i-1}$ of the normal equation system (6.24) may be computed from the contributions to the normal equation system of the deterministic problem for the observation times $t_l \leq t_i$, i.e., from $\boldsymbol{N}_l$ and $\boldsymbol{b}_l$, $l = 0, ..., i-1$, as

$$\begin{array}{rcll} \overline{\boldsymbol{N}}_0 & \doteq & \boldsymbol{N}_0 & \\ \overline{\boldsymbol{b}}_0 & \doteq & \boldsymbol{b}_0 & ; \quad i = 1 \\ & & & \\ \overline{\boldsymbol{N}}_{i-1} & \doteq & \overline{\boldsymbol{N}}^*_{i-2} + \boldsymbol{N}_{i-1} & \\ \overline{\boldsymbol{b}}_{i-1} & \doteq & \overline{\boldsymbol{b}}^*_{i-2} + \boldsymbol{b}_{i-1} & ; \quad i \geq 2 \end{array} \tag{6.25}$$

with $\overline{\boldsymbol{N}}^*_{i-2}$ and $\overline{\boldsymbol{b}}^*_{i-2}$ to be defined later by (6.28).

The normal equation system (6.24) may be expanded into a system in the unknowns $\boldsymbol{o}_i$ and $\boldsymbol{v}_i$ by replacing $\boldsymbol{o}_{i-1}$ on the left-hand side with the transformation (6.23), and by multiplying both sides of the normal equation system (6.24) from the left with the matrix $(\boldsymbol{I}_6 \;\; -\boldsymbol{B}_i)^T$:

$$\begin{pmatrix} \overline{\boldsymbol{N}}_{i-1} & -\overline{\boldsymbol{N}}_{i-1}\,\boldsymbol{B}_i \\ -\boldsymbol{B}_i^T\,\overline{\boldsymbol{N}}_{i-1} & \boldsymbol{B}_i^T\,\overline{\boldsymbol{N}}_{i-1}\,\boldsymbol{B}_i \end{pmatrix} \cdot \begin{pmatrix} \boldsymbol{o}_i \\ \boldsymbol{v}_i \end{pmatrix} = \begin{pmatrix} \overline{\boldsymbol{b}}_{i-1} \\ -\boldsymbol{B}_i^T\,\overline{\boldsymbol{b}}_{i-1} \end{pmatrix}\;. \tag{6.26}$$

The system (6.26) is the key to a most efficient solution of our orbit determination problem. According to the correction equation (6.18), the modeled observations contained in the following subintervals $I_i, I_{i+1}, ..., I_{n-1}$ do not depend on the terms $\boldsymbol{v}_i$ explicitly as their influence is already taken into account by the osculating elements $\boldsymbol{o}_i$, see also Sect. 6.3.4. It is thus possible to apply the parameter pre-elimination technique (see Sect. 4.4.1) to the pseudo-stochastic parameters. The normal equation system reads after the pre-elimination as

$$\overline{\boldsymbol{N}}^*_{i-1}\,\boldsymbol{o}_i = \overline{\boldsymbol{b}}^*_{i-1} \tag{6.27}$$

with

$$\begin{array}{rcl} \overline{\boldsymbol{N}}^*_{i-1} & \doteq & \overline{\boldsymbol{N}}_{i-1} - \overline{\boldsymbol{N}}_{i-1}\,\boldsymbol{B}_i \left(\boldsymbol{B}_i^T\,\overline{\boldsymbol{N}}_{i-1}\,\boldsymbol{B}_i\right)^{-1} \boldsymbol{B}_i^T\,\overline{\boldsymbol{N}}_{i-1} \\ \overline{\boldsymbol{b}}^*_{i-1} & \doteq & \overline{\boldsymbol{b}}_{i-1} - \overline{\boldsymbol{N}}_{i-1}\,\boldsymbol{B}_i \left(\boldsymbol{B}_i^T\,\overline{\boldsymbol{N}}_{i-1}\,\boldsymbol{B}_i\right)^{-1} \boldsymbol{B}_i^T\,\overline{\boldsymbol{b}}_{i-1} \end{array}\;. \tag{6.28}$$

Observe that a priori weights of the pseudo-stochastic parameters (see Sect. 4.4.2), e.g., in the form of absolute constraints given by an identical weight matrix

$$\boldsymbol{W} = \sigma_0^2\,\boldsymbol{C}_{\boldsymbol{vv}}^{-1} \tag{6.29}$$

for all pulse epochs, have to be added prior to the pre-elimination to the sub-matrix $\boldsymbol{B}_i^T\,\overline{\boldsymbol{N}}_{i-1}\,\boldsymbol{B}_i$ of the normal equation matrix in (6.26). If pseudo-stochastic parameters referring to different epochs shall be constrained with respect to each other, e.g., in the form of relative constraints, it is necessary to modify the here presented pre-elimination step.

In analogy to the equations (6.25) and (6.28), the weighted sum $\overline{s}_{i-1}$ of the terms O–C for observation times $t_l \leq t_i$ can be established as

$$\begin{aligned} \overline{s}_0 &\doteq \boldsymbol{l}_0^T \boldsymbol{P}_0 \boldsymbol{l}_0 \quad ; \quad i = 1 \\ \overline{s}_{i-1} &\doteq \overline{s}^*_{i-2} + \boldsymbol{l}_{i-1}^T \boldsymbol{P}_{i-1} \boldsymbol{l}_{i-1} \quad ; \quad i \geq 2 \end{aligned} \tag{6.30}$$

with

$$\overline{s}^*_{i-1} \doteq \overline{s}_{i-1} - \overline{\boldsymbol{b}}_{i-1}^T \boldsymbol{B}_i \left(\boldsymbol{B}_i^T \overline{\boldsymbol{N}}_{i-1} \boldsymbol{B}_i \right)^{-1} \boldsymbol{B}_i^T \overline{\boldsymbol{b}}_{i-1} \quad , \tag{6.31}$$

which is needed for the computation of the a posteriori standard deviation of unit weight.

6.3.2 Intermediate Solution

The procedure outlined by the equations (6.24), (6.26), (6.27), and (6.25) has to be repeated until the very last observation of the subinterval I_{n-1} is incorporated into the reduced normal equation system. After completion of the data collection, we may solve for the initial osculating element corrections $\boldsymbol{o}_{n-1}$ of the last subinterval I_{n-1} by

$$\boldsymbol{o}_{n-1} = \overline{\boldsymbol{N}}^{-1}_{n-1} \overline{\boldsymbol{b}}_{n-1} = \boldsymbol{Q}_{\boldsymbol{o}_{n-1}\boldsymbol{o}_{n-1}} \overline{\boldsymbol{b}}_{n-1} \, , \tag{6.32}$$

where

$\boldsymbol{Q}_{\boldsymbol{o}_{n-1}\boldsymbol{o}_{n-1}}$ is the cofactor matrix of the solved for corrections $\boldsymbol{o}_{n-1}$.

The solution (6.32) shows that there is no need to compute the "intermediary" corrections $\boldsymbol{o}_{i-1}$, $i = 1, ..., n-1$ during data collection. They would actually represent the filter solutions based on all observations of the interval $[t_0, t_i)$, see Sect. 6.6.2.

The estimated (a posteriori) standard deviation of unit weight is computed according to the formulas (4.28) and (4.29) as

$$m_0 = \sqrt{\frac{\overline{s}_{n-1} - \boldsymbol{o}_{n-1}^T \overline{\boldsymbol{b}}_{n-1}}{f}} \, , \tag{6.33}$$

which eventually yields the covariance matrix of the adjusted orbital elements:

$$\boldsymbol{C}_{\boldsymbol{o}_{n-1}\boldsymbol{o}_{n-1}} = m_0^2 \, \boldsymbol{Q}_{\boldsymbol{o}_{n-1}\boldsymbol{o}_{n-1}} = m_0^2 \, \overline{\boldsymbol{N}}^{-1}_{n-1} \, . \tag{6.34}$$

6.3.3 Back-Substitution for the Final Solution

In order to outline the back-substitution process for the corrections $\boldsymbol{o}_{i-1}$ and $\boldsymbol{v}_i$, $i = n-1, ..., 1$, it is advisable to analyze the normal equation system which would have resulted after the incorporation of all observations, but without having performed the pre-elimination of $\boldsymbol{v}_{n-1}$ at time t_{n-1}. This system is obtained from (6.26) by updating the sub-matrix $\overline{\boldsymbol{N}}_{n-2}$ and the sub-array $\overline{\boldsymbol{b}}_{n-2}$ (replace the index i by $n-1$ in (6.26)) according to

$$\begin{aligned} \widetilde{\overline{\boldsymbol{N}}}_{n-1} &\doteq \overline{\boldsymbol{N}}_{n-2} + \boldsymbol{N}_{n-1} \\ \widetilde{\overline{\boldsymbol{b}}}_{n-1} &\doteq \overline{\boldsymbol{b}}_{n-2} + \boldsymbol{b}_{n-1} \end{aligned} \quad , \tag{6.35}$$

and by not pre-eliminating $\boldsymbol{v}_{n-1}$ in (6.26). The resulting system of normal equations thus reads at the end of the very last subinterval as

$$\begin{pmatrix} \widetilde{\overline{\boldsymbol{N}}}_{n-1} & -\overline{\boldsymbol{N}}_{n-2}\,\boldsymbol{B}_{n-1} \\ -\boldsymbol{B}_{n-1}^T\,\overline{\boldsymbol{N}}_{n-2} & \boldsymbol{B}_{n-1}^T\,\overline{\boldsymbol{N}}_{n-2}\,\boldsymbol{B}_{n-1} \end{pmatrix} \cdot \begin{pmatrix} \boldsymbol{o}_{n-1} \\ \boldsymbol{v}_{n-1} \end{pmatrix} = \begin{pmatrix} \widetilde{\overline{\boldsymbol{b}}}_{n-1} \\ -\boldsymbol{B}_{n-1}^T\,\overline{\boldsymbol{b}}_{n-2} \end{pmatrix} , \tag{6.36}$$

because the influence of the observations of the last subinterval is already taken into account by $\boldsymbol{o}_{n-1}$. Based on the already known corrections $\boldsymbol{o}_{n-1}$ by (6.32), the corrections $\boldsymbol{v}_{n-1}$ to the a priori values of the pseudo-stochastic pulses at t_{n-1} may be computed as

$$\boldsymbol{v}_{n-1} = \left(\boldsymbol{B}_{n-1}^T\,\overline{\boldsymbol{N}}_{n-2}\,\boldsymbol{B}_{n-1}\right)^{-1} \left(\boldsymbol{B}_{n-1}^T\,\overline{\boldsymbol{N}}_{n-2}\,\boldsymbol{o}_{n-1} - \boldsymbol{B}_{n-1}^T\,\overline{\boldsymbol{b}}_{n-2}\right) , \tag{6.37}$$

i.e., they may be computed by circumventing the terms $\widetilde{\overline{\boldsymbol{N}}}_{n-1}$ and $\widetilde{\overline{\boldsymbol{b}}}_{n-1}$ in (6.36).

The procedure outlined by (6.36) and (6.37) may be repeated for the computation of the remaining corrections $\boldsymbol{v}_i$, $i = n-2, ..., 1$ in conjunction with the previous and alternate computation of the corrections $\boldsymbol{o}_i$, $i = n-2, ..., 0$ using the transformation (6.23). Finally, all pulse corrections and the "initially" solved for corrections $\boldsymbol{o}_0$ are obtained.

Covariance Matrix

In order to outline the back-substitution process for the covariance matrix of the adjusted pulses, we start deriving the inverse matrix of the normal equation matrix on the left-hand side of (6.36). As we already know the cofactor matrix $\boldsymbol{Q}_{\boldsymbol{o}_{n-1}\boldsymbol{o}_{n-1}}$ of the adjusted orbital elements from (6.32), we may focus on the computation of the sub-matrices $\boldsymbol{Q}_{\boldsymbol{o}_{n-1}\boldsymbol{v}_{n-1}}$ and $\boldsymbol{Q}_{\boldsymbol{v}_{n-1}\boldsymbol{v}_{n-1}}$ in

$$\begin{pmatrix} \widetilde{\overline{\boldsymbol{N}}}_{n-1} & -\overline{\boldsymbol{N}}_{n-2}\,\boldsymbol{B}_{n-1} \\ -\boldsymbol{B}_{n-1}^T\,\overline{\boldsymbol{N}}_{n-2} & \boldsymbol{B}_{n-1}^T\,\overline{\boldsymbol{N}}_{n-2}\,\boldsymbol{B}_{n-1} \end{pmatrix} \cdot \begin{pmatrix} \boldsymbol{Q}_{\boldsymbol{o}_{n-1}\boldsymbol{o}_{n-1}} & \boldsymbol{Q}_{\boldsymbol{o}_{n-1}\boldsymbol{v}_{n-1}} \\ \boldsymbol{Q}_{\boldsymbol{o}_{n-1}\boldsymbol{v}_{n-1}}^T & \boldsymbol{Q}_{\boldsymbol{v}_{n-1}\boldsymbol{v}_{n-1}} \end{pmatrix} = \begin{pmatrix} \boldsymbol{I}_6 & \boldsymbol{0} \\ \boldsymbol{0} & \boldsymbol{I}_3 \end{pmatrix} , \tag{6.38}$$

where $\boldsymbol{I}_k$ denotes the identity matrix of dimension k. Due to the knowledge of matrix $\boldsymbol{Q}_{\boldsymbol{o}_{n-1}\boldsymbol{o}_{n-1}}$, the missing parts of the entire cofactor matrix in (6.38) may be obtained without inversion as

$$\boldsymbol{Q}_{\boldsymbol{o}_{n-1}\boldsymbol{v}_{n-1}} = \boldsymbol{Q}_{\boldsymbol{o}_{n-1}\boldsymbol{o}_{n-1}}\,\overline{\boldsymbol{N}}_{n-2}\,\boldsymbol{B}_{n-1}\,\left(\boldsymbol{B}_{n-1}^T\,\overline{\boldsymbol{N}}_{n-2}\,\boldsymbol{B}_{n-1}\right)^{-1} \tag{6.39}$$

and

$$\boldsymbol{Q}_{\boldsymbol{v}_{n-1}\boldsymbol{v}_{n-1}} = \left(\boldsymbol{B}_{n-1}^T\,\overline{\boldsymbol{N}}_{n-2}\,\boldsymbol{B}_{n-1}\right)^{-1} \left(\boldsymbol{I}_3 + \boldsymbol{B}_{n-1}^T\,\overline{\boldsymbol{N}}_{n-2}\,\boldsymbol{Q}_{\boldsymbol{o}_{n-1}\boldsymbol{v}_{n-1}}\right) , \tag{6.40}$$

which eventually yields the covariance matrix of the last set of adjusted pulses:

$$\boldsymbol{C}_{\boldsymbol{v}_{n-1}\boldsymbol{v}_{n-1}} = m_0^2\,\boldsymbol{Q}_{\boldsymbol{v}_{n-1}\boldsymbol{v}_{n-1}} . \tag{6.41}$$

The procedure outlined by the equations (6.38), (6.39), and (6.40) may be repeated (replace the index $n-1$ by i) for the computation of the remaining sub-matrices $\boldsymbol{Q}_{\boldsymbol{o}_i\boldsymbol{v}_i}$ and $\boldsymbol{Q}_{\boldsymbol{v}_i\boldsymbol{v}_i}$, $i = n-2, ..., 1$ in conjunction with the previous and alternate computation of the sub-matrices $\boldsymbol{Q}_{\boldsymbol{o}_i\boldsymbol{o}_i}$, $i = n-2, ..., 0$, which may be obtained by applying the general law of error propagation (4.32) on the transformation (6.23) as

$$\boldsymbol{Q}_{\boldsymbol{o}_{i-1}\boldsymbol{o}_{i-1}} = (\boldsymbol{I}_6 \;\; -\boldsymbol{B}_i) \cdot \begin{pmatrix} \boldsymbol{Q}_{\boldsymbol{o}_i\boldsymbol{o}_i} & \boldsymbol{Q}_{\boldsymbol{o}_i\boldsymbol{v}_i} \\ \boldsymbol{Q}_{\boldsymbol{o}_i\boldsymbol{v}_i}^T & \boldsymbol{Q}_{\boldsymbol{v}_i\boldsymbol{v}_i} \end{pmatrix} \cdot \begin{pmatrix} \boldsymbol{I}_6 \\ -\boldsymbol{B}_i^T \end{pmatrix} . \tag{6.42}$$

Finally, all cofactor (and covariance) matrices of the adjusted pulses and of the "initially" solved for orbital element corrections $\boldsymbol{o}_0$ are obtained.

6.3.4 Structure of Transformed Normal Equations

For the sake of completeness, we include the complete system of normal equations for the orbital element corrections $\boldsymbol{o}_{n-1}$ and the pulse corrections $\boldsymbol{v}_i$, $i = 1, ..., n-1$. This system would be obtained by transforming the orbital element corrections without pre-eliminating the pulse corrections $\boldsymbol{v}_i$ at the epochs t_i, $i = 1, ..., n-1$, and would read as

$$\begin{pmatrix} \boldsymbol{N} & -\sum_{i=0}^{0} \boldsymbol{N}_i \boldsymbol{B}_1 & \cdots & -\sum_{i=0}^{n-2} \boldsymbol{N}_i \boldsymbol{B}_{n-1} \\ . & \boldsymbol{B}_1^T \sum_{i=0}^{0} \boldsymbol{N}_i \boldsymbol{B}_1 & \cdots & \boldsymbol{B}_1^T \sum_{i=0}^{0} \boldsymbol{N}_i \boldsymbol{B}_{n-1} \\ . & . & \ddots & \vdots \\ . & . & . & \boldsymbol{B}_{n-1}^T \sum_{i=0}^{n-2} \boldsymbol{N}_i \boldsymbol{B}_{n-1} \end{pmatrix} \cdot \begin{pmatrix} \boldsymbol{o}_{n-1} \\ \boldsymbol{v}_1 \\ \vdots \\ \boldsymbol{v}_{n-1} \end{pmatrix} = \begin{pmatrix} \boldsymbol{A}^T \boldsymbol{P}\, \boldsymbol{l} \\ -\boldsymbol{B}_1^T \sum_{i=0}^{0} \boldsymbol{A}_i^T \boldsymbol{P}_i\, \boldsymbol{l}_i \\ \vdots \\ -\boldsymbol{B}_{n-1}^T \sum_{i=0}^{n-2} \boldsymbol{A}_i^T \boldsymbol{P}_i\, \boldsymbol{l}_i \end{pmatrix} . \tag{6.43}$$

Observe the difference in the upper summation limits of the normal equation system (6.43) and the untransformed system (6.20). They illustrate (once more) that the pulses $\boldsymbol{v}_i$ may be pre-eliminated after having processed the observations in the interval $[t_0, t_i)$, $i = 1, ..., n-1$ thanks to the transformation of the initial osculating elements.

6.4 Considering Additional Parameters

The considered orbit determination problem in Sects. 6.2 and 6.3 was governed by six initial conditions and by a user-specified number of pseudo-stochastic pulses only. This case actually is important in practice, e.g., it occurs if satellite positions are used as pseudo-observations for a further orbit analysis as in Sect. 9.2. In most cases, however, the model function contains many more parameters, e.g., carrier phase bias parameters if GPS phase observables are processed, which may vastly outnumber all other parameters.

It is thus important to add a few comments how the efficient methods from Sects. 6.2 and 6.3 can be extended to cope with more general orbit determination problems.

6.4.1 Structure of the Normal Equation System

In order to benefit from the structure of the normal equation system (6.20) of the orbit determination problem considered so far (and from its efficient set up), we formally consider the additional parameters as "deterministic orbit parameters", and define a generalized array of parameters

$$\widetilde{\boldsymbol{o}}^T \doteq \left(\boldsymbol{o}^T \; p_1 \; \ldots \; p_{\widetilde{n}} \right) , \tag{6.44}$$

where $\widetilde{n}$ is the number of additional parameters. As a consequence, the dimensions of the contributions $\widetilde{\boldsymbol{N}}_i$ and $\widetilde{\boldsymbol{A}}_i^T \boldsymbol{P}_i\, \boldsymbol{l}_i$, $i = 0, ..., n-1$ to the system of normal equations (6.20) are no longer six squared and six, respectively, but (much) larger. Of course, the coefficient matrices have to be redefined as well as

$$\widetilde{B}_{m[k;j]} \doteq \begin{cases} \beta_{O_k V_{m,j}} & ; \quad 1 \le k \le 6 \\ 0 & ; \quad 7 \le k \le \widetilde{n} \end{cases} . \tag{6.45}$$

Using the formalism of the equations (6.44) and (6.45), the normal equation system of the generalized orbit determination problem is formally identical to the normal equation system (6.20) of the originally

studied orbit determination problem. In particular, the outlined rules for an efficient set up of the normal equation matrix remain unchanged. Whether or not the procedure is efficient depends on the dimensions of the terms of the partial sums and on the dimensions of the partial sums.

The dimensions of the terms of the partial sums and the dimensions of all partial sums are the same, if the additional parameters occur in all subintervals, e.g., if the additional parameters are deterministic orbit parameters related to an air drag or a radiation pressure model. In this case, the procedure becomes inevitably inefficient if the number of these additional parameters is large, i.e., comparable to the number of pseudo-stochastic orbit parameters.

Other parameters such as the receiver clock corrections or the carrier phase biases are only active at one epoch or during the comparatively short tracking passes of the GPS satellites, respectively, and should be pre-eliminated as soon as possible due to their occurrence in large numbers. Whereas receiver clock corrections may still be pre-eliminated epoch-wise (see Sect. 6.1.3), the pre-elimination of the carrier phase biases may, e.g., be synchronized with the subinterval boundaries (see Sect. 6.4.2). In this case, the efficiency of the solution method is hardly affected by the additional parameters, see Sect. 6.6.3.

6.4.2 Rapid Solution Strategy

In order to benefit from the rapid solution strategy from Sect. 6.3, we distinguish between additional parameters occurring in all subintervals, e.g., deterministic orbit parameters, and additional parameters which may or may not be pre-eliminated at the end of the subintervals, e.g., carrier phase bias parameters. As a consequence, we have to generalize (6.26) to contain a parameter array $\widetilde{\boldsymbol{o}}_i$ with the array $\boldsymbol{o}_i$ and additional $\widetilde{n}_i$ parameters, which are not subject to pre-elimination at time t_i, and a parameter array

$$\widetilde{\boldsymbol{v}}_i^T \doteq \left(\boldsymbol{v}_i^T \; p_1 \; \ldots \; p_{\widetilde{m}_i}\right) , \tag{6.46}$$

which contains additional $\widetilde{m}_i$ parameters to be pre-eliminated at time t_i. The indices for the numbers $\widetilde{n}_i$ and $\widetilde{m}_i$ indicate that we have to keep track of subinterval-dependent parameter arrays $\widetilde{\boldsymbol{o}}_i$ and $\widetilde{\boldsymbol{v}}_i$ (with subinterval-dependent dimensions) to be retained and eliminated at the end of the subintervals, respectively.

Whether or not the resulting algorithm is efficient depends almost uniquely on the dimensions of the arrays $\widetilde{\boldsymbol{o}}_i$. Even in the case of processing doubly differenced phase observables between a spaceborne LEO receiver and a multitude of ground station receivers, the dimensions of the arrays $\widetilde{\boldsymbol{o}}_i$ remain moderatly small, which does not harm the efficiency of the solution strategy very much, see Sect. 6.6.3.

6.5 Estimating Acceleration Parameters

Section 6.4 generalized the orbit determination problem by including additional parameters. In the course of a further generalization, we focus again on the pseudo-stochastic orbit model and replace the pulses by piecewise constant accelerations. The forthcoming upgrade thus requires minor adaptions of the algorithms presented so far.

Let us assume that three accelerations $A_{i,j}$ are set up in three predetermined directions $\boldsymbol{e}_j(t)$, $j = 1, 2, 3$ in the subintervals $[t_{i-1}, t_i)$, $i = 1, ..., n$ as the only orbit parameters apart from the six initial conditions referring to t_0. According to Sect. 5.3.1, the partial derivative $\boldsymbol{z}_{A_{i,j}}$ of the a priori orbit $\boldsymbol{r}_0(t)$ w.r.t. the

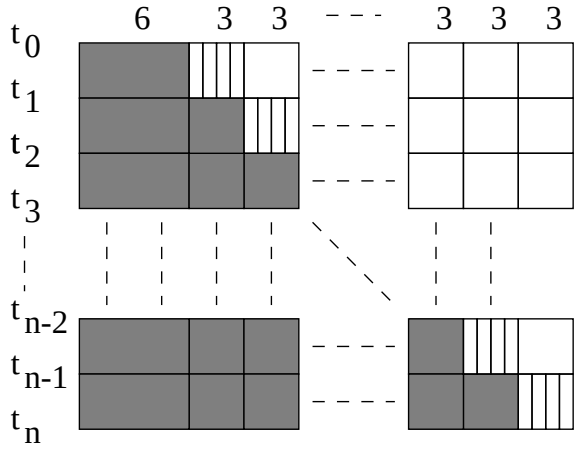

Figure 6.3: Non-zero (non-white) and zero (white) occupation of the first design matrix in the presence of six initial conditions and three piecewise constant accelerations for the intervals $[t_{i-1}, t_i)$, $i = 1, ..., n$. The first non-zero intervals (primed) of all accelerations require a special treatment.

parameter $A_{i,j}$ reads as

$$\boldsymbol{z}_{A_{i,j}}(t) = \begin{cases} \boldsymbol{0} & ; \quad t < t_{i-1} \\ \sum\limits_{k=1}^{6} \alpha_{O_k A_{i,j}}(t) \cdot \boldsymbol{z}_{O_k}(t) & ; \quad t_{i-1} \le t < t_i \\ \sum\limits_{k=1}^{6} \alpha_{O_k A_{i,j}}(t_i) \cdot \boldsymbol{z}_{O_k}(t) & ; \quad t \ge t_i \end{cases} . \tag{6.47}$$

Equation (6.5) shows that $\boldsymbol{z}_{A_{i,j}}$, and as a consequence of (6.3) also $\frac{\partial F_r}{\partial A_{i,j}}$ in the first design matrix (see Fig. 6.3), is generally non-zero for all observation times $t_l \ge t_{i-1}$. This implies that the number of active parameters is increased by 3 after each epoch t_i, $i = 0, ..., n-1$, i.e., from originally only 6 Keplerian elements and 3 accelerations in the subinterval $[t_0, t_1)$ the number grows to a total $6 + 3\ n$ active parameters in the last subinterval $[t_{n-1}, t_n)$. Similar to the case of pulses, the storage requirements are growing quadratically with the number of active accelerations. The only differences merely reside in the total number of parameters ($3\,n$ instead of $3\,(n-1)$) and in the special treatment of the subintervals $[t_{i-1}, t_i)$ for the parameters $A_{i,j}$, $j = 1, 2, 3$.

6.5.1 Changes in the Structure of Normal Equations

In order to highlight the structure of the system of normal equations associated with the considered orbit determination problem, we write in analogy to (6.19) all n_{o_i} correction equations of the subinterval $I_i = [t_i, t_{i+1})$ in a convenient matrix notation

$$\boldsymbol{\epsilon}_i = \boldsymbol{A}_i\, \boldsymbol{o} + \boldsymbol{A}_i \sum_{m=1}^{i} \boldsymbol{B}_m\, \boldsymbol{a}_m + \boldsymbol{A}_{acc,i+1}\, \boldsymbol{a}_{i+1} - \boldsymbol{l}_i\ , \tag{6.48}$$

where

$\boldsymbol{A}_{acc,i+1}$ is the first design matrix of the subinterval I_i related to the accelerations $\boldsymbol{A}_{i+1}$ and

$\boldsymbol{B}_m$ is the coefficient matrix defined by $B_{m[k;j]} \doteq \alpha_{O_k A_{m,j}}(t_i)$.

It is convenient to use the same designation for the coefficient matrices $\boldsymbol{B}_m$ for both types of pseudo-stochastic modeling to underline the analogue structure of the system of normal equations. Taking the correction equations of all subintervals I_i, $i = 0, ..., n-1$ into account, the complete normal equation matrix may be written in the above matrix notation as the sum of the normal equation matrix (6.20), expanded by a $\mathbf{0}$ line and column for the last acceleration corrections $\boldsymbol{a}_n$, and the matrix

$$\begin{pmatrix} \mathbf{0} & \boldsymbol{A}_0^T\,\boldsymbol{P}_0\,\boldsymbol{A}_{acc,1} & \cdots & \boldsymbol{A}_{n-2}^T\,\boldsymbol{P}_{n-2}\,\boldsymbol{A}_{acc,n-1} & \boldsymbol{A}_{n-1}^T\,\boldsymbol{P}_{n-1}\,\boldsymbol{A}_{acc,n} \\ . & \boldsymbol{A}_{acc,1}^T\,\boldsymbol{P}_0\,\boldsymbol{A}_{acc,1} & \cdots & \boldsymbol{B}_1^T\,\boldsymbol{A}_{n-2}^T\,\boldsymbol{P}_{n-2}\,\boldsymbol{A}_{acc,n-1} & \boldsymbol{B}_1^T\,\boldsymbol{A}_{n-1}^T\,\boldsymbol{P}_{n-1}\,\boldsymbol{A}_{acc,n} \\ . & . & \ddots & \vdots & \vdots \\ . & . & . & \boldsymbol{A}_{acc,n-1}^T\,\boldsymbol{P}_{n-2}\,\boldsymbol{A}_{acc,n-1} & \boldsymbol{B}_{n-1}^T\,\boldsymbol{A}_{n-1}^T\,\boldsymbol{P}_{n-1}\,\boldsymbol{A}_{acc,n} \\ . & . & . & . & \boldsymbol{A}_{acc,n}^T\,\boldsymbol{P}_{n-1}\,\boldsymbol{A}_{acc,n} \end{pmatrix}, \tag{6.49}$$

which takes the contributions of the piecewise constant accelerations in their subintervals into account. The right-hand side of the complete normal equation system may be written as the sum of the right-hand side (6.20), expanded by a $\mathbf{0}$ line for the last acceleration corrections $\boldsymbol{a}_n$, and the array

$$\begin{pmatrix} \mathbf{0} \\ \boldsymbol{A}_{acc,1}^T\,\boldsymbol{P}_0\,\boldsymbol{l}_0 \\ \vdots \\ \boldsymbol{A}_{acc,n}^T\,\boldsymbol{P}_{n-1}\,\boldsymbol{l}_{n-1} \end{pmatrix}. \tag{6.50}$$

6.5.2 Changes for the Rapid Solution Strategy

The transformation (6.22) is also in the center of interest for adapting the algorithm of Sect. 6.3 to piecewise constant accelerations. The array $\boldsymbol{o}_i$, however, must be understood in a different way, namely as corrections to the a priori values of the initial osculating elements $\boldsymbol{O}_i$ at t_0 of the particular solution which solves the equation of motion in the subinterval $[t_i, t_{i+1})$. Both parameter arrays $\boldsymbol{O}_i$ and $\boldsymbol{A}_{i+1}$ are necessary in the presence of accelerations to fully characterize the particular solution in the subinterval $[t_i, t_{i+1})$.

In order to perform the rapid solution strategy, it is necessary to modify the transformation (6.23) to

$$\begin{aligned} \begin{pmatrix} \boldsymbol{o}_0 \\ \boldsymbol{a}_1 \end{pmatrix} &\doteq \begin{pmatrix} \boldsymbol{o} \\ \boldsymbol{a}_1 \end{pmatrix} && ;\quad i = 0 \\ \begin{pmatrix} \boldsymbol{o}_{i-1} \\ \boldsymbol{a}_i \end{pmatrix} &\doteq \begin{pmatrix} \boldsymbol{I}_6 & -\boldsymbol{B}_i \\ \mathbf{0} & \boldsymbol{I}_3 \end{pmatrix} \cdot \begin{pmatrix} \boldsymbol{o}_i \\ \boldsymbol{a}_i \end{pmatrix} && ;\quad i \geq 1 \end{aligned}. \tag{6.51}$$

The collection of observations, however, follows the already established pattern. Let us therefore consider the system of normal equations in the presence of initial conditions and accelerations with all observations already incorporated for observations times $t_l \leq t_i$, and let us assume that this system may be written as

$$\begin{pmatrix} \overline{\boldsymbol{N}}_{i-1} & \boldsymbol{A}_{i-1}^T\,\boldsymbol{P}_{i-1}\,\boldsymbol{A}_{acc,i} \\ \boldsymbol{A}_{acc,i}^T\,\boldsymbol{P}_{i-1}\,\boldsymbol{A}_{i-1} & \boldsymbol{A}_{acc,i}^T\,\boldsymbol{P}_{i-1}\,\boldsymbol{A}_{acc,i} \end{pmatrix} \cdot \begin{pmatrix} \boldsymbol{o}_{i-1} \\ \boldsymbol{a}_i \end{pmatrix} = \begin{pmatrix} \overline{\boldsymbol{b}}_{i-1} \\ \boldsymbol{A}_{acc,i}^T\,\boldsymbol{P}_{i-1}\,\boldsymbol{l}_{i-1} \end{pmatrix}. \tag{6.52}$$

Unlike the normal equation system (6.24) of the pulse processing, the system (6.52) always includes one set of acceleration corrections $\boldsymbol{a}_i$ and the associated components of the normal equation matrix and the

right-hand side. The sub-matrix $\overline{\boldsymbol{N}}_{i-1}$ and the sub-vector $\overline{\boldsymbol{b}}_{i-1}$ of the normal equation system (6.52) may still be computed with the same relations (6.25) already established in Sect. 6.3, but with $\overline{\boldsymbol{N}}^{*}_{i-2}$ and $\overline{\boldsymbol{b}}^{*}_{i-2}$ defined differently.

The normal equation system (6.52) may be transformed into a system in the unknowns $\boldsymbol{o}_i$ and $\boldsymbol{a}_i$ by replacing the parameter vector on the left-hand side with the transformation (6.51), and by multiplying both sides of the normal equation system (6.52) from the left with the transposed transformation matrix, which yields a new system similar to (6.26). As the modeled observations contained in the following subintervals do not depend on the terms $\boldsymbol{a}_i$ explicitly, it is possible to apply the parameter pre-elimination technique (see Sect. 4.4.1) to the pseudo-stochastic parameters. The normal equation system may thus be written after the pre-elimination as

$$\overline{\boldsymbol{N}}^{*}_{i-1}\,\boldsymbol{o}_i = \overline{\boldsymbol{b}}^{*}_{i-1} \tag{6.53}$$

with $\overline{\boldsymbol{N}}^{*}_{i-1}$ and $\overline{\boldsymbol{b}}^{*}_{i-1}$ defined differently from (6.28) due to the additional components in (6.52). Finally, the normal equation system (6.53) may be again expanded into a system in the unknowns $\boldsymbol{o}_i$ and $\boldsymbol{a}_{i+1}$ with the transformation

$$\boldsymbol{o}_i \doteq (\boldsymbol{I}_6\ \boldsymbol{0}) \cdot \begin{pmatrix} \boldsymbol{o}_i \\ \boldsymbol{a}_{i+1} \end{pmatrix} , \tag{6.54}$$

and by multiplying both sides of the normal equation system (6.53) from the left with the matrix $(\boldsymbol{I}_6\ \boldsymbol{0})^T$ to be ready for the collection of the observations from the next subinterval.

In a similar way, the computation of an intermediate solution and the back-substitution for the final solution have to be adapted.

Finally, it should be mentioned that the computation of the covariance matrix of the position (and velocity) vector at epochs t of the subintervals $[t_i, t_{i+1})$, $i = 0, ..., n-1$ by the general law of error propagation (4.32) requires not only the covariance matrix associated with $\boldsymbol{o}_i$ as in the case of pulses, but the covariance matrix associated with $\boldsymbol{o}_i$ and $\boldsymbol{a}_{i+1}$, because the improved orbit is written in each subinterval as

$$\boldsymbol{r}(t) = \boldsymbol{r}_0(t) + \sum_{k=1}^{6} \frac{\partial \boldsymbol{r}_0}{\partial O_{i,k}}(t) \cdot o_{i,k} + \sum_{j=1}^{3} \frac{\partial \boldsymbol{r}_0}{\partial A_{i+1,j}}(t) \cdot a_{i+1,j} \ . \tag{6.55}$$

Observe that the partial derivatives of the a priori orbit $\boldsymbol{r}_0(t)$ w.r.t. the six osculating elements $\boldsymbol{O}_i$ are identical to those w.r.t. the "initially" solved for osculating elements $\boldsymbol{O}$. Compared to the conventional processing, the covariance matrix of the position and velocity vector may be obtained very efficiently.

6.6 Numerical Experiments

In order to demonstrate the operational use of the efficient normal equation handling, a few numerical examples are presented in the following with CHAMP data from DOY 198, 2002. On that day, the tracking performance of the BlackJack receiver was nominal with about 22 500 code and phase observations collected on both carriers every 30 s. The ionosphere-free code and phase observations were processed on a HP Compac nc6000 notebook with a 1.6 GHz processor, which should be kept in mind when comparing the results from the performance tests with results from different test environments.

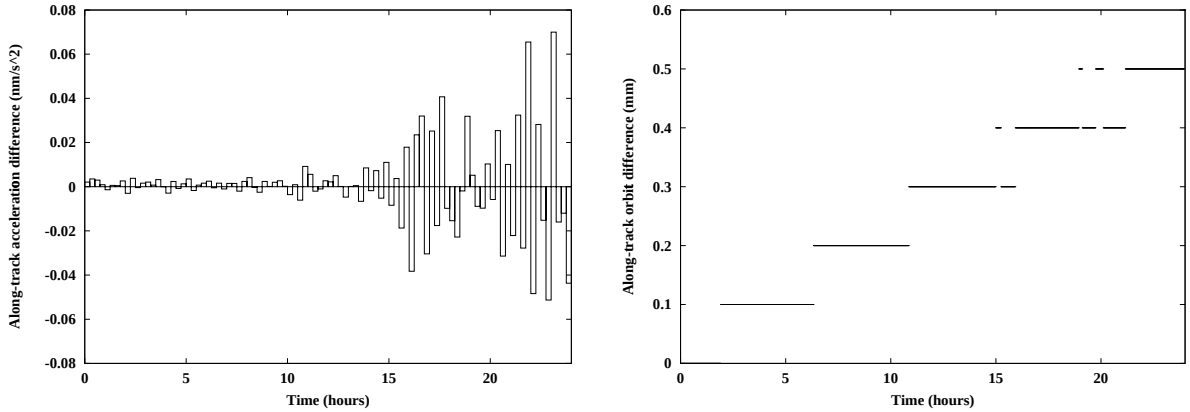

Figure 6.4: Differences between the conventional and the rapid solution strategy for along-track piecewise constant accelerations (left) and along-track orbit positions (right).

6.6.1 Equivalence of Solutions

Compared to the conventional processing, there are major differences in the handling of the normal equations for the rapid solution strategy discussed in Sect. 6.5.2. Different orbits may result for these two approaches. Figure 6.4 (left) depicts the differences in the along-track direction of (constrained) piecewise constant accelerations estimated over 15 min for both approaches. Despite the algebraic equivalence of both methods, small differences occur. The along-track acceleration differences indicate an excellent agreement for the first half of DOY 198, followed by a sudden increase of the quasi-periodic behavior. The observed pattern is probably due to numerical problems, which are accumulated during the processing, and thus tend to show up on the right-hand side of Fig. 6.4 (left). This might be caused by the vast number of manipulations with small matrices necessary for the rapid solution, although it is difficult to attribute this behavior to one or the other method. It is interesting to note, however, that the sign of the acceleration differences often changes in adjacent subintervals, indicating that the impact on the orbit differences is small. Figure 6.4 (right) confirms the smallness of the impact on the orbit as an along-track drift of half a millimeter per day, indicating a slightly wrong mean motion. It should be mentioned that no drifts larger than 1 mm per day have been observed, and that the radial and cross-track components do not show any differences at all, i.e., if present, they are below 0.05 mm.

6.6.2 Intermediary Filter Solutions

It was pointed out in Sect. 6.3.2 that the filter solutions of the considered orbit determination problem might be made available easily on request, which is an advantage compared to the conventional processing. It must be mentioned, however, that our definition of a “filter” solution might differ slightly from other terminologies: it represents the least-squares solution of the considered orbit determination problem based on all observations from the very first epoch to the actually processed epoch. This implies that the orbit trajectory is still represented by pseudo-stochastic parameters, e.g., set up every n-th minute. A new filter solution is thus provided only every n-th minute as well, and not after each newly incorporated observation epoch. Only in the special case of pseudo-stochastic parameters set up at the observation sampling rate, our algorithm should provide equivalent solutions to “classical” filter solutions where stochastic parameters are set up at every measurement epoch.

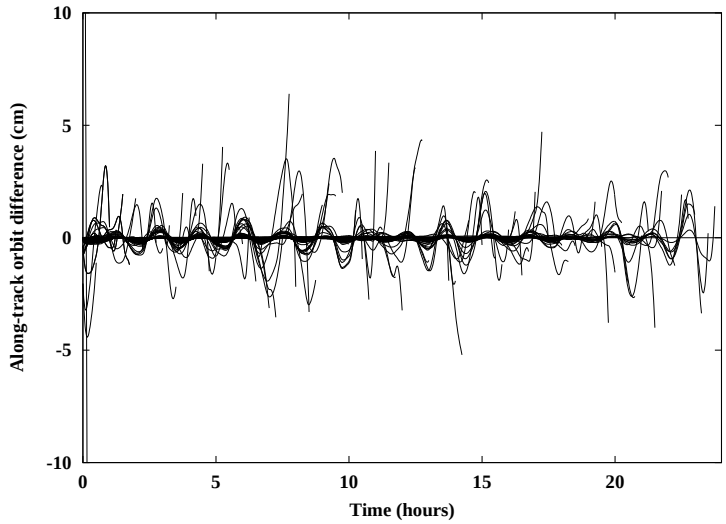

Figure 6.5: Along-track orbit differences between filter and least-squares solutions.

Figure 6.5 shows the along-track orbit differences between the least-squares solution for an orbit determination based on piecewise constant accelerations estimated over 15 min and different filter solutions. The filter trajectories were computed whenever a batch of 15 min of data has been collected, whereas the least-squares solution (last filter solution) was computed after the data collection in the back-substitution process. It can be recognized that large differences occur for the first 15 min which may be attributed to a weak determination of the orbit parameters from a worth of 15 min data only (filter initialization). The consistency between the individual filter solutions and the final least-squares solutions dramatically improves if longer data batches are processed, e.g., sub-millimeter differences at the beginning of the orbital arc are reached for a batch of 8 h. However, Fig. 6.5 also shows that the orbit solution is not very well constrained by the tracking data at the end(s) of the processed time span, which can be seen in this experiment at the right-ends of the individual filter solutions. The orbit consistency may be severely degraded by several centimeters, which is an issue that one has to keep in mind when performing orbit validation by overlap analysis (see Sect. 7.9.4).

6.6.3 Performance Tests

The developments presented in this chapter were motivated by improving the efficiency of the normal equation handling. Figure 6.6 (left) shows the CPU execution times for an orbit determination with pulses for DOY 198 in the described test environment using code zero difference observations only. The conventional processing, the exploitation of the normal equation structure, and the rapid algorithm are compared for different spacings of the pseudo-stochastic pulses. Note that the receiver clock offsets are epoch-wise pre-eliminated for all three methods compared.

It can be seen that the computation times vary for orders of magnitude with the length of the subintervals, which are directly related to the number of solved for parameters (291 and 8643 for pulses every 15 min and 30 s, respectively, including 6 initial conditions). Obviously, the rapid solution strategy is by more than two orders of magnitude more efficient than the alternative two methods, if pseudo-stochastic pulses are set up at the observation sampling rate of 30 s. On the other hand, it is remarkable, as well, that the exploitation of the normal equation structure is comparable to the rapid solution strategy in terms

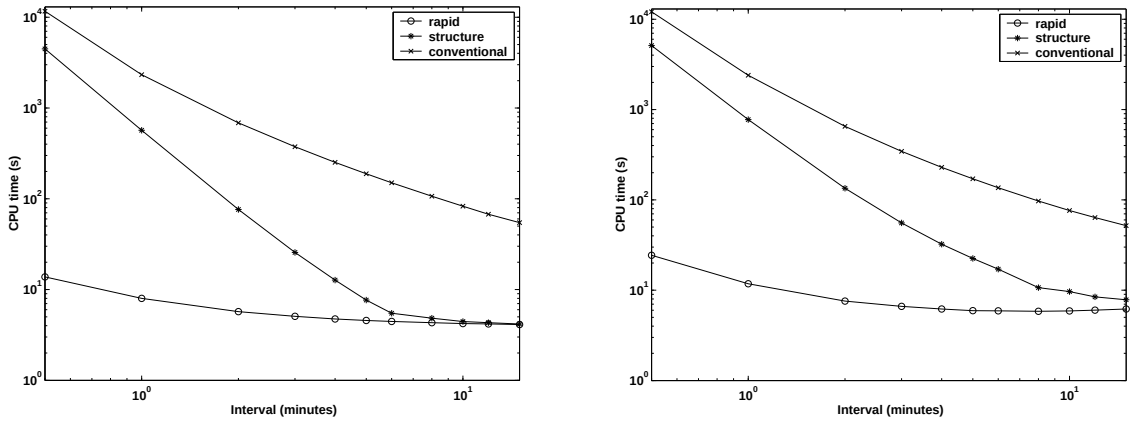

Figure 6.6: CPU execution times for orbit determination with pulses set up at different intervals using undifferenced GPS code (left) or phase observations (right). Compared are the rapid solution strategy, the exploitation of the normal equation structure, and the conventional processing.

of efficiency, if pseudo-stochastic pulses are solved for at moderate rates, e.g., every 6-minutes as it is commonly done for CHAMP and GRACE orbit determination (see Chapter 7). The conventional processing shows a substantially different performance compared to the other two methods: the slope of the curve indicates that the performance is much worse and still dominated by the process of setting up the normal equation system, which is proportional to the dimension squared of the normal equation matrix.

Concerning the exploitation of the normal equation structure, Fig. 6.6 (left) shows that the CPU times are dominated by the inversion of the complete normal equation matrix for subinterval lengths shorter than about 4 min. This can be seen by the steeper slope compared to the conventional method, which is proportional to the dimension cubed (instead of squared) of the normal equation matrix due to the inversion. It has to be expected, however, that both curves become parallel, if the CPU times of the conventional method are dominated as well by the inversion of the complete normal equation matrix, i.e., if the length of the subintervals tends to zero. For subinterval lengths longer than about 4 min, the inversion becomes negligible and the CPU times are thus dominated by the required time for the collection of the observations. Compared to the conventional method, however, data collection is roughly one order of magnitude less time consuming.

The time for the inversion of the reduced normal equation matrix is no issue at all for the rapid solution strategy. Figure 6.6 (left) shows that the CPU times are dominated by the data collection procedure for all subinterval lengths. Even for 30 s subintervals the pre-elimination and back-substitution are at least one order of magnitude less time consuming than the data collection. Only for very high sampling rates the algorithmic part might eventually dominate the data collection part.

The performance of the three methods for piecewise constant accelerations is almost identical to that presented in Fig. 6.6 (left) and need not be shown here. The only difference is a few additional seconds of CPU time spent in the data collection procedure, which is attributed to the slightly larger number of parameters (one additional set of three accelerations), and to the special handling of the first active subinterval of each set of accelerations.

Zero Difference Phase Observations

Figure 6.6 (right) shows the CPU times for an orbit determination with pulses for DOY 198 using the phase zero difference observations only, which makes it necessary to solve for 475 additional carrier phase bias terms. Because they are pre-eliminated at the subinterval boundaries as soon as possible, the CPU times do not change dramatically compared to Fig. 6.6 (left). The overall behavior of the three methods remains basically the same for the processing of code and phase zero difference observations. The only difference resides in slightly larger processing times, e.g., for 1 min subintervals the runs take now 40 min instead of 38 min, 13 min instead of 9 min, and 12 s instead of 8 s, respectively. The reason for this moderate increase of the CPU times is that the carrier phase bias terms are only active during comparatively short time intervals. As the BlackJack receiver was restricted on DOY 198 to track up to 10 GPS satellites at maximum, the number of active phase bias terms was usually below 30 in each subinterval, if the corresponding bias parameters are pre-eliminated as soon as the corresponding GPS satellite sets below the local horizon of the CHAMP antenna. Despite the large number of additional phase bias terms, their impact on the CPU times therefore remains small.

It should be mentioned that it is also possible to not pre-eliminate the carrier phase ambiguities, e.g., for the rapid solution strategy. A discussion about the resulting performance may be found in [*Beutler et al.*, 2006].

Double Difference Phase Observations

Figure 6.7 shows the CPU times for an orbit determination with pulses for DOY 198 using double difference phase observations only. They were formed according to Fig. 8.1 (left) in Sect. 8.1 on space-ground baselines between the CHAMP satellite and 30 IGS ground tracking stations (shown for all three methods), 50 IGS ground stations, and 70 IGS ground stations (only shown for the rapid solution strategy). The coordinates and the troposphere parameters of all ground stations were taken from the CODE final analysis and introduced as known into the LEO analysis, which is then closely related to the processing of zero difference phase observations from one LEO. The main difference resides in the number of ambiguity parameters, which was 3630 in the case of the 30 stations network, 6422 in the case of the 50 stations network, and 8998 in the case of the 70 stations network, and in the number of observations, which was about 115 000, 200 000, and 280 000, respectively. It should be mentioned that all correlations are modeled correctly for all three methods.

Despite of the huge number of unknown parameters, Fig. 6.7 shows that the CPU times are still very small, at least for the rapid solution strategy. The entire orbit determination for a subinterval length of 1 min could be performed in 88 s, 192 s, and 350 s with the 30, 50, and 70 ground stations network, respectively. As expected, the exploitation of the structure of the normal equation system requires much more CPU time than the rapid solution strategy, but it is still much more efficient than the conventional processing. It takes, e.g., about 47 min of CPU time to generate a solution based on subinterval lengths of 1 min with the 30 stations network, but probably more than 10 h to process the observations conventionally. Therefore, the rapid solution strategy should be used if a reduced-dynamic orbit based on short subinterval lengths is determined with a large ground network.

The efficiency of the rapid solution strategy is ensured by the fact that also double difference carrier phase ambiguities are only active during comparatively short time intervals. Even for the 70 ground stations network, the number of active ambiguities was usually below 300 in each subinterval, if they are pre-eliminated as soon as possible. It is interesting to notice that the number of active ambiguities shows

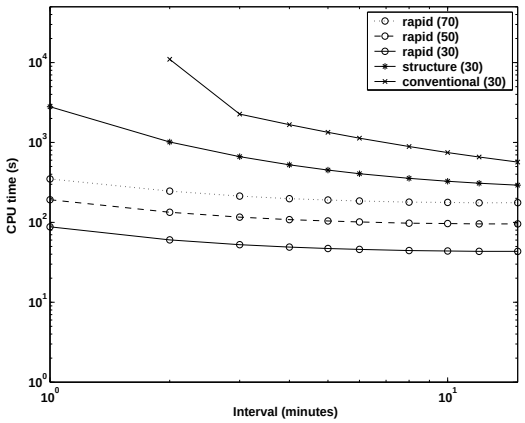

Figure 6.7: CPU execution times for orbit determination with pulses set up at different intervals using GPS double difference phase observations formed between IGS ground stations and CHAMP. Compared are the rapid solution strategy, the exploitation of the normal equation structure, and the conventional processing.

considerable variations for the different subintervals due to the inhomogeneous IGS ground tracking network [*Beutler et al.*, 2006].

6.7 Summary and Comments

The developments presented in this chapter showed that the normal equation systems of different reduced-dynamic LEO orbit determination problems are all governed by a similar and simple structure, which should be taken into account when determining orbits using a large number of pseudo-stochastic parameters. In essence, multiplications of matrices of large dimensions, e.g., $(6 + 3\ (n-1))\ n_{o_i}$ for pulses, can be avoided when considering the relationships between the coefficients compared to the conventional processing based on the observation equations (6.18).

Sections 6.2 and 6.3 showed that both efficient methods are closely related. As a matter of fact, for both approaches an identical data collection step has to be performed first to establish and save the normal equation contributions $\boldsymbol{N}_i = \boldsymbol{A}_i^T\ \boldsymbol{P}_i\ \boldsymbol{A}_i$ and $\boldsymbol{b}_i = \boldsymbol{A}_i^T\ \boldsymbol{P}_i\ \boldsymbol{l}_i$ of all subintervals. Section 6.4 showed that the data collection remains essentially unchanged if additional parameters have to be taken into account, but that the dimensions of $\boldsymbol{N}_i$ and $\boldsymbol{b}_i$ have to be enlarged accordingly. Section 6.5 showed that a similar statement holds for a transition to more refined pseudo-stochastic orbit parameters. Whereas pulses do not show up at all in the data collection step, one set of piecewise constant accelerations, or two sets of piecewise linear accelerations are always active during the data collection procedure.

Section 6.2 showed that the complete normal equation system (6.20) may be constructed efficiently from the contributions $\boldsymbol{N}_i$ and $\boldsymbol{b}_i$ in conjunction with the matrices $\boldsymbol{B}_i$ due to the small dimensions of all submatrices. Sections 6.4 and 6.5 showed that the same statement holds under most other conditions as well if additional parameters or more refined pseudo-stochastic orbit parameters have to be estimated. The main drawback, which is at the same time an advantage, is that the complete normal equation matrix has to be inverted to compute the solution vector. This issue becomes important, e.g., if a large number of pseudo-stochastic parameters has to be set up. The advantage is, however, that the complete variance

matrix is available after the inversion of the complete normal equation matrix.

Section 6.3 showed that a reduced normal equation system may be constructed efficiently from the contributions $\boldsymbol{N}_i$, $\boldsymbol{b}_i$, and the matrices $\boldsymbol{B}_i$ in conjunction with an additional transformation of the initial osculating elements and a pre-elimination step of the pseudo-stochastic parameters, which requires beforehand a transformation of the initial osculating elements. The high efficiency of this algorithm is mainly due to the small dimension of the reduced normal equation systems. Sections 6.4 and 6.5 showed that the same statement holds under most other conditions, as well, if additional parameters or more refined pseudo-stochastic orbit parameters have to be estimated. It is a disadvantage that the complete covariance matrix is not available after the inversion of the last reduced normal equation matrix. However, the complete solution vector (including the pre-eliminated parameters) may be established together with their a posteriori standard deviations by a back-substitution process, which also yields covariance information between pseudo-stochastic orbit parameters referring to the same epoch and between the initial osculating elements.

The processing of undifferenced carrier phase observations requires, in principle, the code observations to separate the carrier phase bias terms from the receiver clock offsets. It is, however, also possible to process undifferenced carrier phase observations alone, if "suitable" a priori information is added to the ambiguities. This problem is usually circumvented in this work by simple regularization, i.e., singular phase bias parameters are fixed to zero when inverting the normal equation matrix. It might happen, however, if a large number of pseudo-stochastic parameters is solved for, that (singular) phase bias parameters and (regular) pseudo-stochastic parameters are not assigned correctly to the singular and non-singular parameters, respectively. To overcome this problem, an additional search of "connected" phase bias parameters was applied to the normal equation matrix, which allows it to constrain one reference ambiguity per connected part to zero before inversion. This procedure turned out to be a necessity, if one strives for the kinematic limit with reduced-dynamic orbits based on pseudo-stochastic parameters.

7. CHAMP and GRACE Orbit Determination Using Undifferenced GPS Data

May 2, 2000, may be considered as the "initiation" of undifferenced GPS data processing for LEO orbit determination. On that day, the intentional dithering of the GPS satellite clocks, selective availability (SA), was switch off. That decision opened the possibility to use the precise IGS GPS satellite clock corrections, nominally available at 5-minute intervals, and to simply interpolate them linearly to the required sampling, typically 30 s, with acceptable precisions of a few centimeters for the individual clock types [*Montenbruck et al.*, 2005]. The same procedure would have completely failed with SA turned on.

Processing undifferenced LEO GPS observations is attractive because only data from the spaceborne receiver is required, unlike to the processing of doubly differenced GPS data. In the latter case, one has to handle a huge amount of observations and ambiguity parameters related to a global terrestrial network of GPS receivers. For the zero difference processing, one only has to introduce GPS satellite clock corrections instead, which implicitly contain the information from the receiver ground network as well. Since the GPS satellite clock corrections are available with full precision at the required 30 s intervals from several IGS ACs, e.g., [*Hugentobler*, 2004a], the zero difference approach is an efficient alternative to the more involved processing of doubly differenced data. CPU times are significantly reduced due to the simpler data handling as shown in Sect. 6.6.3.

In this chapter, we first give an overview of the used GPS orbit- and clock-products of the CODE AC. This is followed by a description of reference frame conventions and transformations used for this work. A short description of the data screening algorithms is given thereafter with the processing scheme for zero difference orbit determination. The chapter concludes with an analysis of CHAMP and GRACE orbits from undifferenced GPS data. Summaries of the results may be found in [*Jäggi et al.*, 2004], [*Jäggi et al.*, 2005a], [*Jäggi et al.*, 2005b], [*Jäggi et al.*, 2006a], [*Jäggi et al.*, 2006c] and [*Jäggi et al.*, 2007]. Results from other research groups are addressed in the corresponding sections.

7.1 GPS Orbit Products

The knowledge of the GPS satellite positions is a prerequisite for any type of positioning application based on GPS observations. Throughout this work, the GPS final ephemerides from the CODE AC of the IGS, see Sect. 4.2, are used to calculate the GPS satellite positions. Like other ACs, CODE derives its own products, which are subsequently used by the IGS AC coordinator to derive the properly weighted combined IGS products using all available submissions from the IGS ACs.

CODE currently provides three types of GPS ephemerides: the final, the rapid, and the ultra-rapid orbits. The final orbits (used in this work) have a reported precision of 2 to 3 cm and are released in weekly batches about 10 days after the end of a GPS week. The rapid orbits are available in daily batches within 17 hours past the end of each day with a, meanwhile, almost identical precision to that of the final orbits.

The ultra-rapid orbits are intended for near-real time users and are made available four times per day with a latency of 3 hours past the last GPS observations included in the analysis. The predicted part of the ultra-rapid orbits has a precision of about 10 cm at present.

The different types of the CODE GPS ephemerides are provided in 24h files on a regular 15 min grid in the standard SP3 format [*Remondi*, 1991], which provides satellite positions in the International Terrestrial Reference Frame (see Sect. 7.3). In order to ensure a highly consistent reconstruction of the original trajectory, the positions are transformed back to the International Celestial Reference Frame where they serve as pseudo-observations to (re)-estimate the GPS orbit parameters, and to finally obtain the original trajectory by a numerical integration based on the same force model standards as used by the CODE AC. It should be mentioned that this procedure is performed in batches of 12 h arc length to properly account for the pseudo-stochastic pulses estimated every 12 h in the original orbit determination scheme at CODE. It is therefore possible to reconstruct GPS trajectories with longer arcs than 24 h, which are, however, no longer fully consistent with the original 3-day arcs from the orbit determination scheme at CODE, where the middle days only define the final orbit products.

The GPS satellite positions of the reconstructed trajectories refer to the center of mass of the satellite, and have to be corrected for the GPS antenna phase center offset before being usable for positioning. Throughout this work these offsets are assumed to be known and they are treated as constant values (as it was common practice for the last twenty-five years of GPS data processing). Nowadays it is well known, however, that antenna phase center variations of the receiver antennas and the transmitter arrays of the GPS satellite antennas represent one of the largest sources for systematic errors in highest-precision GPS analyses, see, e.g., [*Rothacher*, 2001], [*Schmid and Rothacher*, 2003], and [*Schmid et al.*, 2005a]. The implementation of the major change from relative to absolute antenna phase center corrections has been discussed within the IGS for several years [*Schmid et al.*, 2005b], and was finally accomplished on November 6, 2006, starting with the rapid and ultra-rapid products [*Gendt*, 2006]. The CODE products used in this work are still based on the relative phase center correction models of the IGS receiver antennas.

Despite of the high quality of the CODE (IGS) orbit products, the provided ephemerides with the center of mass positions of the individual GPS satellites, as well as the phase center locations of the corresponding GPS antenna arrays, are affected by uncertainties entering into the error budget of an estimated LEO position. In order to assess the mismodeling effect on the computed slant range ρ_{leo}^k (see (5.1)), we consider the linearization

$$\rho_{leo}^k = \rho_{leo0}^k - \boldsymbol{e}_{leo}^k \, \Delta\boldsymbol{r}_{leo} + \boldsymbol{e}_{leo}^k \, \Delta\boldsymbol{r}^k \; , \tag{7.1}$$

where

ρ_{leo0}^k is the a priori slant range between the phase center locations on GPS satellite k and the LEO,

$\Delta\boldsymbol{r}_{leo}$ is the phase center position increment for the LEO,

$\Delta\boldsymbol{r}^k$ is the phase center position increment for GPS satellite k, and

$\boldsymbol{e}_{leo}^k$ is the unit line-of-sight vector pointing from the LEO phase center to the GPS phase center.

The linearization (7.1) would appear in this form at each epoch on the right-hand side of the observation equation (4.22) of GPS satellite k, if one would simultaneously try to estimate the LEO and the GPS position increments kinematically from undifferenced GPS LEO data only. Note that the line-of-sight vector $-\boldsymbol{e}_{leo}^k$ may be identified with the gradient (6.4) addressed in Sect. 6.1.2.

As no GPS position increments are estimated in this work, $\Delta \boldsymbol{r}^k$ is set to zero in (7.1). However, it can be learned from (7.1) that GPS satellite position errors $\delta \boldsymbol{r}^k$ affect the computed slant range according to $\boldsymbol{e}_{leo}^k \, \delta \boldsymbol{r}^k$ when processing zero difference GPS data. This illustrates that errors in the GPS center of mass positions, antenna phase center locations, or GPS satellite clock corrections may directly propagate into the observation equations with the full magnitude, because $\max(|\boldsymbol{e}_{leo}^k \, \delta \boldsymbol{r}^k|) = |\delta \boldsymbol{r}^k|$. Kinematic LEO orbits are most affected by this type of error, but the impact on reduced-dynamic orbits should not be underestimated as the strength of the dynamic models is usually greatly relaxed by pseudo-stochastic parameters [*Švehla and Rothacher*, 2006].

7.2 GPS Clock Products

GPS satellite clock corrections have to be taken into account when processing undifferenced GPS data. In order to achieve the best possible results, use is made of the CODE high-rate GPS satellite clock corrections which are available at 30 s intervals [*Bock et al.*, 2004]. The generation is based on the CODE final GPS orbits, Earth orientation parameters, station coordinates, troposphere parameters, and 5-minute GPS clock corrections. In the CODE analysis clock epoch-differences based on epoch-wise differenced phase observations are estimated and constrained to the 5-minute clock solution, which results in a phase-consistent interpolation of the precise 5-minute clock corrections. A similar procedure may be performed again to obtain GPS satellite clock corrections at even higher rates, e.g., at 10 s or 5 s intervals [*Bock et al.*, 2007], provided that GPS ground station data are available at the targeted sampling rate, e.g., from the IGS sub-network of 1 Hz tracking sites. It is important to mention that the GPS satellite clock corrections are consistent with the GPS orbits and the modeling standards adopted by the IGS, e.g., the relative antenna phase center variations for the GPS receivers, see Sect. 7.1. Note that the clock offsets refer to the IGS realization of the International Terrestrial Reference Frame (see Sect. 7.3), whose origin exhibits an offset from a geocentric reference frame, e.g., [*Hugentobler et al.*, 2005b].

Although the same quality is reported for the high-rate and the original 5-minute clock corrections for kinematic point positioning of terrestrial stations [*Bock et al.*, 2004], the use of GPS clock corrections adds a potential source for errors which is not present when processing doubly differenced GPS data.

7.3 Reference Frame Transformations

GPS data processing requires to express the same vectors in different reference frames. The GPS ephemerides from CODE, e.g., are provided in the International Terrestrial Reference Frame (ITRF), but are conveniently expressed in the International Celestial Reference Frame ICRF for the (re)-integration outlined in Sect. 7.1. The phase center offsets of the receiving GPS antennas aboard LEOs, e.g., are provided in a satellite-fixed (SF) coordinate system, but are conveniently expressed in the ICRF for setting up the GPS observation equations (4.3) and (4.5). The transformations between the three mentioned reference frames are briefly summarized in the following.

7.3.1 ICRF – ITRF

Any position given in the ICRF may be transformed to the ITRF by a series of successive rotations as

$$\boldsymbol{r}_{ITRF} = \boldsymbol{X}^T \boldsymbol{Y}^T \boldsymbol{U} \boldsymbol{N} \boldsymbol{P} \boldsymbol{r}_{ICRF} \, , \tag{7.2}$$

where

$\boldsymbol{X}^T\,\boldsymbol{Y}^T$ are due to polar motion and describe the separation between the third axis of the terrestrial system (Conventional Terrestrial Pole) and the Celestial Ephemeris Pole (IERS 1996 formulation),

$\boldsymbol{U}$ is due to Earth rotation and describes the transition from the rotating system by the Greenwich apparent sidereal time, and

$\boldsymbol{N}\,\boldsymbol{P}$ are due to nutation and precession and describe the transformation between the mean celestial system at epoch J2000 and a system defined by the true equator and equinox of date.

The International Astronomical Union (IAU) conventions define the computation of the matrices $\boldsymbol{U}$, $\boldsymbol{N}$, and $\boldsymbol{P}$, see, e.g., [*McCarthy*, 1996] for the IERS 1996 conventions used in this work, or [*McCarthy*, 2003] for the newly adopted IERS 2000 conventions. For LEO orbit determination discussed in this work, the ITRF convention used is the IGS realization of ITRF2000, called IGS00, which is implied by the GPS ephemerides and Earth rotation parameters used from the CODE AC. When following the reference frame transformations provided by [*McCarthy*, 1996], the ICRF convention then realizes the Earth mean equator and equinox of J2000, also known as the J2000 inertial system.

7.3.2 SF – ICRF

The phase center offsets of the receiving GPS antennas aboard LEOs are provided in a satellite-fixed (SF) coordinate system, which usually has its origin in the LEO center of mass. Table 7.1 lists the offsets for the main POD antennas aboard CHAMP and GRACE as provided by [*Schwintzer et al.*, 2002] and [*Case et al.*, 2002], respectively. The transformation between the SF coordinate system and the ICRF is approximately given by the nominal spacecraft attitude model as

$$\boldsymbol{x}_{ICRF} = \boldsymbol{R}\,\boldsymbol{x}_{SF}\ , \tag{7.3}$$

where

$\boldsymbol{R}$ denotes a rotation matrix defined by the unit vectors (5.15), e.g., as $\boldsymbol{R}_{[1,\ldots,3;1]} \doteq \boldsymbol{e}_a$, $\boldsymbol{R}_{[1,\ldots,3;2]} \doteq -\boldsymbol{e}_c$, and $\boldsymbol{R}_{[1,\ldots,3;3]} \doteq -\boldsymbol{e}_r$.

The concrete form of the approximative transformation (7.3) is valid for the CHAMP nominal, non-yaw-steering attitude model, where the first axis of the SF coordinate system coincides with the along-track direction as indicated by Fig. 7.1, and where the third axis points into the nadir direction. Alternatively and preferably, the attitude information may be obtained from the star camera observations, which provide a much more accurate definition of the actual transformation matrix $\boldsymbol{R}$ in (7.3) by quaternions.

Figure 7.2 shows the deviations between the actual CHAMP SF coordinate system and the nominal orientation as obtained from a reduced-dynamic orbit solution. The angle differences between the actual and the nominal yaw-, roll-, and pitch-axis (not the angle of rotation around these axes) are given as absolute values for a time interval of 300 min, together with information about time and magnitude of

Table 7.1: GPS antenna phase center offsets given in the corresponding SF coordinate systems.

Satellite	x_1 (m)	x_2 (m)	x_3 (m)
CHAMP	-1.4880	0.0000	-0.3928
GRACE A	-0.0004	-0.0004	-0.4514
GRACE B	0.0006	0.0007	-0.4514

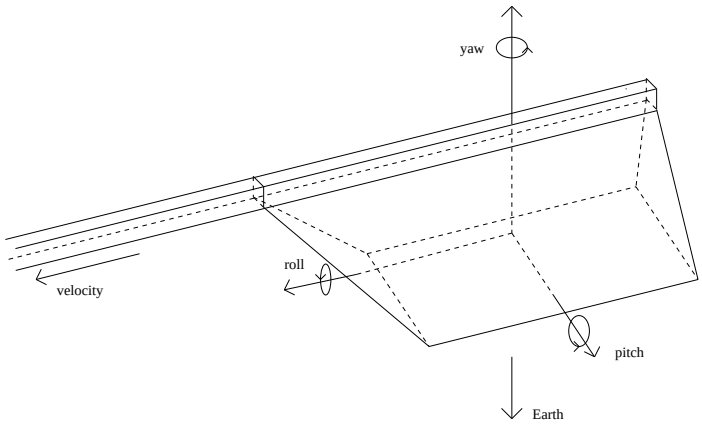

Figure 7.1: The CHAMP roll-, pitch-, and yaw-axis.

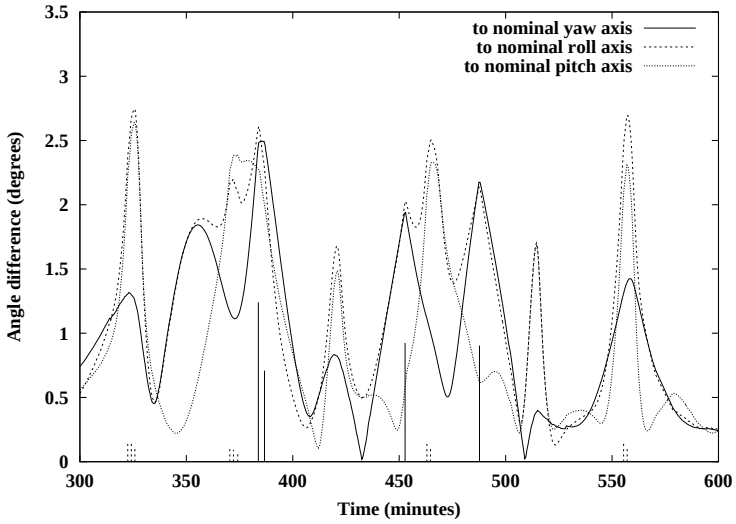

Figure 7.2: Deviations between the actual and the nominal yaw-, roll-, and pitch-axis of the CHAMP satellite on DOY 198, 2002. Time and magnitude of attitude maneuvers for correcting the alignment of the corresponding axes are indicated.

thruster pulses for attitude maintenance. It can be seen that the deviations do not exceed 3° for all axes, which can be only achieved by frequent attitude maneuvers. The largest number of (small) maneuvers is performed to correct the alignment of the roll-axis, which most of the time shows the largest deviations. This might be caused by the inclined front side of the CHAMP satellite (see Fig. 7.1), resulting in an upwards component due to air drag. Less frequent but stronger maneuvers may also be observed in order to align the yaw-axis.

The attitude of the two GRACE satellites is even closer to nominal than in the case of CHAMP. As the GRACE GPS POD antennas are not located at the rear ends of the satellites, but directly above the center of mass locations, see Table 7.1, the nominal attitude model defined by (7.3) would be sufficient. Note that the signs change for GRACE A which was flying “backwards” before the switch maneuver on December 10, 2005 [*Montenbruck et al.*, 2006].

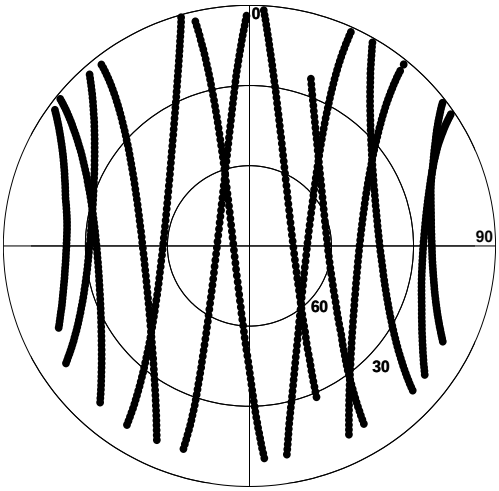

Figure 7.3: PRN 31 on DOY 243, 2003 as observed by the POD antenna of the BlackJack GPS receiver aboard GRACE A. The 14 passes proceed from bottom to top.

7.4 CHAMP and GRACE GPS SST Data

The raw data of the spaceborne GPS receivers is, of course, the most valuable product for orbit determination. At present, all CHAMP and GRACE GPS SST data are publicly available. The GRACE GPS data used in this work, however, are part of the first public data release, which covered DOY 212–335, 2002, DOY 031–365, 2003, and DOY 001–214, 2004 [*Reigber*, 2004a].

The CHAMP and GRACE satellites are not more than 500 km higher above the Earth's surface than any GPS ground station (see Table 2.1). With only slight exaggeration, they may therefore be considered as ordinary, rapidly moving GPS receivers. Whereas the motion of a terrestrial station in the inertial frame is dominated by the Earth's rotation (about 450 m/s at the equator), the LEOs move with $\sqrt{GM/a} \approx 7$ km/s in inertial space (a denotes the semi-major axis of the satellite orbit).

The viewing geometry of the spaceborne receivers is almost the same as that of ground receivers located at the sub-LEO points. However, due to the rapid motion of the spaceborne receivers, it is continuously and rapidly changing from the equatorial to the polar region and vice-versa. Therefore, a particular GPS satellite can only be tracked for about half an hour, and not for several hours as for GPS ground stations. Figure 7.3 shows a sky plot for one GPS satellite, PRN 31, which was observed by the POD antenna of the BlackJack receiver aboard GRACE A on DOY 243, 2003. Azimuth and elevation are referring to the GRACE A SF coordinate system, i.e., azimuth 0° refers to the anti-flight direction.

The 14 tracks are almost straight lines from bottom to top due to the polar orbit of GRACE A; they begin at an initial elevation of approximately 10° and last between 32 and 39 minutes before the receiver loses the lock of the signal due to the fading signal strength at low elevations. The elevation threshold of approximately 10° for satellite acquisition is normal and known from other BlackJack GPS receivers as well, e.g., from CHAMP [*Montenbruck and Kroes*, 2003].

Figure 7.4 shows the number of GPS observations per 1.5° azimuth and 1° elevation bins for a time span of nine weeks. Apart from the elevation threshold of approximately 10° for raising GPS satellites in the bottom part, one recognizes a tracking coverage which is typical for a polar LEO orbit. The four vertical

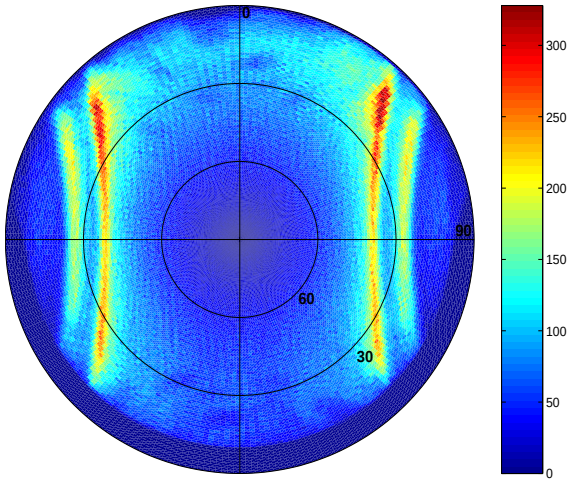

Figure 7.4: Number of GPS observations per 1.5° azimuth and 1° elevation bins as collected by the POD antenna of the BlackJack receiver aboard GRACE A (GPS weeks 1233 – 1241).

"stripes", e.g., indicate the local "horizons" for GPS satellites in the different orbital planes. Their locations change with time because the right ascension of the ascending node of the GRACE orbital plane increases by about -0.136° per day due to the flattening of the Earth. In contrast, GPS orbits are only affected by about -0.039° per day [*Beutler et al.*, 1998]. For the time interval used for Fig. 7.4, the GPS satellites in the orbital planes B and E may appear above the entire horizon, whereas the GPS satellites in the orbital planes F and C may be only observed in-between the "stripes" far left and far right, and the GPS satellites in the orbital planes A and D even only in-between the middle "stripes". Moreover, it can be recognized that generally a smaller number of observations is collected at high elevations (see the transition between dark and light grey in Fig. 7.4), because no observations can be collected above 45° over the poles due to the GPS orbital inclination of 55°. Finally, we notice that setting GPS satellites are tracked down to 0° elevation or even below. A similar statement does not hold for GRACE B where a slightly worse tracking performance is observed, see Sect. 7.9.5.

7.5 Initial Orbit Determination

The initial LEO orbit determination aims at obtaining cleaned LEO GPS phase observations and a priori LEO orbits. A simplified flow chart of the steps involved in this procedure is provided in Fig. 7.5.

First, the LEO RINEX (Receiver-INdependent EXchange [*Gurtner*, 1994]) observation files are converted at the required sampling rate into GPS code and phase binary observation files in the Bernese format [*Dach et al.*, 2007]. At the same time, the CODE final orbit, ERP, and high-rate clock products, as well as additional LEO auxiliary data products like attitude and accelerometer data, are copied into the campaign directories for concatenation to the required arc length. A first code pre-processing is then performed with the ionosphere-free code observation equation (4.3) to detect outliers, and to obtain kinematic LEO positions for initial orbit determination and epoch-specific receiver clock offsets for synchronization purposes. Subsequently, the kinematic LEO positions serve as pseudo-observations for a first orbit determination/integration with six initial conditions and a few dynamical parameters. This first orbit solution enters as reference trajectory into the dual-frequency phase pre-processing schemes

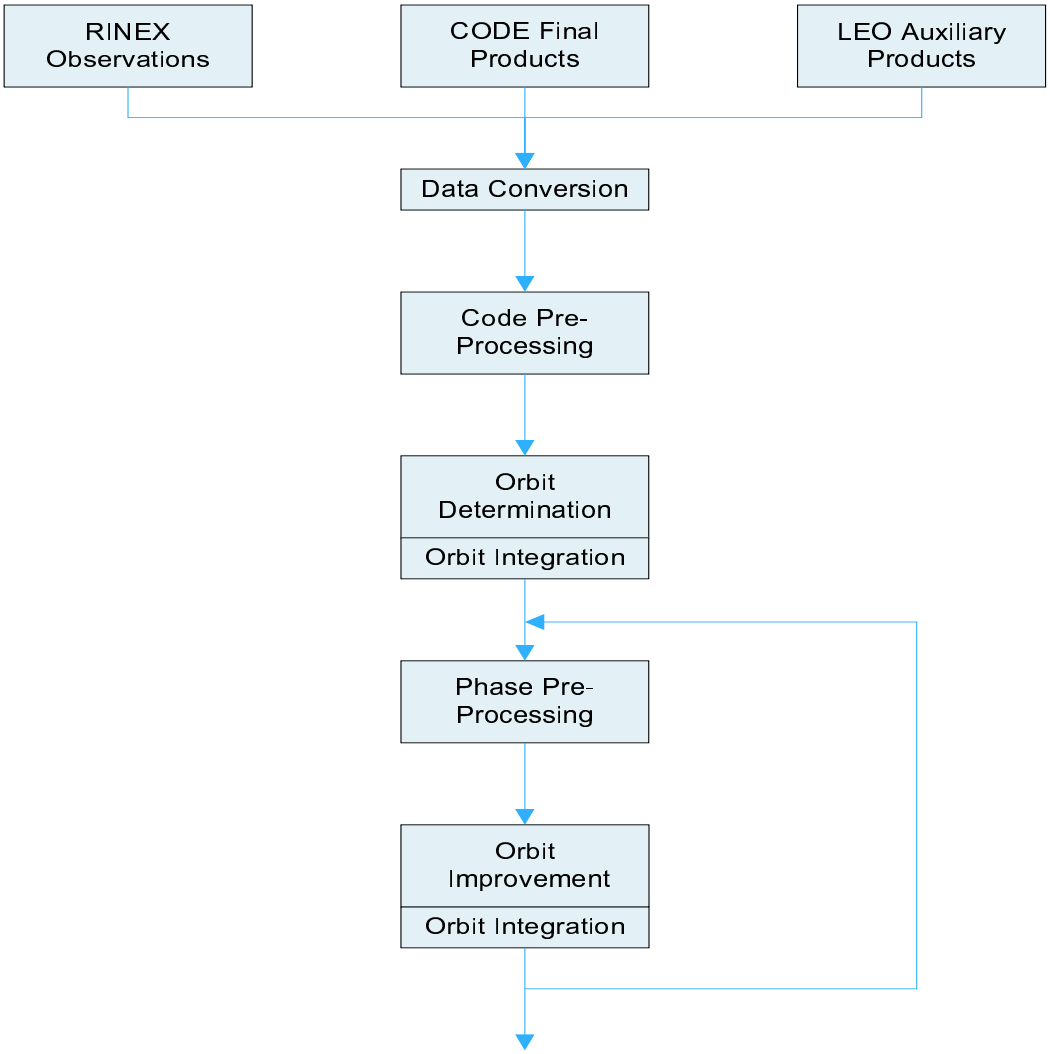

Figure 7.5: Flow chart of the initial LEO orbit determination.

searching for outliers and cycle slips based on the ionosphere-free LC (see Sect. 7.5.1), and as a priori orbit into the orbit improvement with the ionosphere-free phase observation equation (4.5). The improved orbit parameters are then used to update the a priori orbit and the corresponding partial derivatives of the orbit with respect to the orbit parameters by numerical integration.

The very first LEO orbit based on kinematic LEO positions from the code pre-processing is not of the highest quality due to the modest orbit model and the accuracy of the underlying code observations. As a consequence, many GPS phase observations are rejected in the data screening based on the ionosphere-free LC containing the geometric information. It is thus necessary to repeat the search for outliers and cycle slips with the best available orbital information, i.e., with the updated a priori orbit from the first run, to obtain a larger amount of clean phase data. More precise orbital information can then be derived from the newly accepted phase data. Other approaches for phase data screening, e.g., using the Melbourne-Wübbena LC [*Springer*, 2000], have not been applied to LEO POD.

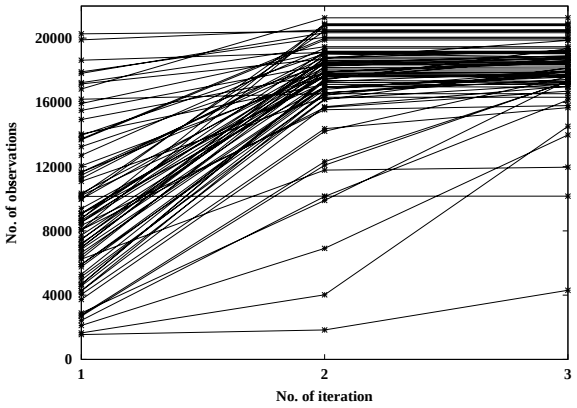

Figure 7.6: Number of accepted CHAMP GPS phase observations for 30 s sampling and 24 h arcs after the first, second, and third screening iteration.

The flow chart 7.5 implies that the data screening, the orbit improvement, and the orbit integration should be repeated to obtain the maximum amount of clean phase data. Despite the geometric information of the ionosphere-free LC, it is important to point out that not the most precise orbit model is necessary to achieve this goal. Experience with CHAMP and GRACE data has shown that a reduced-dynamic orbit parametrization with pulses, e.g., set up every 15 min, is sufficient to obtain clean phase observation files in three iteration steps.

Figure 7.6 shows the number of accepted GPS phase observations after the first, second, and third iteration, respectively, for 75 days of CHAMP data processed with 30 s in arcs of 24 h. This number shows large variations in the first iteration step, ranging from only 1548 observations to 20 270, which makes it necessary to perform at least a second iteration. It can be recognized that two iterations would be sufficient for the majority of the days displayed, because the number of additionally accepted observations after a third iteration is, with a few exceptions, only small. The mean number of accepted observations per day after three iterations is found to be 17 882 for the 75-day period. One has to be aware, however, that the tracking performance may be subject to considerable variations, see Fig. 7.7 for the GRACE A and B receivers. The almost horizontal line at a number of approximately 10 000 observations, e.g., is caused by a large data gap on DOY 174, 2002, whereas the lowest line is caused by bad data quality on DOY 107, 2002.

7.5.1 GPS Data Screening

It is of crucial importance for GPS based precise orbit determination to have GPS data of good quality at our disposal. As bad measurements are frequently encountered even in data obtained from geodetic-type receivers, robust methods have to be used in order to reliably detect and reject bad measurements in pseudo-range and carrier phase data prior to the (final) orbit determination step.

A first quality check of the GPS code measurements is performed simultaneously with the estimation of the kinematic positions in order to detect outliers. For this purpose, the quality of the position solution is examined at each epoch. Whenever the RMS of the associated residuals exceeds a predefined threshold, the code observation that contributes the dominating error is identified and removed from the set of observations. If necessary, the procedure is iterated to reject multiple outliers at the same epoch. The

receiver clock offsets emerging from the same procedure are used later on as a priori values in the orbit determination accompanying the carrier phase cleaning, but are re-estimated after the screening loop with the latest available orbit in order to guarantee a correct receiver clock synchronization for the final orbit determination.

Carrier phase data have to be screened for both outliers and cycle slips (sudden jumps of the size of an integer number of cycles that may occur in the carrier phase data). Since the carrier phase biases should be constant in time, sudden jumps can be detected and separated from outliers by analyzing time-differenced carrier phase observations between consecutive measurement epochs. Similar to the procedure for code observations, the quality of the position difference solution is examined for this purpose using the available a priori orbit. The estimated time-differenced positions and receiver clock offsets from time-differenced ionosphere-free phase measurements are used to derive (time-differenced) residuals Δr_1 and Δr_2 of the original dual-frequency observations in order to test the no-cycle slip hypothesis on the original carriers, see [*Dach et al.*, 2007]. The assumption $\Delta N_1 = 0$ and $\Delta N_2 = 0$ in the residuals

$$\begin{aligned} \Delta r_1 &= \lambda_1 \Delta N_1 + \Delta I \\ \Delta r_2 &= \lambda_2 \Delta N_2 + \xi \Delta I \end{aligned} \tag{7.4}$$

is used to compute the ionosphere-free residual Δr_3 and the ionospheric change ΔI. Whenever these values exceed predefined thresholds, a search for more appropriate values ΔN_1 and ΔN_2 is started around

$$\begin{aligned} \Delta X_1 &= \text{NINT}\left(\frac{\Delta r_1}{\lambda_1}\right) \\ \Delta X_2 &= \text{NINT}\left(\frac{\Delta r_2}{\lambda_2}\right) \end{aligned} \tag{7.5}$$

within predefined search ranges. If exactly one pair ΔN_1 and ΔN_2 is found which passes both thresholds, it would be possible to correct the carrier phase data for the cycle slips ΔN_1 and ΔN_2. Often, however, more than one pair is found due to the difficulty to set the thresholds small enough to guarantee no undetected cycle slips and large enough to avoid many (small) cycle slips which are probably not real. Therefore, no attempt was made in this work to correct the cycle slips during the pre-processing, but to set up a new phase bias parameter whenever one or more pairs ΔN_1 and ΔN_2 are found passing both thresholds. This conservative strategy eliminates the risk to incorporate wrong cycle slip corrections in the carrier phase data. If none of the pairs ΔN_1 and ΔN_2 passes both thresholds, an outlier has to be suspected in the carrier phase data and the satellite that contributes the dominating error is identified and the procedure is repeated without this observation. In order not to delete all observations of one satellite from a certain epoch onward, e.g., because a suspected outlier was not correctly identified as a cycle slip, it is safe to set up a new bias parameter after a predefined time span.

Despite the additional burden on the overall POD process caused by the GPS data editing, in particular for the iterative zero-difference data screening with only poor a priori orbit knowledge discussed in this chapter, data editing is one of the most important steps in the processing scheme of Fig. 7.5. Experiences gained with real GPS data from CHAMP and GRACE have shown that “clean” observations can be obtained under most circumstances, which makes it unnecessary to screen also the postfit residuals of the final orbit determination step.

Figure 7.7 documents the outcome of the GPS data screening for GRACE A (top) and GRACE B (bottom) for the 2003 data set of the first GRACE release, see Sect. 7.4. The daily numbers in Fig. 7.7 reflect the total amount of available GPS observations per day for a sampling rate of 30 s. The colors show the distribution between the number of accepted (light grey) and rejected (dark grey) observations. We

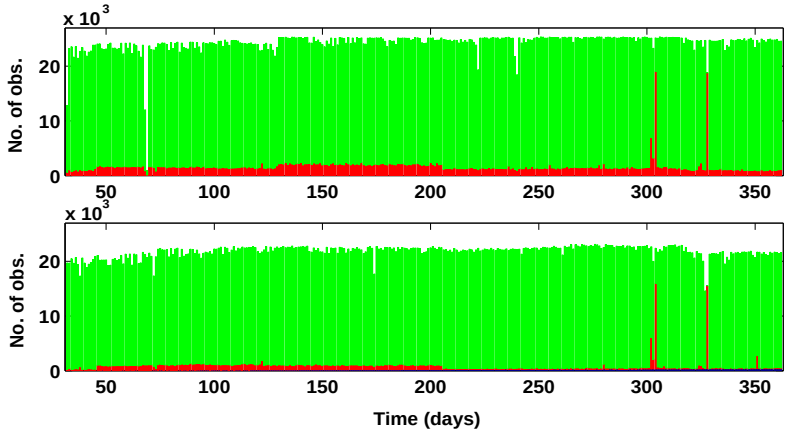

Figure 7.7: Number of accepted (light grey) and rejected (dark grey) GPS observations for GRACE A (top) and GRACE B (bottom) for 30 s sampling and 24 h arcs.

notice a larger amount of available observations for GRACE A due to a generally better tracking performance of its receiver [*Dunn et al.*, 2003]. At the same time it can be recognized that a larger amount of data has to be rejected for GRACE A (6.7%) than for GRACE B (3.1%), which mainly originates from the rejection of low elevation data below a cut-off angle of 0°. Nevertheless, GRACE A offers more accepted observations for orbit determination than GRACE B as indicated by mean values of 22 664 and 20 956 observations per day, respectively.

It is interesting to notice that the number of available GPS observations shows considerable variations in time, that are correlated between both satellites. The most obvious correlations, e.g., a sudden increase of rejected observations on DOY 46 or a sudden decrease on DOY 206, are probably caused by simultaneously executed changes in both receiver configurations. The best tracking performance is observed for DOY 243–298 for both receivers, where the mean number of accepted observations is 23 759 for GRACE A and 22 165 for GRACE B. It is important to remember this time period when analyzing the orbit results in Sect. 7.9, because a good tracking performance is a prerequisite to determine satellite orbits most precisely.

7.6 Final Orbit Improvement and Validation

The final LEO orbit improvement and validation aims at obtaining and validating the final LEO orbits. A simplified flow chart of the steps involved is shown in Fig. 7.8. First, several reduced-dynamic orbit solutions (and a kinematic solution) are computed in parallel with the ionosphere-free phase observation equation (4.5). The flow chart 7.8 implies that each of the reduced-dynamic solutions could be iterated on request, if it is suspected that convergence has not yet been reached. It is worth to mention that this option was not used so far for CHAMP and GRACE POD, although the a priori orbit was only modeled with six initial conditions and three constant accelerations over the entire orbital arc. For the upcoming GOCE satellite and the decaying orbits of the CHAMP and GRACE satellites, however, the situation might be different due to the very low altitudes, which reduce the quality of the a priori trajectories when using the same simple orbit model with only three dynamical parameters.

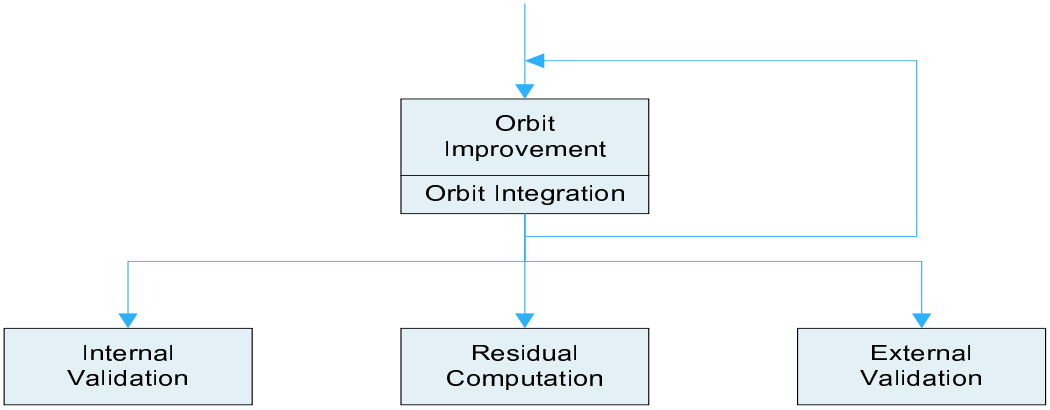

Figure 7.8: Flow chart of the final LEO orbit improvement and validation.

7.6.1 Internal Orbit Validation

Figure 7.8 shows that several internal validation steps are performed in order to assess the precision of the estimated trajectories. Apart from computing the ionosphere-free GPS phase tracking residuals, the different solutions may be compared, e.g., by forming orbit differences. Thereby, the differences between the various reduced-dynamic solutions and the kinematic solution are of particular interest for checking the internal consistency between several types of solutions. Furthermore, formal orbit accuracies along the trajectory and orbital overlaps between consecutive solutions provide additional indicators on the internal quality of the orbits.

7.6.2 External Orbit Validation

Only measurements not used for POD are useful to independently check the GPS-based orbit results. All available observations are used in an attempt to obtain as many indicators as possible to assess the "true" orbital accuracies. For this purpose, Satellite Laser Ranging data are used to compare the computed microwave-based ranges between LEOs and SLR ground stations with the measured ranges, and accelerometer data are used to compare the computed microwave-based accelerations with the measured non-gravitational accelerations. For the two GRACE satellites, inter-satellite K/Ka-band observations are used to validate the computed line-of-sight range and range-rate differences with the measured ones.

Satellite Laser Ranging

Satellite Laser Ranging (SLR) observations are collected, merged, and distributed by the International Laser Ranging Service (ILRS) [*Pearlman et al.*, 2002]. They represent unambiguous range normal points which are constructed from the original roundtrip (two-way) time-of-flight measurements of short laser pulses (< 200 ps) between the SLR ground station telescope i and the satellite k equipped with retro-reflector arrays. Short laser pulses are required to measure the unbiased range between the emitting and the reflecting phase center location with 1 to 2 mm normal point precision. Because SLR stations are usually co-located with GPS permanent stations, SLR observations can be easily time-tagged with GPS system time. The SLR (one-way) range observation equation may thus be formulated in close analogy

to the GPS code observation equation (4.3), and reads at GPS time t_i as

$$S_i^k = \rho_i^k + \Delta\rho_{i,trop}^k + \epsilon_i^k \ , \tag{7.6}$$

where

S_i^k is the SLR normal point range observation, expressed in units of length,

ρ_i^k is the slant range between the laser telescope i and the retro-reflector-equipped satellite k,

$\Delta\rho_{i,trop}^k$ is the signal delay due to the troposphere, expressed in units of length, and

ϵ_i^k is the residual.

The term ρ_i^k includes (in principle) the geometric distance between the telescope reference point and the center of mass position of the satellite, as well as phase center offsets and variations for the telescope and the retro-reflector array. The adopted CHAMP and GRACE phase center offsets are given in Table 7.2 according to [*Schwintzer et al.*, 2002] and [*Case et al.*, 2002], respectively. Phase center variations have not been taken into account, see [*Neubert et al.*, 1998] for the CHAMP retro-reflector array.

SLR observations have to be corrected for the atmospheric signal delay. Most of the SLR stations perform their observations in the visible part of the electromagnetic spectrum, e.g., at 532 nm for a Neodym-YAG laser or at 423 nm for a Titanium-Sapphire laser. Therefore, SLR observations are comparably insensitive to the wet part of the troposphere and there is no ionospheric refraction, which makes it possible to model the remaining part $\Delta\rho_{i,trop}^k$ of the tropospheric delay very accurately [*Marini and Murray*, 1973]. Local meteorological data such as pressure, temperature, and humidity are needed for this purpose.

For the actual SLR validation the slant range ρ_i^k is computed from the known SLR station coordinates, the center of mass position of the satellite, and the known SLR phase center offset. Because SLR observations are unambiguous, the computed range ρ_i^k and the modeled tropospheric delays can be directly compared with the measured range S_i^k without estimating any calibration parameters. The RMS error of the SLR residuals ϵ_i^k, e.g., per day or single pass of the satellite k over the laser observatory i, provides an unambiguous measure of the 1-D accuracy of the line-of-sight distance during the pass.

Accelerometer

The CHAMP STAR accelerometer observations are part of the Level 2 CHAMP data distributed by the GFZ. They represent 10 s normal points of the pre-processed and corrected original Level 1 accelerometer data [*Förste and Choi*, 2004]. The pre-processing is necessary because of various disturbances in the original data [*Grunwaldt and Meehan*, 2003], whereas additional corrections are needed to account for the Lorentz force of the Earth magnetic field, and for the anomalous behavior of one electrode in the radial direction [*Perosanz et al.*, 2003]. The Level 2 accelerometer data represent precise observations of the sum of the non-gravitational accelerations acting on the satellite (see Sect. 2.3.2), but only

Table 7.2: SLR retro-reflector phase center offsets given in the corresponding SF coordinate systems.

Satellite	x_1 (m)	x_2 (m)	x_3 (m)
CHAMP	0.0000	0.0000	0.2500
GRACE A	-0.6000	-0.3275	0.2178
GRACE B	-0.6000	-0.3275	0.2178

within a measurement bandwidth ranging from 10 s to slightly more than one orbital period. As the STAR instrument is not sensitive outside of the specified bandwidth, additional calibration parameters are necessary to relate the measured accelerometer data to the actual non-gravitational accelerations. The accelerometer observation equation for one specific direction d thus reads as

$$A_d = \alpha_d \cdot f_d + b_d + \epsilon_d \,, \tag{7.7}$$

where

A_d is the STAR accelerometer normal point observation,

α_d is the STAR accelerometer scale factor,

f_d is the non-gravitational acceleration,

b_d is the STAR accelerometer bias, and

ϵ_d is the residual.

The calibration parameters α_d and b_d may be subject to long periodic variations, which makes it necessary to adjust them frequently, e.g., once per day. [*Perosanz et al.*, 2004] even propose to adjust them once per revolution.

For the actual accelerometer validation the non-gravitational acceleration f_d is simply identified with the estimated pseudo-stochastic acceleration. The satellite attitude may even be neglected for this purpose because of the relatively large errors in single estimates of pseudo-stochastic parameters. Provided that state-of-the-art models for the gravitational accelerations are used, and no models for the non-gravitational accelerations, this represents an easy way for an approximative validation of the estimated pseudo-stochastic accelerations. One should keep in mind, however, that this procedure is only an approximation, even if a close-to-perfect gravity field model is used. Moreover, only the (scaled) time variations can be compared, because of the estimation of calibration parameters.

Similar procedures can be applied to GRACE accelerometer data, which are part of the Level 1B GRACE data distributed by JPL's Physical Oceanography Distributed Active Archive Center (PODAAC). However, this was not done here.

K/Ka-Band

The GRACE K/Ka-Band Ranging (KBR) system observations are part of the Level 1B GRACE data and are distributed by JPL's PODAAC at 5 s intervals. They represent ionosphere-free carrier phase observations which are constructed from the original Level 1A dual-frequency one-way K- and Ka-band ranging observations on carriers with frequencies of 24.5 GHz and 32.7 GHz, respectively [*Case et al.*, 2002]. The short wavelengths of about 1.2 cm and 0.9 cm of both carriers are a prerequisite to measure the biased range between both GRACE satellites ultra-precisely with about 10 μm at a 1 Hz sampling rate [*Dunn et al.*, 2003]. Because the digital signal processing hardware and CPU host are shared with the GPS function on the Instrument Processing Unit (IPU), the KBR observations can be time-aligned with GPS data with picosecond accuracy. The KBR carrier phase observation equation is thus closely related to the GPS carrier phase observation equation (4.5), and reads for an ionosphere-free KBR observation collected at GPS system time t_i as

$$L_K = \rho_{AB} + \Delta_{\tau K} + B_K + \epsilon_K \,, \tag{7.8}$$

where

L_K is the KBR ionosphere-free observation, expressed in units of length,

ρ_{AB} is the geometric distance between the phase centers of the emitting and the receiving KBR antennas,

$\Delta_{\tau K}$ is the KBR distance correction due to the KBR signal traveling time,

B_K is the KBR bias related to the initial carrier phase ambiguity, and

ϵ_K is the residual.

The term ρ_{AB} includes (in principle) the geometric distance between the center of mass of both GRACE satellites, the KBR antenna phase center offsets with respect to the center of gravity, and the antenna phase center variations with respect to the phase center offsets. The latter two terms are provided in the Level 1B KBR data files, as well as the term $\Delta_{\tau K}$ [*Case et al.*, 2002].

The KBR observations represent highly accurate phase or biased range observations. In order to validate the relative GRACE positions with the KBR observations, the bias term B_K in (7.8) has to be estimated for each continuous arc of KBR measurements. Since the Level 1B KBR data files are provided in 24 h (daily) periods, one bias term has to be calibrated for each day, if no loss of the signal lock occurs in the KBR data. If a loss of lock occurred, cycle slips have to be accommodated by the estimation of multiple bias terms. This can be accomplished easily, because cycle slip epochs or bad measurement epochs are flagged reliably in the Level 1B KBR data files [*Case et al.*, 2002]. An additional pre-processing of KBR observations for cycle slip detection is not necessary.

For the actual KBR validation the relative GRACE position is computed as simply as

$$\rho_{AB} = |\boldsymbol{r}_B(t_i) - \boldsymbol{r}_A(t_i)| \,, \tag{7.9}$$

where $\boldsymbol{r}_A(t_i)$ and $\boldsymbol{r}_B(t_i)$ are the orbit positions at GPS system time t_i of GRACE A and B, respectively. The mean KBR antenna phase center offsets and the satellite attitude are neglected because the KBR measurements are only able to validate the change of the relative GRACE orbit positions in the line-of-sight direction. Due to the very small KBR observation noise, the RMS error of the KBR residuals thus provides a direct measure of the 1-D precision (standard deviation) of the relative GRACE orbit solution. One should keep in mind, however, that the KBR RMS error could reflect a too optimistic quality, if multiple biases have to be calibrated over a 24 h arc.

The Level 1B KBR data files also report KBR range-rate and range-acceleration observations [*Case et al.*, 2002]. Both quantities are derived from the KBR phase observations by numerical differentiation and may be used, e.g., to directly measure the precision of the line-of-sight component of the relative GRACE orbit velocities

$$v_{AB} = (\dot{\boldsymbol{r}}_B - \dot{\boldsymbol{r}}_A) \cdot \frac{\boldsymbol{r}_B - \boldsymbol{r}_A}{|\boldsymbol{r}_B - \boldsymbol{r}_A|} \,, \tag{7.10}$$

where $\boldsymbol{r}_A$, $\dot{\boldsymbol{r}}_A$ and $\boldsymbol{r}_B$, $\dot{\boldsymbol{r}}_B$ are the orbital positions and velocities at GPS system time t_i of GRACE A and B, respectively.

7.7 CHAMP Orbit Comparison Campaign

Until today it is possible to validate CHAMP orbit results in the context of the CHAMP orbit comparison campaign [*Boomkamp*, 2003], which was started in October 2001 on an initiative within the IGS LEO Pilot Project with the goal to assist the IGS LEO centers to develop their POD methods by providing

external reference orbits. The campaign attracted much attention in CHAMP POD in the first few months and reached the maximum interest when the First CHAMP Science Meeting was held at the GFZ in Potsdam, Germany (21–24 January, 2002 [*Reigber*, 2001]). Since then, CHAMP orbit solutions were submitted only sporadically by some IGS LEO centers to monitor the fine-tuning of their POD methods.

After the start of our work in October, 2002, we recomputed reduced-dynamic CHAMP orbit solutions based on piecewise constant accelerations for the period from May 20 to May 30, 2001 (DOY 140 to 150) of the CHAMP orbit comparison campaign. The orbits were presented in July 2003 at the 23th General Assembly of the International Union of Geodesy and Geophysics (IUGG) in Sapporo, Japan, see [*Jäggi et al.*, 2005b], and were submitted later on to the IGS LEO AC coordinator for further analysis [*Boomkamp*, 2004]. In the following, we present the outcome of this analysis, but we emphasize that utmost caution has to be taken when interpreting the results, because some of the older submissions from other institutions might not have fully exploited the GPS data at the time of their creation. Therefore, only the better performing solutions from eight IGS LEO centers are included in the following discussion, but valuing conclusions about the quality of these solutions should be omitted as well, because they possibly do not reflect the state-of-the-art capabilities of orbit determination at these institutions.

7.7.1 Individual Orbit Solutions

The CHAMP orbit solutions of the eight LEO centers presented below are all based on different realizations of the reduced-dynamic methodology. They all rely on the most recent geopotential models of that time, EIGEN1-S or TEG-4 [*Tapley et al.*, 2000], which both already incorporated CHAMP data. The processing strategies and the POD software packages used at the individual LEO centers, however, differ considerably. Below we provide information about the key elements of the POD methodologies (if available), and in addition, we refer to newer and newest developments with respect to LEO orbit determination at these institutions. Our solutions, labeled AIUB, are described in full detail, including the "secrets" of an "optimal" tuning.

AIUB

LEO orbit determination at the Astronomical Institute of the University of Bern (AIUB) has been performed within a development environment of the Bernese GPS Software [*Dach et al.*, 2007]. The extensions discussed in this work have been implemented in this version, and will be used in the near future for the official Precise Science Orbit (PSO) determination of ESA's upcoming GOCE satellite in the framework of the High-level Processing Facility (HPF), see Chapter 2. It is important to acknowledge that major parts of the LEO implementations have been carried out as well by the science team of the Institute for Astronomical and Physical Geodesy (IAPG) at the Technical University of Munich (TUM), in particular by Dražen Švehla. Their cooperation and support was essential for the success of our work.

The reduced-dynamic 24 h solutions computed for the CHAMP orbit comparison campaign are solely based on GPS carrier phase observations with a sampling of 30 s. The GPS pseudo-range observations are only used for synchronization purposes. Data screening and processing follows the schemes described in Sects. 7.5 and 7.6, and relies on equally weighted phase observations from all in view GPS satellites above 0° elevation. Full use is made of the orbit and high-rate clock solutions from CODE as summarized in Sects. 7.1 and 7.2, and of attitude data from GFZ. The gravity field model EIGEN-1S, but no non-gravitational models, are used for the pseudo-stochastic CHAMP orbit modeling based on piecewise constant accelerations, see Sect. 5.3.

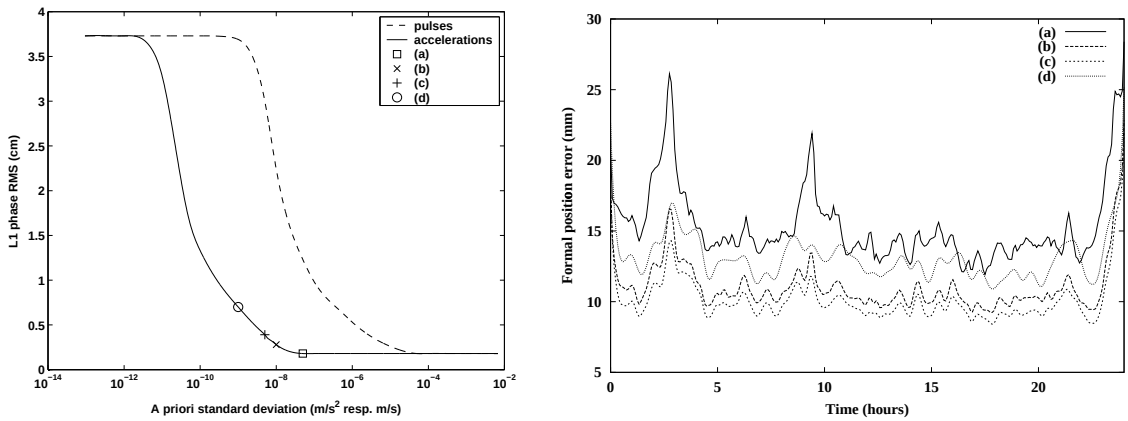

Figure 7.9: Postfit RMS errors of the ionosphere-free phase residuals (scaled to L_1) on DOY 141, 2001 plotted as a function of the constraints applied to piecewise constant accelerations or pulses which are set up every six minutes for reduced-dynamic POD (left). Formal errors of postfit orbit positions as a function of time for different solutions (a), (b), (c), and (d) (right).

The settings of the pseudo-stochastic modeling such as the number and a priori standard deviations of the estimated parameters are options which may be varied. It is to some extent the analyst's responsibility to select "reasonable" settings for the pseudo-stochastic modeling of a LEO trajectory. This choice may be completely different for different LEOs, reasonably different for the same LEO if different a priori force models are used, or slightly different for the same LEO if data from different time periods are analyzed.

Figure 7.9 (left) shows fitted curves for the postfit RMS errors of the ionosphere-free phase residuals (scaled to L_1) on DOY 141, 2001 as a function of the constraints applied for the radial, along-track, and cross-track direction (equal per direction) for piecewise constant accelerations or pulses set up every six minutes. The subinterval length of six minutes is selected somewhat arbitrarily. In principle, it is a compromise between the longest period of an unmodeled disturbing acceleration to be tolerated, and the actual sensitivity of the GPS data to have access to such an acceleration. In practice, the subinterval length of six minutes was simply found to be adequate to model the GPS data from the CHAMP (and GRACE) satellite(s), because appropriate a priori standard deviations of the pseudo-stochastic parameters exist to compute "similar" orbits when using different types of pseudo-stochastic parameters. Section 7.8 will confirm this statement.

Figure 7.9 (left) shows that the selection of the a priori standard deviations has a significant impact on the postfit RMS error of the GPS data. Symbolically speaking, the curves reflect perpendicular transections to the (# Par.) axis in Fig. 5.2. The postfit RMS errors in the upper-left-hand corner of Fig. 7.9 (left) are the result of a dynamic orbit determination, where both types of pseudo-stochastic parameters are heavily constrained to zero with very small a priori standard deviations. In contrast, the postfit RMS errors in the lower-right-hand corner result if a "kinematic-like" reduced-dynamic orbit is determined, where both types of pseudo-stochastic parameters are estimated freely with very large a priori standard deviations. The area in-between represents the kind of reduced-dynamic POD which will usually be performed in this work to obtain high-quality trajectories. Note that the shift between the two curves is a result of the different units of piecewise constant accelerations and pulses; it is not caused by a different response to the constraining.

The size of the postfit RMS errors of the dynamic solutions in the upper-left-hand corner indicates that the dynamic models are insufficient to model the GPS observations. This is mainly caused by not modeling the non-gravitational forces in the orbit determination, which shall be absorbed by the pseudo-stochastic orbit parameters. Therefore, it is necessary to select much larger a priori standard deviations for the solutions discussed in the following, e.g., $5 \cdot 10^{-8}$ m/s^2 for the solution (a), $1 \cdot 10^{-8}$ m/s^2 for the solution (b), $5 \cdot 10^{-9}$ m/s^2 for the solution (c), and $1 \cdot 10^{-9}$ m/s^2 for the solution (d). It can be recognized in Fig. 7.9 (left) that all of these four values are close to the kinematic-like reduced-dynamic orbit solutions, as the pseudo-stochastic orbit parameters have to be able to absorb rather large accelerations, such as the unmodeled air drag in the along-track direction. One should keep in mind, however, that the marked solutions as well as the kinematic-like reduced-dynamic orbit solutions in the lower-right-hand corner still differ significantly from a kinematic solution, because of the subinterval length of six minutes.

Figure 7.9 (left) shows that better postfit RMS errors occur for larger a priori standard deviations. The same statement is true if the number of pseudo-stochastic parameters is increased. This does, however, not necessarily indicate a better quality of the estimated orbits, because they might be "over-parametrized". This might easily occur if one estimates too many pseudo-stochastic orbit parameters with too large a priori standard deviations. In order to avoid "over-parametrization", a better quality indicator is needed, such as the formal accuracies of the orbit positions in the radial, along-track, and cross-track directions. They are computed from the covariance matrix of the estimated parameters according to the general law of error propagation (4.32). Besides the scaling with the estimated standard deviation of unit weight, they could be computed a priori as they only depend on the complete observation scenario, but not on the actual observations.

Figure 7.9 (right) shows the formal accuracies (3-D) of the orbit positions on DOY 141, 2001 as a function of time for the four acceleration-based solutions marked in Fig. 7.9 (left). A few common patterns may be immediately recognized, e.g., the less accurate positions at the arc boundaries as well as around 02:53:00 and 09:35:00. The boundary effects have to be expected because the orbital positions at the arc boundaries are less constrained by the observations in a least-squares estimation. A first indication for this fact was already found in Fig. 6.5 by comparing a complete least-squares solution with different filter solutions. The less accurate positions around 02:53:00 and 09:35:00, however, may be attributed to many marked observations by the GPS data screening and to a less favorable observation scenario including a data gap, respectively. Both situations are governed by a strong reduction of useable GPS observations, which is reflected in the formal accuracies of the orbit positions. Because the BlackJack receiver was able to track only up to 8 satellites at that time, a few missing satellites may considerably influence the quality of the orbit positions even for reduced-dynamic POD. It can be recognized that the "most" kinematic solution (a) suffers most from the unfavorable observation scenarios, whereas the "most" dynamic solution (d) is less affected and, e.g., almost ignores the outage around 09:35:00 which lasts only for 8 min. Moreover, it can be recognized that the formal position accuracies of solution (d) exhibit a much smoother time behavior than those of the solution (a). This is a characteristic of the dynamic models, which prevent a "more" dynamic trajectory to be changed as much as a "more" kinematic orbit by individual observations.

Figure 7.9 (right) shows that neither the solution (a) nor the solution (d) exhibit the lowest level in the formal accuracies of the orbit positions. According to Fig. 7.9 (right), it is the solution (c) for which the CHAMP orbit is determined most precisely on DOY 141, 2001. The same performance is observed for the other days of the CHAMP orbit comparison campaign (DOY 140–150, 2001) when using the same constraints in the radial, along-track, and cross-track direction. This type of solution was given prefer-

ence among various other CHAMP orbit solutions based on 6-minute piecewise constant accelerations, and was submitted as the "optimal" solution to the CHAMP orbit comparison campaign. The "optimal" settings, however, might be different for CHAMP data from a different time period, e.g., due to upgrades in the receiver firmware, and should be checked from time to time. Moreover, one should keep in mind that a further fine-tuning of the pseudo-stochastic orbit modeling is still possible, if different constraints are applied to the piecewise constant accelerations in the radial, along-track, and cross-track directions. This would much better characterize the different amplitudes of the perturbing accelerations that are present in these directions.

It should also be mentioned that the along-track component exhibits the largest formal uncertainties of all of the four solutions discussed. This has to be expected for reduced-dynamic trajectories, and illustrates (once more) that even the "most" kinematic solution (a) significantly differs from a kinematic orbit where the radial component is determined weakly. Additional information about the orbit solutions, including a validation with independent SLR observations, may be found in [*Jäggi et al.*, 2005b].

TUM

LEO orbit determination at the Technical University of Munich (TUM) is also performed within a development environment of the Bernese GPS Software, because major parts of the LEO implementations have been carried out as well by the science team from the Institute for Astronomical and Physical Geodesy (IAPG). Apart from their common interest in reduced-dynamic orbit determination, e.g., [*Švehla and Rothacher*, 2002] and [*Švehla and Rothacher*, 2003b], their research focuses on the determination and promotion of precise kinematic LEO positions for gravity field recovery, see [*Švehla and Rothacher*, 2003a], [*Švehla and Rothacher*, 2003c], [*Švehla and Rothacher*, 2004a], [*Švehla and Rothacher*, 2004b], and [*Švehla and Rothacher*, 2005a]. The successful application of kinematic orbits for gravity field recovery based on kinematic orbits is well documented by [*Gerlach et al.*, 2003c], [*Földváry et al.*, 2004], and [*Wermuth et al.*, 2004].

The reduced-dynamic 24 h solutions computed for the CHAMP orbit comparison campaign are solely based on doubly differenced GPS carrier phase observations with a sampling of 30 s. The GPS pseudo-range observations are only used for synchronization purposes. The GPS final orbits from CODE and the attitude data from GFZ are used as the necessary external sources for POD. Reduced-dynamic orbit determination based on pulses at 6-minute intervals is performed with the EIGEN-1S gravity field model.

DEOS

LEO orbit determination at the Department of Earth Observation and Satellite systems (DEOS) of the Technical University of Delft is performed with the GEODYN [*Rowlands et al.*, 1995] or the GPS High precision Orbit determination Software Tools (GHOST), e.g., [*van Helleputte*, 2004]. Apart from their common interest in reduced-dynamic orbit determination [*van den IJssel et al.*, 2003], their research focuses on GPS-based accelerometry, [*van den IJssel and Visser*, 2005] and [*van den IJssel and Visser*, 2007], and on the exploitation of the formation flying GRACE constellation [*Kroes*, 2006].

The reduced-dynamic 30 h solutions computed for the CHAMP orbit comparison campaign are based on triply differenced GPS carrier phase observations with a sampling of 30 s between the CHAMP satellite and a ground network of about 40 GPS stations [*van den IJssel et al.*, 2003], and are computed with the GEODYN software. The GPS pseudo-range observations are only used for synchronization and for the screening of the undifferenced GPS observations with the Melbourne-Wübbena linear combination. The

GPS final orbits from IGS and the attitude data from GFZ are used as the necessary external sources for POD. Reduced-dynamic orbit determination based on piecewise constant accelerations over 20 min is performed with the EIGEN-1S gravity field model and models for non-gravitational accelerations.

CSR

LEO orbit determination at the Center for Space Research (CSR) of the University of Texas at Austin is performed with the Multi Satellite Orbit Determination Program (MSODP). Latest results achieved with this software package for GRACE orbit determination may be found in [*Kang et al.*, 2006].

The reduced-dynamic 30 h solutions computed for the CHAMP orbit comparison campaign are based on doubly differenced GPS pseudo-range and carrier phase observations between the CHAMP satellite and a ground network of about 50 GPS stations [*Rim et al.*, 2002]. The GPS final orbits from IGS and the attitude data from GFZ are used as the necessary external sources for POD. Reduced-dynamic orbit determination based on once-per-revolution accelerations estimated every 48 minutes and drag coefficients estimated every 90 minutes is performed with the TEG-4 gravity field model and models for non-gravitational accelerations.

GFZ

LEO orbit determination at the GeoForschungsZentrum (GFZ) Potsdam is performed with the Earth Parameter & Orbit System (EPOS) software, e.g., [*Angermann et al.*, 1997]. A selection of recent results for CHAMP orbit determination with this software package may be found in [*König et al.*, 2004]. Advanced studies on combining GPS tracking data from ground station and LEO receivers may be found in [*Zhu et al.*, 2004] and [*König et al.*, 2005].

The reduced-dynamic solutions of the rapid science orbits (RSO) computed for the CHAMP orbit comparison campaign are based on undifferenced CHAMP GPS pseudo-range and carrier phase data. They consist of two overlapping 14 h arcs per day. The GPS orbit positions and high-rate clock corrections needed for undifferenced LEO POD are derived in a separate step prior to LEO orbit determination without making use of the IGS core products. The reduced-dynamic LEO orbit determination is performed with the EIGEN-1S gravity field model and attitude data. Details about the orbit parametrization are, unfortunately, not known to us.

GRGS

LEO orbit determination at the Groupe de Recherches de Géodésie Spatiale (GRGS) of the Centre National d'Etudes Spatiales (CNES) is performed with the GINS software package, which was developed at GRGS/CNES. Early results of CHAMP orbit determination with this software package may be found in [*Bruinsma et al.*, 2003].

The reduced-dynamic solutions of the rapid science orbits (RSO) computed for the CHAMP orbit comparison campaign are based on undifferenced CHAMP GPS pseudo-range and carrier phase data. The IGS GPS final orbits, the high-rate GPS clock corrections from CODE, and the attitude data from GFZ are used as the necessary external sources for POD. Details of the reduced-dynamic LEO orbit determination are, unfortunately, not known to us.

Table 7.3: RMS (cm) of the norm of the difference between orbits from several IGS LEO centers.

Satellite	DEOS	AIUB	TUM	JPL	CSR	GRGS	GFZ	NCL
DEOS	*							
AIUB	6.85	*						
TUM	7.67	5.33	*					
JPL	9.63	10.45	10.71	*				
CSR	8.22	9.52	10.43	8.94	*			
GRGS	9.10	9.33	9.82	10.96	10.57	*		
GFZ	9.11	10.09	10.09	9.91	10.86	11.48	*	
NCL	9.96	10.86	11.39	8.44	8.59	11.75	11.07	*

JPL

LEO orbit determination at the Jet Propulsion Laboratory (JPL) is performed with the GIPSY/OASIS II software package.

The 30 h solutions computed for the CHAMP orbit comparison campaign are based on undifferenced GPS pseudo-range and carrier phase observations. The needed GPS satellite high-rate clock corrections are derived in a separate step from the JPL orbit and clock products for the IGS. The LEO orbit determination is based on a two-step method, where an orbit based on a few dynamic parameters is determined first. Based on this dynamic solution, a reduced-dynamic filtering is performed by introducing stochastic accelerations into the orbit determination process.

NCL

LEO orbit determination at the School of Civil Engineering and Geosciences at the University of Newcastle upon Tyne is performed with the GIPSY/OASIS II software package.

The 13.5 h solutions computed for the CHAMP orbit comparison campaign are based on undifferenced GPS pseudo-range and carrier phase observations. Similar to the JPL solution strategy, a two-step method based on dynamic POD (TEG-4 gravity field model) with additional iterations based on stochastic accelerations is applied. The GPS satellite orbits and the high-rate clock corrections from JPL are used.

7.7.2 Orbit Comparison Results

The ultimate goal of the CHAMP orbit comparison campaign was to estimate the 3-D orbit error for each of the submissions, i.e., to estimate the RMS σ_x of the norm of the difference vector between a CHAMP trajectory computed by the IGS LEO center "x" and the true CHAMP orbit. As this error is not directly accessible, it must be inferred from the entire set of available submissions, possibly by including other available information. Table 7.3 summarizes the RMS σ_{xy} of the norm of the difference vector between orbit solutions from the different IGS LEO centers for the eleven-day period of the CHAMP orbit comparison campaign. The smallest RMS, 5.33 cm, is found between TUM and AIUB. The largest RMS, 11.75 cm, resulted between NCL and GRGS.

We have a number of RMS values related to the differences between individual CHAMP orbit solutions at our disposal. If we assume that the individual solutions are independent, each RMS σ_{xy} of Table 7.3 may be written as $(\sigma_x^2 + \sigma_y^2)^{\frac{1}{2}}$, where σ_x and σ_y denote the unknown RMS errors of the orbit solutions

Table 7.4: SLR validation (cm) for orbits from different IGS LEO centers.

Satellite	RMS	MEAN	SIGMA	Date of submission
AIUB	3.00	0.93	2.86	Feb. 2004
CSR	3.12	0.17	3.11	Jan. 2002
DEOS	3.59	1.30	3.35	Jun. 2002
TUM	3.67	1.77	3.22	Feb. 2003
GRGS	3.97	1.66	3.60	Sep. 2002
GFZ	4.62	0.76	4.56	Sep. 2002
NCL	4.83	1.31	4.65	2002
JPL	4.92	2.42	4.28	2002

from the centers "x" and "y", respectively. Expressed as variances, the relationship $\sigma_{xy}^2 = \sigma_x^2 + \sigma_y^2$ is linear and could thus be used to adjust the 8 individual RMS values in the least-squares sense from the 28 pair-wise RMS values from Table 7.3. The description of the individual solutions, however, indicates that the solutions are in general not independent. The very small RMS value resulting for TUM and AIUB, e.g., indicates that their orbit solutions are highly correlated as both institutions use the same POD software. A similar underestimation has to be expected if the same systematic errors are present in two or more solutions. The RMS errors from Table 7.3 therefore estimate a lower limit of the true pair-wise orbit errors.

7.7.3 SLR Validation

The individual submissions to the CHAMP orbit comparison campaign are all derived from GPS data. The analysis of SLR residuals (see Sect. 7.6.2) thus provides an independent validation of the quality of each orbit solution. Therefore, the SLR validation was taken into account for the CHAMP orbit comparison campaign to derive the orbit quality not only from the pair-wise orbit comparison results shown in Sect. 7.7.2, but (mainly) from the SLR validation in order to provide more reliable estimates of the 3-D orbit quality.

1716 differences of computed and observed ranges between the CHAMP satellite and the SLR observatories could be formed for the 11-day period of the CHAMP orbit comparison campaign. These SLR residuals were computed without the estimation of any additional parameters like range or time biases. Despite the rather large number of collected SLR observations during the 11-day period, the distribution of the available SLR observations in space and time is still very sparse. The 1716 SLR residuals are momentary snapshots of the projection of the total orbit error onto the line-of-sight vector between the SLR observatory and the satellite.

Table 7.4 shows the validation results for the eight best submissions. The smallest RMS of 3.00 cm is found for AIUB, the largest RMS with 4.92 cm resulted for JPL. Despite the good results for all eight solutions, it must be pointed out that more recent submissions, e.g., from JPL, might be better than the available solutions. This is also the reason why only eight of a total of thirteen solutions are given in the tables of these paragraphs; other solutions do not fully reflect the potential of reduced-dynamic CHAMP POD with GPS data.

Table 7.4 separates the SLR RMS for the eight submissions into a mean offset and a standard deviation around the mean. It is striking that all solutions show a positive SLR offset, even if the scatter between

Table 7.5: Pair-wise RMS (cm) of SLR residuals between different IGS LEO centers (top triangle) and ratios of RMS errors from Table 7.3 and from this Table (bottom triangle).

Satellite	AIUB	CSR	DEOS	TUM	GRGS	GFZ	NCL	JPL
AIUB	*	4.33	4.68	4.75	4.97	5.51	5.69	5.76
CSR	*2.20*	*	4.76	4.82	5.04	5.57	5.75	5.82
DEOS	*1.46*	1.73	*	5.14	5.35	5.85	6.02	6.09
TUM	*1.12*	2.17	1.49	*	5.41	5.90	6.07	6.14
GRGS	1.88	2.10	1.70	1.82	*	6.09	6.25	6.32
GFZS	1.83	1.95	1.56	1.71	1.87	*	6.68	6.75
NCL	1.91	1.50	1.66	1.88	1.88	*1.66*	*	6.89
JPL	1.81	1.54	1.58	1.75	1.74	*1.47*	*1.23*	*

the individual solutions is rather large. By far the smallest mean value can be found with 0.17 cm for the CSR submission. This might be due to the fact that CSR solves for a daily center-of-mass x_3-offset parameter together with the other orbit parameters within the POD process. Such a parameter accounts for a possibly wrong offset of the GPS antenna phase center, which would cause an almost perfect radial orbital error as the CHAMP satellite is well aligned to the nominal attitude (see Fig. 7.2). A radial orbit error maps into the SLR residuals and shows up mainly as an offset. As CSR is the only center solving for a x_3-offset within their POD process, the observed SLR offsets in Table 7.4 are, if at all, rather caused by an erroneous GPS phase center offset than by an erroneous SLR phase center offset, which would affect all submissions in the same way. Concerning the SLR offset of 0.93 cm for the AIUB submission, it will be shown in Sect. 7.8.2 that no significant offset can be detected over longer time spans. Eleven days thus seem to be too short to draw firm conclusions about wrong sensor offsets.

In order to correlate the pair-wise RMS orbit errors from Table 7.3 with the individual RMS errors of the SLR residuals from Table 7.4, pair-wise SLR RMS values can be computed from the values provided in Table 7.4, assuming that the individual contributions are independent. Table 7.5 (top triangle) summarizes these pair-wise SLR RMS values, as well as the ratios (bottom triangle) between the pair-wise orbit error signal from Table 7.3 and the pair-wise RMS of SLR residuals. The ratios in the bottom triangle are well suited to recognize dependencies between individual solutions, which is the case if the comparison for a single center shows a significant difference from comparisons with the other solutions. The ratios of 1.12 for the pair AIUB+TUM and 1.23 for the pair NCL+JPL suggest, e.g., correlations induced by the use of the same POD software.

A "proper" elimination of such outliers yields 57 ratios (stemming also from 4 LEO centers not listed in the tables) which were acceptable for the computation of a mean ratio of 1.81 with a standard deviation of 0.16. [*Boomkamp*, 2003] showed that the mean value of the accepted ratios from Table 7.5 (indicated by non-italics) is identical to the ratio for single orbit results, which is the single-solution orbit error divided by the single-solution RMS of the SLR residuals. As the same is true for the standard deviation, the absolute orbit error may be estimated by the empirical relation

$$\mathrm{RMS}_{\mathrm{orbit}} = (1.81 \pm 0.16) \cdot \mathrm{RMS}_{\mathrm{SLR}} \,. \tag{7.11}$$

Table 7.6 shows the individual orbit error estimates with their errors according to relation (7.11) for the solutions of the CHAMP orbit comparison campaign. The ranking of the individual solutions is uniquely determined by the SLR validation results from Table 7.4. It should be mentioned that [*Boomkamp*, 2003]

Table 7.6: 3-D orbit error estimates (cm) for orbits from different IGS LEO centers.

Satellite	RMS	SIGMA
AIUB	5.45	0.48
CSR	5.65	0.50
DEOS	6.52	0.58
TUM	6.67	0.59
GRGS	7.20	0.64
GFZ	8.38	0.74
NCL	8.76	0.77
JPL	8.93	0.79

found a mean ratio of 1.52 with a standard deviation of 0.18 in an analysis of earlier submissions, which is closer to $\sqrt{2}$ and not to $\sqrt{3}$ as the value of 1.81 from [*Boomkamp*, 2004] used in this section.

7.7.4 Discussion

The assessment of the absolute orbit errors, i.e., the determination of the ratios between the pair-wise orbit errors and the pair-wise SLR errors is not free from assumptions [*Boomkamp*, 2001]. Let us therefore briefly discuss some of the central issues.

As mentioned in the previous paragraph, several ratios from Table 7.5 (bottom triangle) were excluded in order to justify to some extent the assumption of independency between individual solutions. This is probably the weakest point of that kind of analysis, because the individual solutions are not at all independent and uncorrelated. If all submissions from the LEO centers were, e.g., kinematic orbit solutions, they would tend to be even more correlated than the reduced-dynamic orbit solutions, because only the GPS data selection and modeling would differ from solution to solution. The pair-wise orbit errors from Table 7.3 would thus decrease, even while the actual orbit error would increase. Obviously, the ratios in Table 7.5 (bottom triangle) are affected by the POD strategy as well and need not to be equal, which questions the computation of *one* mean ratio. Individual error sources in one of the solutions, e.g., are evenly distributed to the error estimates of all solutions if one mean ratio is computed.

The above mentioned points illustrate some of the difficulties which limit our ability to reliably assess the 3-D orbital errors of the individual submissions to the CHAMP orbit comparison campaign.

7.8 CHAMP Orbit Determination with Improved GPS Tracking

This section presents CHAMP orbit determination results obtained with GPS data collected after the receiver firmware update on DOY 064, 2002. On that day the GPS BlackJack receiver was enabled to simultaneously track up to ten GPS satellites (see Sect. 2.3.2). In order to study possible implications on the settings and results of pseudo-stochastic orbit modeling, a time period of 201 days beginning on March 1, 2002 (DOY 060 to 260) has been selected for processing. The first five days at the beginning were intended to visualize different orbit qualities before and after DOY 064, if they should exist. The gravity field model EIGEN-2 was used for the processing as it represented the state-of-the-art CHAMP-only gravity field model at that time.

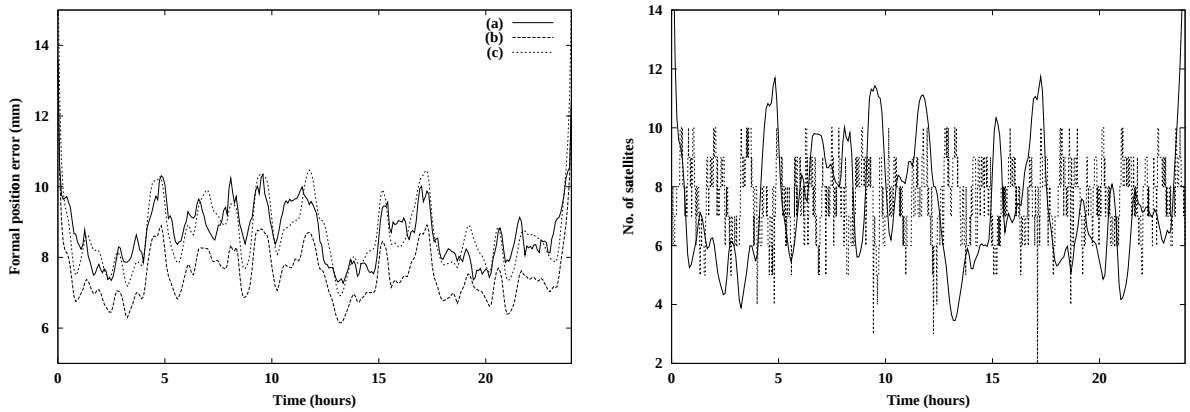

Figure 7.10: Formal errors of postfit orbit positions on DOY 198, 2002 as a function of time for different solutions (a), (b), and (c) (left). Variations of the number of used GPS satellites and overlaid variations of the formal position errors of the solution (b) (right).

7.8.1 Tuning CHAMP POD: Some Words On ...

It has been discussed in the context of the CHAMP orbit comparison campaign in Sect. 7.7 how the "best" processing options were found for the CHAMP 2001 data set, and that they should be checked each time when a new set of spaceborne GPS data is analyzed. The following paragraphs review these options for one selected week of GPS data (DOY 195–201, 2002) within the newly analyzed data set. They illustrate that changes in the subinterval lengths and the a priori standard deviations of pseudo-stochastic parameters may have, within certain limits, almost the same impact on the orbit positions. The same statement is also true for the different types of pseudo-stochastic parameters, provided that the length of the subintervals is short enough.

... A Priori Standard Deviations

Figure 7.10 (left) shows the formal accuracies (3-D) of the orbit positions achieved on DOY 198, 2002 as a function of time for three out of the four 6-minute acceleration-based solutions defined in Sect. 7.7.1. The scale of Fig. 7.10 (left) indicates that the accuracies are generally better than those shown in Fig. 7.9 (right) for DOY 141, 2001. Instead of 12.2 mm we now observe a mean level of 8.3 mm. The reason for this improvement may probably be attributed to the improved tracking performance of the CHAMP BlackJack receiver, caused by the firmware update. Another piece of evidence for this conclusion is given by the solution (a) which now has formal accuracies comparable to the other solutions (which was not the case on DOY 141, 2001, see Fig. 7.9 (right)). Because solution (a) is the "most" kinematic solution, it benefits most from the better receiver performance as it is nicely reflected by the formal position accuracies.

Figure 7.10 (right) shows the correlation between the number of simultaneously observed GPS satellites and the formal position accuracy. The position errors often tend to be larger when only a few GPS observations are available, and vice-versa, see, e.g., around 09:30:00 and 13:00:00. Keep in mind, however, that there is no one-to-one correlation, because other factors such as the viewing geometry influence formal position errors as well.

Figure 7.10 (left) shows that it is no longer solution (c) having the lowest level in the formal accuracies

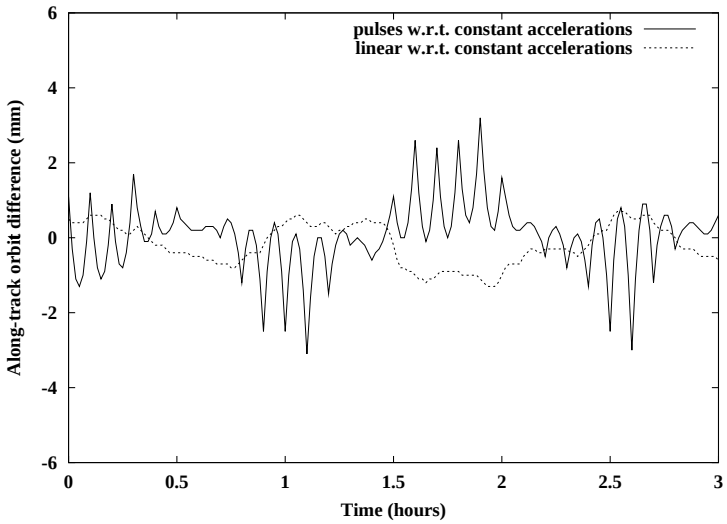

Figure 7.11: Along-track differences on DOY 198, 2002 between an orbit based on piecewise constant accelerations and orbits based on pulses and piecewise linear accelerations, respectively.

of the orbit positions (as it was found for the time period of the CHAMP orbit comparison campaign). Solution (b) now shows the best performance, which is also the case for the entire GPS week 1175. As the constraints were $1 \cdot 10^{-8}$ m/s^2 for solution (b) and $5 \cdot 10^{-9}$ m/s^2 for solution (c), our result favors the "more" kinematic solutions, possibly due to the improved GPS tracking. An orbit comparison between the solutions (b) and (c) on DOY 198 shows, however, that the differences between the two solutions are not dramatic (with a 3-D RMS error of 7.9 mm).

... Different Types of Pseudo-Stochastic Parameters

Figure 7.11 zooms on a specific time interval including the first three hours of DOY 198, 2002, and shows the along-track differences between a 6-minute pulse-based orbit with respect to solution (b), which is based on 6-minute piecewise constant accelerations. In addition, the differences between an orbit based on 6-minute piecewise linear accelerations and solution (b) are displayed. The scale of Fig. 7.11 indicates that the differences induced by the different kinds of pseudo-stochastic orbit models are marginal, provided that the subinterval length of the underlying parameters are not too long and that the a priori standard deviations are chosen "most" appropriately. The latter issue is of particular importance as shown in the previous paragraph. Figure 7.11 illustrates that from the point of view of orbit (position) modeling there is no significant gain to be expected when using more refined pseudo-stochastic parameters, e.g., piecewise linear accelerations instead of piecewise constant accelerations. Even the differences between the pulse and the acceleration solution are very small, although the effect of the instantaneous velocity changes can be well observed as sharp peaks at the pulse epochs every 6 min. Figure 7.11 gives one important reason for selecting piecewise constant accelerations for most of the applications discussed in this work: they avoid "unphysical" phenomena in the orbits, but are easier to use than piecewise linear accelerations.

Figure 7.12 shows the formal accuracies (3-D) of the orbit positions (left) and orbit velocities (right)

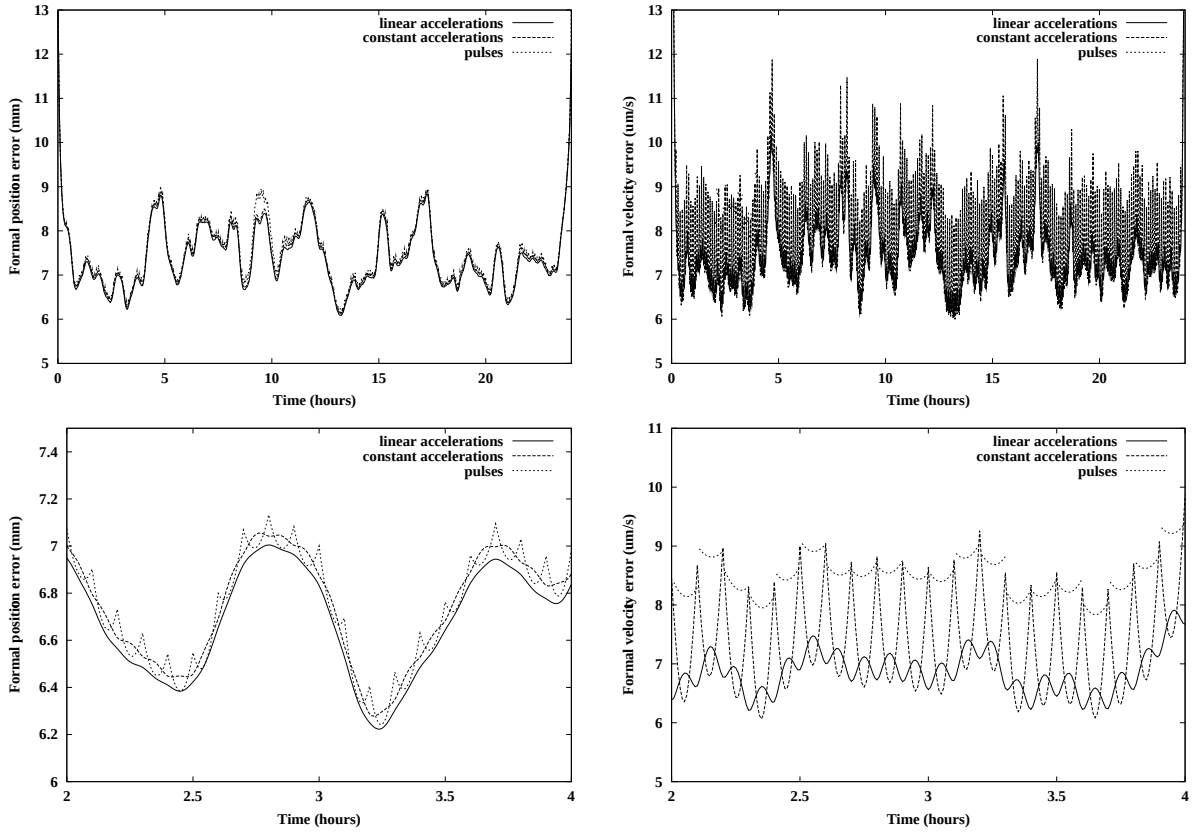

Figure 7.12: Formal errors of postfit orbit positions (left) and orbit velocities (right) on DOY 198, 2002 as a function of time for pulses, piecewise constant, and piecewise linear accelerations. The bottom row shows details for a two-hour interval of the top row.

obtained for the almost identical orbit solutions displayed in Fig. 7.11. The formal position errors in Fig. 7.12 (left) underline the almost identical qualities of the estimated positions. Only the zoom reveals the sharp peaks from Fig. 7.11 for the pulse-based solution. It is interesting that piecewise constant accelerations show an opposite behavior with a slightly lower quality around the middle of the subintervals, whereas the formal accuracies for piecewise linear accelerations are almost free from intra-interval excursions.

As expected, the differences between the pseudo-stochastic orbit models become more pronounced at the velocity level. Figure 7.12 (right) shows a high-frequency pattern with sizeable amplitude, which however, cannot be separated from the other curves in the figure for the entire day, but the detailed view nicely resolves the different patterns and assigns them to the three pseudo-stochastic orbit models. It can be seen that the orbital velocities derived from the pulse solution are formally determined with the lowest accuracy, followed by the velocities derived from piecewise constant and piecewise linear accelerations. Apart from the (expected) discontinuities at the interval boundaries, the formal accuracies of the pulse-based velocities do not show very large variations. A similarly small variation is observed as well for the solution based on piecewise linear accelerations. In contrast, the solution based on piecewise constant accelerations shows very pronounced intra-interval oscillations between the quality level of orbital velocities derived with pulses and orbital velocities derived with piecewise linear accelerations.

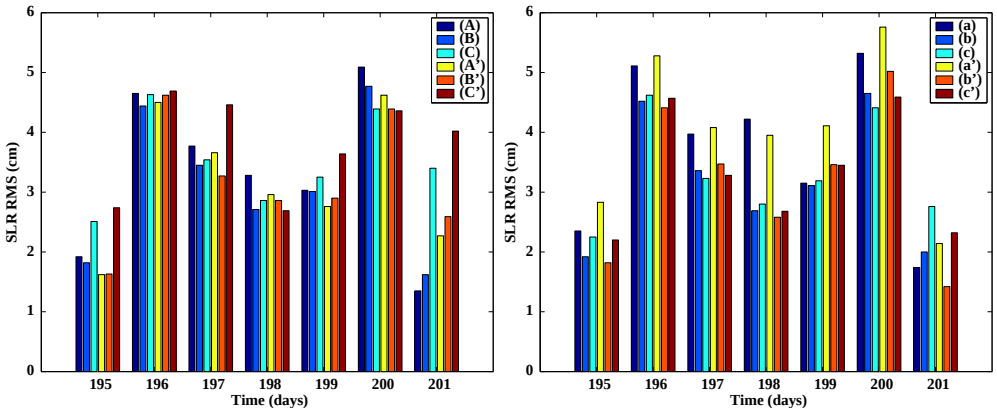

Figure 7.13: Daily SLR RMS errors for GPS week 1175 for reduced-dynamic orbits based on differently constrained pulses (left) or piecewise constant accelerations (right). Solution IDs with and without primes indicate subinterval lengths of 15 and 6 minutes, respectively.

Comparing Fig. 7.12 (right) and (left) shows that piecewise constant accelerations act like pulses on the velocity level.

... Different Subinterval Lengths

For any given subinterval length of pseudo-stochastic parameters, it is rather straightforward to find the "optimal" a priori standard deviations using the criteria outlined in the previous sections. The selection of the subinterval length itself, however, is arbitrary to a certain extent. Throughout this work, a nominal subinterval length of six minutes has been adopted, which is a compromise between the computational effort and the capability to resolve short-term perturbations. Figure 7.11 showed, moreover, that almost identical orbits can be obtained with different pseudo-stochastic parametrizations based on six minute time intervals. This is one more reason to select the rather short time intervals, although more refined parametrizations such as piecewise linear accelerations could cope as well with much longer subinterval lengths.

Figure 7.13 shows the daily SLR RMS errors (DOY 195–201, 2002) for CHAMP orbit solutions based on pulses (left) and piecewise constant accelerations (right), when using different a priori standard deviations and subinterval lengths. The a priori standard deviations for the piecewise constant accelerations are $5 \cdot 10^{-8}$ m/s^2 for solution (a), $1 \cdot 10^{-8}$ m/s^2 for solution (b), and $5 \cdot 10^{-9}$ m/s^2 for solution (c). The a priori standard deviations for the pulses read as $1 \cdot 10^{-5}$ m/s for solution (A), $5 \cdot 10^{-6}$ m/s for solution (B), and $1 \cdot 10^{-6}$ m/s for solution (C). The first three bars (from left) on each day represent orbit solutions based on 6 min subintervals, the last three solutions are based on 15 min subintervals. A screening threshold of 0.3 m was used for computing the SLR residuals.

The best performance with respect to the SLR residuals is obtained for the 6-minute solutions (B) and (b), respectively, which were found to be optimal, as well, from the analysis of the formal position accuracies. This justifies our selection criteria. Over the seven days, the solutions (B) and (b) show an almost identical overall SLR RMS of 3.4 cm. In view of the almost identical orbits in Fig. 7.11, it has to be expected that the SLR validation is almost the same as well.

When comparing the first three bars with the last three bars on each day we get the (correct) impression

that it is sometimes difficult to decide which subinterval length is actually more appropriate. This reflects the difficulty when validating microwave-based orbits with sparse SLR observations. Strictly speaking, firm conclusions can be obtained only by analyzing much longer residual series – which indeed supported our decision.

7.8.2 SLR Validation

Satellite Laser Ranging (SLR) is the only space geodetic technique which can provide an independent validation of the CHAMP satellite orbits in an absolute sense. Unfortunately, SLR measurements to LEO satellites are usually sparse, mainly due to the short and rare tracking passes above the individual SLR stations. In order to best meet the most immediate data needs, the ILRS assigns priorities for tracking specific satellites. In April 2001, e.g., CHAMP was given the highest tracking priority among all target satellites [*Pearlman et al.*, 2002], which significantly contributed to the successful conduction of the CHAMP orbit comparison campaign one month later. Despite all these efforts, CHAMP SLR observations usually remain sparse.

For the SLR validation of our CHAMP reduced-dynamic orbits, we used all available SLR observations of CHAMP for the period between DOY 060 and 260, 2002, which resulted in a total of 21 SLR observatories involved. In order to obtain a reliable statistics, we rejected SLR residuals larger than 0.3 m which reduced the amount of available data by about 3%. Such an outlier elimination is necessary, because unrealisticly large and obviously erroneous normal points may still be present in the SLR data. However, it is clear that such a procedure may also reject residuals which are not bad, but large due to problems with the orbit determination. In order to derive a reliable estimate of the orbit quality under "normal" conditions, we completely eliminated days from the comparison which showed any indication of an exceptional behavior. This conservative approach removed as many as 20 days from the comparison due to a large variety of reasons, including large gaps in the GPS data, large amounts of GPS observations marked as unusable by the screening procedure, orbit maneuvers, missing attitude information, etc.

Figure 7.14 (left) shows the daily SLR RMS errors for the CHAMP reduced-dynamic orbits of the "optimal" solution (b). The daily values show a considerable scatter between 0.63 cm and 8.45 cm for DOY 76 and 178, respectively. Both days are extreme insofar as only the small number of 38 and 67 residuals contribute to the mentioned RMS errors. The number of accepted SLR residuals per day varies between 6 and 334. The majority of the errors is between 2 and 4 cm with a mean value of 3.2 cm, which is close to the 3.0 cm found for the much shorter time period of the CHAMP orbit comparison campaign in Sect. 7.7.3.

It is interesting that no significant difference exists between the SLR validation of reduced-dynamic CHAMP orbits before and after DOY 064, 2002, which can be seen by looking at the left part of Fig. 7.14 (left). Unlike to kinematic orbits, which are very sensitive to the number of available GPS observations, the changed tracking conditions do not significantly influence the quality of the reduced-dynamic orbit solutions, at least not on a level seen by the SLR validation if the solutions are properly tuned. This confirms the robustness of the reduced-dynamic solutions, although the need to adapt the settings of the pseudo-stochastic orbit parameters reflects that there is, of course, a certain sensitivity to the tracking conditions.

Figure 7.14 (right) shows the daily mean values of the SLR residuals used to obtain Fig. 7.14 (left). A few of the large errors can be correlated to large offsets, e.g., on DOY 178. Apart from these large values, one fortunately does not recognize (large) mean values over the 201 day period, but one gets the impression

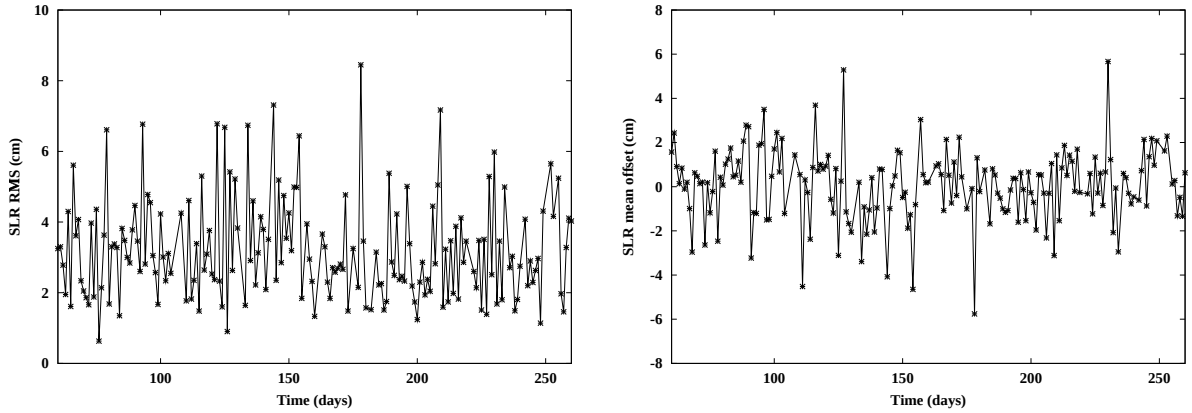

Figure 7.14: Daily SLR RMS errors (left) and offsets (right) for DOY 060–260, 2002 for CHAMP reduced-dynamic orbits based on piecewise constant accelerations set up every six minutes.

that some systematic patterns are occasionally visible in Fig. 7.14 (right). This might be a reason for the somewhat larger SLR offset found in the context of the CHAMP orbit comparison campaign where only a limited time span of eleven days were analyzed (see Sect. 7.7.3). No attempt has been made, however, to further investigate this issue.

7.8.3 Validation with Accelerometer Data

The STAR accelerometer aboard CHAMP directly measures the total non-gravitational acceleration acting on the spacecraft (see Sect. 7.6.2). Because the very precise measurements are band-limited to the high-frequency part between 10^{-4} to 10^{-1} Hz of the measured signal [*Grunwaldt and Meehan*, 2003], they need to be calibrated for the low-frequency part before being useful for further applications. In the following, this is achieved by applying the calibration parameters provided as part of the Level 2 CHAMP data distributed by the GFZ.

It is clear that a comparison of accelerometer data with estimated accelerations from GPS observations is not a strict validation, e.g., [*van den IJssel and Visser*, 2005], because pseudo-stochastic orbit parameters may compensate for any deficiencies in the dynamic models, but not only for the non-gravitational part of the models. Even if a CHAMP state-of-the-art gravity field model like EIGEN-2 is used without models for the non-gravitational accelerations for the reduced-dynamic orbit determination, one may not hope to strictly validate "GPS accelerometry" with accelerometer data. Nevertheless, accelerometer data are the only independent measurements for CHAMP, which have the potential to provide a rough but continuous verification of the estimated accelerations from GPS. Obviously, this also validates the orbits to a certain extent.

Figure 7.15 illustrates, for a specific time interval of about three orbital revolutions on DOY 198, 2002, how the along-track 6-minute piecewise constant accelerations (solution (b)) and the 6-minute piecewise linear accelerations agree with the measured accelerations from the STAR accelerometer. The accelerometer bias and scale were removed by applying the values provided by the GFZ, which are -3555 nm/s^2 and 0.833 for the along-track bias and scale, respectively. The generally good agreement in Fig. 7.15 underlines the quality of the EIGEN-2 gravity field model for the CHAMP orbit on this day, which was not part of the data period used for the generation of the EIGEN-2 model. Apart from the well repro-

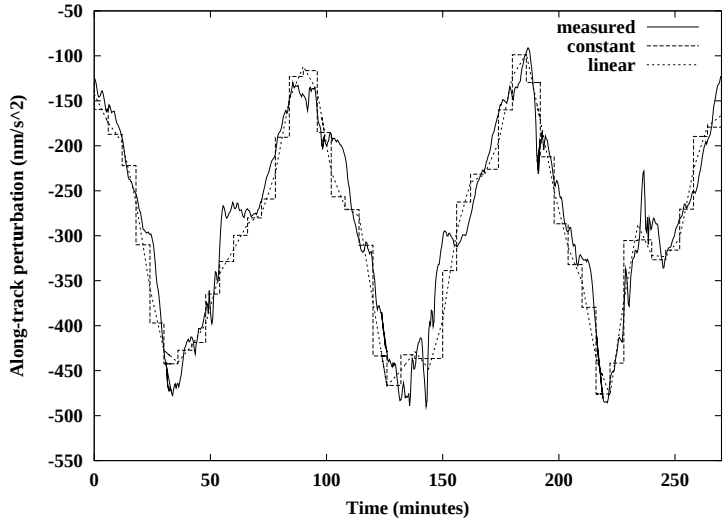

Figure 7.15: Along-track comparison on DOY 198, 2002 (1–5.5 h) between STAR accelerometer measurements (bias and scale removed) and estimated accelerations using the gravity field model EIGEN-2.

duced once-per-revolution signature caused by air drag, additional structures are occasionally tracked by the estimated accelerations as well, e.g., the striking peak at 230 min during a North pole passage. Some obvious disagreements may be recognized as well, e.g., around 60 min. Both features are probably real as they could be reproduced as well with accelerations derived from the air-density model MSIS-86 [*Hedin,* 1987].

Figure 7.15 shows that single acceleration estimates from GPS data are not very sensitive to many fluctuations tracked by accelerometer data. It is clear that GPS accelerometry has a time resolution of the subinterval lengths of the piecewise constant or piecewise linear accelerations. However, even if the subinterval length is reduced, the single acceleration estimates do not contain much information about the high-frequency content of the perturbing acceleration. Also in the case of the relatively long 6-minute intervals used for Fig. 7.15, a good part of the agreement is caused by the information introduced by the a priori standard deviations of the pseudo-stochastic parameters. This is also the reason for the deviations observed around 60 min in Fig. 7.15. As soon as the constraints get more relaxed, the acceleration estimates start following the feature around 60 min, but other accelerations start deviating from the accelerometer curve, as well. This behavior illustrates that the single acceleration estimates are highly dependent on the settings of the pseudo-stochastic parameters. A discussion of the contribution of a priori information to GPS accelerometry may be found in [*van den IJssel and Visser,* 2007].

We correlated the accelerations estimated from the GPS observations with the accelerometer data. The correlation coefficient r_{xy} of two (daily) time series x and y may be empirically derived by

$$r_{xy} = \frac{\sum_{i=1}^{n}(x_i - \bar{x})\,(y_i - \bar{y})}{\sqrt{\sum_{i=1}^{n}(x_i - \bar{x})^2 \sum_{i=1}^{n}(y_i - \bar{y})^2}}\,, \tag{7.12}$$

where

x_i, y_i are the values of the two time series referring to the same epoch number i,

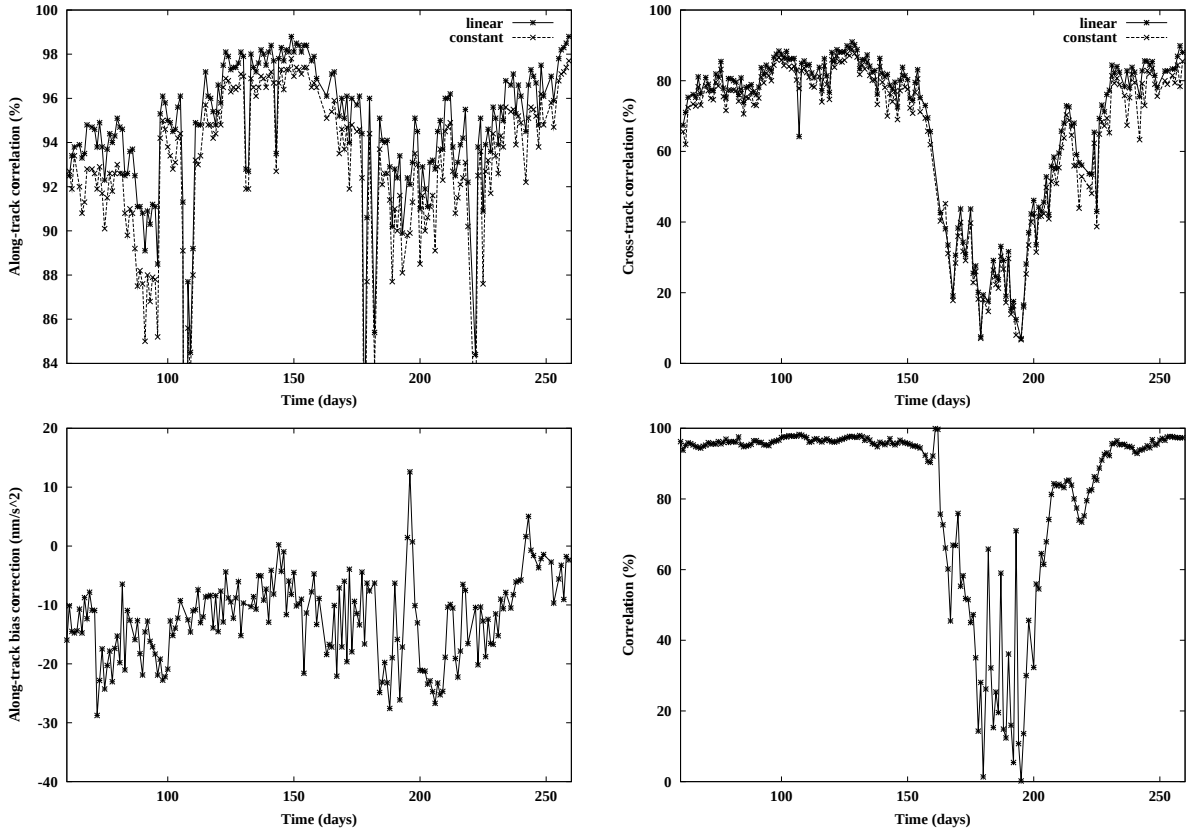

Figure 7.16: Daily correlation coefficients for DOY 060–260, 2002 between STAR accelerometer data and estimated along-track (top, left) and cross-track (top, right) accelerations using the gravity field model EIGEN-2. Daily along-track bias corrections (bottom, left) and correlation coefficients between cross-track accelerometer data with and without the Lorentz correction (bottom, right).

$\bar{x}, \bar{y}$ are the arithmetic mean values of the two time series, and

n is the number of common epochs.

Figure 7.16 (top row) shows the daily correlation coefficients between the estimated 6-minute piecewise constant or piecewise linear accelerations and the measured accelerations for the considered 201 day period. The daily values of (7.12) are based on all available 10 s normal points from the Level 2 accelerometer data files and are given for the same days as shown in Fig. 7.14. According to (7.12), they do not depend on the accelerometer scale and offset, which makes them appropriate to measure the (dis)agreement between STAR and GPS accelerometry. Note that the radial comparison is not given in Fig. 7.16 (top row) due to the well known failure in one of the accelerometer electrodes [*Perosanz et al.*, 2003]. The corrected radial accelerometer measurements still suffer from residual instrumental drifts [*Perosanz et al.*, 2004].

Figure 7.16 (top, left) indicates that the along-track accelerations are, almost without exception, well represented by pseudo-stochastic parameters with a time resolution of 6 min. The scale of Fig. 7.15 showed that the main along-track signal is very pronounced with an amplitude of up to 200 nm/s^2, which

facilitates a good recovery as it is reflected by Fig. 7.16 (top, left). Nevertheless, noticeable variations over time may be observed as well, e.g., a reduced quality and stability of the comparison results around DOYs 100 and 200. In particular for the second period of instability, we notice an even more pronounced impact on the cross-track comparison shown in Fig. 7.16 (top, right). The correlation coefficients suddenly drop from a normal level of about 82% to only 39%.

The SLR validation in Fig. 7.14 did not indicate an inferior orbit quality around DOY 200. Therefore, we attribute this effect to the accelerometer data rather than to the orbit. Another piece of evidence for this suspicion may be found in Fig. 7.16 (bottom, right), which shows the daily correlation coefficients between cross-track accelerometer data with and without the application of the Lorentz correction provided with the Level 2 accelerometer data [*Förste and Choi*, 2004]. Obviously, both series show a striking discrepancy from DOY 163 onwards, which results in completely different accelerations for the cross-track direction. It is interesting to note that the start of this pattern coincides with the termination of an orbit maneuver sequence carried out on DOYs 161 and 162 to raise the perigee by about 20 km [*Reigber*, 2002a].

Because the application of the Lorentz correction was found to significantly degrade the cross-track comparison during this time period, we decided not to apply this correction to the accelerometer data, which also holds for the results presented in Fig. 7.16. According to [*Förste and Choi*, 2004] it should be further studied whether it is necessary or not to apply the Lorentz correction.

Figure 7.16 (top, left) shows that the differences in the along-track correlation coefficients between both pseudo-stochastic acceleration models are very stable at almost the same level of about 1.6%. A similar level, although slightly less stable, can be observed as well in Fig. 7.16 (top, right) for the cross-track direction. More pronounced effects for both directions could be expected for longer subintervals lengths. For 15 min, e.g., the differences in the correlation coefficients increase to about 8%, which is somewhat larger than the effect found for a pure once-per-revolution signal, 4.2%, in simulation studies.

In principle, pseudo-stochastic acceleration parameters could be used as pseudo-observations to derive approximate estimates of the accelerometer bias and scale parameters of the observation equation (7.7) in a least-squares adjustment. Such an "off-line" derivation, however, cannot be competitive with other available calibration techniques, e.g., [*Perosanz et al.*, 2004] or [*Gerlach et al.*, 2003c], due to the limited precision of the underlying single acceleration estimates. Nevertheless, an easy monitoring of the accelerometer calibration can be facilitated in this way. For a fixed along-track scale parameter of 0.833, Fig. 7.16 (bottom, left) shows daily correction values to the mean along-track accelerometer bias of $-3555\,\mathrm{nm/s^2}$ provided by the GFZ. It can be well recognized that there are different regimes with different stabilities. The observed patterns are comparable with those given in [*Bruinsma et al.*, 2004], and are a result of the accelerometer and data handling electronics aboard CHAMP. Accelerometer bias parameters may change, e.g., if switches occur between the main and the redundant electronics.

Figure 7.16 (bottom, left) also reveals that the daily corrections have a small offset with respect to the mean along-track accelerometer bias provided by GFZ, which might be due to different dynamic models used at GFZ and AIUB. Strictly speaking, accelerometer calibration parameters are only valid if exactly the same background models are applied for POD as used for the derivation of the calibration parameters. Note that the magnitude is too small to be obvious in Fig. 7.15.

7.8.4 Accelerometer Data as Additional Observations – A Simulation Study

If accelerometer calibration parameters are known at least at the few percent level, dynamic orbit determination can be much improved by replacing the non-gravitational accelerations from dynamic force models with the measured accelerations from the STAR accelerometer [*Bruinsma et al.*, 2003], e.g., with a best-fitting or smoothed function obtained from the Level 2 data. Of course, the same procedure is also applicable to reduced-dynamic POD, but the usually large number of pseudo-stochastic parameters heavily reduces the impact of the accelerometer data, which questions such a procedure. The following simulation study estimates the level of improvement for reduced-dynamic POD based on piecewise constant accelerations by taking accelerometer data as additional observations into account. Thereby, we assume that the gravitational accelerations are perfectly known from a state-of-the-art gravity field model.

In order to facilitate a statistically correct incorporation of accelerometer data in reduced-dynamic LEO POD based on pseudo-stochastic accelerations, use is made of the GPS observation equations (4.3) or (4.5), and the accelerometer observation equation (7.7) for each accelerometer component that shall be taken into account. The inherent singularity of the accelerometer observation equations is removed by the pseudo-stochastic accelerations, which are common to the accelerometer and the GPS observation equations. For the piecewise constant acceleration model, f_d may be simply identified with $A_{i,d}$ for $t_{i-1} \leq t < t_i$ in (7.7). A drawback of this combination is, however, that the accelerometer observation equation (7.7) is no longer linear in the unknown parameters due to products of the type $\alpha_d \cdot A_{i,d}$. Therefore, an iterative procedure is required.

The impact of the GPS and accelerometer data on the resulting parameters depends on the weight ratio w between accelerometer and GPS measurements. For $w \to 0$, accelerometer measurements have no impact on the common pseudo-stochastic parameters, and thus no impact on orbit determination. As a consequence, the estimated accelerometer calibration parameters are the same as from an "off-line" derivation using GPS-based accelerations as pseudo-observations, provided that the accelerometer data are represented by the same model as used to represent f_d in (7.7), e.g., the piecewise constant model. For $w \to \infty$, the estimated pseudo-stochastic accelerations reproduce the pattern introduced by the accelerometer data. As a consequence, the estimated accelerometer calibration parameters are the same as those from a dynamic orbit determination from GPS data where the non-gravitational accelerations are replaced by the accelerometer data, provided that they are represented by the same model as used to represent f_d in (7.7). Weighting accelerometer measurements is thus, to some extent, equivalent to constraining pseudo-stochastic accelerations to the accelerometer measurements.

In order to study the impact of accelerometer data on reduced-dynamic orbit determination, real accelerometer data were used together with the physical and mathematical models of the real data processing to simulate undifferenced GPS phase and accelerometer observations for the CHAMP satellite for two different accelerometer scenarios. CHAMP orbits not affected by the accelerometer signals served as a priori orbits for POD with the simulated GPS phase and accelerometer observations.

Impact of Accelerometer Data

In a first scenario, the GPS final orbits and a CHAMP orbit based on true piecewise constant accelerations over 15 min, subsequently denoted as the true CHAMP orbit, were the basis to simulate the GPS data with a white noise random error of 1 mm RMS. Consistent piecewise constant accelerometer data affected by an arbitrary scale and offset were simulated with a white noise random error of 1 nm/s^2 RMS. Finally,

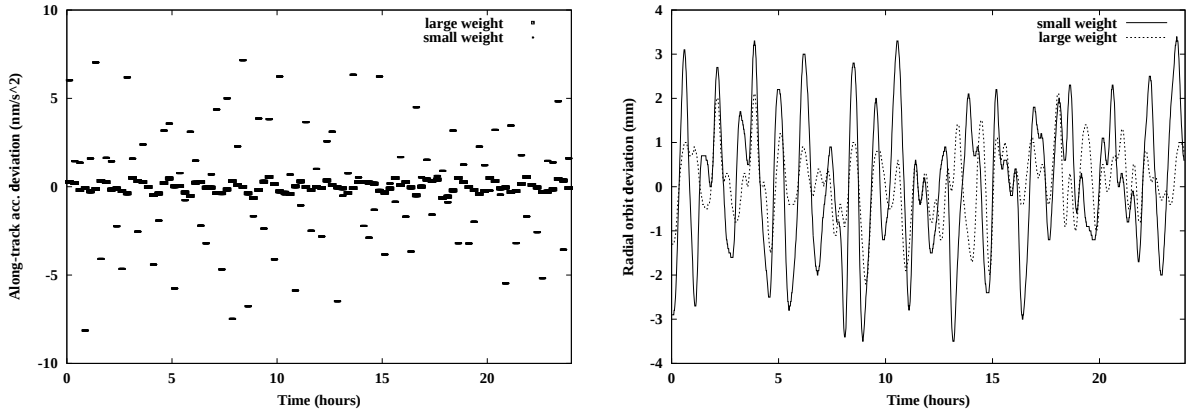

Figure 7.17: Along-track deviations w.r.t. the true accelerations (left) and radial deviations w.r.t. the true orbit (right) in a combined processing of GPS and accelerometer observations when using small or large accelerometer weights (simulated data, no modeling deficiencies).

orbit determination was performed with the simulated GPS phase and accelerometer observations using different weights. Note that only along-track accelerometer observations were taken into account to perform POD with 15 min piecewise constant accelerations. Therefore, along-track accelerometer scale and bias parameters had to be solved for simultaneously with the orbit parameters.

Figure 7.17 (left) shows the deviations of the estimated along-track accelerations with respect to the true piecewise constant along-track accelerations for the two extreme cases of weighting. As to be expected, the inclusion of very precise along-track accelerometer observations considerably improves the quality of the along-track acceleration estimates, provided that large accelerometer weights are used. No comparable effect can be observed for the radial and the cross-track acceleration estimates as no accelerometer observations are taken into account for these components in this simulation. Despite the considerable improvement with respect to the GPS-only along-track estimates (small weight), the orbit quality does not change dramatically. Fig. 7.17 (right) shows that the potential for an improvement is confined to a few millimeters for the radial component, provided again that large accelerometer weights are used. The same order of magnitude is also observed for the along-track and the cross-track orbit components.

Impact of Accelerometer Modeling

In the first scenario the true accelerations were piecewise constant in order to avoid any errors due to an inaccurate accelerometer modeling. In a second scenario, realistic true accelerations in all three directions, stemming from real accelerometer data, were used to simulate the GPS and accelerometer data in analogy to the first scenario. Only along-track accelerometer observations were taken into account to perform POD with 15 min piecewise constant accelerations.

Figure 7.18 shows the results of the along-track acceleration recovery and the radial orbit recovery, which should be compared to Fig. 7.17 from the first scenario. Obviously, a significant degradation results due to the insufficient modeling of the accelerations (compare the different scales). We noticed that even for the case of a slowly varying once-per-revolution acceleration, piecewise constant accelerations may be related to the pointwise acceleration values only at the few percent level (see Sect. 9.1.2). Due

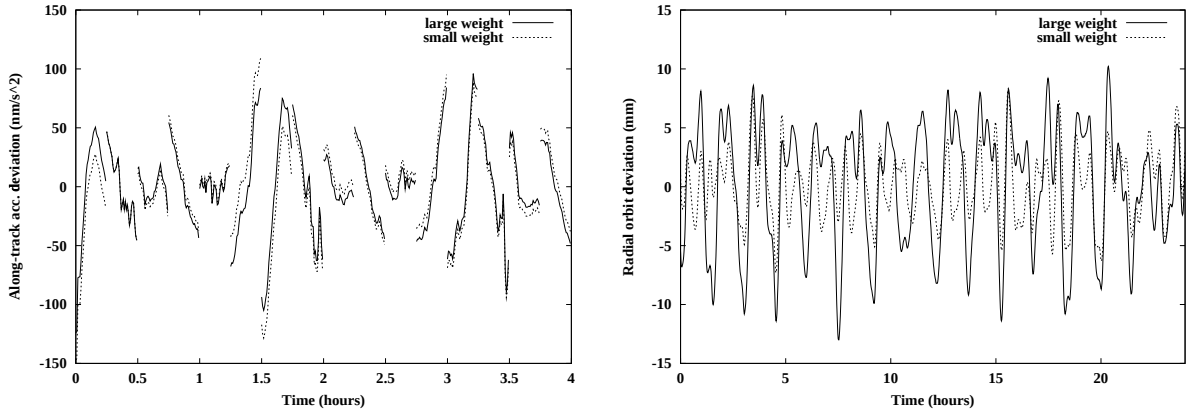

Figure 7.18: Along-track deviations w.r.t. the true accelerations (zoom) (left) and radial deviations w.r.t. the true orbit (right) in a combined processing of GPS and accelerometer observations when using small or large accelerometer weights (simulated data, with modeling deficiencies).

to more pronounced time variations in the used accelerometer data, even larger errors are introduced by the piecewise constant acceleration model, which primarily map into the accelerometer calibration parameters, but also into the orbit parameters to a certain extent. Nevertheless, the piecewise constant accelerations are better determined for the large accelerometer weights than for the small ones, which might be difficult to recognize, however, in Fig. 7.18 (left) due to the much larger model errors. On the other hand, Fig. 7.18 (right) clearly shows the alarming result that the orbit parameters are more degraded for large accelerometer weights than for small ones. A similar deterioration may also be observed for the along-track and cross-track components, because the piecewise constant accelerations are constrained to incompatible values. Obviously, accelerometer modeling errors may easily destroy the (small) benefits which could be expected from a combined processing of GPS and accelerometer observations in the absence of modeling errors.

In order to avoid this kind of errors, a better parametrization of the accelerations is required. The along-track acceleration deviations from Fig. 7.18 (left) seem to indicate that the piecewise linear model could already be sufficient to remove the largest part of the observed discrepancies. This is further supported by the fact that piecewise linear accelerations may be directly related at the level of 0.1% to the pointwise acceleration values of a slowly varying once-per-revolution acceleration (see Sect. 9.1.2). We did not perform such a study because the potential benefits seemed to be too small, even when using large accelerometer weights, which have to be put in relation with the very stringent requirements for the accelerometer modeling. One should not forget either that the pseudo-stochastic accelerations do not only compensate for non-gravitational errors, which makes it even more difficult to meet the modeling requirements.

7.8.5 Validation with Kinematic Orbits

Kinematic orbit determination is not the primary scope of this work, but a comparison of reduced-dynamic with kinematic solutions shows the consistency between positions relying on a pseudo-stochastic orbit modeling and positions derived by purely geometric means. For the scientific use of kinematic orbit positions, we refer to the work performed at IAPG, e.g., [*Švehla and Rothacher*, 2003c] and [*Gerlach et al.*, 2003c].

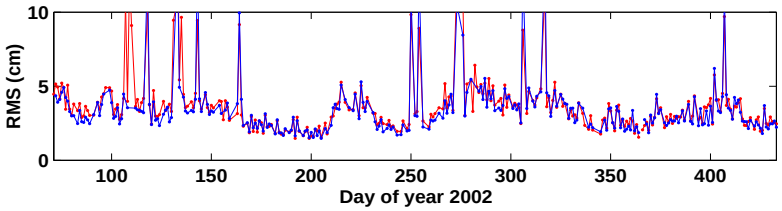

Figure 7.19: Daily RMS errors (1-D) of differences between kinematic CHAMP positions derived at AIUB (black) and reduced-dynamic CHAMP orbits. The comparable differences emerging from kinematic CHAMP orbits derived at IAPG (grey) are displayed as well.

Figure 7.19 shows daily 1-D RMS errors of orbit differences between CHAMP kinematic and reduced-dynamic orbit positions from the "optimal" solution (b). As a reference, we include the very similar differences emerging from kinematic CHAMP orbits derived at IAPG [*Švehla and Rothacher*, 2003c]. We do not compare the two kinematic solutions, and do not give an interpretation from where the differences between reduced-dynamic and kinematic orbits originate, but refer to [*Švehla and Rothacher*, 2003b] for more information. We like to emphasize, however, that the outcome of such a comparison strongly depends on GPS data screening (as kinematic orbits are very sensitive to bad measurements and data outages) and even more on the subinterval length and a priori standard deviations of the pseudo-stochastic parameters. A "more" kinematic orbit like the reduced-dynamic solution (a) would show significantly smaller differences than the solution (b) displayed here. Therefore, we rather show Fig. 7.19 to be aware of time periods with problematic data than to derive an estimate on orbital consistency. Because the same GPS data are used for both types of orbits, we assume that the reduced-dynamic solutions are as well partly affected by a degraded orbit quality if the comparison reveals serious problems.

Apart from a few days with bad quality, which are mainly caused by poor observation scenarios or by large amounts of rejected observations by the data screening, Fig. 7.19 shows significant variations in the consistency between both orbits over time. It can be recognized that the kinematic orbits fit well to the reduced-dynamic orbits, e.g., around DOYs 200 and 350, which, however, is not representative for the entire interval. A detailed comparison with the SLR validation results (Fig. 7.14 (left)) seems to indicate a similar variation which, however, is much more difficult to recognize due to the much larger day-to-day variations in the SLR RMS errors. This underlines the need for auxiliary validation procedures, even if they are not based on independent data like the comparison presented here with less precise kinematic orbits. Precision estimates for kinematic orbits (GRACE) may be found, e.g., in Sects. 7.9.2 and 7.9.3.

7.9 GRACE Orbit Determination

This section presents orbit determination results for the 2003 data set of the first GRACE data release covering DOY 031–365. If not explicitly stated, the gravity field model EIGEN-CG03C has been used for GRACE orbit determination up to degree and order 120, because it was (one of) the state-of-the-art CHAMP/GRACE gravity field model(s) at that time. Of course, the CSR gravity field models, e.g., GGM02C, would have been also well suited to perform state-of-the-art GRACE orbit determination [*Kang et al.*, 2006]. High-quality results of GRACE orbit determination may also be found in [*Švehla and Rothacher*, 2004b] and [*Kroes*, 2006].

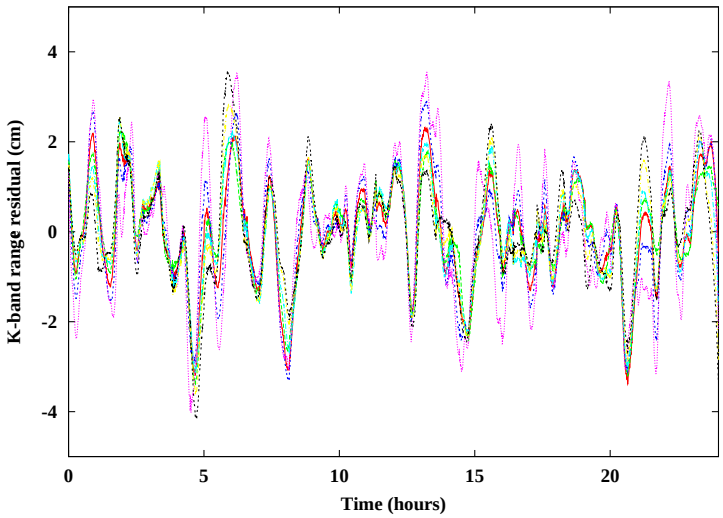

Figure 7.20: K-band range residuals on DOY 200, 2003 for reduced-dynamic orbits based on 6-minute piecewise constant accelerations with different a priori standard deviations.

7.9.1 Tuning GRACE POD

GRACE orbit solutions may be tuned in the same way as described for CHAMP in Sect. 7.8.1, where the formal accuracies of the estimated positions are considered the primary indicator for the orbit quality. For GRACE, however, an additional indicator is available thanks to the ultra-precise K-band range and range-rate observations, see Sect. 7.6.2. Because these observations are provided at 5 s intervals, the solutions can be (so to speak) continuously validated by the K-band residuals obtained from the relative positions and velocities, which may be constructed from the individual orbit solutions.

Figure 7.20 shows the K-band range residuals for several identically parametrized reduced-dynamic GRACE trajectories based on 6-minute piecewise constant accelerations. The various curves correspond to different a priori standard deviations which were equally applied to the radial, along-track, and cross-track piecewise constant accelerations defining the two GRACE satellite orbits. All solutions show a common pattern which does not change much if the settings of the pseudo-stochastic model are changed. The K-band range RMS errors vary between 10.5 mm for an a priori standard deviation of $5 \cdot 10^{-9}$ m/s^2 and 15.2 mm for $5 \cdot 10^{-8}$ m/s^2.

Interestingly, it is again solution (c) with constraints of $5 \cdot 10^{-9}$ m/s^2 that yields the best results. This solution was already found to be optimal for the 2001 CHAMP data set of the orbit comparison campaign (see Sect. 7.7.1), but it was only sub-optimal for the more recent CHAMP data processed in Sect. 7.8.1. Although the GRACE receivers were able to track up to ten GPS satellites as well, see Sect. 2.6.2, a "less" kinematic modeling is favored. The formal accuracies of the estimated orbit positions confirm this finding.

The periodic variations of the K-band range residuals in Fig. 7.20 are typical for zero difference reduced-dynamic GRACE orbit solutions. Spectral analysis reveals a pronounced line at the orbital period. These once-per-revolution signatures may be seen even more clearly in Fig. 7.21 (left), where three weeks of K-band range residuals of the solution (c) are shown as a function of the argument of latitude u (see Fig. 5.1). A periodic dependency on the position in the orbital plane is obvious.

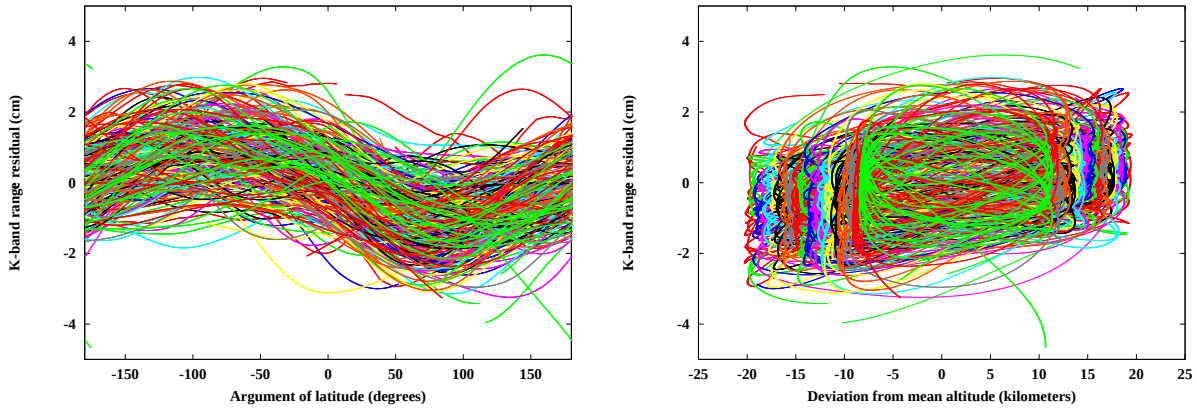

Figure 7.21: K-band range residuals of the solution (c) as a function of the argument of latitude (left) and of the deviation from the mean geocentric distance (GPS weeks 1234–1236).

What is the reason for the observed variations in the K-band residuals? On one hand, a once-per-revolution signature is often an indication that the relative positioning solutions heavily depend on spacecraft dynamics. On the other hand, similar patterns may be observed for kinematic relative position solutions as well, even for simulated solutions with white noise GPS data. The periodic signal may be explained by the float ambiguity parameters whose occurrence is related to orbital motion, see [*Švehla and Rothacher*, 2005a]. In an attempt to further constrain the main error source observed in Fig. 7.21 (left), we show the same residuals as a function of the deviation from the mean geocentric distance in Fig. 7.21 (right). A clear pattern is expected due to the one-to-one relationship between the argument of latitude and the geocentric distance, but it is interesting to see that the most negative residuals tend to occur at the lowest geocentric distances and vice-versa. This could be an indication that atmospheric drag is one of the most important sources of errors, as it is expected, and that the signal is not absorbed entirely by the pseudo-stochastic parameters. The slight asymmetry in Fig. 7.21 (right) seems to support this hypothesis, because residuals of larger size tend to occur at the lowest geocentric distances, where stronger perturbations are expected.

7.9.2 Validation with K-Band Data

K-band data provide a precise and independent validation of the relative GRACE orbit positions and velocities, because the K-band noise is negligible compared to the orbit errors, see Sect. 7.6.2. Because the along-track component of a satellite orbit is difficult to validate by other measurements, e.g., by SLR, this is a unique advantage for validating GRACE orbit solutions. Any errors in common to both GRACE satellite orbits cannot be revealed by the K-band measurements, however.

We used all K-band range observations, available at 5 s intervals, in the period between DOY 031 and 365 to compute daily K-band range RMS errors from the residuals obtained using the individual GRACE A and B reduced-dynamic orbit solutions (c). In order to obtain representative statistics, we had to rejected seven days for which no high-quality orbit solutions could be obtained due to a poor GPS tracking performance, e.g., on DOYs 68/69 and 302/303 which already showed a strange behavior in Fig. 7.7. Apart from these outlying days, Fig. 7.22 provides a representative estimation of the line-of-sight K-band validation for GRACE zero difference orbit solutions. The overall K-band range RMS error is 12.5 mm, if we take into account that the number of K-band observations per day may fluctuate as well

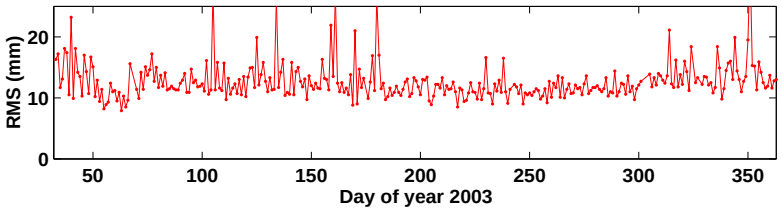

Figure 7.22: Daily K-band range RMS errors for GRACE zero difference solutions based on 30 s sampling and 24 h arc length.

due to data gaps in the Level 1B data files.

The overall K-band range RMS error of 12.5 mm does not represent a general line-of-sight precision. Figure 7.22 shows that the day-to-day scatter is generally small, but there clearly are periods governed by different precisions. The period between DOY 200 and 300, e.g., shows a very good performance, in particular the period between DOY 243 and 298 which yields an excellent overall K-band range RMS error of only 11.4 mm without any outliers. Figure 7.7 confirms that the GPS tracking performance was excellent for these 56 days, as well.

The large spikes occasionally occurring in Fig. 7.22 are usually due to extended gaps in the GPS data, either caused by gaps in the original GPS data or caused by large amounts of GPS observations marked as unusable by the screening procedure. For such a scenario, e.g., on DOY 351 for GRACE B (see Fig. 7.7), the orbit quality degrades considerably because no pseudo-stochastic parameters can be estimated within data gaps. Because no models were used for the non-gravitational accelerations, centimeter accuracy can then no longer be achieved. As a consequence, K-band residuals in the decimeter range may result during data gaps, e.g., on DOY 351 where a RMS error of 32.2 mm has to be noticed (see the last and largest spike in Fig. 7.22). One should also be aware that even more of such problematic situations without GPS data are present than those reflected in Fig. 7.22, because gaps in the K-band data often coincide with gaps in the GPS data, e.g., on DOY 222 where about 5.5 hours of missing GRACE A GPS data remain unnoticed in the K-band validation. This might be due to the fact that K-band and GPS observations are collected by the same Instrument Processing Unit, see Sect. 2.6.2.

DOY 243–298

Due to the good performance in the K-band validation, the GRACE GPS data for DOY 243–298 (GPS weeks 1234–1241) have been selected for performing additional test solutions. Results based on zero differences are presented in the following paragraphs, double difference results follow in Chapter 8.

In the course of the preparation for the upcoming GOCE mission, see Sect. 2.9, zero difference GRACE POD has been performed with settings similar to the planned operational precise science orbit determination for GOCE [*Bock et al.*, 2007]. This includes changes with respect to the arc length and the GPS sampling rate. Instead of 24 h arcs, "daily" batches of 30 h lengths shall be processed for GOCE to deliver 24 h orbital arcs without a degraded orbit quality at the day boundaries (see, e.g., Fig. 7.10 for the degradation of 24 h CHAMP arcs at the day boundaries). As a consequence, all input data required for POD, see Sects. 7.5 and 7.6, have to be concatenated to 30 h. In particular, the (re)-integration explained in Sect. 7.1 has to be applied to the GPS ephemerides. The GPS sampling rate will be 1 Hz for the GOCE mission. As the GRACE mission is restricted to 10 s GPS data, only 10 s GPS high-rate clock corrections

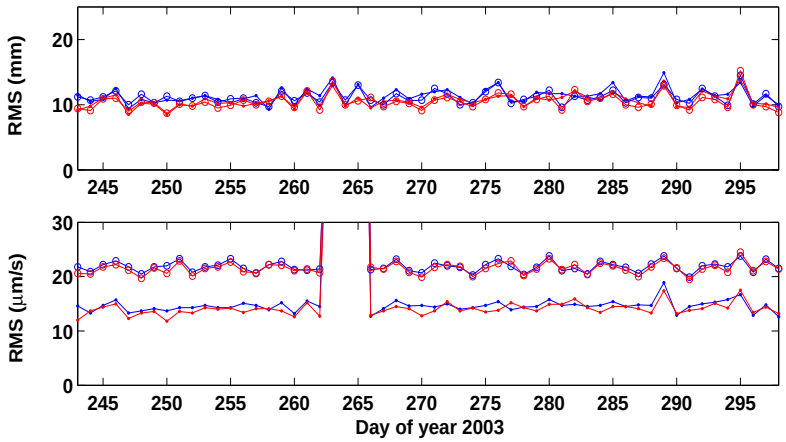

Figure 7.23: Daily K-band range (top) and range-rate (bottom) RMS errors for GRACE zero difference solutions based on 30 h arcs. The solutions are based on 10 s (grey) or 30 s (black) GPS data sampling using the gravity field model EIGEN-2 (circles) or EIGEN-CG03C (no circles).

had to be generated for these experiments (see Sect. 7.2).

Figure 7.23 shows the daily K-band range (top) and range-rate (bottom) RMS errors for four different test solutions, all based on data spans of 30 h. The validation covers, however, only the central 24 h, and is based on all available K-band observations at 5 s intervals. The grey curves denote solutions based on 10 s GPS data sampling, whereas the black curves refer to solutions based on 30 s GPS data sampling. As mentioned at the beginning of Sect. 7.9, the gravity field model EIGEN-CG03C is the nominal model used for GRACE POD in this work. Solutions marked with circles, however, denote that the CHAMP-only gravity field model EIGEN-2 was used for POD. Table 7.7 summarizes the solutions, and gives the overall K-band range and range-rate RMS errors for the analyzed eight weeks of data.

The K-band range RMS errors are all similar as opposed to the K-band range-rate residuals which show a clear distinction between the solutions based on the gravity field model EIGEN-CG03C and EIGEN-2. This is simply due to the fact that K-band range-rate data contributed to the generation of the more recent EIGEN-CG03C gravity field model, but not to the generation of the CHAMP-only model EIGEN-2. Despite of the superior quality of the EIGEN-CG03C model due to the incorporation of additional GRACE data, no improvement can be observed in the fit to the K-band range observations (Table 7.7 even indicates a small degradation). This illustrates that improvements coming from state-of-the-art GRACE gravity field models are no longer very important for the determination of high-quality (reduced-dynamic)

Table 7.7: Overall K-band range and range-rate RMS errors using different GPS sampling rates and gravity field models for DOY 243–298, 2003.

10 s	30 s	Gravity Field Model
10.7 mm 14.0 μm/s	11.4 mm 14.6 μm/s	EIGEN-CG03C
10.5 mm 21.5 μm/s	11.2 mm 21.9 μm/s	EIGEN-2

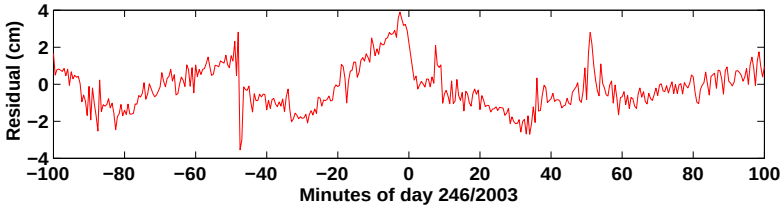

Figure 7.24: K-band range residuals of a 30 h kinematic solution at midnight. The set up of new ambiguities to all GPS satellites at midnight causes a jump in the residuals.

relative orbit positions, because they are not very sensitive to the improved high-frequency content of the recent gravity field models. A similar remark is valid for DOYs 263, 264, and 265 where unrealisticly large K-band range-rate residuals are caused by spurious antenna correction values provided in the Level 1B KBR data files, but almost no effect is observed in the K-band range residuals thanks to the smoothing effect of integration.

Table 7.7 lists a K-band range RMS of 11.4 mm for the solution based on 30 s GPS data sampling. This is identical with the value found for the 24 h arc length in the last paragraph, and indicates that no degradation can be detected towards the arc boundaries in the 24 h solution by the K-band range validation. This certainly indicates a good quality of the 24 h solutions, but it is not a very strong indication, because a common deviation at the arc boundaries cannot be revealed by the K-band observations. A small indication for the presence of a boundary effect may be found in the K-band range-rate residuals only: Table 7.7 lists a K-band range-rate RMS error of 14.6 μm/s, which is marginally smaller than the RMS error of 14.8 μm/s obtained from the 24 h solution.

The comparison between the solutions based on 10 s and 30 s GPS sampling in Table 7.7 shows that the 10 s solutions are slightly superior. This has to be expected, because the additional GPS observations constrain the reduced-dynamic trajectories closer to the true trajectories in-between the 30 s intervals. Because both reduced-dynamic solutions are validated by the K-band observations at 5 s intervals, the improvement mainly comes from the 10 s epochs between the 30 s epochs. It should be mentioned, however, that the higher sampling rate required a new tuning of the a priori standard deviations of the piecewise constant accelerations. If the same settings would have been used as for the 30 s solution, K-band RMS errors of 11.3 mm (range) and 14.7 μm/s (range-rate) would have resulted.

Because the GPS products from CODE are generated in a fixed 24 h processing scheme, this leads, strictly speaking, to small inconsistencies between the GPS orbits and clocks at the day boundaries for the 30 h LEO processing scheme, see [*Bock et al.*, 2007]. However, this does not matter for the GRACE results, because the Level 1B GPS carrier phase data are affected by cycle slips at the midnight epochs, which is, e.g., not the case for the Level 1 GPS carrier phase data from CHAMP. As a consequence, the 30 h solutions do not fully exploit the potential of the longer arcs at the day boundary. This could be another reason for the almost identical K-band validation results obtained for the 24 h and 30 h processing. Figure 7.24 illustrates that a 30 h kinematic solution is affected by a jump of several centimeters in the K-band validation, because new ambiguities have to be set up for all GPS satellites tracked by GRACE A and B. It is clear that this also weakens reduced-dynamic orbit solutions. We do not know the reason for these (unnecessary) cycle-slips in the GRACE data.

Finally, it should be mentioned that kinematic orbits (based on 24 h arcs and 30 s GPS sampling) may be

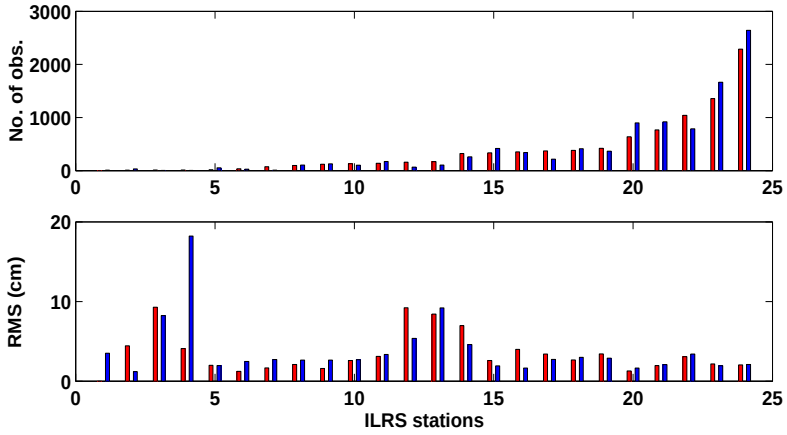

Figure 7.25: Station-specific comparison of the number (top) and the RMS error (bottom) of SLR residuals for GRACE A (left bars) and GRACE B (right bars).

validated at an overall K-band range RMS error of 20.5 mm for the considered time period. Due to the high sensitivity of kinematic orbits to the GPS observations, this good result is only possible thanks to the excellent data quality of this period. Kinematic POD for the other periods of the year 2003 might be more difficult.

7.9.3 Validation with SLR Data

For the SLR validation of our GRACE reduced-dynamic orbits, we performed a pre-analysis of the SLR observations for the period between DOY 243 and 365, 2003 to assess the data quality from the individual tracking stations of the ILRS network [*Pearlman et al.*, 2002]. In analogy to the SLR validation of the CHAMP orbits (see Sect. 7.8.2), we rejected residuals larger than 0.3 m, and computed station-specific RMS errors from all remaining residuals. Figure 7.25 (bottom) shows the overall SLR RMS errors for the total of 24 SLR observatories for GRACE A (left bars) and GRACE B (right bars). The top part of Fig. 7.25 shows that the stations are ordered according to the increasing number of available SLR observations from GRACE A (left bars). The number of observations from GRACE B is provided by the right bars, as well.

Figure 7.25 (top) tells that there is no preference of the SLR tracking network to track preferably GRACE A or B. It was reported by [*Dunn et al.*, 2003] that GRACE A, being the leading satellite at that time, was favored in the early days of the mission. This seems to be no longer the case as GRACE B was even observed more often during the time period analyzed here. Concerning the SLR fits to the orbits, it can be seen in Fig. 7.25 (bottom) that the majority of the stations score an overall SLR RMS error between 1.5 and 3.5 cm for both GRACE satellites. For five stations, larger results are registered. One may suspect that this is rather related to station problems than to problems in the orbit determination. This assumption holds with utmost certainty for stations no. 3 and 4, which both contributed with very few and rather bad measurements only, but possibly also for stations no. 12, 13, and 14. Therefore, the stations no. 3 (1824: Golosiiv, Ukraine), 4 (7249: Beijing, China), 12 (7355: Urumqi, China), 13 (7830: Chania, Greece), and 14 (7806: Metsahovi, Finland) have been excluded from the further SLR analysis. The exclusion of Metsahovi was a borderline case.

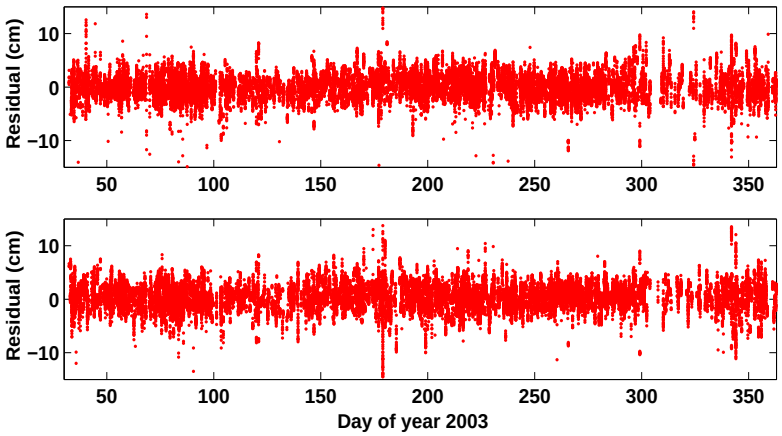

Figure 7.26: SLR residuals for GRACE A (top) and GRACE B (bottom) zero difference solutions based on 30 s sampling and 24 h arc length.

For the remaining 19 stations, Fig. 7.26 shows the SLR residuals for DOY 031–365 to both GRACE 24 h reduced-dynamic orbits of the "optimal" solution (c) based on 30 s GPS data. The overall SLR RMS is 2.44 cm for GRACE A (top) and 2.47 cm for GRACE B (bottom), which is in good agreement with [*Kang et al.*, 2006] who analyzed GRACE A and B data separately for DOY 182–304 in the double difference mode. It is important to note that no offset can be detected for GRACE A in the residuals, and only a very small mean offset of 3.8 mm for GRACE B.

Figure 7.26 exhibits the same time periods with better and worse orbit qualities than those found in Fig. 7.22. Again, DOY 200–300 show generally small residuals, in particular for the outstanding period between DOY 243 and 298 where SLR RMS errors of 2.25 cm and 1.95 cm are observed for GRACE A and B, respectively. We have thus demonstrated that it is possible to meet a 1-D accuracy requirement of 2 cm under good GPS tracking conditions for GRACE B by pseudo-stochastic orbit modeling. The worse results obtained for GRACE A and for the other time periods underline, however, that it will be a challenge to actually meet this requirement in the near future for the GOCE satellite flying much lower (see Sect. 2.9). The larger residuals occasionally occurring in Fig. 7.26 are critical for high-precision orbit determination, but may easily occur if extended gaps in the GPS data are present.

Let us also mention that the temporal coverage with SLR data is not really optimal. There exist several days after DOY 300 where the GRACE satellites were not observed at all.

DOY 243–298

The additional 30 h test solutions discussed in the context of the K-band validation, see Table 7.7, have also been validated by SLR. Table 7.8 summarizes the overall SLR RMS errors for the analyzed eight weeks of data for the solutions.

Slightly better overall SLR RMS errors are observed for the solutions based on the more recent gravity field model EIGEN-CG03C. The distinction between the EIGEN-CG03C and the EIGEN-2 gravity field model is more pronounced than indicated by Table 7.7 for the K-band range validation. This is probably due to the fact that SLR actually validates the orbits in an "absolute sense", and not only relatively as K-band does. Nevertheless, the superior quality of the EIGEN-CG03C model does not lead to a dramatic

Table 7.8: Overall SLR RMS errors for DOY 243–298, 2003.

GRACE	10 s	30 s	Gravity Field Model
A	2.28 cm	2.24 cm	EIGEN-CG03C
B	1.96 cm	1.95 cm	
A	2.48 cm	2.46 cm	EIGEN-2
B	2.25 cm	2.24 cm	

improvement of the reduced-dynamic orbits. This is because of the considerable number of estimated piecewise constant accelerations, which illustrates the success of pseudo-stochastic orbit modeling, but also the challenge to validate state-of-the-art gravity field models by orbital fits of very low Earth satellites.

Table 7.8 lists SLR RMS errors of 2.24 and 1.95 cm for the GRACE A and B solutions based on 30 s GPS data sampling. This is almost identical with the values of 2.25 and 1.95 cm found for the 24 h arcs, and indicates that almost no degradation can be detected towards the arc boundaries in the 24 h solution by the SLR validation. Only a study of the orbit overlaps at the arc boundaries is able to reveal the orbit deficiencies (see Sect. 7.9.4).

The comparison between the solutions based on 10 s and 30 s GPS sampling in Table 7.8 shows that the 10 s solutions are slightly inferior. Although the effect is small, this result was not expected. Most probably, it is related to small deficiencies in the 10 s GPS clock corrections. This would also explain that no comparable effect could be found in the K-band validation, see Table 7.7, because small deficiencies in the GPS satellite clocks are common to the orbit determination of GRACE A and B, and thus cancel out in the K-band validation. This result underlines the need for several independent validation techniques which are sensitive to different kinds of errors. The analysis of SLR observations is most valuable for this purpose due to their unbiased nature. This statement does not hold only for LEO satellites but also for GNSS satellites, e.g., [*Urschl et al.*, 2005].

Finally, it should be mentioned that kinematic orbits (based on 24 h arcs and 30 s GPS sampling) have been validated showing an overall SLR RMS error of 3.08 cm and 2.88 cm for GRACE A and B, respectively. Note that the SLR validation of kinematic orbits requires a reduced-dynamic orbit solution to interpolate the discrete kinematic ephemerides to the epochs of the SLR observations.

7.9.4 Overlap Analysis

The analysis of orbit overlaps provides an internal validation of the orbit quality, and may serve several purposes. In the case of the 30 h reduced-dynamic orbit solutions centered at noon, a full 6-hour orbital overlap may be computed at each day boundary for the radial, along-track, and cross-track direction. The analysis of these individual pieces of orbital differences may help to estimate the order of magnitude for orbit deviations at the day boundaries. If only the central part of the 6-hour overlaps is analyzed, e.g., the central 4-hours, an estimate of the orbit consistency is obtained which is free from the "edge effects" which dominate the first and the last hour of each overlapping period. In the case of the 24 h reduced-dynamic orbit solutions centered at noon, the deviations of the orbit positions from two adjacent arcs may be computed at each day boundary for the radial, along-track, and cross-track direction. These midnight overlaps (one value per day and direction) provide a pessimistic estimate of the orbit errors. It is important to mention that this is the only overlap test which compares orbits that are obtained from

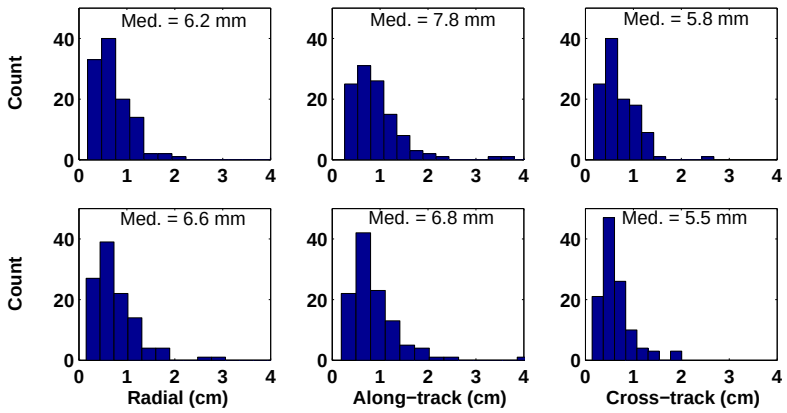

Figure 7.27: Histograms of the RMS errors per day of the full 6-hour orbital overlaps of the 30 h arcs for GRACE A (top) and GRACE B (bottom).

completely different sets of GPS data.

Figure 7.27 shows histograms of the RMS errors per day of the full 6-hour orbit overlaps of the 30 h solution based on 30 s GPS data for GRACE A (top) and GRACE B (bottom). The time period analyzed covers DOY 243–365, 2003. The median values of the daily RMS errors are mostly dominated by the degradation at the arc boundaries, which may grow to several centimeters. As mentioned earlier, see Fig. 6.5, the orbit is not very well constrained by the tracking data at the endpoints of the orbital arcs. Therefore, the length of the daily data arc is often extended to avoid degraded orbit positions when using only the middle 24-hours. The median values in Fig. 7.27 are similar for GRACE A and B, and tend to be largest for the along-track direction. As mentioned in the context of the formal position accuracies, the reduced-dynamic orbit solutions are affected with the largest uncertainty in the along-track direction. Finally, it should be mentioned that no significant systematic offsets could be found in the 6-hour overlap analysis.

If the same time period is used to analyze only the central 4-hours of the daily overlaps, the median values decrease to 1.7 mm, 3.3 mm, and 3.8 mm for GRACE A, and 1.4 mm, 2.9 mm, and 3.4 mm for GRACE B in the radial, along-track, and cross-track direction. These values mainly reflect the consistency between two subsequent GRACE orbit solutions around midnight. It is interesting to note that the median values are systematically smaller for GRACE B, which could be due to the lower noise in the GRACE B GPS carrier phase observations [*Kroes*, 2006]. Moreover, it can be recognized that the median values of the RMS errors in the radial and along-track direction are small, but that the median values of the cross-track RMS errors are higher, which could indicate small inconsistencies. The cross-track overlap is particularly sensitive for inconsistencies, which may show up as a small systematic offset with different size for the individual days.

Figure 7.28 shows histograms of the deviations per day between the orbit connecting points of subsequent 24 h orbit solutions based on 30 s GPS data for GRACE A (top) and GRACE B (bottom). Observe that Fig. 7.28 is based only on data between DOY 243 and 298 (therefore the incomplete impression). For normally distributed GPS data with zero mean, this observable should be normally distributed with zero mean as well, which can be (more or less) confirmed for most directions, although clearly a longer time series needs to be analyzed in order to draw firm conclusions. We do not compare the standard deviations

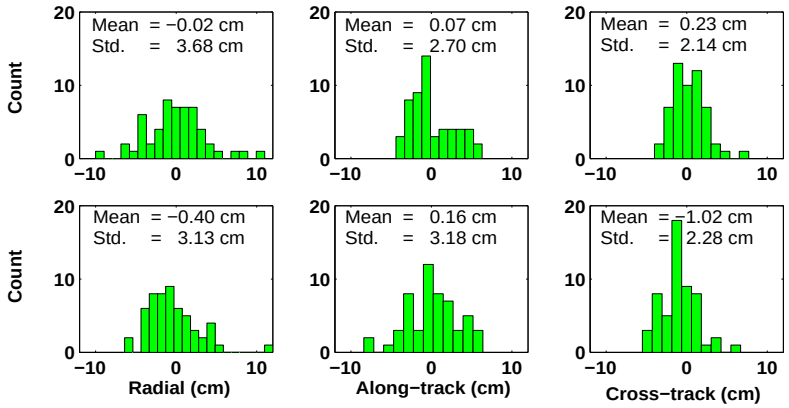

Figure 7.28: Histograms of the orbital overlaps at the day boundary epochs of the 24 h arcs for GRACE A (top) and GRACE B (bottom).

with each other, but emphasize the rather large values of orbit differences that may be reached at the arc boundaries. It is difficult to decide whether the differences between the GRACE B arc connecting points really show a systematic deviation from zero in the cross-track direction or not.

7.9.5 Analysis of Ionosphere-Free Phase Residuals

Postfit ionosphere-free carrier phase residuals do not directly disclose information on the orbit quality. They are generally small and, at first sight, similar for different orbit solutions. Therefore, they are not used as an indicator for the orbit quality in this work. However, they are useful to reveal the presence of systematic errors, which may be either caused by systematic errors in the original GPS observations or by a deficient modeling of the observations.

Typical sources for systematic errors in GPS observations are multipath, i.e., the superposition of the direct signal with interfering signals following a different path, and electronic signal interference. Both types of systematic errors mainly affect pseudo-range observations, but they may be present as well in carrier phase observations, where multipath is fortunately confined to a quarter of the wavelength. In an effort to minimize multipath reflections caused by the satellite's surfaces, choke-ring antennas are often used for the collection of spaceborne GPS data. For the visualization of systematic errors in the different code observables from CHAMP and GRACE, we refer to [*Kroes*, 2006]. Unfortunately, carrier phase systematic errors are more difficult to visualize as they cannot be easily separated from other systematic errors.

Sources for a deficient modeling of the GPS carrier phase observations may be either attributed to the transmitting side of GPS satellites, or to the receiving side of the LEO satellite. Typical sources from the transmitter side are erroneous GPS satellite clock corrections or orbit positions. Neglected phase center variations or polarization induced phase wind-up may be mentioned as typical sources from both the transmitting and the receiving side.

Figures 7.29 and 7.30 show mean postfit carrier phase ionosphere-free residuals from the final orbit determination for GRACE A (top) and B (bottom) as a function of the elevation and the azimuth in the satellite-fixed coordinate system (see Sect. 7.3.2). For a good visualization a data span of nine weeks and a dense azimuth and elevation grid of 1.5° and 1° was chosen. In order to exclude that there is any

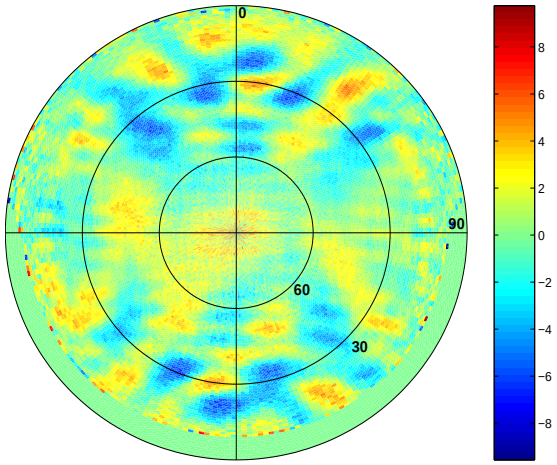

Figure 7.29: Mean postfit carrier phase ionosphere-free residuals (millimeters) per 1.5° azimuth and 1° elevation bins for GRACE A (GPS weeks 1233–1241).

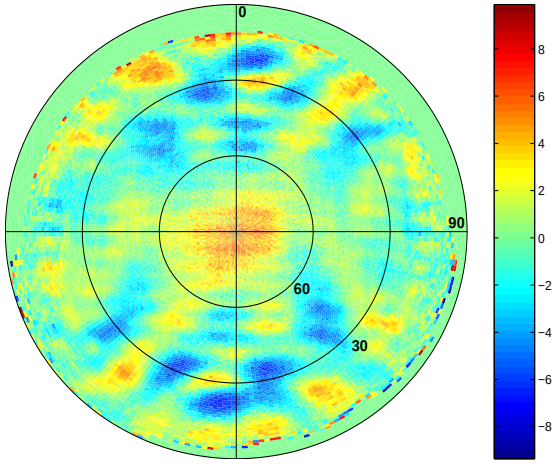

Figure 7.30: Mean postfit carrier phase ionosphere-free residuals (millimeters) per 1.5° azimuth and 1° elevation bins for GRACE B (GPS weeks 1233–1241).

significant pattern change over time, the resulting figures were compared with figures of other, shorter time spans. They were found to be constant.

Figures 7.29 and 7.30 show that the ionosphere-free phase residuals are generally small and appear to have maximum values of around 1 cm. Larger residuals are encountered as well, but they are likely to be averaged out by the binning. Apart from a different location of the elevation threshold of approximately 10° for raising satellites and a different coverage with low elevation data for setting satellites, the systematic patterns are very similar for the GRACE A and B satellites, which are identical by construction, and which both use the same type of POD antennas. Because the patterns were found to be constant in time, we suspect that their source is rather related to the receiver side and not to the transmitter side. This conclusion is also supported by [*Haines et al.*, 2005], who found patterns of carrier phase ionosphere-free

residuals to resemble the results from multipath simulations. Electronic signal interference can be excluded, because the GRACE GPS occultation antennas were not active during the time period analyzed. Therefore, multipath is strongly favored as a plausible source for the observed pattern. A further piece of evidence is given by the fact that the largest residuals, e.g., the negative blue patches, tend to occur towards the azimuths 0° and 180°, which point towards the front and rear side of the satellite, where multipath reflections are more likely to be caused by the larger surfaces. The observed patterns seem to be symmetric with respect to a rotation of 180° around the antenna boresight vector, which also holds for the entire satellite. Both arguments favor a source for the patterns which is related to the satellite body, such as multipath. Nevertheless, the patterns should be interpreted carefully, because contributions from other effects, e.g., from neglected antenna phase center variations, cannot be excluded. Further investigations in the near future will be necessary to better confine the origin of the observed systematic errors, and to assess their impact on orbit determination.

8. GRACE Orbit Determination Using Doubly Differenced GPS Data

Doubly differenced GPS data from the global IGS tracking network are routinely processed at the CODE AC, e.g., for station coordinate determination, ionosphere monitoring, and GPS orbit determination [*Hugentobler et al.*, 2004b]. It is well known that doubly differenced GPS observations are the key to precise relative positioning due to the reduction of common errors, e.g., induced by erroneous GPS satellite clock offsets, and, last but not least, due to the possibility to exploit the integer nature of the doubly differenced GPS carrier phase ambiguities. Once correctly resolved to integer values, they transform the corresponding carrier phase observations into highly precise ranges with a noise level of only a few mm. The advantages of the double difference approach are achieved, however, at the expense of a more complex data handling.

The relative positioning of spaceborne GPS receivers has many similarities with the relative positioning of terrestrial receivers. It is, e.g., identical to the case of a moving GPS ground receiver (rover) which is positioned kinematically with respect to one or more GPS reference stations; it only differs if the receiver motion is actually modeled and the deformation of the Earth's crust is replaced by the spacecraft dynamics. Both, terrestrial and spaceborne applications share the need for appropriate reference receivers, which may be either ground- or space-based for spaceborne applications. In view of the present LEO constellations such as GRACE and COSMIC, a big variety of candidate reference receivers are available to examine different processing strategies.

In the Bernese GPS Software [*Dach et al.*, 2007], single differences are explicitly formed and saved in baseline-specific files. Double differences are then formed implicitly for the pre-processing and the subsequent parameter estimation, where sophisticated algorithms are available to resolve the doubly differenced carrier phase ambiguities to their integer values [*Mervart*, 1995]. Compared to the processing of undifferenced data, changes only concern a more complex handling of the GPS observations. The fundamentals of LEO orbit determination, however, do not change at all.

In this chapter, a selection of different strategies for processing doubly differenced data from spaceborne GPS receivers are analyzed. The first part deals with separate and combined orbit determination for GRACE A and B by processing the spaceborne GPS data together with data from the IGS ground receiver network. The second part focuses on processing the baseline in space between GRACE A and B alone. This restricted test configuration turns out to be perfectly suited to meet the challenge for relative spacecraft positioning with the ultimately achievable precision. Validations with the ultra-precise K-band microwave link between GRACE A and B and the comparison with an extensive study performed by [*Kroes*, 2006] confirm the potential of relative positioning using GPS. A summary of the presented results may be found in [*Jäggi et al.*, 2007].

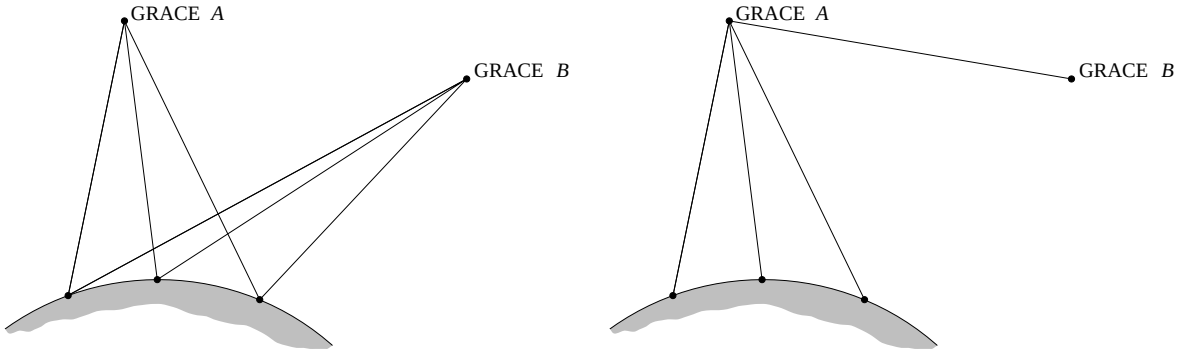

Figure 8.1: Separate baseline formation between the two GRACE satellites and several GPS ground stations (left) and combined baseline formation between one GRACE satellite and the GPS ground network and the other GRACE satellite (right).

8.1 Baseline Formation

Doubly differenced (DD) GPS observations are by definition related to a pair of GPS satellites and receivers (see Sect. 4.3.3). By convention, we group them by the pairs of receivers which are used to form them on the associated baselines (straight line between two receivers), and not by the pairs of GPS satellites. The "active" receivers of a terrestrial or spaceborne GPS campaign define all possible baselines on which DD observations could be formed from the originally undifferenced GPS data, but it is not necessary to actually form all possible DD observations since a subset of linearly independent baselines with a subset of linearly independent DD observations are sufficient for data processing.

In essence, we distinguish between two scenarios of orbit determination in the following: (a) the orbit determination for single LEOs carrying GPS receivers such as CHAMP, (b) the combined determination of orbits for formation flying spacecrafts carrying onboard GPS receivers such as the two GRACE satellites. Depending on the number of LEOs flying in formation, several space baselines between the individual spacecrafts may be formed in addition to the space-ground baselines between the LEOs and the GPS stations of a terrestrial ground network.

Figure 8.1 illustrates the baseline formation from the purists point of view for both scenarios of GRACE orbit determination. In Fig. 8.1 (left) only space-ground baselines are formed between each spaceborne GPS receiver and several GPS ground station receivers. This scenario is closely related to the processing of GPS data from a single LEO such as CHAMP where no other than space-ground baselines can be formed. It is actually equivalent to the separate processing of the GPS data from both GRACE satellites, if only LEO-specific parameters and no common parameters have to be estimated, e.g., no station-specific troposphere parameters. Note that the number of selected space-ground baselines needs to be much larger than sketched in Fig. 8.1 to ensure a good global coverage with DD observations along the LEO orbits.

Figure 8.1 (right) illustrates the combined processing of the GPS data from both GRACE satellites where the space-ground baselines between GRACE B and the GPS ground receivers are all replaced by the single space baseline between the two GRACE satellites. The inclusion of this space baseline is attractive due to its very short and rather constant baseline length. Typical variations per revolution are about ± 2 km from the mean separation which is kept within the limits of 170 to 270 km by the satellite operators. The length of the space-ground baselines, in contrast, may vary considerably from about 500 up

to 10 000 km due to the orbital motion. Resolving DD ambiguities and exploiting the full potential of relative precise positioning is thus much easier on the space baseline than on the space-ground baselines. Note that the replaced space-ground baselines between GRACE B and the GPS ground stations would be linearly dependent on the space-ground baselines between GRACE A and the same GPS ground stations due to the space baseline. Therefore, no loss of information occurs if the space-ground baselines to GRACE B are not taken into account in a combined processing. However, baselines between GRACE B and additional GPS ground stations could be included in a combined processing as long as they are linearly independent from all other baselines. This deviating strategy from the purists point of view of a combined processing could be beneficial to compensate for the asymmetry between the two GRACE satellites as shown in Fig. 8.1 (right).

Subsequently we address the processing of DD GPS data which either match the separate processing from Fig. 8.1 (left), or the combined processing from Fig. 8.1 (right), or, alternatively, we process the space baseline without any space-ground baselines by fixing one of the two GRACE orbits to a known reference trajectory, e.g., previously established by a zero difference solution. Remember that a correct processing of DD ionosphere-free observations requires to take the correlations between the individual baselines into account, even if the observation scenarios are basic as given by Fig. 8.1.

8.1.1 Ground Station Selection

GPS data from at maximum 150 globally distributed GPS ground stations are processed at the CODE AC to derive the final products for the IGS. For the purpose of LEO orbit determination, we may profit from the results of the CODE final analysis and introduce the station coordinates and troposphere zenith path delays as known into the LEO orbit analysis, as well as the GPS satellite orbits and the Earth orientation parameters. This guarantees that both the space- and the ground segments are modeled consistently with state-of-the-art products, and it removes the need to estimate other than LEO-specific parameters. Therefore, LEO orbits determined from DD GPS data automatically refer to the same reference frame as the CODE final orbits and station coordinates, which is the IGS realization of ITRF2000 (IGS00).

From the pool of GPS ground station data processed at CODE, a reasonably large subset of stations has to be selected for DD LEO POD. Because differenced GPS observations may be formed only if a GPS satellite is observed quasi-simultaneously by the LEO and a ground station receiver, the presence of commonly observed GPS satellites is the only reasonable basis to decide which ground stations to select in order to obtain a good coverage of GPS DD observations along the LEO orbit. One should keep in mind, however, that a variety of different criteria may be used to select the GPS ground stations on such a basis, and that it could make sense to take additional information into account like the geographical distribution of the GPS ground stations, or the receiver type in view of a possible resolution of the ambiguities to their integer values (see Sect. 8.2.4). Nevertheless, we will use a simple approach below, which solely optimizes the number of simultaneously observed GPS satellites.

First, the commonly observed GPS satellites from the LEO and from each ground station are counted for each observation epoch. From this record those stations are extracted epoch-wise that observed the maximum number of GPS satellites simultaneously with the LEO receiver. This number may vary due to the changing viewing geometry for the LEO and the GPS ground stations around the different sub-satellite points (it varies usually between six and ten for CHAMP or GRACE data). The number of GPS ground receivers which simultaneously observed the maximum number of GPS satellites, however, is subject to much larger variations due to the substantially different geographical distributions of the GPS ground stations around the sub-satellite points. Therefore, it may be as small as one for sub-satellite

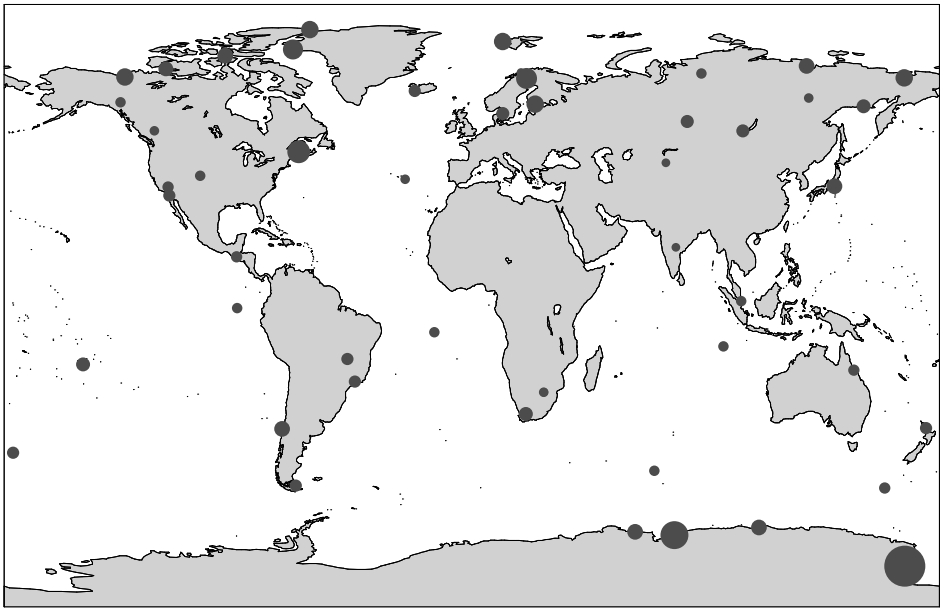

Figure 8.2: Globally distributed IGS stations used for GRACE orbit determination on DOY 250, 2003. The diameter of the circles is proportional to the incidence of a maximum number of simultaneously observed GPS satellites with the GRACE A BlackJack receiver.

points located in "isolated" regions such as large oceans and polar regions, and thirty to forty, if the LEO is flying over regions with a high density of permanent GPS sites, e.g., over Europe or North America.

It is important to include isolated GPS ground stations into the LEO analysis to ensure that the orbit is covered globally with (more or less) homogeneously distributed GPS DD observations. Therefore, the ranking of all receiver sites, which observed at least at one epoch the maximum number of GPS satellites simultaneously with the LEO receiver, is based on the number of such incidences over an entire arc, and not on the actual number of simultaneously observed satellites. This enhances the probability for isolated sites to get more counters as it is very likely that they observe the maximum number of GPS satellites if the sub-satellite point is in their vicinity – even if the number of simultaneously observed GPS satellites is small.

Figure 8.2 shows the global distribution of fifty IGS stations which met the above defined criteria best for GPS data from the GRACE A BlackJack receiver on DOY 250, 2003. The diameter of the circles indicates the frequency at which a ground receiver simultaneously observed the maximum number of GPS satellites with the spaceborne receiver. One can see that a set of (more or less) homogeneously distributed ground stations has been selected, including a few sites at isolated islands which successfully fill regional gaps, e.g., Ascension Island in the Atlantic Ocean or Tahiti in the Pacific Ocean. It is also obvious, however, that sites in the polar regions tend to dominate this ranking (indicated by the generally larger diameters of the corresponding circles). This behavior is due to the rather sparse coverage of the polar regions with IGS permanent stations and the near polar orbits of the GRACE satellites, implying a crossing of both polar regions at each revolution. The station McMurdo in Antarctica, e.g., leads the ranking by more than a factor 1.5 with respect to the second best station. Note that a different situation may be expected for other LEOs such as JASON-1, where the polar sites play only a minor role due to the much lower orbital inclination [*Hugentobler et al.*, 2005a].

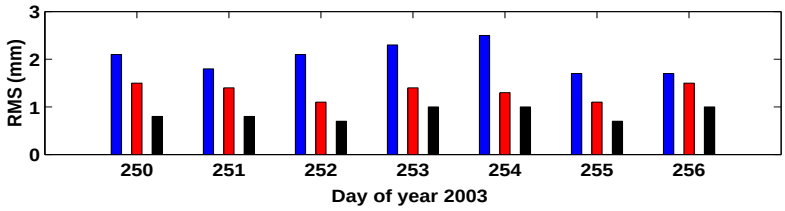

Figure 8.3: Daily 1-D RMS of the differences between GRACE A DD ambiguity-float orbits based on 70 ground stations and orbits based on 40, 50, and 60 stations (from the left to the right bars), respectively.

There is still room for further reducing regional gaps. The rather large gap over Central Africa, e.g., might be reduced to some extent by including an additional station in the South of Europe. Furthermore, it could make sense to suppress the selection of more than one GPS receiver within regions of a predefined minimal area. This measure would also exclude co-located receivers at one site, as it is the case for the station Hartebeesthoek, South Africa, which is actually present with two GPS receivers in the LEO analysis on DOY 250, 2003. The impact of refined solution strategies on the LEO orbit quality is probably not dramatic. This statement is supported by the following discussion concerning the maximum number of stations.

Maximum Number of Stations

The total number of selected GPS ground stations is a user specified input variable. In principle, it is desirable to include as many ground stations as possible into the LEO processing to make full use of the entire available information. From computational economy's point of view, however, only a subset of the available ground stations should be included due to the strong dependency of the CPU times on the number of processed observations (see Sect. 6.6.3). This finding is further supported by the analyst's point of view, who only expects marginal benefits from increasing the number of space-ground baselines due to the strong clustering of the GPS ground stations over densely populated areas like Europe. Consequently, additional baselines would be formed predominantly with stations located in regions from which the LEO orbit is already well observed, and thus provide only little additional and independent information.

Figure 8.3 shows the daily 1-D RMS of the total differences between GRACE A DD ambiguity-float orbits based on 70 GPS ground stations and orbits based on 40, 50, and 60 GPS ground stations, respectively. The differences are negligible between the solutions based on 60 and 70 stations (0.9 mm mean 1-D RMS) and still they are very small between the solutions based on 50 and 70 stations (1.3 mm mean 1-D RMS), where the largest differences occur in the along-track direction with a mean RMS of 1.8 mm. As expected, the differences start to become slightly more pronounced for the solutions based on only 40 stations, where a mean 1-D RMS of 2.0 mm is observed with a mean along-track RMS of 2.7 mm. In general, the results for GRACE B are marginally worse than for GRACE A due to the inferior tracking performance of the GRACE B BlackJack receiver (see Fig. 7.7), e.g., 1.4 mm mean 1-D RMS for the 50 station solution. Nevertheless, they completely fit into the picture shown in Fig. 8.3. It is thus save to state that observations from a moderate number of GPS ground receivers, e.g., fifty stations, provide a sufficiently dense data base to derive LEO orbits of good quality in the DD mode. The orbit differences

between solutions relying on ground networks with a large number of receivers are at the (few) millimeter level only, which may be partly explained by the dense clustering of stations over a few regions such as Europe and North America.

8.2 Orbit Results using GRACE and IGS Ground Station Data

A time span of five weeks (DOY 243–277, 2003) has been selected to compute reduced-dynamic GRACE orbit solutions based on several strategies using doubly differenced GPS data. For this purpose fifty IGS sites have been selected for each day according to Sect. 8.1.1 for the baseline formation between the GRACE BlackJack receivers and the ground network. We distinguish between the following solutions:

(1) a separate processing of the GPS data from GRACE A and B (see Fig. 8.1 (left)), with ambiguities treated as float values,

(2) a combined processing of the GPS data from GRACE A and B (see Fig. 8.1 (right)), with ambiguities treated as float values, and

(3) a combined processing of the GPS data from GRACE A and B, with ambiguities on the space-ground baselines treated as float values and ambiguities on the space baseline resolved to integer values where possible.

The information about the GPS satellite orbits, the Earth orientation parameters, the GPS ground station coordinates, and the zenith troposphere path delays for the IGS sites are introduced as known from the CODE final analysis. Note that the same set of GPS ground station data was used when the GPS observations from both GRACE satellites were processed separately, but that the station selection may be different from day to day due to our selection strategy.

In the following, we discuss the estimated GRACE orbits for all three data processing strategies applied to the "optimal" reduced-dynamic solution (c) with piecewise constant accelerations estimated over 6 min and equally applied a priori standard deviations of $5 \cdot 10^{-9}$ m/s^2 in the radial, along-track, and cross-track direction (see Sect. 7.9). Ambiguity resolution for solution (3) is based on the wide-lane/narrow-lane approach as described in Sect. 4.3.4.

8.2.1 Orbit Differences

Figure 8.4 gives a first impression of the orbit differences between the reference solution (combined DD ambiguity-float solution (2)) and the separate DD ambiguity-float solution (1), the combined DD ambiguity-fixed solution (3), and a zero difference solution (ZD), respectively. The orbit differences are shown for DOY 251, 2003 in the radial (top), along-track (middle), and cross-track (bottom) direction for both GRACE satellites. It can be well observed that the radial and along-track orbit differences are of periodic nature with different amplitudes for different solutions. A much less pronounced periodicity can also be recognized for the cross-track direction, especially for the solution (ZD) which is substantially different from the DD solutions. It could not be expected, however, that larger differences are not only observed for the solution (ZD), but also for the combined DD ambiguity-fixed solution. One recognizes, e.g., a strongly periodic pattern in the radial and along-track directions, which is strictly anti-correlated for the GRACE A and B orbit solutions, and an anti-correlated offset of considerable amplitude in the cross-track direction. This finding is important and makes it necessary to quantify the variability and

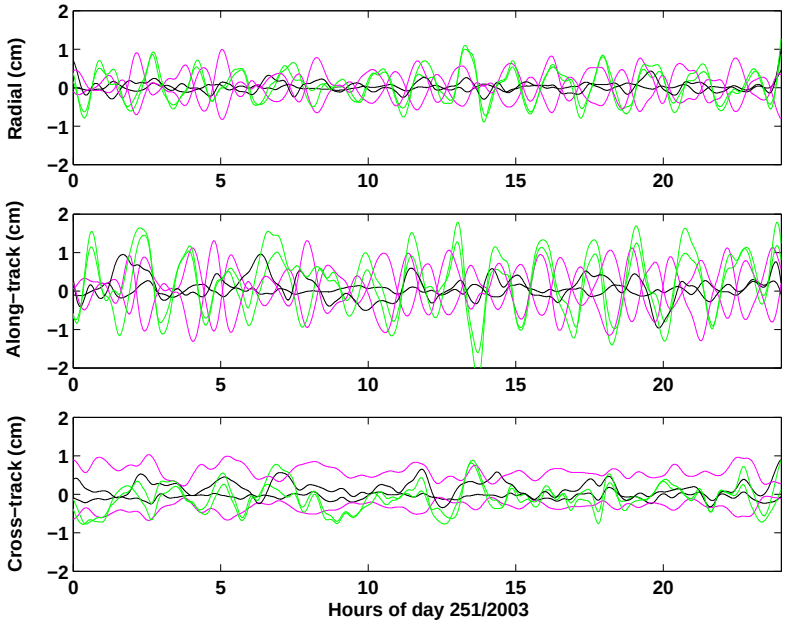

Figure 8.4: Orbit differences for both GRACE satellites in the radial (top), along-track (middle), and cross-track (bottom) direction between the DD ambiguity-float solution (2) and the DD ambiguity-float solution (1), the DD ambiguity-fixed solution (3), and the zero difference solution (ZD), respectively.

offset between the different orbit solutions for longer time intervals than just one day.

Figure 8.5 shows the daily standard deviations (STD) of the position differences between the discussed solutions. For a better visibility, the results are only given for DOY 243–260, 2003, because no substantial differences were found for the other days of the analyzed time period (DOY 261–277). First, it can be recognized that the individual orbit solutions for GRACE A show generally a better agreement with respect to the solutions (2) than the corresponding solutions for GRACE B. This could be expected for the comparisons with the solutions (1), where the same GRACE A data (apart from the space baseline) were processed in the same way as for the reference solutions (2) (see Fig. 8.1). This also explains why the differences between the GRACE A and B comparisons are larger than for the other comparisons.

The better agreement with the solutions (3) and (ZD) for GRACE A might be less obvious. The occurrence in the comparisons with the solutions (3), which only differ in the handling of the space baseline ambiguities from the reference solutions (2) but not in the used observations, indicates that this effect may be mostly attributed to a more robust determination of the GRACE A orbits due to the attachment of the space-ground baselines to this satellite as shown in Fig. 8.1 (right). The better tracking performance of the GRACE A BlackJack receiver (see Fig. 7.7) does not play the dominating role in this issue, which could not be concluded by only considering the comparisons with the solutions (ZD). In order to support this statement, one can exchange the roles of GRACE A and B in the baseline formation and confirm that in this case the individual orbit solutions for GRACE B show a generally better agreement with respect to the solutions (2) than the corresponding solutions for GRACE A. Moreover, it was noticed in the exchanged situation (not shown) that the solutions (1) and (ZD) for the attached GRACE A satellite show a clearly more degraded agreement than for the attached GRACE B satellite in the reverse situation. This

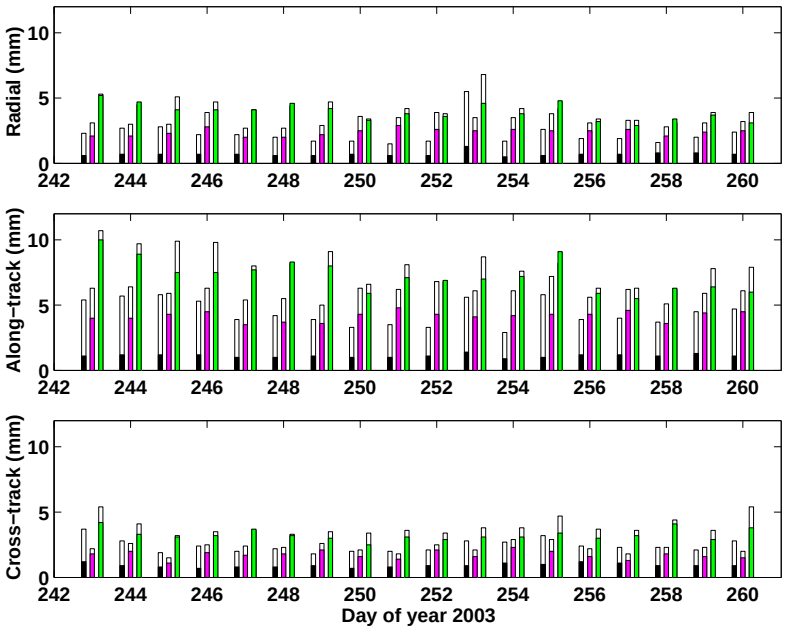

Figure 8.5: Daily standard deviation of orbit differences for GRACE A (filled bars) in the radial (top), along-track (middle), and cross-track (bottom) directions between the DD ambiguity-float solution (2) and the DD ambiguity-float solution (1) (left bars), the DD ambiguity-fixed solution (3) (middle bars), and the zero difference solution (ZD) (right bars), respectively. Empty bars show the corresponding results for GRACE B.

additional effect has to be attributed to the performance differences of the two GRACE GPS receivers, because no comparable effect was present in the comparisons with the solutions (3) when exchanging the roles of GRACE A and B. It is therefore preferable to use the better performing LEO receiver for establishing a well stabilized connection with the GPS ground stations, especially for an asymmetric scenario as it is shown in Fig. 8.1 (right).

Figure 8.5 shows that the level of the comparisons is similar for the radial and the cross-track direction, but worse for the along-track direction as it is to be expected for conventional reduced-dynamic orbits (see Sect. 8.3.3). The largest overall standard deviations (5.1 and 5.8 mm mean 1-D STD for GRACE A and B over the entire analyzed time period) result for the comparisons with the solutions (ZD), but non-negligible standard deviations are present in the comparisons with the solutions (3) as well (2.9 and 4.3 mm mean 1-D STD). The somewhat ”larger” differences between the solutions (2) and (ZD) have to be expected due to the different observation scenarios used for double difference and zero difference LEO POD. Differences between the double difference float solutions (2) and the fixed solutions (3) have to be expected as well, but the patterns from Fig. 8.4 indicate that one (or both) of the solutions might possibly be affected by systematic errors.

In an attempt to quantify such errors, we first analyze the offsets between the discussed solutions for both GRACE satellites. Figure 8.4 already indicated that only the cross-track direction is subject to such offsets, a finding which is confirmed for the remaining days of the analyzed time period, as well. Figure 8.6 thus focuses on the daily cross-track offsets between the different solutions. Whereas the offsets between the solutions (1) and (2), and (ZD) and (2) do not exceed 5 mm and do not show any obvious systematic

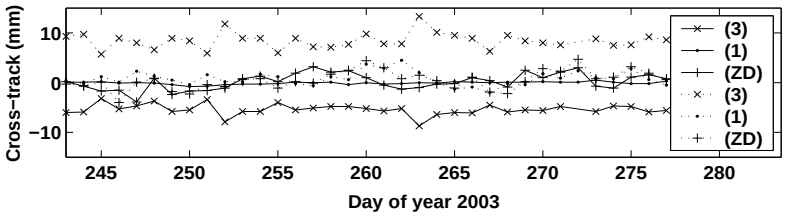

Figure 8.6: Daily cross-track offsets for GRACE A (solid lines) and B (dotted lines) between the DD ambiguity-float solution (2) and the DD ambiguity-float solution (1), the DD ambiguity-fixed solution (3), and the zero difference solution (ZD), respectively.

patterns over this rather short time interval, Fig. 8.6 clearly confirms the systematic offsets between the solutions (3) and (2). The offsets for GRACE A and B are strongly anti-correlated, i.e., a larger positive value for GRACE B induces a larger negative value for GRACE A. Furthermore, the absolute values for GRACE B tend to be larger than for GRACE A. It is interesting to note that this observed asymmetry seems to be less pronounced, if the role of GRACE A and B are exchanged in the baseline formation.

The reason for the observed discrepancy between the ambiguity-float and the ambiguity-fixed orbit solutions remains unresolved, but will be partly explained in Sect. 8.3.4. Nevertheless, a few possible error sources may be already excluded here. The observed offsets are most likely not caused by a mismodeling in the spacecraft dynamics, because the only difference between the two solutions resides in the treatment of the space baseline ambiguities. Therefore, the observed systematic effect may be attributed with utmost certainty to a mismodeling in the GPS observations. Whether the systematics may be attributed to the multipath errors shown in Figs. 7.29 and 7.30, or to the asymmetric formation of the DD observations according to Fig. 8.1 (right), or to any other mismodeling is not further analyzed in this section. As a consequence, it is not possible to decide whether the ambiguity-fixed solution only, the ambiguity-float solution only, or both solutions are affected.

8.2.2 K-Band Validation

K-band measurements provide the unique opportunity to directly measure the precision of the along-track orbit positions of the discussed solutions. One should keep in mind, however, that K-band observations are biased range observations which are only sensitive to variations in the distance between the two GRACE spacecrafts. Any common mode along-track errors remain undetected in the K-band validation.

Figure 8.7 shows the daily K-band range RMS errors for the discussed solutions for the entire time period analyzed (DOY 243–277). It is obvious that resolving space baseline ambiguities to integer values has an impressive impact on the performance of the line-of-sight validation of the GRACE baseline vector. The overall K-band range RMS error is 3.1 mm, which is significantly better than the K-band validation of the two ambiguity-float solutions or the orbit solution based on zero differences. The result is comparable with [*Švehla and Rothacher*, 2004b], who demonstrated ambiguity resolution on the GRACE baseline for the first time with preliminary GRACE data.

The combined DD ambiguity-float solution (2), the separate DD ambiguity-float solution (1), and the zero difference solution (ZD) show all a similar performance in the K-band validation with overall RMS errors of 10.2 mm, 10.8 mm, and 11.3 mm, respectively. Despite of their similar qualities, it is interesting

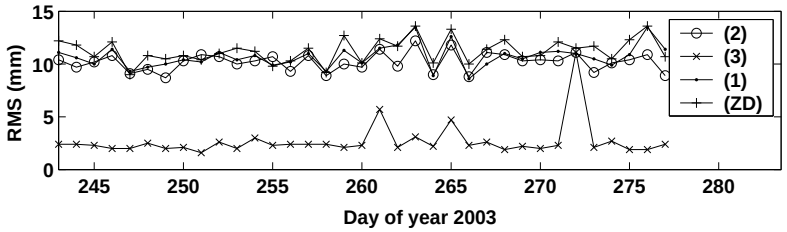

Figure 8.7: Daily K-band range RMS errors for the separate GRACE DD ambiguity-float solution (1), the combined DD ambiguity-float solution (2), the DD ambiguity-fixed solution (3), and the zero difference solution (ZD), respectively.

to note that the three solutions show a clear ranking as it can be seen in Fig. 8.7, as well. We recognize that the processing of DD GPS observations is beneficial to the quality of the space baseline.

The ambiguity-fixed solution in Fig. 8.7, however, does not yet reflect the ultimately achievable precision for the space baseline when the DD ambiguities are resolved. This is indicated, e.g., by a few outlying K-band range RMS values in the series, most notably the one on DOY 272, 2003, which is identical with the combined DD ambiguity-float solution, because the fixing of the space baseline ambiguities completely failed on this particular day. The reason for this failure was a "too generous" screening of the code observations, which did not allow it to resolve the wide-lane ambiguities to their integer values with the Melbourne-Wübbena LC. Sect. 8.3 will examine the optimal determination of the space baseline more closely and will show that better results may be obtained for this day as well.

It is important to mention that the level of the K-band validation in Fig. 8.7 does not yet reflect the ultimate precision even if a few outlying days are excluded, which would lower the RMS error to about 2.5 mm. We refer to Sect. 8.3, where it will be shown, that (sub)-mm precision in the K-band validation is feasible for this period (DOY 243–277, 2003).

8.2.3 SLR Validation

Satellite Laser Ranging is the only space geodetic technique which may provide an independent validation of the discussed solutions in an absolute sense. One should not forget, however, that the validation only takes place over the short time spans of the tracking passes above the SLR observatories.

Figure 8.8 shows the daily SLR RMS errors for the discussed solutions for GRACE A (top) and GRACE B (bottom) for the entire time period analyzed. It can be recognized that the SLR analysis shows for both satellites almost the same results for the individual orbit solutions. This has to be expected because SLR residuals reflect to a large extent the radial orbit errors, which are very similar for the individual solutions according to Fig. 8.5 (top). The curves thus rather reflect the errors in-common to all orbit solutions than the solution-specific differences. Nevertheless, differences occur and may be seen in Fig. 8.8 as subtle differences between the individual curves. The combined DD ambiguity-float solutions (2), the separate DD ambiguity-float solutions (1), and the zero difference solutions (ZD) exhibit almost identical overall SLR RMS errors of 2.20 cm, 2.20 cm, and 2.21 cm for GRACE A, and 1.87 cm, 1.83 cm, and 1.88 cm for GRACE B. The ambiguity-fixed solutions (3) show a slightly better overall SLR RMS, namely 2.03 cm for GRACE A and 1.81 cm for GRACE B. The ranking of the results from the SLR analysis thus confirms the K-band validation from Sect. 8.2.2, where the solutions (3) and (ZD) were found to be the best and worst ones, as well, respectively. Resolving the space baseline ambiguities seems thus to have a

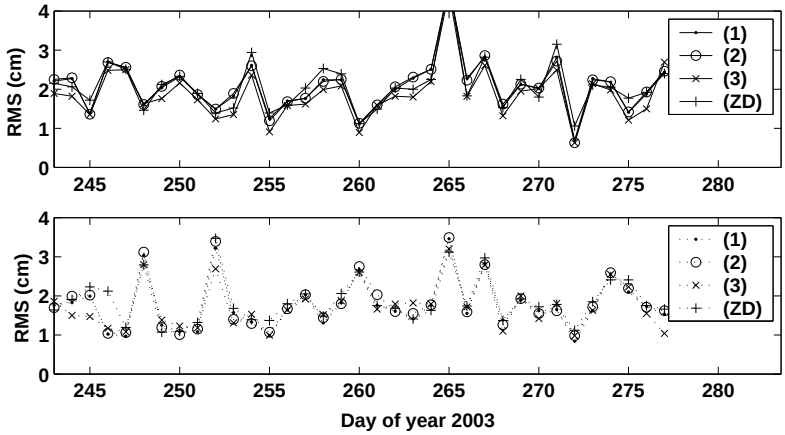

Figure 8.8: Daily SLR RMS errors for GRACE A (top) and GRACE B (bottom) for the separate DD ambiguity-float solution (1), the combined DD ambiguity-float solution (2), the DD ambiguity-fixed solution (3), and the zero difference solution (ZD), respectively.

very small but positive impact on the absolute orbit quality. More pronounced effects could be expected (at best) if a significant number of space-ground baseline ambiguities were correctly resolved to integer values, which is addressed in the following paragraph.

8.2.4 Special Solutions

It is commonly believed that the resolution of the space-ground baseline ambiguities should have a significant (positive) impact on the orbit quality of a LEO trajectory. However, this statement has not yet been confirmed, at least not as far as we know. [*Švehla and Rothacher*, 2002] used GPS data from the CHAMP satellite to quantify the orbit differences between using float or resolved space-ground baseline ambiguities, and found orbital changes in the order of 1–2 cm. It is, however, difficult to decide whether the ambiguity-fixed CHAMP orbit solutions are actually superior or not if only sparse SLR measurements are available for an independent validation. This might be one reason that no further studies are available about this issue, another one might be attributed to the heavy demands on CPU times needed to resolve the space-ground baseline ambiguities. Concerning the first reason, the GPS data from the two GRACE satellites offer nowadays a much better basis for such an investigation, because the K-band observations may be used in addition to the SLR measurements to validate the resulting orbits.

One week of GPS data (DOY 243–249, 2003) from the two GRACE satellites has been selected to compute GRACE double difference orbit solutions with resolved space-ground baseline ambiguities. In essence, we compare the separate processing of the GPS data from GRACE A and B with all space-ground baseline ambiguities treated as float values (solution (1)) with the same separate processing where as many space-ground baseline ambiguities as possible are resolved to their integer values. This situation is compatible with the processing of DD GPS observations from a single LEO such as CHAMP where no space baseline can be formed, and is thus well suited to check whether there is a (hopefully positive) impact on the relative GRACE orbit positions by the independent K-band observations when resolving the space-ground baseline ambiguities.

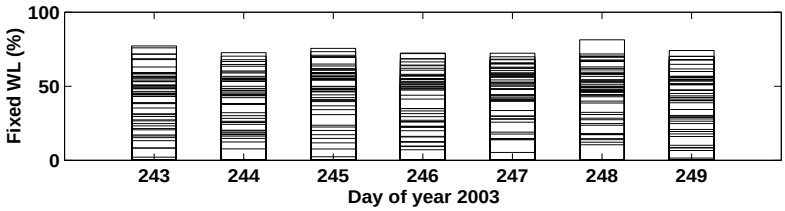

Figure 8.9: Percentage of resolved wide-lane DD ambiguities for space-ground baselines between GRACE A and fifty GPS ground stations.

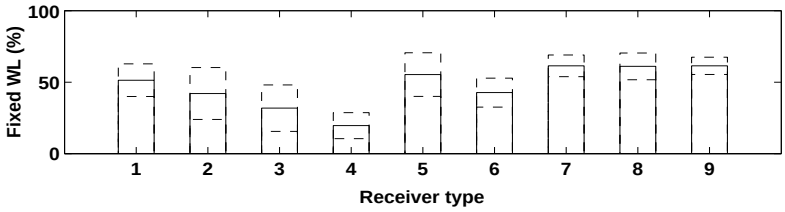

Figure 8.10: Mean percentage of resolved wide-lane DD ambiguities for different types of receivers: 1: ASHTECH Z-XII3, 2: ASHTECH UZ-12, 3: JPS LEGACY, 4: TRIMBLE 4000SSI, 5: AOA ICS-4000Z ACT, 6: ASHTECH Z18, 7: AOA BENCHMARK ACT, 8: AOA SNR-12 ACT, 9: AOA SNR-8000 ACT

Success Rate of Ambiguity Resolution

The task to resolve the DD ambiguities to integer values is considerably more difficult for the space-ground baselines than for the space baseline. The difficulties may be either attributed to the different quality of the code observations of the GPS ground receivers, which directly affects the resolution of the wide-lane ambiguities with the Melbourne-Wübbena LC, or they may be attributed to the baselines which are much longer than the space baseline considered so far, which complicates the fixing of the narrow-lane ambiguities. The superposition of both effects may have a severe impact on the overall success rates of resolving DD ambiguities to integer values on space-ground baselines.

Figure 8.9 shows for each day analyzed the percentage of the resolved wide-lane DD ambiguities for the fifty baselines between GRACE A and the GPS ground stations selected according to Sect 8.1.1. It can be immediately recognized that the success rates from the wide-lane ambiguity fixing differ significantly from the rates achieved with the space baseline. Instead of rates of about 95.6% (see Sect. 8.3.3), a maximum value of only 81.3% is encountered on DOY 248 for the best performing station Norilsk, Russia, and only poor 1.5% on DOY 249 for the worst performing station N'Koltang, Gabon. These extreme values and the scatter in the patterns from Fig. 8.9 illustrate that almost the entire spectrum of success rates has to be expected when resolving the wide-lane ambiguities. As no significant differences may be observed when the statistics for the fifty baselines between GRACE B and the same ground stations are analyzed, and because the noise of the Melbourne-Wübbena LC is dominated by the quality of the code observations, it has to be concluded that quality differences in the code observations of the GPS ground receivers play a crucial role when fixing the wide-lane ambiguities to their integer values.

In order to confirm that the observed scatter in Fig. 8.9 may be attributed to different types of GPS ground station receivers, Fig. 8.10 displays the average success rates (and standard deviations) of the

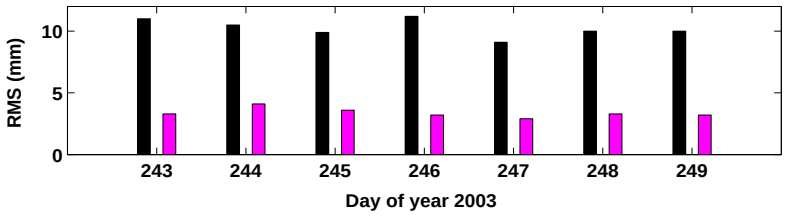

Figure 8.11: Daily K-band range RMS errors for the separate GRACE DD ambiguity-float solutions (1) (left bars) and for the separate GRACE DD solutions with resolved space-ground baseline ambiguities (right bars).

wide-lane ambiguity fixing for a few types of GPS ground station receivers for all $7 \cdot 50$ processed baselines of DOY 243–249, 2003. The receiver types are ordered according to the frequency of their occurrence in the baseline formation for this particular week, e.g., receiver type 1 (ASHTECH Z-XII3) was most frequently used with 93 occurrences, whereas receiver type 9 (AOA SNR-8000 ACT) was least frequently used with only 14 occurrences. Unfortunately, it can be recognized that the best success rates of about 61% are obtained for the receiver types 7, 8, and 9 which are not well represented in the set of selected GPS ground stations. Fortunately, the receiver encountered most frequently (type 1) shows an acceptable success rate of 51%, as well. It can be further recognized that receiver type 4 (TRIMBLE 4000 SSI) shows the worst performance of all displayed receiver types and, even worse, it shows up rather often in the baseline formation. This might be an argument for the incorporation of additional (receiver-specific) criteria in the GPS ground station selection if ambiguity resolution is aimed at.

The reason for the different performance in Fig. 8.10 is due to the fact that not all of the receiver types provide P-code measurements on both the L_1 and the L_2 carrier. In essence, there are three classes of GPS ground station receivers, namely cross-correlators observing C/A and $P_2' = C/A + (P_2 - P_1)$, e.g., types 4 and 5, Y-codeless observing P_1 and P_2, e.g., types 1, 7, 8, 9, and Y-codeless which should observe P_1 and P_2, but report C/A (instead of P_1) and P_2 (none of the listed receivers). Differential code biases $(P_1 - C/A)$ have therefore to be taken into account for receivers that do not provide P-code observations on both carriers [*Schaer et al.*, 2002].

K-Band Validation

Independent K-band measurements are very useful to clarify two issues concerning the impact of resolved space-ground baseline ambiguities on the orbit quality, namely whether they are capable to improve the relative GRACE orbit positions “alone” without the assistance of resolved space baseline ambiguities, or in the presence of resolved space baseline ambiguities. For both experiments, only 42 baselines (instead of 50) were included that allowed at least to fix 20% of the wide-lane ambiguities.

Figure 8.11 shows the daily K-band range RMS errors for the separate processing of the GPS data from GRACE A and B with all space-ground baseline ambiguities treated as float values (solution (1)), and for the same separate processing, where as many space-ground baseline ambiguities as possible are resolved to integer values. It is important to mention that the narrow-lane ambiguity resolution has been performed simultaneously with the pseudo-stochastic orbit modeling, and that all baselines have been processed together in one (large) adjustment to generate the best possible solution. Note that a baseline-wise resolution of the narrow-lane ambiguities with the float orbit solution (1) would be critical due to the small narrow-lane wavelength of only 10.7 cm (see Sect. 4.3.4).

It can be easily seen that resolving space-ground baseline ambiguities to integer values improves the overall K-band range RMS from 10.3 mm for the float solutions to 3.4 mm, if the space-ground ambiguities are resolved to integer values to the extent possible. This clearly demonstrates that correctly resolved space-ground baseline ambiguities strengthen the individual GRACE orbit solutions, which improves the orbit difference between GRACE A and B, which in turn improves the K-band validation. If one keeps in mind that only 47.1% of all (narrow-lane) ambiguities could be fixed to integer values, it becomes clear that the overall RMS error of the K-band validation is not as small as observed in Fig. 8.7 (2.2 mm), where only space baseline ambiguities were fixed to integer values (solution (3)). Besides the difficulty to resolve more space-ground baseline ambiguities, it cannot be completely ruled out that also a few of the resolved space-ground baseline ambiguities were fixed to incorrect integer values, due to the strong correlations that exist between the narrow-lane ambiguities.

Facing both difficulties, it is not a surprise that ambiguity resolution on all baselines (solution (3) with resolved space-ground baseline ambiguities) does not yet provide the aimed-for results. We noticed that the overall K-band range RMS error improved from 3.4 mm to 2.9 mm if the space baseline is included. Unfortunately, this is worse than the 2.2 mm resulting from fixing space baseline ambiguities only (solution (3)). Therefore, we conclude that we have to be able to fix significantly more space-ground baseline ambiguities to their correct integer values in order to avoid a degradation of the space baseline in a combined solution.

SLR Validation

SLR residuals may indicate whether resolved space-ground baseline ambiguities are not only capable to improve the quality of the relative GRACE orbit positions, but also of the absolute positions. Therefore, we compared the separate GRACE DD ambiguity-float solutions (1) and the separate GRACE DD solutions with resolved space-ground baseline ambiguities with SLR observations for DOY 243–249, 2003.

For GRACE A, we noticed a considerable improvement of the overall SLR RMS error from 2.21 cm (float) to 1.72 cm (fixed). Unfortunately, we noticed an opposite behavior for GRACE B, namely a degradation from 1.84 cm (float) to 1.98 cm (fixed). Therefore, it is impossible to formulate a firm conclusion based on this limited set of data. It is only clear that there is a rather significant impact on the orbit when fixing space-ground baseline ambiguities to integer values. However, the ultimate indication for an improvement of the orbit quality in an absolute sense could not be given.

8.3 Analysis of the Space Baseline

55 days of GPS data (DOY 243–297, 2003) from the two GRACE satellites have been selected to evaluate several nominal and experimental double difference solutions when processing the space baseline only. Because DD GPS observations from the space baseline alone do not contain enough information to reliably estimate both GRACE satellite orbits in an absolute (and relative) sense, it is a must to introduce an accurate reference orbit as known for one of the two satellites. For this purpose, the GRACE A zero difference orbits (solution (c)) described in Sect. 7.9 have been selected, because they fully meet the accuracy requirement formulated in Sect. 8.3.1. Such a procedure is very attractive with respect to the required CPU times, because only the space-baseline and no space-ground baselines have to be introduced into the processing. The same configuration was already successfully used by [*Kroes*, 2006] to demonstrate (sub)-mm precision of reduced-dynamic GRACE baseline estimates for the first time. In our analysis, we distinguish between the following solutions:

- reduced-dynamic determination of the GRACE B orbits, ambiguities on the space baseline are resolved to integer values whenever possible, or remain float, and
- kinematic determination of the GRACE B orbit positions, ambiguities on the space baseline are resolved to integer values whenever possible.

In analogy to the previous Sect. 8.2, the information about the GPS satellite orbits and the Earth orientation parameters are introduced as known from the CODE final analysis. The settings of the "optimal" solution (c) have been used for reduced-dynamic orbit determination. It turned out, however, that this is not optimal for the baseline processing, see Sect. 8.3.2.

8.3.1 Quality of the Reference Trajectory

In order to get insight into the baseline estimation from doubly differenced GPS GRACE data only, we should consider the geometric part of the observation equations (4.9). However, to keep the expression simple, we may analyze the observation geometry on the single difference level without loss of generality.

In analogy to (7.1), the difference ρ^k_{AB} between the slant ranges ρ^k_A and ρ^k_B from GRACE A and B to GPS satellite k reads as

$$\rho^k_{AB} \doteq \rho^k_A - \rho^k_B = \rho^k_{AB0} - \boldsymbol{e}^k_A \, \Delta\boldsymbol{r}_A + \boldsymbol{e}^k_B \, \Delta\boldsymbol{r}_B + \left(\boldsymbol{e}^k_A - \boldsymbol{e}^k_B\right) \, \Delta\boldsymbol{r}^k \, , \tag{8.1}$$

where

ρ^k_{AB0} is the a priori difference of the slant range between the phase center locations on GPS satellite k and GRACE A and B, respectively,

$\boldsymbol{e}^k_A$, $\boldsymbol{e}^k_B$ are the unit line-of-sight vectors pointing from the GRACE A and B phase centers to the GPS phase center location,

$\Delta\boldsymbol{r}_A$, $\Delta\boldsymbol{r}_B$ are the phase center position increments for GRACE A and B, and

$\Delta\boldsymbol{r}^k$ is the phase center position increment for GPS satellite k.

The linearization (8.1) would be used in this form at each epoch if one would simultaneously try to estimate the GRACE A, the GRACE B, and the GPS position increments kinematically from single difference GPS GRACE data only. For short baselines, the GRACE A and B position increments are almost one-to-one correlated, because the line-of-sight vectors $\boldsymbol{e}^k_A$ and $\boldsymbol{e}^k_B$ are nearly identical. Therefore, it is not possible to accurately estimate both GRACE satellite orbits simultaneously from differenced GPS GRACE data only. It can be verified that position errors at the meter-level have to be expected, which also affects the quality of the relative positions, especially towards the arc boundaries.

In order to highlight the sensitivity of (8.1) to the baseline vector, and to estimate the accuracy requirements for the reference trajectory, we rearrange this equation as

$$\rho^k_{AB} = \rho^k_{AB0} - \boldsymbol{e}^k_B \, \Delta\boldsymbol{r}_{AB} - \boldsymbol{e}^k_{AB} \, \Delta\boldsymbol{r}_A + \boldsymbol{e}^k_{AB} \, \Delta\boldsymbol{r}^k \, , \tag{8.2}$$

where

$\Delta\boldsymbol{r}_{AB} \doteq \Delta\boldsymbol{r}_A - \Delta\boldsymbol{r}_B$ and

$\boldsymbol{e}^k_{AB} \doteq \boldsymbol{e}^k_A - \boldsymbol{e}^k_B$, which is not a unit vector.

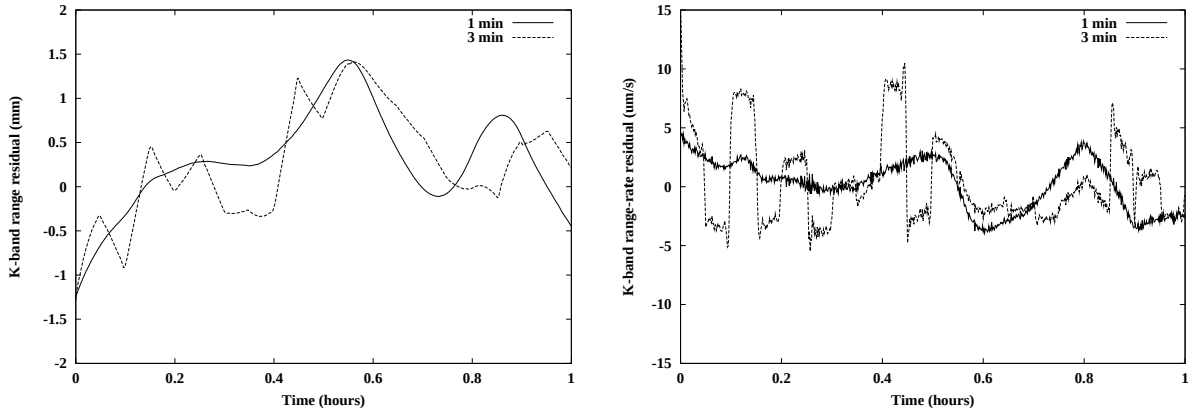

Figure 8.12: K-band range (left) and range-rate (right) residuals for the first hour of DOY 258, 2003 for reduced-dynamic ambiguity-fixed GRACE orbit solutions based on different subinterval lengths of the numerical integration.

Since no increments for GRACE A and GPS positions are estimated in this work, $\Delta\boldsymbol{r}_A$ and $\Delta\boldsymbol{r}^k$ are both set to zero in (8.2). However, it can be learned from (8.2) that position errors $\delta\boldsymbol{r}_A$ in the reference trajectory (GRACE A) and errors $\delta\boldsymbol{r}^k$ in the GPS satellite positions both affect the computation of ρ^k_{AB} in the same way. The impact of the uncertainty in the GPS satellite position errors on the baseline estimates is, however, much smaller than for zero difference positioning (see Sect. 7.1), because $|\boldsymbol{e}^k_{AB}| << 1$ for short baselines. Concerning the propagation of reference orbit errors $\delta\boldsymbol{r}_A$ into ρ^k_{AB}, [*Teunissen and Kleusberg*, 1998b] give the upper limit

$$|\boldsymbol{e}^k_{AB}\,\delta\boldsymbol{r}_A| \leq \frac{|\boldsymbol{r}_A - \boldsymbol{r}_B|}{|\boldsymbol{r}_B - \boldsymbol{r}^k|} \cdot |\delta\boldsymbol{r}_A| \;, \tag{8.3}$$

where it is assumed that $|\boldsymbol{r}_A - \boldsymbol{r}^k| \cong |\boldsymbol{r}_B - \boldsymbol{r}^k|$. Assuming a quality of $\delta\boldsymbol{r}_A \cong 10$ cm in the reference positions, the propagation into ρ^k_{AB} is below the millimeter level for the GRACE constellation, where $|\boldsymbol{r}_A - \boldsymbol{r}_B| \cong 200$ km and $|\boldsymbol{r}_B - \boldsymbol{r}^k| \cong 20\,000$ km.

8.3.2 Tuning Space Baseline Solutions

In Sect. 8.2.2 the level of the K-band validation was found in Fig. 8.7 to be about 2.5 mm, if the space baseline ambiguities were resolved to integer values, and if a few outlying days were excluded from the statistics. Although this is not bad, it does not yet represent the ultimately achievable limit. In this paragraph we discuss a few issues such as the settings of the numerical integration and the constraints of the pseudo-stochastic parameters, which were found to be relevant in order to obtain high-precision baseline estimates from reduced-dynamic GRACE orbits.

Numerical Integration

In Sect. 8.3.1 we mentioned that the reference orbit has to be known to approximately 10 cm in order to avoid an error propagation into the baseline solution. If this is the case, and if the baseline shall be estimated kinematically, the epoch-wise estimates of the baseline vector may be attached without difficulties to the positions of the reference orbit, even if they were affected by (small) systematic errors.

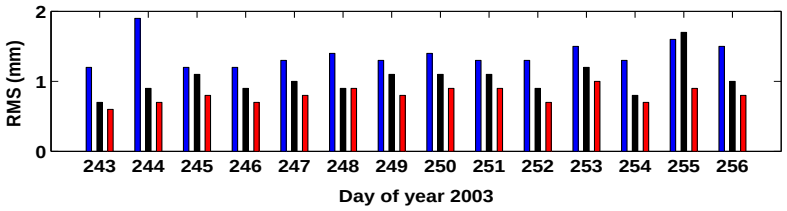

Figure 8.13: Daily K-band range RMS errors for reduced-dynamic ambiguity-fixed GRACE orbit solutions based on 6-minute accelerations (left bars), 60-minute accelerations (middle bars), and 6-minute accelerations with relative constraints between GRACE A and B (right bars).

In other words, kinematic baseline estimates simply take over (small) systematic errors induced by the reference orbit. These errors cannot be detected in the K-band validation, because they are common to both orbits and cancel out in the relative position.

Unlike kinematic baseline estimates, reduced-dynamic baseline solutions have to solve the equation of motion (5.12). One may therefore expect that the reduced-dynamic baseline estimates may not take over (all) systematic errors induced by the reference orbit, even if the reference orbit has a quality of better than 10 cm. Figure 8.12 supports this hypothesis and reveals remaining systematic errors in the baseline solution, when selecting too long subintervals for the numerical integration. Figure 8.12 shows a zoom on the first hour of the K-band range (left) and range-rate (right) residuals on DOY 258, 2003 for reduced-dynamic ambiguity-fixed GRACE orbit solutions based on 6-minute piecewise constant accelerations, which were numerically integrated with a constant subinterval length of 1 min and 3 min, respectively. The differences between the two reference orbits are on the few mm-level. Figure 8.12 (left) shows that the differences in the K-band range residuals are on the mm-level, as well, which does not seem to be dramatic at first sight. One should be aware, however, that every (small) effect is potentially important when striving for the "last millimeter". Figure 8.12 (right) shows that the systematic errors in the K-band range-rate residuals are indeed striking. Pronounced changes, not jumps, in the K-band range-rate residuals may be observed every 3-minutes at the boundaries of the subintervals of the numerical integration. Thanks to the piecewise-constant accelerations only a comparably small part finally affects the orbit positions. On the one hand, this underlines the capability of pseudo-stochastic parameters to absorb almost any orbit modeling deficiencies, but it also reflects, on the other hand, the difficulty to separate "true" orbit signals from "artificial" signals in a subsequent analysis.

Figure 8.13 shows for a test period of 14 days (DOY 243–256, 2003) that the level of the K-band range validation improved from about 2.5 mm (see Fig. 8.7) to an overall RMS error of 1.39 mm (left bars), by simply changing the subinterval length of the numerical integration from 3 to 1 min. This demonstrates the usefulness of K-band measurements for a precise validation of orbit solutions. Currently, there is no other independent validation technique available to detect this kind of subtleties in orbit modeling. We have to keep in mind, however, that other systematic effects of similar nature might still be present in our GRACE orbit solutions – but remain undetected as they are common to both GRACE trajectories.

Constraining Pseudo-Stochastic Parameters

Appropriate subinterval lengths and constraints are essential to obtain very precise baseline estimates from reduced-dynamic ambiguity-fixed orbits. Figure 8.13 compares the level of the K-band range validation obtained for the standard solution (based on piecewise constant accelerations over six minutes (left

bars)), and for an experimental solution (based on ten times longer subintervals of sixty minutes length (middle bars)). It may be disturbing, at the first sight, that the K-band range validation is systematically better for the experimental solution for the majority of the considered days (with an overall RMS error of 1.03 mm), despite the very long acceleration subintervals. As a matter of fact, the two GRACE orbits (the reference orbit is based on sixty minutes intervals as well) are much worse in the "absolute" sense and show deviations of up to 10 cm w.r.t. "state-of-the-art" GRACE orbits, but they agree much better "relatively" – as it is confirmed by the K-band validation. This "paradox" situation is, of course, not satisfying, but demonstrates that requirements differ for "absolute" and "relative" orbit determination.

Inspecting the individual acceleration parameters for both solutions reveals that the long subintervals naturally constrain the estimates for GRACE A and B much closer to each other than short subintervals. Because the two GRACE satellites are only separated by about 30 s on the same orbital trajectory, they experience almost the same perturbing forces. This special configuration is useful, e.g., for a relative calibration of the GRACE A and B accelerometer data [*Perosanz et al.*, 2006]. For the estimation of piecewise constant accelerations, one may therefore expect estimates which are very close to each other for long subintervals, e.g., 60 min, due to the almost negligible time shifts of only 30 s at the beginning and at the end of each subinterval.

It is clear that orbit solutions based on too long acceleration subintervals are not ideal for modeling the space baseline due to unacceptable orbit qualities in an "absolute" sense. We know from experience when processing undifferenced GRACE GPS data, that subinterval lengths of about 6 min are well suited to achieve a reference trajectory of good quality. Therefore, we have to combine this knowledge with the lesson learned from the previously discussed experimental solution. Figure 8.13 (right bars) shows that the level of the K-band range validation can indeed be further decreased to an overall level of 0.80 mm by estimating piecewise constant accelerations over 6 min with additional constraints between the GRACE A and B accelerations. The short subinterval length ensures a high-quality reference trajectory in an "absolute" sense, whereas the relative constraints between the GRACE A and B accelerations take the special orbit configuration into account. The a priori variances of the acceleration differences could thereby be lowered to 1 nm/s^2 for the along-track and cross-track direction. The radial acceleration differences were constrained to "zero" due to a strong in-plane coupling between radial and along-track accelerations.

In the following, we investigate this kind of reduced-dynamic ambiguity-fixed baseline solution with relatively constrained piecewise constant accelerations in more detail. The following illustrations are drawn in closest analogy to the figures provided by [*Kroes*, 2006], in order to facilitate a comparison between both sets of results.

8.3.3 Analysis of Tuned Space Baseline Solutions

Figure 8.14 shows the K-band range (top) and range-rate (bottom) residuals on DOY 243, 2003 as a function of time for the ambiguity-fixed reduced-dynamic baseline. As expected, the resolved space baseline ambiguities and the relative constraining of the piecewise constant accelerations dramatically strengthen the orbit solution, which has a striking impact on the K-band validation. Discrepancies between the dynamic models and the GPS tracking data now tend to be removed from the position solution, because the ambiguity parameters, once correctly resolved to integer values, can no longer absorb them.

The very low K-band range RMS error of 0.6 mm shows that the K-band range residuals are mostly below the 1 mm level on this particular day. This indicates that sub-mm precision is feasible for the rel-

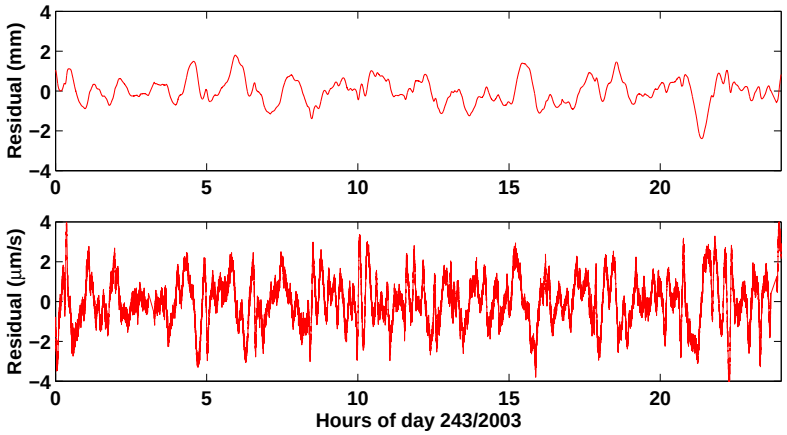

Figure 8.14: K-band range (top) and range-rate (bottom) residuals on DOY 243, 2003 for the reduced-dynamic ambiguity-fixed GRACE orbit solution.

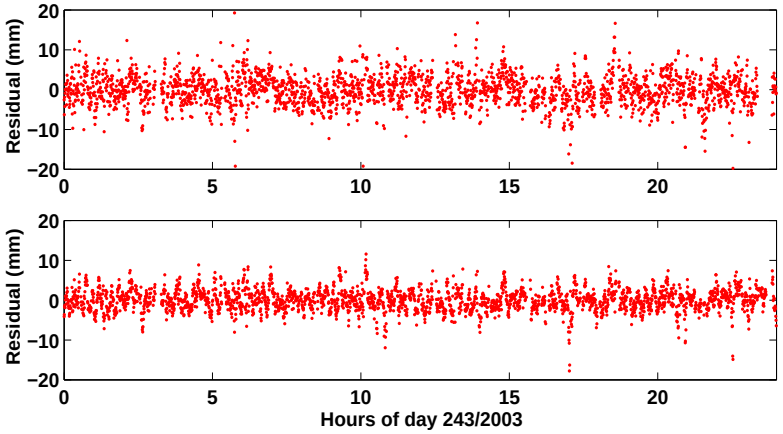

Figure 8.15: K-band range residuals on DOY 243, 2003 for the kinematic ambiguity-fixed GRACE orbit solution based on the "normal" ionosphere-free observable (top) and on the ionosphere-free observable constructed from L_A and L_2 (bottom).

ative positioning of the two GRACE spacecrafts in a reduced-dynamic batch least-squares environment. One might suspect that the precision in Fig. 8.14 could reflect a too optimistic quality because four KBR biases had to be adjusted due to KBR phase breaks at 03:15:40, 16:45:10, and 23:50:40. It is nice to see, however, that no obvious discontinuities occur at the mentioned epochs, indicating that the precision claimed in Fig. 8.14 (top) is real.

When comparing Fig. 8.14 (top) with 8.14 (bottom) we get the (correct) impression that the K-band range-rate residuals are much noisier than the K-band range residuals. Although the same "periodic" patterns may be recognized in both figures, pronounced short-term fluctuations clearly influence the residuals as well. The K-band range-rate RMS error of 1.2 μm/s is, however, largely dominated by the "periodic" variations which are in common to both the range and range-rate residuals. The nature of the short-term fluctuations will be discussed at the end of this section.

From the modeling point of view, the following aspect has to be highlighted. The K-band range residuals in Fig. 8.14 (top) are strictly continuous by construction, if no multiple K-band bias parameters have to be adjusted in the validation process. This is a difference to the results presented by [*Kroes*, 2006], who used a Kalman filter approach. Small discontinuities are unavoidable.

Figure 8.15 (top) shows the K-band range residuals on DOY 243, 2003 as a function of time for the kinematic ambiguity-fixed baseline. Apart from the fact that the solution shows a much larger K-band RMS error of 4.5 mm, a few correlations with Fig. 8.14 (top) may be recognized. More insight, however, is gained from Fig. 8.15 (bottom) where kinematic POD is performed with an "alternative" ionosphere-free GPS observable constructed from the L_A and the L_2 carrier phase observations instead of the normally used L_1 and L_2 carrier phase observations. Due to the much lower noise on the L_A observations, systematic effects such as the "periodic patterns" may now be recognized remarkably well in the kinematic K-band validation, which exhibits a K-band RMS error of 2.7 mm only. The comparison with Fig. 8.14 (top) shows that the reduced-dynamic solution offers some protection against random errors and systematic outliers, e.g. such as that at 17:00, but it is not immune to systematic errors which can be identified in both kinematic and reduced-dynamic solutions.

What is the reason for the "periodic" patterns in Figs. 8.14 and 8.15? Compared to the (much larger) K-band residuals of a zero-difference solution (see Fig. 7.20), no pronounced once-per-revolution periodicity may be observed, indicating that the deviations cannot be attributed exclusively to a mismodeling of the satellite dynamics. This conclusion is in accordance with the kinematic baseline solutions shown in Fig. 8.15, which are affected by the "periodic" patterns. Spectral analysis of K-band residuals from reduced-dynamic ambiguity-fixed solutions reveals that periods between 15 and 20 min, and between 30 and 40 min dominate the spectrum. According to Sect. 7.4, a time between 30 to 40 min is the typical time that a GPS satellite can be tracked from the GRACE receivers. The observed "periodic" patterns therefore most likely reflect systematic effects in the GPS observations, e.g., carrier phase multipath or unmodeled phase center variations.

K-Band Range Validation

Figure 8.16 shows the statistics of the percentage of resolved wide-lane (top) and narrow-lane (bottom) space baseline ambiguities for DOY 243–297, 2003. It is obvious that the wide-lane ambiguity resolution with the Melbourne-Wübbena LC is much easier on the space baseline than on space-ground baselines as discussed in Sect. 8.2.4. The good P-code quality of the two GRACE BlackJack receivers (see [*Kroes*, 2006]) allows us to resolve 95.6% of all wide-lane ambiguities to integer values. Only for DOY 272 a reduced performance may be observed due to problematic code measurements. This comfortable situation provides an excellent basis for resolving a significant number of the narrow-lane ambiguities, as well, which is simultaneously performed with the pseudo-stochastic orbit modeling. Figure 8.16 (bottom) shows that on average 89.8% of the narrow-lane ambiguities are resolved to integer values.

Figure 8.17 (top) shows the daily K-band range RMS errors for DOY 243–297, 2003. It is interesting to notice an almost invariant level of the K-band fit, which is at an overall RMS error of 0.88 mm when properly accounting for the number of all underlying residuals. The daily values vary between 0.64 mm for the (already presented) solution on DOY 243, and 1.64 mm for the "outlying" solution on DOY 272 due to the smaller number of resolved ambiguities. The overall K-band range RMS error of 0.88 mm confirms the 0.91 mm found by [*Kroes*, 2006], where the longer time span between DOY 190 and 290, 2003 was analyzed.

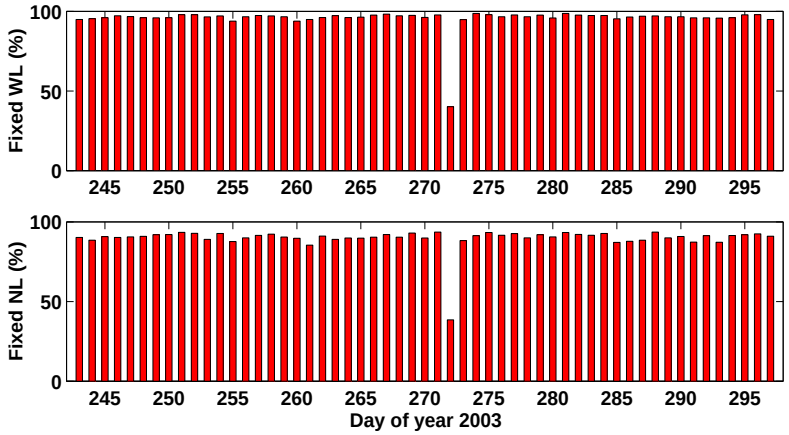

Figure 8.16: Daily percentage of resolved wide-lane (top) and narrow-lane (bottom) ambiguities for reduced-dynamic ambiguity-fixed orbit determination of the GRACE baseline.

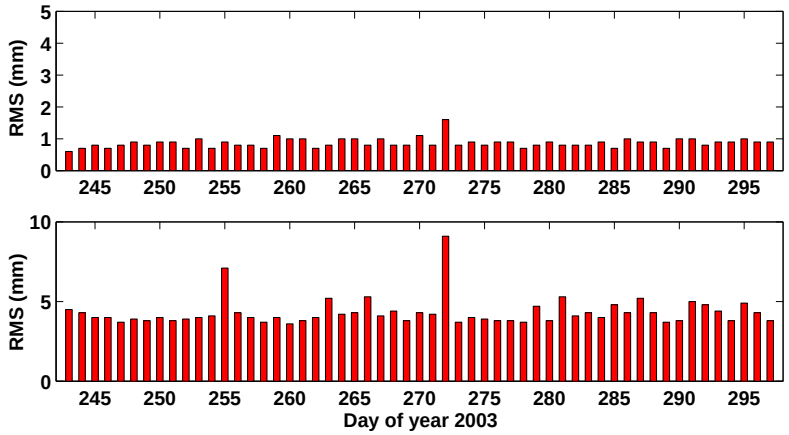

Figure 8.17: Daily K-band range RMS errors for reduced-dynamic ambiguity-fixed GRACE orbit solutions (top) and kinematic ambiguity-fixed orbit solutions (bottom). Note the different scale for both figures.

Figure 8.17 (bottom) shows the daily K-band range RMS errors for the corresponding kinematic ambiguity fixed solutions. We notice a larger overall RMS error of 4.41 mm and a slightly worse repeatability from day to day. Obviously, the solution of DOY 272 shows again the worst performance. An inspection of both residual time series showed that a few larger oscillations locally increased the K-band fit, which offers a basis for further investigations to avoid such a situation. It is interesting to note, however, that the second worst kinematic solution on DOY 255 does not have a counterpart in Fig. 8.17 (top), which again illustrates that the reduced-dynamic solution generally offers a better protection against data problems. A similar robustness was observed, e.g., on DOY 222 (not shown) where the reduced-dynamic solution could be propagated over an extended gap with about 5.5 hours of missing GPS and KBR data, and still showed a K-band range RMS of only 1.0 mm.

Let us finally inspect the K-band range validation for reduced-dynamic ambiguity-float GRACE orbit

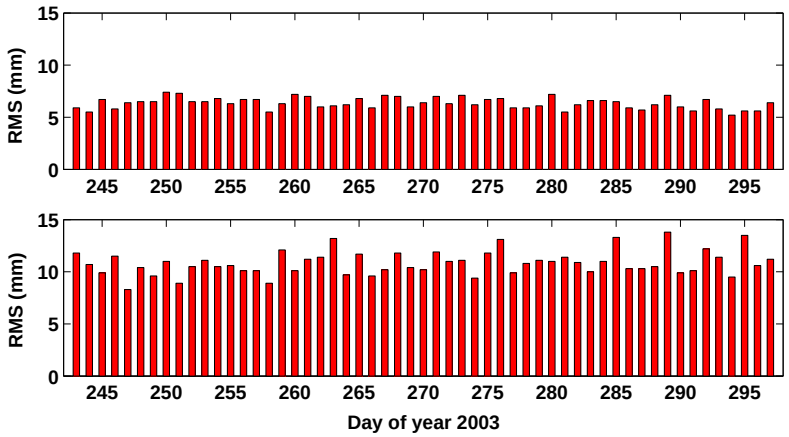

Figure 8.18: Daily K-band range RMS errors for reduced-dynamic ambiguity-float GRACE orbit solutions (top) and zero difference GRACE orbit solutions (bottom). Relative constraints between GRACE A and B accelerations are only applied to the ambiguity-float solutions.

solutions. Figure 8.18 shows the daily K-band range RMS errors for the DD (top) and the ZD (bottom) solutions. First, we notice (again) the significantly degraded line-of-sight precision of the ambiguity-float solutions compared to the ambiguity-fixed solutions in Fig. 8.17 (top). When comparing Fig. 8.18 (top) with Fig. 8.17 (top), we observe an overall RMS error of 6.38 mm instead of 0.88 mm. Because the two solution-types differ only in the treatment of the ambiguity parameters, this difference directly reflects the impact of the resolved space baseline ambiguities on the line-of-sight baseline precision.

Figure 8.18 (bottom) shows that the ZD solution exhibits an overall K-band range RMS error of 10.90 mm (better than in Table 7.7 due to the improved setting for the numerical integration), which is worse than the 6.38 mm observed for the DD solution (top). Two reasons are responsible for this degradation. First, relative constraints have been applied to the piecewise constant accelerations between GRACE A and B for all DD solutions as explained in Sect. 8.3.2, which strengthens the solutions considerably. Second, the processing of doubly differenced GPS data itself is preferable for relative positioning, because common error sources are reduced or eliminated by forming differences as already mentioned in Sect. 4.3.3. One should be aware of the fact, however, that the application of relative constraints is the main reason for the observed K-band range RMS error of 6.38 mm. A value between 9 and 10 mm could be expected without applying relative constraints.

It may be mentioned that the results in Fig. 8.18 seem to be better than those provided by [*Kroes*, 2006], if ambiguities are treated as float values. The thereby reported overall RMS errors of 7.85 and 16.01 mm may indicate an advantage for our processing based on the Bernese GPS Software, where one and the same type of batch least-square adjustment is used for all of the presented solutions.

K-Band Range-Rate Validation

K-band range-rate residuals are well suited to detect quality differences between the pseudo-stochastic orbit models discussed in Chapter 5. A zoom on one hour of K-band range-rate residuals can be inspected in Fig. 8.19 for the "standard" reduced-dynamic ambiguity-fixed GRACE orbit solutions based on piecewise constant accelerations over six minutes, and for an analogue solution based on pulses set up

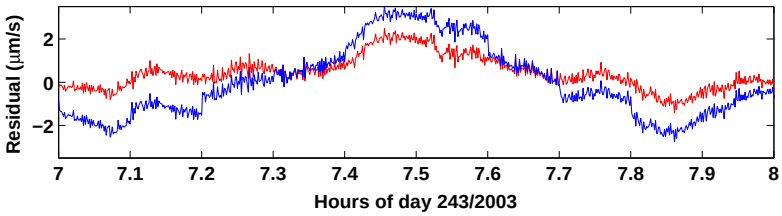

Figure 8.19: Zoom on one hour of K-band range-rate residuals on DOY 243, 2003 for the reduced-dynamic ambiguity-fixed GRACE orbit solutions based on piecewise constant accelerations (grey) and pulses (black), respectively.

every six minutes. The zoom directly reveals the subtle differences in the K-band range-rate validation for the two types of orbit parameters. As expected, the orbits based on piecewise constant accelerations show continuous K-band range-rate residuals, whereas small discontinuities occur for the pulse-based orbits at every 0.1 h. Some of the jumps may be recognized, e.g., at 7.2 h, 7.6 h, 7.7 h, and 7.8 h. One should not forget, however, that Fig. 8.19 validates the line-of-sight difference of the orbital velocities of GRACE A and B. Consequently, the sizes of the individual velocity changes are considerably larger than those reflected by the K-band range-rate validations.

In Fig. 8.19 we notice in general larger values of the "long-term" variation for the solution based on pseudo-stochastic pulses. Possible causes for this observation are either not optimally chosen a priori standard deviations, or the less favorable orbit modeling by instantaneous velocity changes. No attempt was made to further tune pulse-based baseline solutions.

Let us finally comment on the pronounced short-term fluctuations already noticed in Fig. 8.14 (bottom). A close inspection of Fig. 8.19 shows that the same patterns occur for both the pulse- and the acceleration-based orbit solutions. Spectral analysis confirms the short-term nature of these fluctuations with periods of 11.5 and 23 s. It is thus very unlikely to attribute the fluctuations to the (different) orbit solutions since a subinterval length of 1 min was used for the numerical integration.

In order to roughly estimate the magnitude of the short-term fluctuations, we first performed a daily smoothing of the K-band range-rate residuals by computing moving averages using a Gaussian kernel as weighting function:

$$\bar{k}(t) \doteq \frac{\sum_{i=1}^{n} W(t_i)\, k(t_i)}{\sum_{i=1}^{n} W(t_i)} \qquad \text{with} \qquad W(t_i) \doteq \exp\left(-\frac{(t_i - t)^2}{2\,\Delta t^2}\right) , \tag{8.4}$$

where

$\bar{k}(t)$ is the smoothed K-band range-rate residual at time t,

$k(t_i)$ is the original K-band range-rate residual at time t_i,

$W(t_i)$ is the Gaussian kernel, and

Δt is the characteristic width of the Gaussian kernel.

Δt was set to 23 s to compute smoothed K-band range-rate residuals for a test period of 20 days. Aiming at a rough estimate of the scatter of the short-term fluctuations, we compute the daily RMS error m with

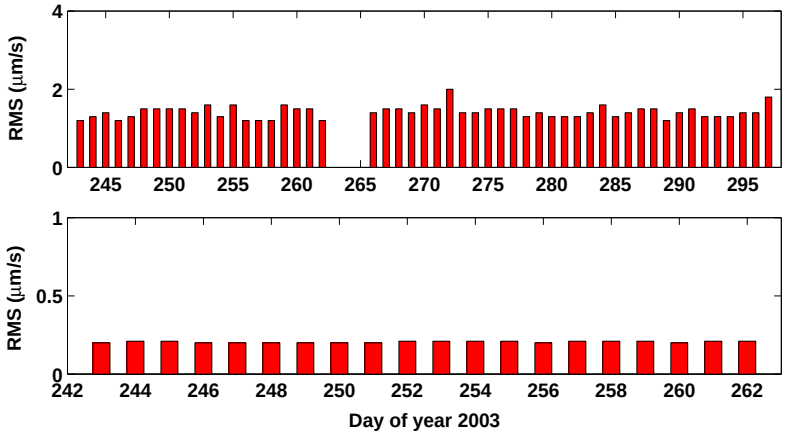

Figure 8.20: Daily K-band range-rate RMS errors for reduced-dynamic ambiguity-fixed GRACE orbit solutions. Total effect (top) and short-term fluctuations (bottom).

respect to the smoothed residuals according to

$$m = \sqrt{\frac{\sum_{i=1}^{n} (k(t_i) - \bar{k}(t_i))^2}{n-1}} \,, \tag{8.5}$$

where

t_i are the measurement epochs and

n is the number of measurements considered.

The use of the relation is based on the assumption that most of the long-term variations may be attributed to the orbit (mis)modeling.

Figure 8.20 compares the daily K-band range-rate RMS errors (overall value of 1.4 μm/s) obtained from the original residuals (top) and from (8.5) (bottom). Note that the three days at the end of the test period (DOY 243–262) were left out in Fig. 8.20 (top) due to unrealisticly large K-band range-rate residuals, caused by spurious antenna correction values provided in the Level 1B KBR data files.

It can be seen that the scatter of the short-term fluctuations is almost constant at a level of about 0.21 μm/s. This constant level is a further indication that the fluctuations may be actually attributed to the K-band range-rate data and not to orbit (mis)modeling. Another piece of evidence for this is the observed order of magnitude of the fluctuations, which agrees with the expectations concerning the RMS of K-band range-rate data. [*Biancale et al.*, 2005] report, e.g., a RMS level of about 0.24 μm/s for the official Level 1B KBR range-rate data on DOY 227, 2003, and a RMS level of about 0.19 μm/s for KBR range-rate data derived at CNES-GRGS for the same day. Our value of 0.21 μm/s might thus be too optimistic due to a too weak smoothing of the range-rate residuals. Our estimate is only intended for illustrating purposes.

8.3.4 Formal Errors and Orbit Differences

It has been shown in the previous section by the K-band validation that the true precision of the along-track component of the relative position between GRACE A and B is 0.88 mm for the ambiguity-fixed

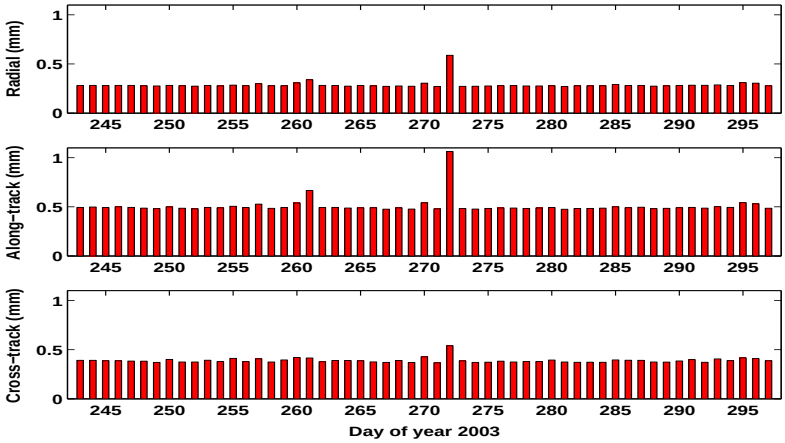

Figure 8.21: Daily mean values of formal errors of orbit positions for GRACE B in the radial (top), along-track (middle), and cross-track (bottom) direction for the ambiguity-fixed baseline solution.

solution, and 6.38 mm for the ambiguity-float solution. In order to gain some insight about the other components, formal orbit accuracies are computed for the fixed solution, and orbit comparisons are analyzed between the fixed and float solutions.

Figure 8.21 shows the daily mean values of the formal errors for the GRACE B reduced-dynamic ambiguity-fixed solution in the radial (top), along-track (middle), and cross-track (bottom) direction. As GRACE A was fixed to the zero difference solution, no corresponding values may be given for GRACE A. Therefore, the displayed values may be interpreted as the mean formal errors of the baseline components. Excluding the outlying solution on DOY 272, see also Fig. 8.17, overall values of 0.28, 0.49, and 0.38 mm result. Keeping in mind that the true along-track precision was found to be 0.88 mm by the K-band validation, the formal accuracies are a little bit too optimistic. It can also be recognized that they do not reflect all the variations that are revealed by the K-band validation in Fig. 8.17 (top). Nevertheless, they seem to indicate that not only the along-track component is determined with a high precision, but also the radial and the cross-track components.

Figure 8.22 shows the daily standard deviations of the orbit differences for GRACE B between the reduced-dynamic ambiguity-float and -fixed solution in the radial (top), along-track (middle), and cross-track (bottom) direction. As GRACE A was fixed to the zero difference solution, no differences occur in the reference orbits. Therefore, the displayed standard deviations may be interpreted as the standard deviations of the differences in the baseline components. The largest values may be observed in the along-track direction with an overall standard deviation of 6.41 mm. Similar as for zero difference orbit determination, see Sect. 7, the along-track component is worst determined for our reduced-dynamic orbits. Assuming that only small correlations are present between the along-track components of both solutions, we may use the true precisions from the K-band validation to compute $\sqrt{6.38^2 + 0.88^2}$ = 6.44 mm, which is in good agreement with the observed standard deviation of 6.41 mm. Therefore, the differences in the along-track component may almost be uniquely attributed to the degradation of the float solution.

The observed overall standard deviations for the radial and cross-track components are 3.00 mm and 1.14 mm, respectively. Assuming similar small correlations as for the along-track component and a

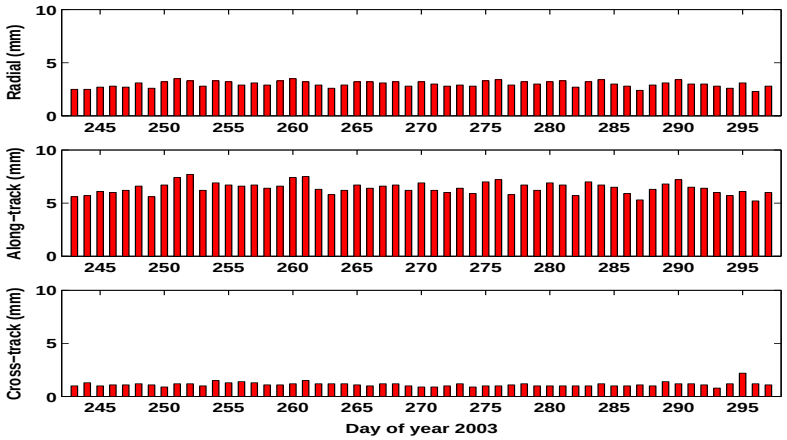

Figure 8.22: Daily standard deviation of orbit differences for GRACE B in the radial (top), along-track (middle), and cross-track (bottom) direction between the ambiguity-float and ambiguity-fixed baseline solution.

more precise ambiguity-fixed solution, the values provide a certain indication about the precision of the ambiguity-float solution for these components. It must be noticed, however, that the differences between both solutions are much smaller than for the along-track component, which shows that resolved space baseline ambiguities predominantly improve the precision of the along-track component.

Similar comparisons may be performed between the ambiguity-fixed reduced-dynamic and kinematic solutions to confirm, e.g., that the radial component is worst determined for the kinematic case. A detailed discussion may be found in [*Kroes*, 2006], which also shows that the overall quality of the kinematic ambiguity-fixed solution is inferior to the reduced-dynamic float solution, although the K-band validation favors the kinematic solution in the along-track direction, compare Figs. 8.17 (bottom) with 8.18 (top).

Figure 8.22 shows standard deviations of orbit differences instead of RMS values to exclude systematic offsets between the ambiguity-fixed and -float solutions. Since the presentation of Fig. 8.6 in Sect. 8.2.1 we know, however, that a systematic offset in the cross-track direction between the two solution types was detected in the analysis of DD solutions with ground network data. Here, the same effect has to be noticed again when analyzing the cross-track orbit differences between the GRACE B ambiguity-float and fixed baseline solutions. For DOY 243–297, 2003 an overall mean value of -0.9 cm results, whereas the effect is suppressed for GRACE A due to the fixing to the zero difference solution. Because the same pattern has to be observed for kinematic and reduced-dynamic solutions, we tend to attributed this to a mismodeling in the GPS observations, as already speculated in Sect. 8.2.1. Because no comparable effect is reported by [*Kroes*, 2006], we can neither exclude a msimodeling in the GPS observations, nor a software or processing bug from our side.

8.4 Summary and Comments

The results presented in this chapter showed that pseudo-stochastic orbit modeling techniques may be applied without substantial changes to doubly differenced GPS observations, as well. The prospect to reduce or eliminate error sources already by forming differenced GPS observables is a clear advantage

of the double difference with respect to the zero difference approach, as well as the chance to resolve the carrier phase ambiguities to their integer values. CPU times for ambiguity-float solutions are no longer an issue thanks to the developments from Chapter 6.

Sections 8.1 and 8.2 showed that about 50 receivers from globally distributed GPS ground sites are sufficient to compute high-quality GRACE reduced-dynamic orbits. The orbit differences due to the baseline selection revealed that a well-balanced number of space-ground baselines between the two GRACE satellites and the ground sites would probably offer the best alignment of the two orbits in an absolute sense. The quality of the relative orbit positions is improved by including the very short space baseline (≈ 220 km) into the processing, especially if the carrier phase ambiguities are resolved to integer values. Resolved space baseline ambiguities were found to significantly improve the relative GRACE orbit positions. A similar statement holds as well for resolved space-ground baseline ambiguities, which are more difficult to correctly fix to integer values due to their length of up to 10 000 km and the (different) quality of the code measurements from the GPS ground receivers. Due to average success-rates below 50%, a clear improvement of the orbit quality in an absolute sense could, unfortunately, not be demonstrated so far. Moreover, CPU times are not yet optimized for an operational resolution of the very large numbers of space-ground baseline ambiguities.

Section 8.3 focused on the space baseline and demonstrated that (sub-)mm precision is feasible for the reduced-dynamic approach with fixed ambiguities and with relative constraints between the pseudo-stochastic orbit parameters of GRACE A and B. The solution strategy is tailored to the special GRACE orbit configuration where both satellites are following each other on the same trajectory. A most precise knowledge of the 3-D inter-satellite vector will be of interest for future satellite formations, as well, e.g., for the planned Synthetic Aperture Radar (SAR) interferometry formation consisting of the TerraSAR-X and TanDEM-X satellites which shall generate highly accurate digital elevation models in a bistatic operation mode [*Moreira et al.,* 2004].

Sections 8.1 and 8.2 reported that systematic differences between orbit solutions based on float and resolved ambiguities were found in the cross-track component. Because the same differences were found for reduced-dynamic and kinematic solutions, we speculated that they might be attributed to a systematic mismodeling of the GPS observations, which reminds us of the GPS phase residual patterns shown in Sect. 7.9.5. Although the displayed residuals were small and difficult to interpret, they revealed a highly systematic pattern which did not seem to change in time. As it is a common practice, e.g., for the orbit determination of the JASON-1 satellite [*Luthcke et al.,* 2003], to simply introduce such empirically determined antenna patterns for POD, we started a very first experiment and determined a very rough correction map out of only two weeks of GRACE data, and repeated our baseline analysis with the correction map taken into account. Obviously, such a “trick” has to formally improve the results, but it was not a priori obvious where this would be seen. It was thus promising to see that the unexplained cross-track offset could be reduced by this measure by about half a centimeter, and that is was only the ambiguity-float solution that changed by taking the correction map into account.

It is too early to draw any hard conclusions from the sketched experiment about the true origin of the discrepancy, but it offers a basis for further investigations based on more reliable correction maps.

9. Analyzing Pseudo-Stochastic Parameters

Chapters 7 and 8 showed that the different types of pseudo-stochastic orbit parameters are well suited for precise LEO POD. Properly tuned, the reduced-dynamic LEO orbits based on continuous GPS tracking data probably offer the most precise reconstruction of the actual LEO trajectories in an only partially known force field. The continuous availability of the strong GPS tracking data was thereby found to be essential, not only for kinematic POD, which would be more difficult under aggravated tracking conditions with only few observations per epoch, but also for the reduced-dynamic approach to ensure a safe estimation of the usually large number of pseudo-stochastic parameters.

The focus of this chapter is no longer on the generation of "the most precise" orbits, but on a possible interpretation of the estimates of the pseudo-stochastic parameters and the related reduced-dynamic orbits. It seems obvious that these estimates have to reflect, at least to a certain extent, the deficiencies of the force field, but the comparisons with accelerometer data in Chapter 7 also indicated limitations about the content of information of pseudo-stochastic parameters, which have to be carefully assessed.

Extensive simulation studies were performed to get insight into the estimation of pseudo-stochastic parameters and the resulting reduced-dynamic orbits. First, we determine the level of the direct interpretability of single acceleration estimates, then we address discretization effects associated with pseudo-stochastic parameters, and finally we analyze reduced-dynamic LEO trajectories with respect to their capability for recovering an entire and unbiased set of gravity field coefficients. Summaries of the simulations may be found in [*Jäggi et al.*, 2006a], [*Jäggi et al.*, 2006b], and [*Jäggi et al.*, 2006d].

9.1 Interpretability of Single Acceleration Estimates

It is convenient to compare pseudo-stochastic parameters with accelerometer measurements, e.g., [*van den IJssel and Visser*, 2005]. A direct comparison, however, has to be interpreted with care as an accelerometer measurement is either a normal point of the raw (pointwise) accelerometer measurements (CHAMP), or a raw accelerometer measurement (GRACE). Piecewise constant or piecewise linear accelerations estimated from GPS data, however, are usually valid for a certain time interval and do rather reflect an "integrated" acceleration than a pointwise acceleration. Depending on the resolution and the type of the solved for accelerations, the estimates represent the pointwise accelerations only approximately at a certain level.

9.1.1 Simulation Scenario

We used the same physical and mathematical models as used and described for the real data processing in Chapter 7 to simulate undifferenced GPS phase observations for the CHAMP satellite. The GPS final orbits and a CHAMP orbit, subsequently denoted as the true CHAMP orbit, were the basis to simulate the error-free GPS data. Thereby, the true CHAMP trajectory was not a particular solution of the equation of motion used in the data processing, but was affected by an additional and artificial

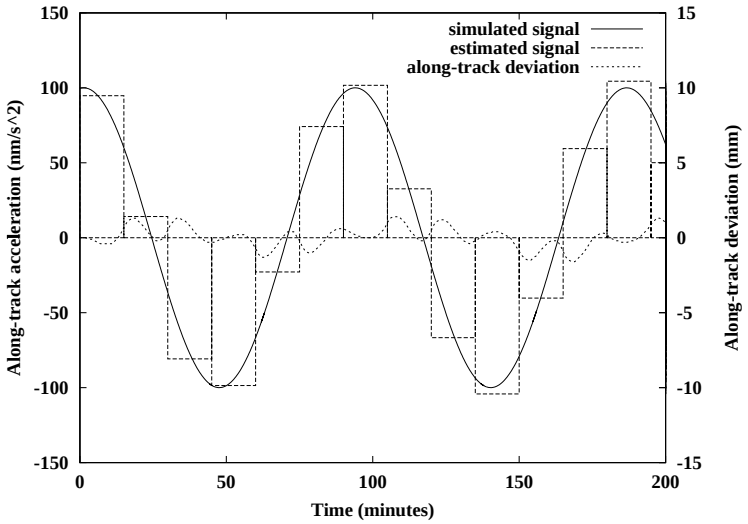

Figure 9.1: Piecewise constant accelerations over 15 min compensate for an unmodeled along-track acceleration (solid line). The dotted curve denotes deviations w.r.t. the true orbit.

once-per-revolution along-track acceleration $S \cos u$, where u denotes the argument of latitude and S an amplitude of 100 nm/s^2. An orbit with identical initial conditions, but not affected by the artificial acceleration, served as the a priori CHAMP orbit for POD with the simulated GPS phase observations.

9.1.2 Orbit and Acceleration Recovery

Pseudo-stochastic parameters were primarily introduced as additional parameters into the equation of motion (5.12) to cope with unmodeled systematic effects, e.g., caused by deficiencies in the force models such as the unmodeled along-track acceleration $S \cos u$ in this simulation. Figure 9.1 shows, for a specific time interval of about two orbital revolutions, how unconstrained piecewise constant accelerations over 15 min compensate for the deficient force model and approximate the once-per-revolution characteristics of the disturbing acceleration. The rather large subinterval length of 15 min was chosen to provoke noticeable discrepancies between the estimated accelerations and the true disturbing acceleration, which are still of minor nature only. The overall characteristics of the once-per-revolution signal may be easily recognized despite the large subinterval length, but a systematic overestimation may be observed as well, e.g., at the symmetrically covered maximum near 185 min. This effect is a consequence of the inability to represent a disturbing acceleration with non-zero curvature by a piece-wise constant model if only GPS SST data are used as observations.

The quality of the orbit recovery is indicated in Fig. 9.1 by the along-track deviations from the true CHAMP orbit. Despite the coarse resolution in time of the piecewise constant accelerations, the along-track orbit deviations are in general below the 2-mm level. The periodic pattern is caused by the inability to fully represent a once-per-revolution acceleration by a piecewise constant model, which in turn shows up as once-per-subinterval and once-per-revolution variations. In accordance with the formal position errors from Fig. 7.12, we note that the largest deviations tend to occur close to the subinterval middles.

Figure 9.2 shows, for the same specific time interval of about two orbital revolutions, how unconstrained and continuous piecewise linear accelerations over 15 min compensate for the deficient force model and

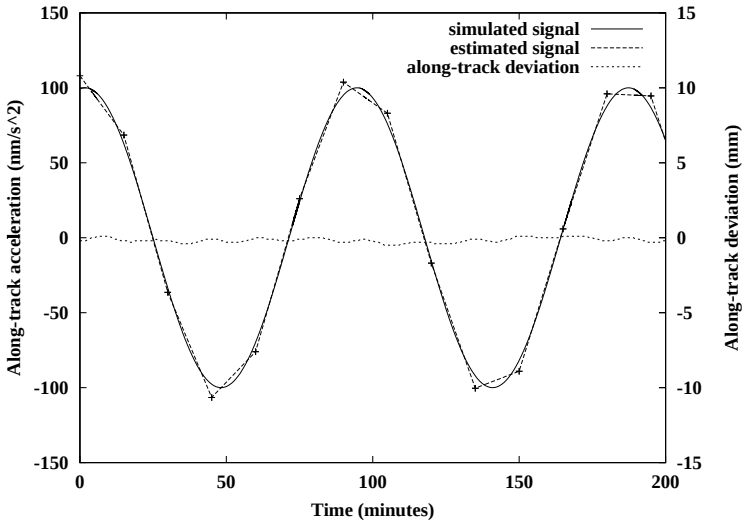

Figure 9.2: Continuous piecewise linear accelerations over 15 min compensate for an unmodeled along-track acceleration (solid line). The dotted curve denotes deviations w.r.t. the true orbit.

approximate the once-per-revolution characteristics of the disturbing acceleration. Despite the rather large subinterval length of 15 min, an almost perfect agreement between the estimated accelerations and the true disturbing acceleration can be recognized. A careful inspection shows that the discrepancies are now of a truly minor nature and only manifest themselves as a small systematic overestimation of the pointwise accelerations at the subinterval boundaries.

The quality of the orbit recovery is also indicated in Fig. 9.2 by the along-track deviations from the true CHAMP orbit. The comparison with Fig. 9.1 shows that the once-per-subinterval and once-per-revolution periodic patterns have been greatly reduced with the consequence that the orbit solution based on piecewise linear accelerations shows no deficiencies at the millimeter level. The estimation of only one more parameter in the along-track direction thus resulted in a considerable relative improvement of the orbit quality. The gain is, however, very small on an absolute scale.

Approximative Method

One might try to estimate the best fitting amplitude S of a function $f(t)\,\boldsymbol{e}(t)$ from previously estimated piecewise constant accelerations A_i pointing into the direction $\boldsymbol{e}(t)$ in a separate parameter estimation problem. In this simulation, $f(t)$ would be identified with $\cos u$ and $\boldsymbol{e}(t)$ would be identified with the along-track direction, which yields a pseudo-correction equation

$$\epsilon_i = \frac{\partial A_i}{\partial S} \cdot s - a_i \tag{9.1}$$

for each acceleration correction a_i with the corresponding residual ϵ_i. In view of approximating the function $S\,f(t)$ piecewise with Taylor series of degree zero, the partial derivatives necessary for evaluating (9.1) would intuitively be written as

$$\frac{\partial A_i}{\partial S} \doteq f(t_{m_i}) \qquad \text{with} \qquad t_{m_i} \doteq \frac{1}{2}(t_{i-1} + t_i)\ . \tag{9.2}$$

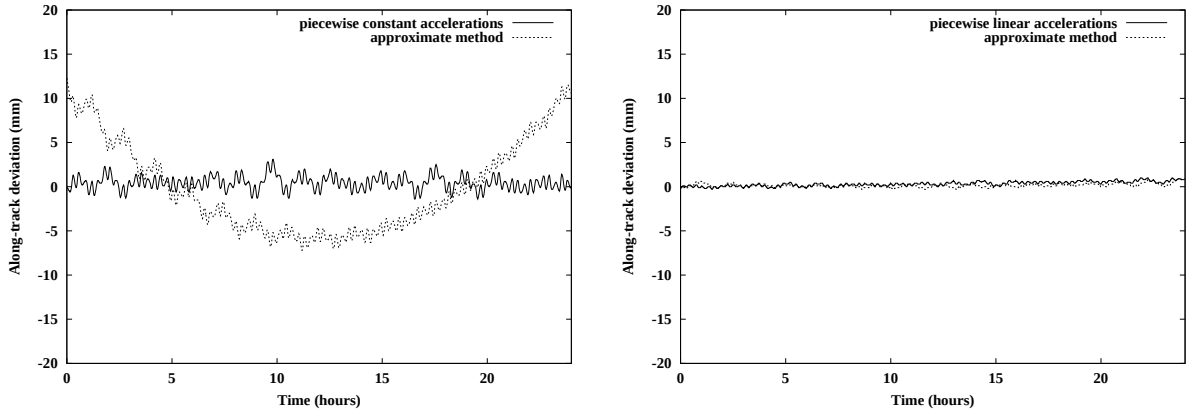

Figure 9.3: Along-track deviations w.r.t. the true orbit due to piecewise constant accelerations (left) and due to piecewise linear accelerations (right).

The relations (9.1) and (9.2) implicitly define an approximate transformation between the "initially" estimated piecewise constant accelerations A_i and the amplitude S of the function $f(t)$. The transformation could thus be already incorporated into the original POD process, which would be attractive in view of the computation of the partial derivatives $\boldsymbol{z}_S$ of the a priori orbit $\boldsymbol{r}_0(t)$ as a direct computation would be unnecessary. Instead, $\boldsymbol{z}_S$ could be computed as a function of the m partial derivatives $\boldsymbol{z}_{A_i}$ with respect to the accelerations A_i as

$$\boldsymbol{z}_S(t) = \sum_{i=1}^{m} \boldsymbol{z}_{A_i}(t) \cdot \frac{\partial A_i}{\partial S} \,, \tag{9.3}$$

where the partial derivatives $\boldsymbol{z}_{A_i}$ would be efficiently at hand according to Chapter 5.

An estimation of the amplitude S with (9.1), or alternatively with (9.3), leads to the overestimation of the true disturbing acceleration as noted, e.g., in Fig. 9.1. The amplitude of the true once-per-revolution signal is apparently overestimated by about 4% for piecewise constant accelerations and by about 0.07% for continuous piecewise linear accelerations. The main reason for this is that the partial derivatives (9.2) are correct only up to terms of order zero in the length of the subintervals, which implies that the attempt to relate a single pseudo-stochastic parameter A_i directly to the pointwise acceleration may introduce comparably large model errors. For piecewise constant accelerations, an error level of a few percent is generally too large to be acceptable for most applications as shown in Sect. 7.8.4, where a combination with precise accelerometer measurements was studied. It must be mentioned, however, that results from comparisons with accelerometer data as shown in Sect. 7.8.3 are not that much affected, if the partial derivatives are taken from the accelerometer data.

Figure 9.3 confirms the introduction of model errors and shows the along-track orbit deviations from the true orbit emerging from the original parameter estimation and from the parameter estimation according to (9.3) for piecewise constant (left) and piecewise linear (right) accelerations. An unacceptable deterioration of the orbit quality due to a residual acceleration may be immediately recognized for the approximate solution with piecewise constant accelerations. Although the approach clearly fails for piecewise constant accelerations over 15 min, it is interesting to note that piecewise linear accelerations may be directly related to pointwise accelerations without introducing noticeable orbit errors. It is subject to further investigations whether this would still be the case if the true acceleration was affected by more rapid than once-per-revolution oscillations.

9.2 Interpretability of Reduced-Dynamic Trajectories

Figure 9.3 showed that the recovered orbits are of high quality for both pseudo-stochastic acceleration models. Even for piecewise constant accelerations with a modest time resolution the orbit errors are below the 2-mm level, implying that the "discretization" errors introduced by pseudo-stochastic accelerations must be much smaller than the few percent level suggested by the analysis of a single acceleration estimate. In order to make better use of the results achieved with pseudo-stochastic parameters, it is necessary to perform either an integrated analysis of all acceleration estimates or, alternatively, an analysis of the recovered orbit trajectory. Because the stochastic model of orbit positions, e.g., from kinematic orbits, is better described by a white noise process than the stochastic model of orbit accelerations [*Ditmar et al.*, 2004], we confine ourselves in this chapter to the analysis and interpretation of orbit positions.

9.2.1 Orbit Reparametrization

Let us now introduce a new set of $\tilde{n}$ orbit parameters $\tilde{P}_1, ..., \tilde{P}_{\tilde{n}}$. In order to simply reparametrize the orbit determination after having solved for the pseudo-stochastic parameter corrections $p_1, ..., p_n$, we may use the orbital positions $\boldsymbol{r}(t_{m_i})$ established so far as pseudo-observations in a new orbit determination process to solve for the parameter corrections $\tilde{p}_1, ..., \tilde{p}_{\tilde{n}}$. The correction equations read as

$$\boldsymbol{\epsilon}_{\boldsymbol{r}_i} = \sum_{k=1}^{\tilde{n}} \frac{\partial \boldsymbol{r}_0(t_{m_i})}{\partial \tilde{P}_k} \cdot \tilde{p}_k - \delta \boldsymbol{r}(t_{m_i}) \tag{9.4}$$

with

$$\delta \boldsymbol{r}(t_{m_i}) \doteq \sum_{l=1}^{n} \frac{\partial \boldsymbol{r}_0(t_{m_i})}{\partial P_l} \cdot p_l \tag{9.5}$$

being the orbit improvements of the previously performed reduced-dynamic orbit determination and $\boldsymbol{\epsilon}_{\boldsymbol{r}_i}$ the residuals of the new orbit determination problem. Thereby some parameters $\tilde{P}_k$ may be identical to the reduced-dynamic orbit determination, e.g., the initial osculating elements, whereas others are replaced. Typically, the pseudo-stochastic representation is substituted by a physical representation accounting for force field deficiencies, e.g., a series of spherical harmonic coefficients representing the Earth's gravity field according to Chapter 3, or scaling factors for non-gravitational force models.

The main advantage of a two-step method as defined by (9.4) and (9.5) is that the GPS-based LEO orbit determination, typically performed on a daily basis, may be completely separated from the physical interpretation of (many) LEO trajectories. Kinematic CHAMP positions computed by [*Švehla and Rothacher*, 2003c], e.g., received much attention for subsequent global gravity field recovery and have been successfully used by many research institutions in conjunction with a broad variety of gravity field recovery methods as mentioned in Chapter 3. Because kinematic LEO positions are computed independently from force models, it seems a priori obvious that they are well suited for gravity field recovery, but not reduced-dynamic LEO positions [*Gerlach et al.*, 2003c]. Whether or not reduced-dynamic LEO positions might be used for the same purpose depends on the parametrizations used in (9.5) as pointed out by [*Jäggi et al.*, 2006b] and [*Jäggi et al.*, 2006d]. We postpone this discussion to Sect. 9.5, where it will be shown under which conditions reduced-dynamic orbits might be used for global gravity field recovery.

Finally, it has to be mentioned that a physical interpretation of LEO trajectories with (9.4) and (9.5) is not completely equivalent to a direct estimation of the parameter corrections $\tilde{p}_1, ..., \tilde{p}_{\tilde{n}}$ from the GPS

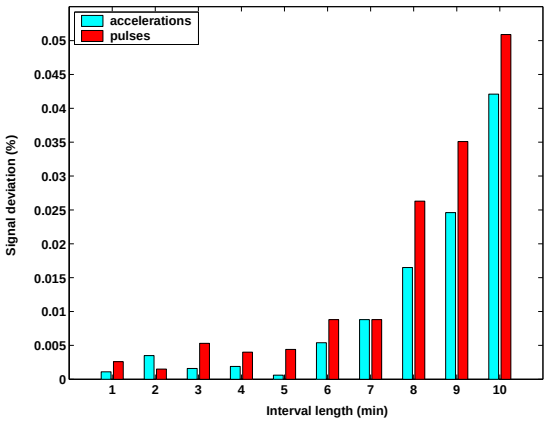

Figure 9.4: Deviations (%) of a recovery of the term $C_{6,3}$ with reduced-dynamic orbit positions.

observations. Even if the pseudo-observations $\boldsymbol{r}(t_{m_i})$ actually contain the information to be recovered, a (small) degradation has to be expected, if the correlations between the pseudo-observations are neglected.

9.2.2 Simulation Scenario

We performed a similar simulation as described in Sect. 9.1.1 in order to estimate the level of the "discretization" errors introduced by pseudo-stochastic parameters. A true CHAMP orbit was computed in a true gravity field (complete up to degree 45) and was used to simulate error-free CHAMP orbit positions every 10 s. The same gravity field model, but with one arbitrarily selected geopotential term ($C_{6,3}$) set to zero, was used for POD with unconstrained pseudo-stochastic parameters to simulate the CHAMP pseudo-observations. In analogy to Sect. 9.1.2, the pseudo-stochastic orbit parameters had to compensate for an unmodeled signal of a comparable amplitude (57 nm/s^2), but with a principal period of one sixth of the orbital period (≈ 15 min).

9.2.3 Acceleration Recovery

The CHAMP pseudo-observations were used to recover the amplitude of the unmodeled geopotential term $C_{6,3}$ according to (9.4) and (9.5). Figure 9.4 shows the deviations of the recovered amplitude with respect to the true value for different subinterval lengths of pulses and piecewise constant accelerations. In general, the recovery is slightly better for orbital positions derived from accelerations than from pulses. The difference between the two parametrizations, however, is rather small, if only one force field parameter has to be recovered.

The recovery errors shown in Fig. 9.4 may be interpreted as the pure discretization errors of pseudo-stochastic parameters, if the subinterval lengths are well below half of the shortest period of the signal to be recovered. It is encouraging to see that a deviation of about 0.002% would result in the situation comparable to Sect. 9.1.2, i.e., at a subinterval length of 2.5 min, which is much better than the few percent level found in Sect. 9.1.2. This implies that the signal amplitude can be recovered with a quality almost comparable to a direct estimation of the parameter, and that pseudo-stochastic parameters preserve the information about a deficient force field very well, if they are set up with an "appropriate" spacing.

Remark concerning the Approximative Method

Let us assume that we only consider pseudo-observations $\boldsymbol{r}(t_{m_i})$ referring to the midpoints of previously estimated pseudo-stochastic accelerations. Starting with the second time derivative of (9.4), we can illustrate additional assumptions implicitly made for the approximative method presented in Sect. 9.1.2. For the special case of estimating one correction s to the amplitude of the known function $f(t)\,\boldsymbol{e}(t)$, the correction equation (9.4) reads at time t_{m_i} as

$$\boldsymbol{\epsilon}_i = \ddot{\boldsymbol{z}}_S \cdot s - \sum_{l=1}^{n} \ddot{\boldsymbol{z}}_{A_l} \cdot a_l \ . \tag{9.6}$$

In order to eventually obtain (9.1), we replace all partial derivatives in (9.6) by the leading term of (5.8), which then read at time t_{m_i} as

$$\ddot{\boldsymbol{z}}_S \approx \frac{\partial \boldsymbol{f}_1}{\partial S} \qquad \text{and} \qquad \ddot{\boldsymbol{z}}_{A_l} \approx \begin{cases} \frac{\partial \boldsymbol{f}_1}{\partial A_l} & ; \quad l = i \\ \boldsymbol{0} & ; \quad l \neq i \end{cases} \ , \tag{9.7}$$

where $\boldsymbol{f}_1(t_{m_i}) = A_i\,\boldsymbol{e}(t_{m_i})$. This finally leads to

$$\epsilon_i\,\boldsymbol{e}(t_{m_i}) = \frac{\partial A_i}{\partial S} \cdot s\,\boldsymbol{e}(t_{m_i}) - a_i\,\boldsymbol{e}(t_{m_i}) \ , \tag{9.8}$$

which is identical to the relation (9.1), but formulated in the inertial system.

9.3 Highly Reduced-Dynamic Trajectories

Highly reduced-dynamic (HRD) LEO orbits are reduced-dynamic orbits with pseudo-stochastic parameters set up with a frequency close to the GPS observation sampling rate. Typical subinterval lengths thus range from only 10 s to about 60 s if GPS observations are available every 10 s, which is, e.g., the case for the BlackJack receivers aboard CHAMP and the two GRACE satellites. The developments in Chapter 6 showed, however, that the computational burden heavily increases for large numbers of pseudo-stochastic parameters in a conventional processing of the normal equation systems associated with HRD orbits. Thanks to the estimation scheme based on the rapid solution strategy presented in Sect. 6.3, it is still feasible to compute HRD orbits with any subinterval lengths of pseudo-stochastic parameters with reasonably short CPU times (see Fig. 6.6).

CHAMP data from DOY 198, 2002 were used to compute kinematic and HRD orbits with different parameter spacings. Figure 9.5 (left) shows the cross-track differences of the kinematic and of two HRD orbits with respect to a "conventional" reduced-dynamic CHAMP orbit based on piecewise constant accelerations over six minutes. Both HRD orbits are represented by six initial conditions and three unconstrained pulses set up every minute and every three minutes, respectively. As expected, the HRD orbits are already fairly close to the kinematic orbit due to the "heavy" parametrization. The 1-minute HRD orbit is actually almost identical to the kinematic orbit. Compared to conventional reduced-dynamic orbits, the "smoothing" effect of reduced-dynamic trajectories is greatly suppressed for HRD orbits and only occasionally visible, e.g., for the 3-minute HRD orbit around 15:31:00 and 15:33:00. The GPS phase breaks occurring there can be "bridged" to some extent by the HRD orbit solution based on 3-minute subintervals, and is thus less affected by artificial jumps than the other solutions, if new phase bias parameters have to be set up at a certain epoch for all GPS satellites. Similar patterns may be found in the radial and along-track directions as well, but they are not as clearly visible due to more pronounced once-per-revolution oscillations with respect to the conventional reduced-dynamic orbit.

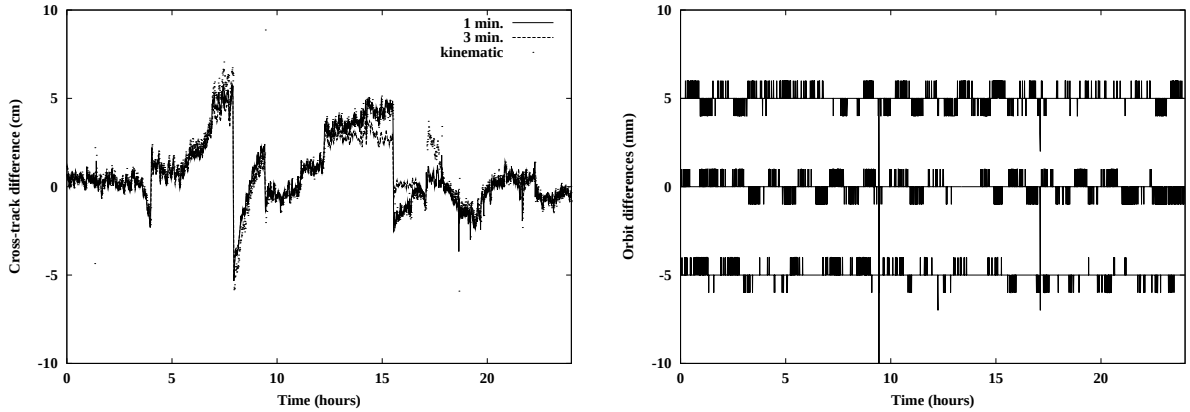

Figure 9.5: Cross-track differences of a kinematic and two HRD orbits w.r.t. a conventional reduced-dynamic orbit (left) and differences (radial/cross-track shifted by ± 5 mm) between the kinematic and the MRD orbit (right).

9.3.1 Properties of Maximum Reduced-Dynamic Trajectories

Maximum reduced-dynamic (MRD) LEO orbits are a special case of highly reduced-dynamic LEO orbits with pseudo-stochastic parameters set up at a frequency equal to the GPS observation sampling rate. This setting corresponds to the shortest possible subinterval length that still results in a regular normal equation system for reduced-dynamic LEO orbit determination. In order to illustrate the close relationship between MRD orbits and a kinematic orbit, we consider the MRD orbit based on pulses from Fig. 9.5 (right). There, three unconstrained pulses are set up at all n_{obs} observation epochs, except for the very first and the very last one where no pulses can be estimated from the GPS data. Together with the six initial conditions a total number of $3\,n_{obs}$ orbit parameters are estimated, which is obviously the same number of unknown orbit parameters as for a kinematic orbit determination. Provided that at least four GPS observations are available for every observation epoch when processing undifferenced data, all epoch parameters can be estimated for both approaches, which are the three pulses and the three kinematic coordinates for the MRD and the kinematic orbit determination, respectively, and one receiver clock correction. Both orbit ephemerides are thus equivalent at the observation epochs despite the different parameter types used for the two approaches. The characteristic pattern in Fig. 9.5 (right) results from the restriction to 1-mm precision in the SP3 orbit file format [*Remondi*, 1991].

Figure 9.6 (top) illustrates the characteristics of a MRD trajectory based on unconstrained pulses and kinematic positions estimated for each observation epoch. If we assume to have at least four error-free GPS observations at our disposal at each measurement epoch, we could reconstruct the true orbit trajectory in the kinematic mode at these discrete epochs without errors. The same statement is also valid for the MRD orbit based on pulses if the same assumptions hold. The only difference between both trajectories resides at times in-between the observation epochs. Whereas a kinematic orbit yields position estimates only at the (discrete) observation epochs, the MRD orbit is defined throughout the entire orbital arc. The positions at the left and at the right boundary epochs of each subinterval provide the necessary six conditions to define a trajectory between these two points, which solves the equation of motion (5.12). It must be emphasized that the positions at the observation epochs are completely independent from the force models like in the kinematic case, but that the trajectory in-between fully reflects the a priori force models, if pulses are used as pseudo-stochastic parameters. Despite the maximum resolution of

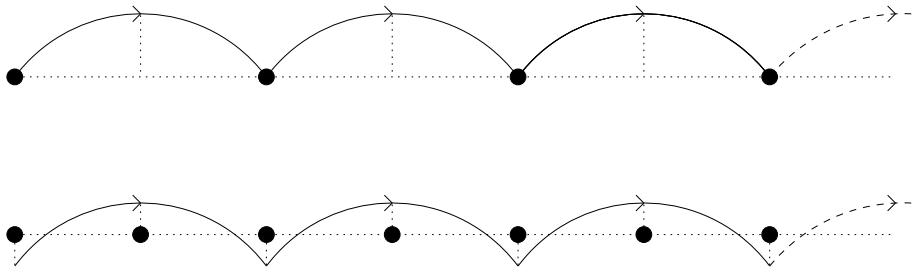

Figure 9.6: MRD orbit (solid line) based on pulses in comparison with the true orbit (dotted line) and kinematic positions (circles) (top) and the impact of an increased sampling rate (bottom).

pseudo-stochastic pulses (or accelerations, see below), orbital velocities or orbital accelerations derived from MRD orbits do not provide independent information concerning the force field. This statement is important when the recovery of force field parameters is addressed.

If there are less than four GPS observations available at a certain measurement epoch, it is not possible to estimate all epoch parameters when processing undifferenced data. Whereas no position can be estimated at all for a kinematic solution, not all pulses can be estimated for a MRD orbit at such "problematic" epochs, but the MRD trajectory is still defined throughout the entire orbital arc. As a consequence, however, the estimated positions may differ at the neighboring epochs because the filtering due to the dynamic orbit model starts to affect the MRD orbit around the "problematic" epochs. This is also the reason for the observed deviations between the kinematic and the MRD orbit from Fig. 9.5 (right), where the largest ones occur at 09:25:30 and 09:26:30, and at 17:05:30 and 17:07:00. Usually this effect is limited to the neighboring epochs of the "problematic" intervals only, but sometimes it may propagate further and affect more epochs than just the neighboring ones.

The close relationship between MRD orbits and a kinematic orbit holds as well if acceleration parameters instead of pulses are set up. If, e.g., three unconstrained piecewise constant accelerations are set up for all $n_{obs} - 1$ observation intervals, except for the very first one where no accelerations can be estimated from the GPS data due to a full correlation with the initial conditions, a total number of $3\,n_{obs}$ orbit parameters are estimated together with the six initial conditions. Again, both ephemerides are equivalent at the observation epochs.

Transition between MRD and HRD Trajectories

The transition between MRD and HRD orbits is accomplished by decreasing the number of pseudo-stochastic parameters, by introducing constraints, or by increasing the sampling rate of the observations to be processed. As the subinterval length of pseudo-stochastic parameters (and the constraints) will play a most important role for the recovery of force field parameters, we focus in the following on the case of increasing the sampling rate of the observations to be processed. Figure 9.6 illustrates the transition from a MRD orbit based on unconstrained pulses (top) to an identically parametrized HRD orbit based on a higher observation sampling rate (bottom). The main difference between both trajectories resides in the arcs between the pulse-epochs, which rather reflect the true orbit due to the additional observations. The obtained orbital positions from the HRD orbit differ from the kinematic positions estimated at the observation epochs because the filtering due to the dynamic orbit model affects the bottom trajectory over the entire orbital arc. It is important to note that this is also the case for the HRD orbit positions

at the pulse epochs. Unlike a maximum reduced-dynamic orbit, where the positions at the observation epochs are independent from the force models, the positions of highly reduced-dynamic orbits depend on the applied force models, even if the same resolution of pseudo-stochastic parameters is used.

There would be no need to study HRD LEO orbits in an error-free environment where the true trajectory could be perfectly reconstructed by kinematic positions obtained from error-free GPS observables. Real-world kinematic LEO orbit positions are governed, however, by a considerable noise component [*Ditmar et al.*, 2004], which might be a nuisance when using them for gravity field recovery. This is the main motivation for considering highly reduced-dynamic LEO orbits as alternative. There is the chance to reduce the position (and velocity) noise and to improve the gravity field coefficients. Sections 9.4 and 9.5 present simulation studies which shall show on which level benefits may be expected.

9.4 Analysis of HRD Orbit Positions and Velocities

Highly reduced-dynamic trajectories are filtered due to the underlying dynamic orbit model, whereas kinematic orbit positions reflect the unfiltered (discrete) positions solely defined by the GPS observations. The characteristics of a HRD orbit heavily depends on the type and number of the estimated pseudo-stochastic orbit parameters with their (optionally defined) constraints, and to some extent on the underlying dynamic orbit model and the processed observation sampling rate. Depending on the settings used for HRD orbit determination, trajectories with strongly reduced position- and velocity-noise may be obtained similar to the case of conventional reduced-dynamic orbit determination. [*Gerlach et al.*, 2003c] already showed, however, that conventional reduced-dynamic orbits heavily reflect the underlying force models. An interpretation of HRD orbit positions or velocities for independent information about the force field has thus to be made with utmost care as any noise reduction is always obtained on the cost of introducing a priori information from the underlying dynamic models.

9.4.1 Simulation Scenario

We used the same physical and mathematical models as used and described for the real data processing in Chapter 7 to simulate undifferenced GPS observations for the CHAMP satellite with 10 s sampling or, alternatively, with 30 s sampling. The GPS final orbits and a particular CHAMP orbit, subsequently denoted as the true CHAMP orbit, were the basis to simulate GPS code and phase data. The GPS code observations were affected by a white noise of 0.1 m RMS error and the GPS phase observations were simulated either error-free or, alternatively, with a white noise of 1 mm RMS error. Thereby, the true CHAMP trajectory was a particular solution of the equation of motion given by the EIGEN-2 gravity field model up to degree and order 120 without inclusion of any non-gravitational forces. An orbit obtained from the processing of the simulated code observations (see Sect. 7.5) served as the a priori CHAMP orbit for POD with the simulated GPS phase observations. The complete EIGEN-2 gravity field model up to degree 120 or, alternatively, a modified gravity field model was used as (poor) a priori model for the HRD orbit determination. The modified model was the EIGEN-2 model truncated after degree and order 20 and the remaining spherical harmonic coefficients were modified by applying random errors corresponding to the RMS errors of the EIGEN-2 terms.

The most realistic HRD orbit and velocity reconstruction is of course obtained when all error sources are switched on. It is instructive, however, to either switch off the GPS phase observation noise or the a priori gravity field errors in order to study the different impacts of both random and systematic errors on the HRD orbital positions and velocities. Solutions without errors are useful for software tests.

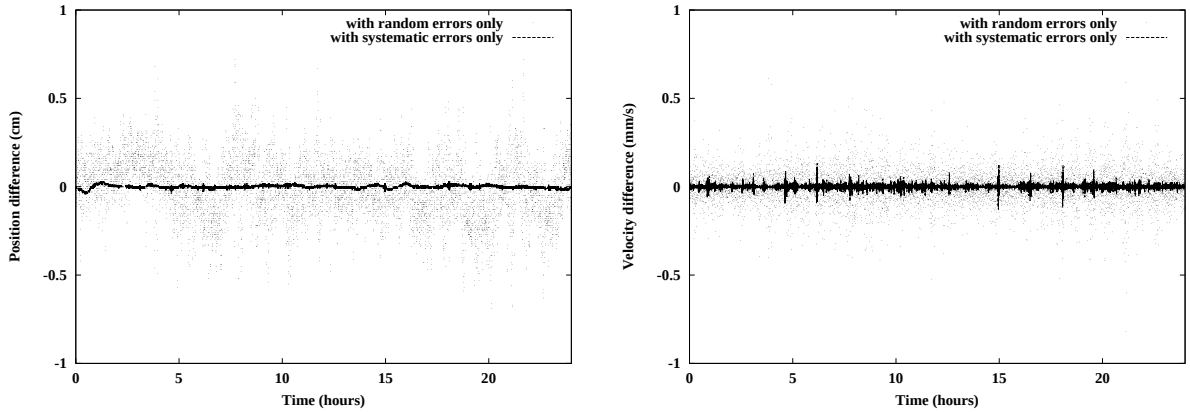

Figure 9.7: Position differences (left) and velocity differences (right) w.r.t. the true CHAMP orbit obtained from HRD orbit determination in the presence of random errors only or systematic gravity field model errors only.

9.4.2 Orbit and Velocity Reconstruction

Figure 9.7 shows position differences (left) and velocity differences (right) in one specific coordinate in the Earth-fixed reference frame with respect to the true CHAMP orbit for a HRD orbit determination based on 10 s GPS data sampling with unconstrained piecewise constant accelerations estimated over 30 s. Both solutions are either affected by the GPS phase white noise random errors only, which is subsequently denoted as a solution of type (N), or by the systematic a priori gravity field model errors only, which is subsequently denoted as a solution of type (A). The differences in the other coordinate directions are of the same nature and are thus not displayed.

The scatter in the position differences of solution (N) is uniquely caused by the 1 mm GPS phase white noise RMS error, although it is not white but colored due to the phase biases. As the estimated phase biases are not identical with the true values due to the phase noise, they introduce a correlation in the position differences, which is visible as the long wavelength variation which would vanish if the ambiguities could be fixed to integer values with zero difference observations.

Despite the poorly known a priori gravity field model used for POD, the position differences of solution (A) exhibit a RMS error of 0.1 mm only, which is much smaller than the noise-induced differences of solution (N) with a RMS error of 1.6 mm. Obviously, the piecewise constant accelerations compensate to a large extent for the mismodeling in the a priori force models. The remaining differences are very small and only visible as very small short-term variations in Fig. 9.7 (left). The observed longer wavelength variations are of a different origin as they are caused by the linearization of the observation equations (4.3) and (4.5). The coarse a priori orbit obtained with the poor a priori gravity model is slightly out of the linearity domain, which makes it necessary to iterate the orbit determination process if this effect should be avoided.

Figure 9.7 (right) shows that the same comparison may look slightly different on the velocity level. The velocity differences of solution (A) exhibit a RMS error of 0.012 mm/s, which is not that much smaller than the noise-induced differences of solution (N) with a RMS error of 0.093 mm/s. It can be furthermore recognized that a characteristic pattern due to the mismodeling in the a priori force models is more clearly visible on the velocity level, e.g., as some larger spikes that occasionally occur. On the other

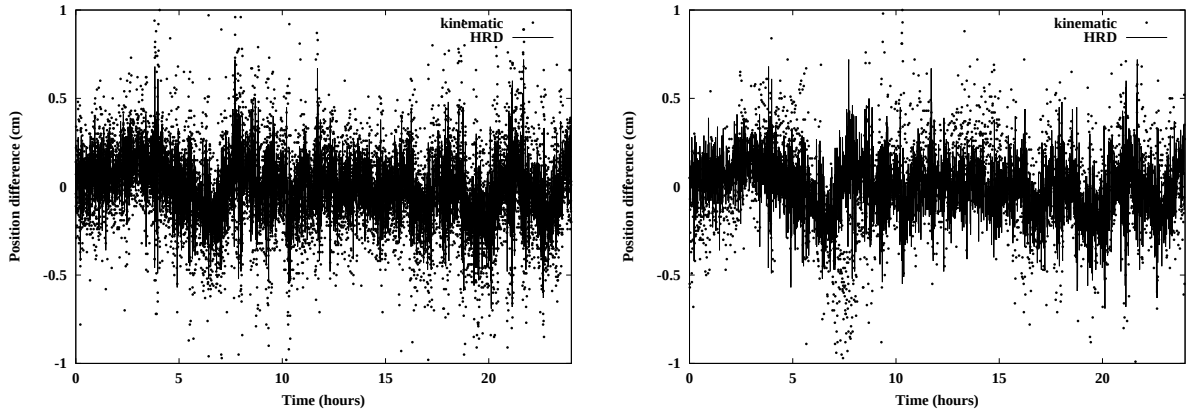

Figure 9.8: Position differences for a HRD orbit and 10 s kinematic (left) and 30 s kinematic (right) orbits w.r.t. the true CHAMP orbit in the presence of random errors only.

hand, all long wavelength features from Fig. 9.7 (left) have disappeared on the velocity level due to the time differentiation.

Comparison with Kinematic Orbits

It is important to compare HRD orbits with kinematic orbits in order to identify advantages and disadvantages of both types of orbits. Figure 9.8 shows the impact of the GPS phase white noise random errors on the position differences with respect to the true CHAMP orbit for the same promising HRD orbit from Fig. 9.7 based on 10 s GPS data sampling and unconstrained piecewise constant accelerations estimated over 30 s, and for kinematic orbits based on 10 s GPS data sampling (left) and 30 s GPS data sampling (right). It can be recognized that the HRD position differences exhibit a reduced scatter of 1.6 mm RMS error with respect to the kinematic solutions which exhibit RMS errors of 2.6 mm and 2.9 mm for the 10 s and 30 s GPS data sampling, respectively. The better performance for the HRD orbit of approximately $\sqrt{3}$ has to be expected as the 30 s piecewise constant accelerations have a smoothing effect on the resulting trajectory. It must be admitted, however, that the comparison from Fig. 9.8 (right) is not completely fair as not the same amount of data was used for POD. This is also the reason for the more pronounced long wavelength features which are only present in the 30 s kinematic orbit from Fig. 9.8 (right) due to the slightly weaker determined phase biases.

The reduced noise of HRD orbital positions (and velocities) with respect to positions from a kinematic point positioning is the main motivation to investigate whether HRD orbits might serve as a suitable alternative product to kinematic orbits for deriving more precise information about the force field. It is encouraging to see the small impact of the systematic errors (Fig. 9.7 (left)) of a deficient a priori gravity field model on the estimated HRD orbit positions. On the other hand, the velocity differences from Fig. 9.7 (right) also indicate that the almost negligible position differences might suggest a too simplistic view. Obviously, it is necessary to analyze the orbital positions and velocities with better diagnostic tools such as Fourier analysis to achieve meaningful conclusions.

A second motivation to investigate HRD orbit determination for gravity field recovery are the HRD orbital velocities which may readily be computed from the estimated orbit parameters. As opposed to the kinematic case, no cumbersome empirical derivation of velocities is necessary [*Földváry et al.*, 2004].

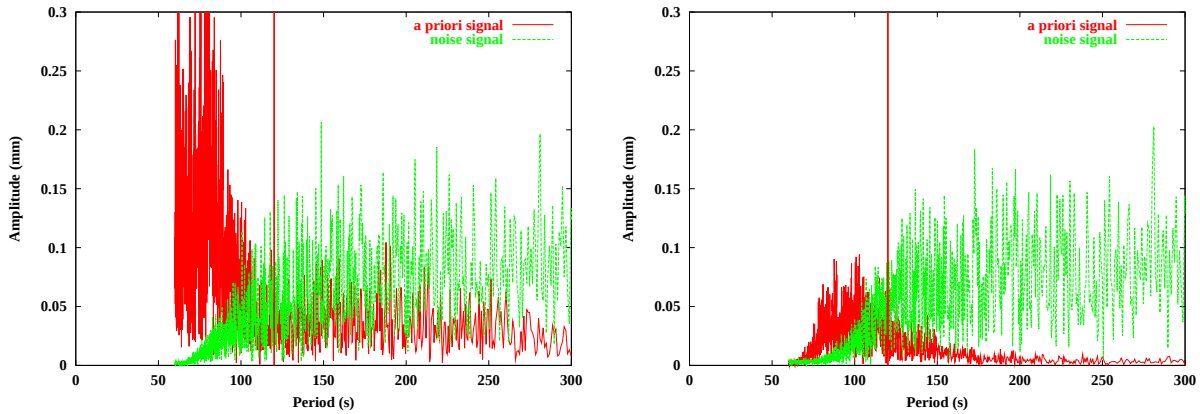

Figure 9.9: Amplitude spectra of position differences w.r.t. the true CHAMP orbit obtained from HRD orbit determination with pulses (left) and accelerations (right) in the presence of random errors only (solution (N)) or systematic a priori gravity field model errors only (solution (A)).

9.4.3 Fourier Analysis of HRD Orbit Positions

Figure 9.9 shows amplitude spectra of position differences in one specific coordinate in the Earth-fixed reference frame with respect to the true CHAMP orbit for a HRD orbit determination based on 30 s GPS data sampling with unconstrained pulses estimated every 60 s (left) and unconstrained piecewise constant accelerations estimated over 60 s (right). The two amplitude spectra of each figure are either affected by the GPS phase white noise random errors only or by the systematic a priori gravity field model errors only, and demonstrate the different impact of both error sources on HRD orbits.

The amplitude spectra of the position differences of solution (N) are almost identical for both types of pseudo-stochastic parameters with a strongly reduced position noise in the highest frequency range due to the smoothing effect of reduced-dynamic orbit determination. The amplitude spectra of solution (A), however, differ significantly for the two orbit parametrizations. The most striking difference is observed for periods shorter than twice the subinterval length of $2 \cdot 60\,\mathrm{s} = 120\,\mathrm{s}$ (indicated by a vertical line), where large amplitudes dominate the spectrum of the pulse solution. This part of the spectrum is also responsible for the fact that the position differences of the pulse solution (A) exhibit a RMS error of 2.5 mm in the time domain, which is even slightly larger than the noise-induced differences of the pulse solution (N) with a RMS error of 2.4 mm. The acceleration solution (A) does exceed the amplitude spectrum of the acceleration solution (N), as well, for periods shorter than twice the subinterval length, implying that the a priori gravity field induced signal amplitudes exceed the apparent amplitudes caused by the observation noise, but the dependency on the a priori gravity field model is greatly reduced with respect to the corresponding solution with pulses, because the unmodeled gravity field signals can be absorbed to a great extent by the piecewise constant accelerations.

Figure 9.9 shows that the total amplitude spectra of HRD orbits are dominated by the a priori gravity field model for periods shorter than twice the subinterval length. Moreover, it can be recognized that the impact of the a priori gravity field model is not only restricted to these short periods as one might expect from an ideal filter, but also leaks into the lower frequency range. This becomes in particular obvious in Fig. 9.9 (left) for the pulse solution where a significant signal is present over the entire range of periods. A much better behavior is observed when piecewise constant accelerations are used.

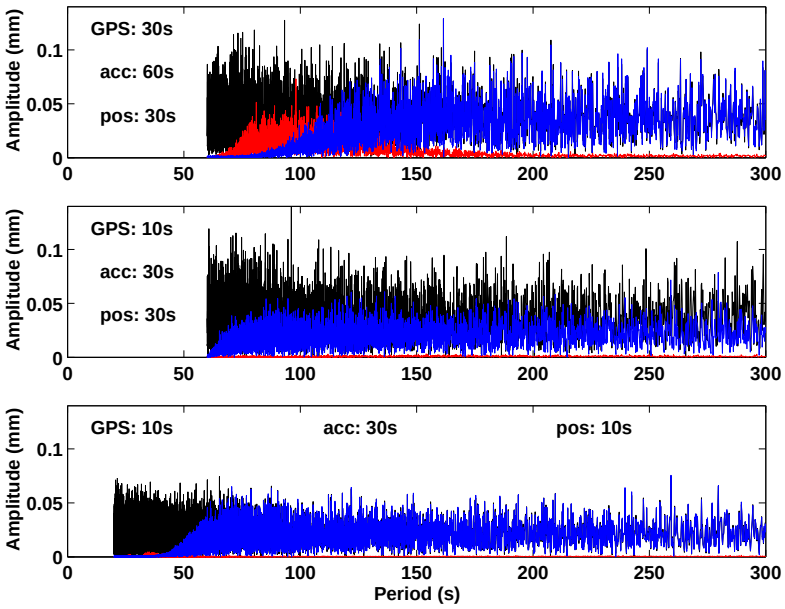

Figure 9.10: Amplitude spectra of position differences w.r.t. the true CHAMP orbit obtained from kinematic (black) or HRD orbit determination in the presence of random (dark grey) or systematic (light grey) errors.

Comparison with Kinematic Orbits

It is interesting to compare the amplitude spectra of the different HRD orbits from Fig. 9.9 with the amplitude spectra obtained from kinematic orbits, which are, by definition, free of a priori gravity field model errors. Figure 9.10 (top) puts amplitude spectra analogue to Fig. 9.9 (right) into relation with the amplitude spectrum obtained from a kinematic orbit based on 30 s GPS data sampling for an extended simulation covering four adjacent days. As expected, the position differences with respect to the true CHAMP orbit from a kinematic point positioning exhibit a mostly white spectrum over the displayed frequency range. Deviations from a white noise process are only expected for the very low frequency range with periods larger than 300 s due to the long wavelength features shown in Fig. 9.8 (right). It can be further recognized that the amplitude spectra of the kinematic orbit and of the HRD solution (N) are essentially identical for periods larger than 150 s. This implies that the reduced noise of HRD orbital positions is only due to the suppression of the high-frequency noise by the reduced-dynamic filtering. An appropriate subinterval length of pseudo-stochastic parameters is thus of utmost importance to balance the aimed at reduction of position noise (solution (N)) and to only allow for a minimal influence of the a priori gravity field model (solution (A)). Although a subinterval length of 60 s still contains too much signal from the a priori gravity field model, it is encouraging to note that there exists a small frequency range between 120 s (twice the subinterval length) and 150 s where the HRD solution exhibits a smaller total signal than the kinematic solution.

The amplitude spectra of solutions (N) and (A) for the promising HRD orbit from Fig. 9.7 based on 10 s GPS data sampling and unconstrained accelerations over 30 s are shown for the same simulation period in Fig. 9.10 (bottom, middle) together with the amplitude spectrum obtained from a kinematic orbit based on 10 s GPS data sampling. The bottom part shows the spectra obtained from the 10 s position sampling

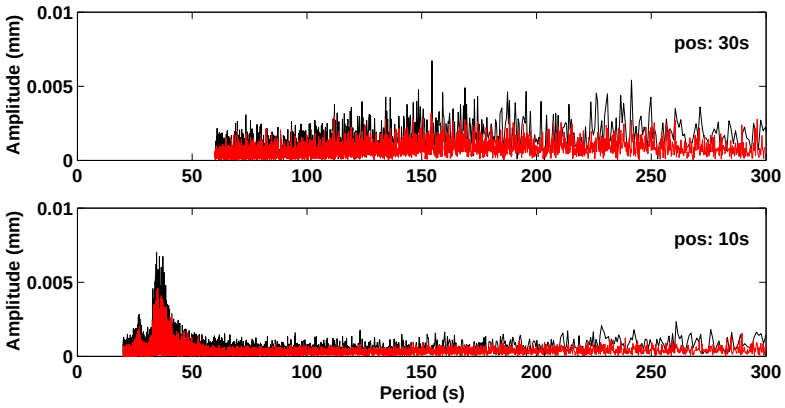

Figure 9.11: Amplitude spectra of position differences w.r.t. the true CHAMP orbit obtained from HRD orbit determination for one (black) or four (grey) days in the presence of systematic errors.

whereas the middle part only used orbital positions coinciding with the 30 s subinterval boundaries.

Figure 9.10 (bottom, middle) confirms on the 4-day level the conclusions drawn from Fig. 9.7 (left), where the systematic position errors due to the a priori gravity field model errors were found to be almost negligible with respect to the scatter induced by the GPS phase noise random errors. At the same time it can be recognized in Fig. 9.10 (bottom) that the spectrum of the HRD solution (N) is more favorable in the high-frequency range than the kinematic spectrum (see also Fig. 9.8 (left)). A difference, however, is observed in Fig. 9.10 (middle), where the entire spectrum of solution (N) exhibits smaller apparent amplitudes than the corresponding kinematic spectrum. As opposed to the kinematic case, where the "noise amplitudes" revealed by the Fourier analysis are uniquely determined by the position sampling (or the length of the analyzed data), the reduction of the position noise is "inherent" in the spectra of the HRD solution (N) for both the 10 s and 30 s position sampling. A closer inspection of Fig. 9.10 (middle) reveals in addition a somewhat sharper reduction of the position noise for periods between 60 s and 80 s than in Fig. 9.10 (bottom), which is due to the restriction of using orbital positions at subinterval boundaries only. An opposite effect could be observed for the same solution if only orbital positions within the subintervals were used, or if orbital positions from a pulse-based solution (N) were used at subinterval boundaries only (see Fig. 7.12 for the intra-interval variation of the precision of reduced-dynamic orbital positions).

Different GPS data sampling rates, position sampling rates, and data lengths are not only expected to influence the amplitude spectra of the HRD (and kinematic) solutions (N) but also the spectra of the HRD solutions (A). Figure 9.11 (top, bottom) zooms on the amplitude spectra of the 4-day solution (A) from Fig. 9.10 (middle, bottom) and adds the spectra of the corresponding 1-day solution. As opposed to the apparent amplitudes of a pure noise process, the amplitudes caused by the systematic a priori gravity field model errors are *not* reduced by the square root of the number of accumulated daily batches, but only partially by a factor of about 1.5 instead of 2 due to the permanently changing orbit geometry, which weakens the impact of small systematic errors to a certain extent. A striking difference is again observed between the 30 s position sampling (top) and the 10 s position sampling (bottom). The 30 s solution shows generally larger amplitudes with a tendency to increase up to periods of about 270 s, where the more reliable part of the a priori gravity field model up to degree 20 starts to dominate the spectrum. This effect has to be kept in mind when analyzing gravity field coefficients in Sect. 9.5.

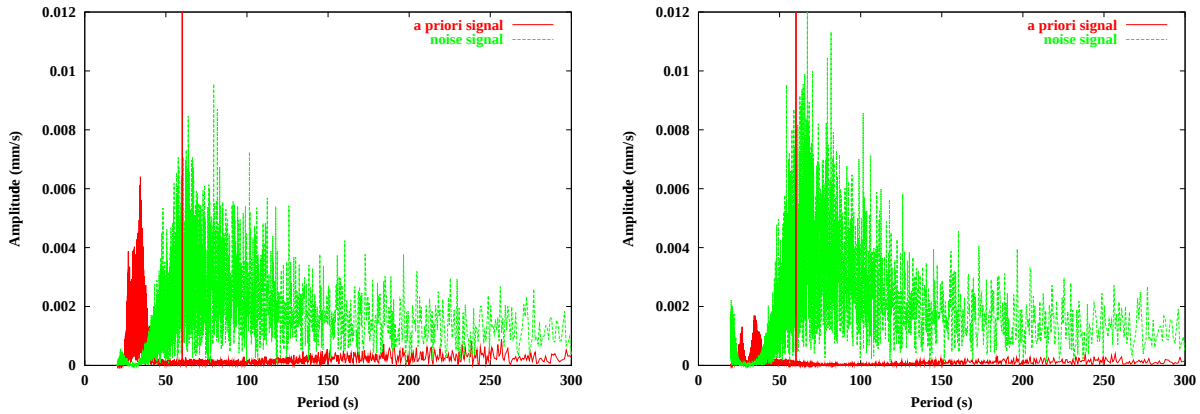

Figure 9.12: Amplitude spectra of velocity differences w.r.t. the true CHAMP orbit obtained from HRD orbit determination with pulses (left) and accelerations (right) in the presence of random errors only (solution (N)) or systematic a priori gravity field model errors only (solution (A)).

9.4.4 Fourier Analysis of HRD Orbit Velocities

Figure 9.12 shows the amplitude spectra of velocity differences over one day in one specific coordinate in the Earth-fixed reference frame with respect to the true CHAMP orbital velocities for a HRD orbit determination based on 10 s GPS data sampling with unconstrained pulses estimated every 30 s (left) and unconstrained piecewise constant accelerations estimated over 30 s (right). The two amplitude spectra of each figure show the impact of random errors only (solution (N)) and of systematic errors only (solution (A)).

The characteristics of the amplitude spectra of the velocity differences of solution (N) are similar for both types of pseudo-stochastic parameters with a slightly better RMS error of 0.077 mm/s for the pulse solution. The somewhat larger RMS error of 0.093 mm/s of the acceleration solution is caused by the amplified “bulge” of apparent amplitudes around twice the subinterval length, which may be attributed to the continuity constraint imposed on reduced-dynamic velocities by the piecewise constant acceleration model. A comparison of Fig. 9.12 with the amplitude spectra of the position differences of the solutions (N) from Fig. 9.9 shows that the velocity differences exhibit a completely different noise characteristic than the position differences. It could already be suspected in Fig. 9.7 (right) that the HRD velocity differences of solution (N) are dominated by a strong high-frequency noise which is not white over the entire frequency range due to the time differentiation. Similar to the position differences in Fig. 9.9, the amplitude spectra of solution (A) differ significantly for the two orbit parametrizations. The RMS error of 0.044 mm/s of the velocity differences of the pulse solution is reflected in the spectrum by rather large amplitudes for periods shorter than twice the subinterval length of 60 s, and a generally worse performance with respect to the acceleration solution (A) which exhibits a RMS error of 0.012 mm/s. For the sake of completeness we mention that the orbital velocities of the pulse solution are computed as mean values of the left- and right-hand side limits of the discontinuous velocity vectors at the subinterval boundaries. Finally, it is interesting to note that the transition between the more reliable part of the a priori gravity field model below degree 20 and the less reliable part higher than degree 20 can be much better recognized as a small jump in the spectra of solution (A) at 270 s for both types of pseudo-stochastic parameters than in the corresponding spectra from Figs. 9.9 and 9.11 on the position level.

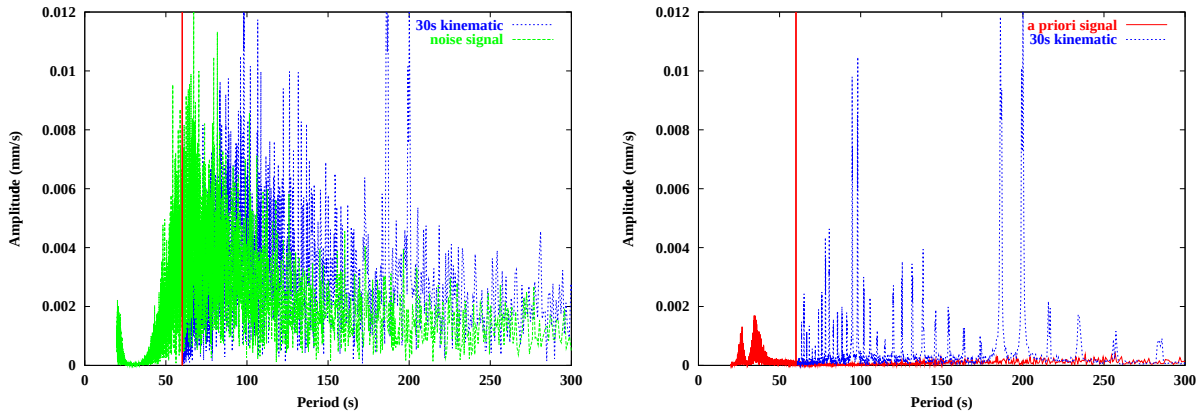

Figure 9.13: Amplitude spectra of velocity differences w.r.t. the true CHAMP orbit obtained from kinematic and HRD orbit determination with accelerations in the presence of random errors (left) or systematic errors only (right).

Comparison with Kinematic Orbits

It is instructive to compare the amplitude spectra of the HRD velocity differences from Fig. 9.12 (right) with amplitude spectra of velocity differences derived from kinematic orbits. However, the kinematic point positioning method cannot provide (pointwise) information about orbital velocities from the relative geometry between the LEO and the GPS satellite constellation, which is measured at discrete epochs only. Therefore, approximative methods have to be used to estimate pointwise velocities from a set of adjacent kinematic positions, which (of course) contain information about the mean velocities between them. [*Földváry et al.*, 2004] propose to directly apply a 7-point Newton-Gregory interpolation to each coordinate direction of a 30 s kinematic ephemerides in the Earth-fixed reference frame to obtain estimates of the kinematic velocity components v_i at time t_i as

$$v_i = \frac{1}{60\,h}\,\left(-x_{i-3} + 9\,x_{i-2} - 45\,x_{i-1} + 45\,x_{i+1} - 9\,x_{i+2} + x_{i+3}\right)\ , \tag{9.9}$$

where h is the position sampling rate and x_l, $l = i \pm 3, i \pm 2, i \pm 1$, are the kinematic position components at times t_l. Equation (9.9) is a compact expression of the first time derivative at time t_i of the interpolating polynomial of degree 5 applied to the position components x_l.

Figure 9.13 (left) compares the amplitude spectrum of the HRD solution (N) from Fig. 9.12 (right) with the amplitude spectrum of kinematic velocities obtained with (9.9) from kinematic positions based on 30 s GPS data sampling. The RMS error of 0.090 mm/s of the kinematic solution is similar to the RMS error of 0.093 mm/s of the HRD solution (N), which is also reflected in the similar characteristics of both spectra, if the apparently higher amplitudes (due to the lower sampling rate) of the kinematic spectrum are taken into account. The slightly better performance of the kinematic velocities is due to the very efficient smoothing by the relatively long interpolation intervals of (9.9), which is comparable to the smoothing effect of piecewise constant accelerations over 60 s of a HRD solution (N). The drawback of the Newton-Gregory interpolation is reflected by a few very large amplitudes in the spectrum of the kinematic velocities due to interpolation errors, e.g., at periods of 180 s and 200 s, which clearly exceed the noise level even for the considered 1-day data set. Figure 9.13 (right) compares the amplitude spectrum of the kinematic velocity differences in the absence of GPS phase random errors with the

spectrum of the HRD solution (A) from Fig. 9.12 (right), and confirms that the large amplitudes in Fig. 9.13 (left) are due to interpolation errors of formula (9.9). It is clear that the signals introduced by the Newton-Gregory interpolation are not random in nature. They result in a RMS error of 0.029 mm/s which is larger than the RMS error of 0.012 mm/s of the signals introduced by the a priori gravity field model errors of the HRD solution (A). The discrete spectral lines caused by the interpolation process are not restricted to the period range shown in Fig. 9.12 (right), but continue to lower frequencies down to the orbital frequency. For the sake of completeness, we mention that almost the same kinematic results are obtained if the same 7-point Newton-Gregory interpolation, i.e., 30 s spacing between the positions used for interpolation, is applied to 10 s kinematic positions, but worse results if the spacing of the used interpolation points is changed to 10 s.

9.5 Gravity Field Recovery from HRD Orbit Positions

The spectral analysis of HRD orbit positions and velocities presented in Sects. 9.4.3 and 9.4.4 suggested that there are HRD orbits which exhibit reduced high-frequency noise with respect to kinematic orbits and which show only minor dependencies on the underlying dynamic models. However, it is not possible to finally answer the following two key-questions from such an analysis: (1) how do the systematic and random orbital errors map into the gravity field coefficients derived from HRD orbits, (2) are we able to derive a better estimate of the gravity field from HRD orbits than from kinematic orbits? In order to obtain better answers of these two questions, we address in this section the recovery of gravity field coefficients from either HRD orbit positions or from kinematic orbit positions. We confine ourselves to the analysis of orbital positions only in order to avoid the use of further approximations for either the one or the other type of orbit: Sect. 9.4.4 showed that the additional numerical derivation of kinematic velocities makes it more difficult to compare the performance of kinematic and HRD orbital velocities as no similar step is needed when analyzing the HRD orbits.

9.5.1 Simulation Scenario

We use a very similar simulation scenario as that described in Sect. 9.4.1 for the spectral analysis of HRD orbit positions and velocities. Undifferenced GPS code and carrier phase observations were simulated with the same noise characteristics for the CHAMP satellite with 10 s sampling or, alternatively, with 30 s sampling, but the true CHAMP trajectory was a particular solution of the equation of motion given by the EIGEN-2 gravity field model up to degree and order 90 (instead of 120) without inclusion of any non-gravitational forces. The complete EIGEN-2 gravity field model up to degree 90 or, alternatively, the modified model (see Sect. 9.4.1) was used as a priori model to perform HRD orbit determination for four consecutive days (DOYs 100–103, 2002) either in the presence or in the absence of systematic a priori gravity field model errors, respectively.

The synthetic CHAMP orbital positions from the individual arcs were used as equally weighted pseudo-observations of the Earth-fixed coordinate positions in a new orbit determination problem to recover the true gravity field according to (9.4) and (9.5) with a modified version of the SATORB program of the Celestial Mechanics Software [*Beutler*, 2005]. Thereby, corrections to the normalized spherical harmonic (SH) coefficients (see Chapter 3) of the a priori gravity field model were estimated up to degree and order 90 as the “only” global parameters, whereas the corrections to the initial osculating elements were estimated arc-specific for the 24 h arcs, which means that one set of initial conditions was estimated for each of the four daily arcs in this simulation scenario. No more arc-specific parameters were needed

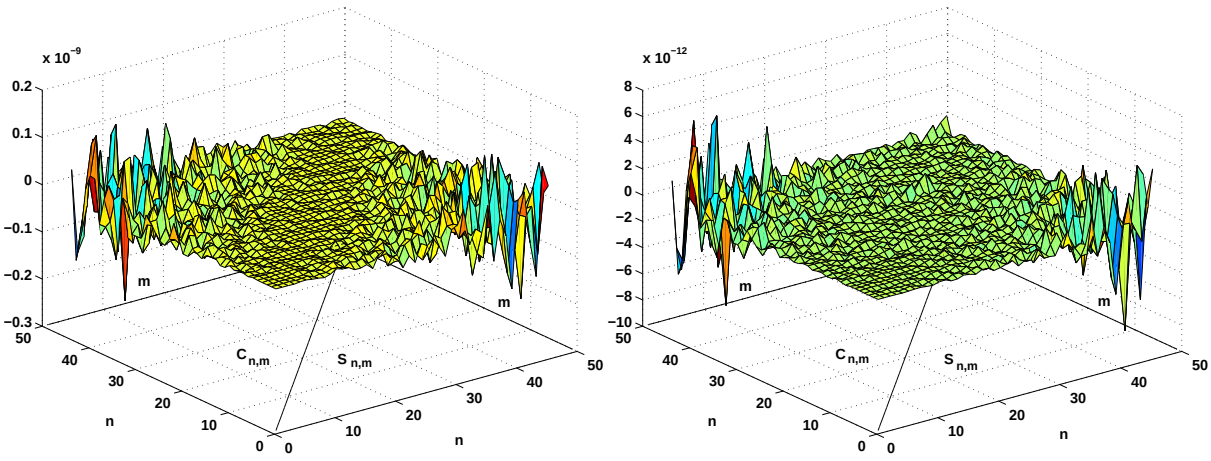

Figure 9.14: Differences of SH gravity field coefficients when using HRD orbit positions based on 30 s pulses (left) or 30 s accelerations (right). Note the different scale.

due to the complete absence of non-gravitational forces and due to the truncation of the true gravity field model at the same degree and order 90 which was estimated at maximum. Note that it is possible to set up initial conditions more frequently (short-arc method) or to solve for more arc-specific parameters in SATORB when using real observations, because it is difficult to model non-gravitational forces (see comments in Sect. 9.5.6). It is, however, out of the scope of this work to study aliasing effects on the SH coefficients caused by truncation errors and non-gravitational errors, but to isolate the pure impact of the noise and of systematic errors in the HRD orbit positions to the estimated SH coefficients.

9.5.2 A Few Introductionary Remarks

A few basic issues concerning observability, orders of magnitude, and validation of (synthetic) gravity field SH coefficients (we refer to [*Sansò and Rummel*, 1989] for a broad introduction) have to be shortly addressed before discussing the "subtleties" of the relevant simulation study introduced in Sect. 9.5.1. For this purpose a closed-loop gravity field recovery simulation has been conducted based on only one day of data. Thereby, error-free orbit positions at 10 s intervals have been used to directly fit different HRD trajectories, i.e., by completely circumventing the GPS analysis part, and to subsequently use them for gravity field recovery. As it is impossible to determine SH coefficients up to degree and order 90 from only one day of data, the true gravity field model was chosen to be represented by the SH coefficients of the EIGEN-2 model up to degree and order 45 for this closed-loop simulation, and a "zero" a priori gravity field model (except for the degrees 0 and 1) was used for gravity field recovery.

Figure 9.14 shows the differences of the estimated SH gravity field coefficients with respect to the true values when using HRD orbit positions based on unconstrained pulses estimated every 30 s (left) or unconstrained piecewise constant accelerations estimated over 30 s (right). Note that the connecting lines between the individual points as well as the shading of the resulting surfaces were added for a better visibility only.

It can be recognized that the overall characteristics of the SH coefficient differences due to different HRD orbit models are similar for both types of pseudo-stochastic parameters, but that the differences of the acceleration solution are more than twenty times smaller than the differences of the pulse solution. It

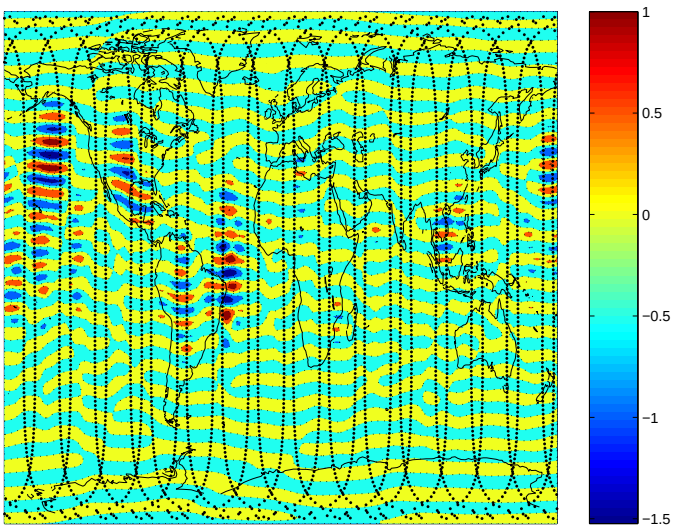

Figure 9.15: Geoid height differences (millimeters) when using HRD orbit positions based on 30 s accelerations. The CHAMP ground-tracks correspond to the used 1-day data set.

is conspicuous that the maximum deviations ($8 \cdot 10^{-12}$ for the acceleration solution) are predominantly reached for some high degree zonal terms in the SH expansion. This is also reflected in the formal accuracies of the estimated SH coefficients which indicate that the (almost) zonal terms of any degree are always less well determined than the (almost) sectorial terms, which mainly exert low-frequency perturbations on near polar orbits. The small systematic errors in the pseudo-observations, (caused by the applied "zero" a priori gravity field model) thus mostly affect the quality of these terms.

If the true orbit positions instead of the HRD positions were used for gravity field recovery, one could observe that the most dominant structures from Fig. 9.14 disappear and that the remaining differences in the SH coefficients mainly reflect the numerical limitations in the least-squares adjustment by about ten times smaller values than shown in Fig. 9.14 (right). This underlines, on the one hand, the very high sensitivity of selected SH coefficients on smallest differences in the used pseudo-observations, and, on the other hand, the still acceptable impact when using HRD orbit positions based on 30 s accelerations in this particular simulation up to degree 45, which is a best case closed-loop simulation considering only the effect of the HRD orbit model.

Validation Methods

Figure 9.15 illustrates geoid height differences of the estimated gravity field model with respect to the true gravity field model when using HRD orbit positions based on unconstrained piecewise constant accelerations over 30 s. The computation of such height differences is a commonly used method to compare different gravity field solutions and, of course, to validate simulated results with respect to a ground truth. In a simulation environment they may be computed for illustration purposes in a spherical approximation, e.g., on a $1^\circ \times 1^\circ$ grid without applying any area weights, simply as

$$\delta h(\beta, \lambda) \doteq R \sum_{n=0}^{n_{max}} \sum_{m=0}^{n} \bar{P}_{n,m}(\sin\beta) \ \left(\Delta\bar{C}_{n,m} \cos(m\,\lambda) + \Delta\bar{S}_{n,m} \sin(m\,\lambda)\right) \ , \qquad (9.10)$$

where $\Delta\bar{C}_{n,m}, \Delta\bar{S}_{n,m}$ are the differences between the recovered and the true normalized SH coefficients (see Chapter 3). The scale of Fig. 9.15 shows that the differences δh do only occasionally exceed the 1-mm level on the entire globe, which results in an overall RMS of only 0.2 mm (7 mm for the 30 s pulse solution). For accelerations over 60 s, in contrast, an overall RMS of already 8.0 cm would result (14.5 cm for the 60 s pulse solution), which underlines that an adequate subinterval length is of utmost importance. Geoid height differences are, however, not particularly well suited to study the differences between SH coefficients derived from differently parametrized HRD orbit trajectories as the corresponding figures are, like Fig. 9.15, mostly dominated by conspicuously parallel patterns which are caused by the larger deviations of high degree zonal terms. Nevertheless, Fig. 9.15 can be used to illustrate the necessity of a global distribution of the pseudo-observations over the entire globe for gravity field recovery. It is not by coincidence that the largest height differences tend to occur in-between the ground-tracks of the simulated one-day trajectory. A much more homogeneous coverage is a prerequisite to separate high degree SH coefficients from each other and to improve the overall quality of the recovered gravity field, which is usually achieved by processing long series of LEO data, e.g., over one year. If no incidental commensurabilities between the revolution period and the sidereal day length occur, the ground-track pattern changes continuously from day to day which yields a sufficiently good spatial coverage already after 2 or 4 days, at least good enough for the simulation scenario defined in Sect. 9.5.1.

A very "compact" way to validate SH coefficients in a simulation environment with respect to the ground truth is given for each degree by the so-called difference amplitude

$$\delta d_i \doteq \sqrt{\sum_{m=0}^{i} \left(\Delta\bar{C}_{i,m}^2 + \Delta\bar{S}_{i,m}^2 \right)} \tag{9.11}$$

per degree i. Equation (9.11) is a measure for the agreement over all orders of one degree, i.e., it is very likely to be mostly dominated by the agreement of the high degree zonal terms according to Fig. 9.14. Difference degree amplitudes are well suited to easily compare different solutions in one and the same figure. It would hardly make sense to compare all individual coefficients with each other, keeping in mind that a complete SH expansion up to degree and order n contains $(n+1)^2$ terms.

9.5.3 Effect of Data Accumulation

In analogy to Sect. 9.4, we present results from the simulation study defined in Sect. 9.5.1 in the following paragraphs, where either the GPS phase observation noise only, or the a priori gravity field model errors only, are "switched on" in order to separate their propagation from the HRD orbital positions into the recovered SH coefficients. Before analyzing these results in more detail, it is important to emphasize the importance of processing longer time series of orbital data to reduce the impact of (random) orbital errors on the recovered SH coefficients.

Figure 9.16 underlines this fact by showing the difference degree amplitudes (9.11) with respect to the true SH gravity field coefficients obtained from recoveries based on simulated 2-day and 4-day CHAMP 10 s GPS data, which are both either processed in the presence of the GPS phase white noise random errors only (denoted as solutions of type (N)) or in the presence of the systematic a priori gravity field model errors only (denoted as solutions of type (A)). For all four solutions the full 10 s GPS data sampling was used to perform HRD orbit determination based on unconstrained piecewise constant accelerations over 30 s, but the subsequent recovery of the SH coefficients from the two and the four daily arcs, respectively, relied on a subset of positions coinciding with the 30 s POD subinterval boundaries (see Sect. 9.4.3). This

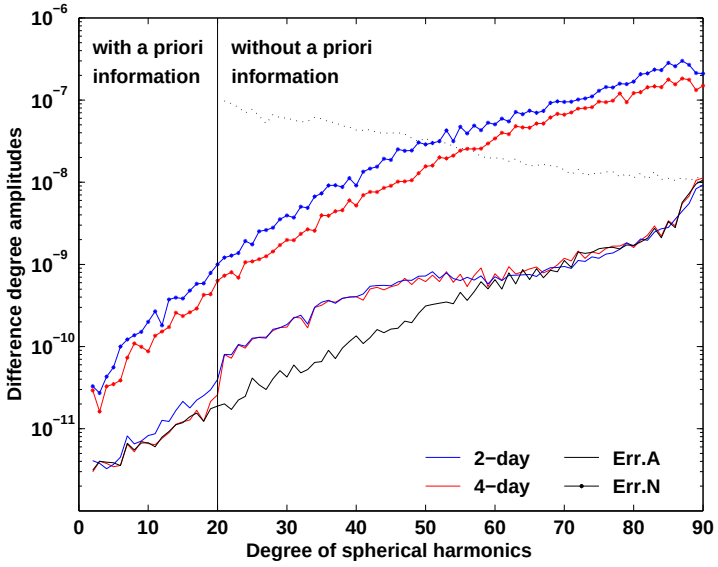

Figure 9.16: Difference degree amplitudes for a recovery with 2 or 4 days of HRD orbit positions based on 30 s accelerations (GPS sampling: 10 s, position sampling: 30 s).

position sampling for gravity field recovery was primarily chosen for the reason of efficiency.

Three additional lines are drawn in Fig. 9.16 to improve the interpretabiliy of the difference degree amplitudes: (1) the vertical line at degree 20 indicates that the systematic errors of the used a priori gravity field model are much smaller below degree 20 than above degree 20, where a "zero" model was assumed, (2) the dotted line starting at degree 20 represents the difference degree amplitudes of the "zero" model with respect to the true model, i.e., any points above the dotted line indicate larger difference degree amplitudes than obtained for the "zero" assumption, (3) the lowest line represents the difference degree amplitudes of a recovery based on four days of error-free 30 s GPS data, i.e., the difference degree amplitudes reflect the limitation of the simulation study due to small linearization errors in the corresponding kinematic orbits as already mentioned in Sect. 9.4.2. All three lines will be drawn in all the following, similar figures as well. Strictly speaking, the last mentioned line will thus not fully correspond in each case to the kinematic solution (A), e.g., due to the varying GPS and position sampling in the subsequent figures.

Figure 9.16 reveals that random and systematic orbital errors have a substantially different impact on the estimates of SH coefficients when varying the amount of orbital input data. Whereas the difference degree amplitudes of the solutions (A) are more or less the same for the 2-day and the 4-day sample, the difference degree amplitudes of the solutions (N) differ by (more than) a factor $\sqrt{2}$. This reduction of random errors has to be expected when doubling the amount of pseudo-observations, provided that the orbital positions cover the entire globe homogeneously. Because the 2-day ground track coverage is, however, still not homogeneous enough for the SH coefficients below degree 60, a somewhat higher factor may be noticed in Fig. 9.16 for the difference amplitudes of lower degrees. The difference degree amplitudes of the 2-day and the 4-day solutions (N) intersect the dotted line at degree 51 and 56, respectively, which gives a rough indication above which degree no more "signal" can be captured for the given scenarios. These limits demonstrate that high degree SH coefficients may be determined in general from

long series of orbital data only. One should be aware, however, that a few (almost) sectorial terms always exist that may be safely determined even above these limits due to their higher sensitivity to polar orbits than the (almost) zonal terms of the same degree.

Let us now discuss the more or less identical difference degree amplitudes of the solutions (A) for the 2-day and the 4-day sample. As opposed to the expectations raised in Sect. 9.4.3 where a small reduction was found in the spectra of the corresponding orbit position differences (see Fig. 9.11), no evidence for such a behavior can be recognized in Fig. 9.16. In other words, even if the systematic errors in the HRD orbit positions are small, e.g., caused by the here applied a priori gravity field model errors, it cannot be expected that the propagation into the SH coefficients may be reduced by accumulating orbital data. The different responses in Figs. 9.11 and 9.16 to systematic errors are due to the fact that SH coefficients are capable to capture signals at well defined frequencies only, whereas the spectrum of the corresponding orbit position differences "smears" out for longer orbit samples due to the permanently changing orbit geometry.

Greatest care is required to only use HRD orbit positions, which are free of systematic errors, or more strictly speaking, which contain seemingly negligible systematic errors. For Fig. 9.16 the important question arises whether the systematic effects in the difference degree amplitudes of the solutions (A), which are already visible above degree 20 where no a priori information was used to perform HRD orbit determination (a similar effect could already be observed in the low-frequency part above degree 20 in Fig. 9.11 (top)), are negligible or not. For the moment, we only mention that approximately one year of data would have to be accumulated to lower the level of the random noise in the estimates of the SH coefficients to the level of the inherent systematic errors. This indicates that the effect is rather small – and probably irrelevant in real-world applications which are governed by larger systematic effects – but the issue will be revisited in Sect. 9.5.4.

9.5.4 Solutions with 10 s GPS Data Sampling

Here we compare the difference degree amplitudes with respect to the true SH gravity field coefficients obtained from recoveries based on either HRD orbits with 30 s pseudo-stochastic parameters or kinematic orbits derived from the simulated 10 s GPS data covering 4 days. The GPS data are processed in the presence of either the GPS phase white noise random errors only (solutions (N)) or the systematic a priori gravity field model errors only (solutions (A)), or in the presence of both sources of errors (solutions (N+A)).

30 s Position Sampling

In analogy to Sect. 9.5.3, this first part of the analysis considers the recovery of SH coefficients from the subset of orbital positions coinciding with the 30 s POD subinterval boundaries. Figure 9.17 shows the difference degree amplitudes for the solutions of type (N), (A), and (N+A) based on either HRD orbits (unconstrained piecewise constant accelerations or pulses at 30 s subintervals) or kinematic orbits.

Figure 9.17 shows that the solution (N+A) based on HRD pulse orbits is still heavily affected and even partly dominated by the systematic errors of the a priori gravity field model. This can be recognized by the difference degree amplitudes of the solution (A) which exceed the corresponding amplitudes of the solution (N) between degrees 20 and 35 and eventually dominate the solution (N+A). In other words, even if unconstrained pseudo-stochastic pulses are set up at a very high-rate such as every 30 s, they are not capable to compensate adequately for unmodeled systematic effects in the underlying dynamic

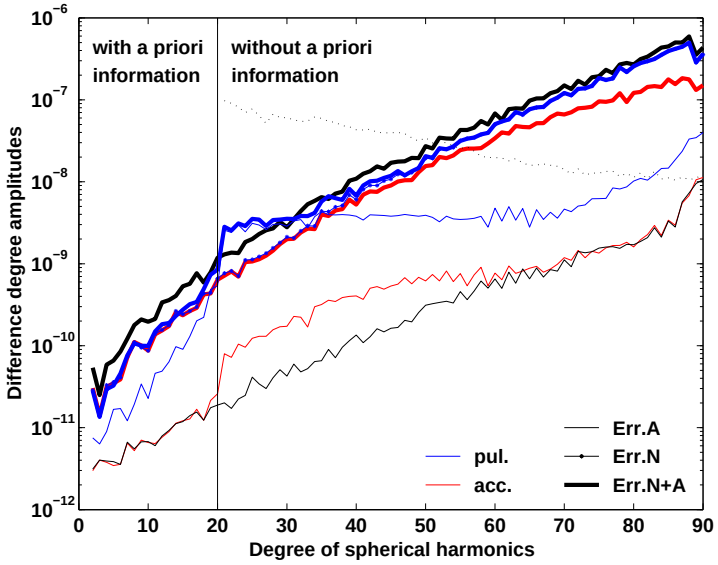

Figure 9.17: Difference degree amplitudes for a recovery with 4 days of kinematic (black) or HRD orbit positions (colored) based on 30 s pseudo-stochastic parameters (GPS sampling: 10 s, position sampling: 30 s).

models, which may propagate into a subsequent recovery of SH gravity field coefficients. It is alarming to observe such a bad behavior, which partly exceeds the kinematic solution already with only four days of analyzed data, i.e., even before the reduction of random errors starts to significantly improve the kinematic solution.

Let us now compare the difference degree amplitudes of the solutions (N+A) based on the kinematic and the acceleration-based HRD orbit positions. Both curves in Fig. 9.17 coincide with the corresponding difference degree amplitudes of the solutions (N) due to the much smaller impact of the systematic errors. Keep in mind that the kinematic orbit positions are only governed by small linearization errors, whereas the systematic errors in the HRD orbit positions are considerably larger, but still negligible compared to the random noise level obtained for four days of analyzed data (see Sect. 9.5.3). Therefore, the difference degree amplitudes of the kinematic and the HRD solutions (N+A) are dominated by random errors and thus differ by (more than) a factor of $\sqrt{3}$ due to the reduced random errors in the HRD orbit positions, see Sect. 9.4.3. A closer inspection of the difference degree amplitudes in Fig. 9.17 reveals, however, an even stronger reduction than $\sqrt{3}$ for the HRD solution (N+A) above degree 60. This effect could also be seen in Fig. 9.10 (middle) and is related to the special selection of orbital positions coinciding with the 30 s POD subinterval boundaries, which tend to be determined more precisely when performing HRD orbit determination based on piecewise constant accelerations. One might argue that this effect is irrelevant as it starts to affect the HRD solution (N+A) only above degree 60 in Fig. 9.17 where no more "signal" can be captured by the SH coefficients. We have to keep in mind, however, that the difference degree amplitudes experience more or less a parallel shift when more data has been accumulated (see Fig. 9.16), which in turn might make this effect relevant for the high degree SH coefficients. Note that a similar but opposite effect can be observed for the HRD pulse solution (N) where the observed factor $\sqrt{3}$ with respect to the kinematic solution for low degree terms becomes rapidly smaller for higher degree terms, which may be seen as an other disadvantage when using HRD pulse orbits.

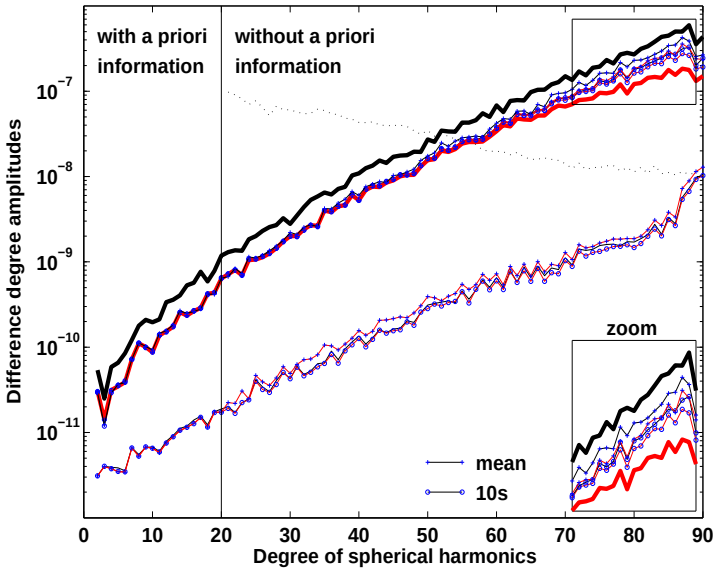

Figure 9.18: Difference degree amplitudes for a recovery with 4 days of kinematic (black) or HRD orbit positions (red) based on 30 s accelerations (GPS sampling: 10 s, position sampling: see explanations in the text).

10 s Position Sampling

As opposed to the previous paragraph, this part of the analysis considers the recovery of SH coefficients from the full set of orbital positions. Figure 9.18 shows the difference degree amplitudes for the solutions of type (N) and (A) based on either HRD orbits (only solutions based on unconstrained piecewise constant accelerations over 30 s are displayed) or kinematic orbits. For comparison, the solutions of type (N+A) from Fig. 9.17 are included here, as well as solutions that will be addressed in the next paragraph.

Figure 9.18 reveals that the difference degree amplitudes of the HRD solution (A) do no longer show the striking increase above degree 20 (see Fig. 9.17). This result could indeed be hoped for when looking at Fig. 9.11, which already showed that the systematic errors in the HRD orbit positions predominantly occur in a frequency range which is out of interest. Moreover, it is encouraging to see that no major part of these systematic errors was propagated into the SH coefficients, which can be seen in the identical level for both the HRD and the kinematic solutions (A). One may also recognize that the HRD solution (A) is apparently even slightly below the kinematic solution (A), which has to be attributed to the small inconsistency of the displayed kinematic solution (A) as explained in the beginning of Sect. 9.5.3.

Figure 9.18 shows that the maximum resolution of the HRD solution (A) did not change with respect to Fig. 9.17 despite the increased position sampling; it is still approximately located at degree 90 due to the chosen subinterval length of 30 s. A 10 s kinematic solution (A), in contrast, would allow us to recover SH coefficients up to a higher degree than 90, which is, admittedly, an advantage of the kinematic solution. Further simulations seemed to indicate that the (theoretical) gain in resolution is rather small and most probably irrelevant for real-world gravity field solutions based on high-low SST data, which are nowadays limited to approximately degrees 60–70, e.g., [*Földváry et al.*, 2004].

Let us now consider the difference degree amplitudes of the HRD and kinematic solutions (N) in Fig. 9.18.

As opposed to Fig. 9.17, where the corresponding solutions differed by a factor $\sqrt{3}$, we recognize very similar curves in Fig. 9.18, in particular for the low degree SH coefficients where the two solutions are virtually the same. Only a slightly better performance may be recognized for the HRD solution (N) in the zoom of the high-frequency part of Fig. 9.18, which is, however, less striking than the corresponding improvement found in Fig. 9.17. This "moderate" improvement with respect to the kinematic solution actually reflects the "pure" suppression of the high-frequency noise in the HRD orbit positions with 30 s acceleration parameters as already shown in Fig. 9.10 (bottom). As no special data selection is invoked this time (compare the reduction of the position noise for periods between 60 s and 80 s in Fig. 9.10 (middle, bottom)), no further reduction of the difference degree amplitudes can be expected.

Mean Observation Equations

Figure 9.18 demonstrated that it is possible to generate HRD orbits which do not introduce systematic errors due to the a priori gravity field model into a subsequent recovery of SH gravity field coefficients, and at the same time, which allow it to recover the SH coefficients at least equally well – or even slightly better – than in the case of kinematic orbits. A major drawback, however, has to be seen in the additional computational burden which is necessary when processing the pseudo-observations with the full 10 s sampling interval. The increased sampling rate from 30 s to 10 s increases the CPU times for each daily batch of data by about a factor of 3, as well, which becomes time-relevant when setting up large normal equation systems. Therefore, it is questionable, whether or not this effort is justified in order to (only) eliminate an effect which is probably irrelevant for applications using real data. Remember that the spatial resolution does not benefit from an increased sampling rate of the HRD positions.

An approximative, but simple and CPU time saving way to cope with this situation is to still process the full amount of data but to average the pseudo-observation equations within the 30 s subintervals given from POD before setting up the normal equation system for gravity field recovery. Formally, the number of observation equations is reduced by a factor 3 by this measure but the full amount of data is still taken into account to set up the normal equation system. It is clear, however, that the resulting solution is not (fully) equivalent to a correct processing of all pseudo-observations.

Figure 9.18 shows that the difference degree amplitudes of the "mean" HRD solution (A) do not show any dramatic increase above degree 20 (compare Fig. 9.17). In fact they are only marginally larger due to the approximation than the difference degree amplitudes of the solution (A) obtained from the correct processing of the 10 s pseudo-observations. Note that the averaging of pseudo-observations from 10 s kinematic orbits would reduce the better spatial resolution again to the resolution obtained from pseudo-observations sampled at 30 s.

From Fig. 9.18 we also learn that the difference degree amplitudes of the "averaged" HRD and kinematic solutions (N) are virtually the same as obtained from the correct processing of the 10 s pseudo-observations. Only in the zoom of the high-frequency part one may recognize, as to be expected, a slightly inferior performance of both "averaged" solutions with respect to the correct ones. Thereby, the "averaged" HRD solution (N) shows an only moderate improvement with respect to the "averaged" kinematic solution (N) and coincides – more or less – with the correct kinematic solution (N).

It is beyond the scope of this work to investigate various conceivable (pre-) processing techniques for orbital input data to enable an optimal gravity field recovery. The intention of introducing "averaging" was rather to demonstrate that simple and rapid strategies exist to keep SH coefficients free from the discussed (small) systematic and increased random errors (see Fig. 9.17) introduced by the 30 s sampled

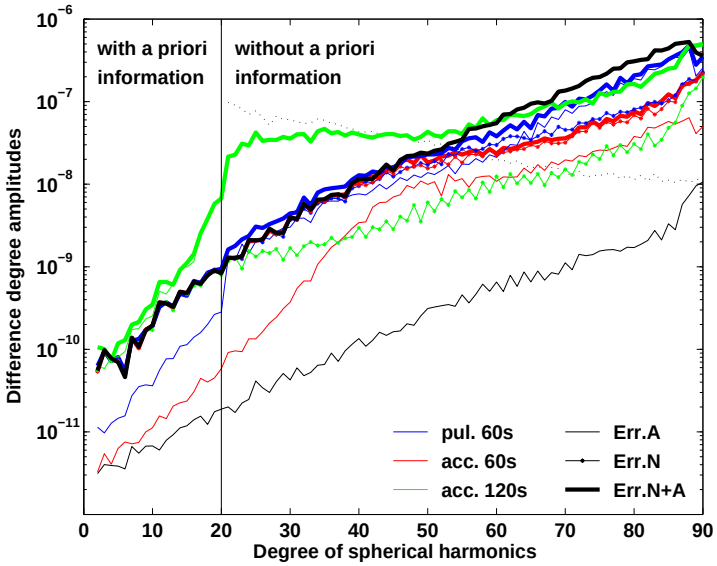

Figure 9.19: Difference degree amplitudes for a recovery with 4 days of kinematic (black) or HRD orbit positions (colored) (GPS sampling: 30 s, position sampling: 30 s).

HRD and kinematic orbit positions, respectively.

9.5.5 Solutions with 30 s GPS Data Sampling

In this section we compare the difference degree amplitudes with respect to the true SH gravity field coefficients obtained from recoveries based on either HRD orbits ($\neq$ MRD orbits) or kinematic orbits derived from the simulated 30 s GPS data covering 4 days. As in the previous sections the GPS data are processed in the presence of either the GPS phase white noise random errors only (solutions (N)) or the systematic a priori gravity field model errors only (solutions (A)), or in the presence of both sources of errors (solutions (N+A)).

Figure 9.19 shows that the solution (N+A) based on HRD 60 s acceleration orbits exhibits better difference degree amplitudes above degree 40 than the kinematic solution (N+A) due to the reduction of the high-frequency position noise by the 60 s piecewise constant accelerations. At the same time we can see that the HRD solution (N+A) is only slightly dominated by random errors for the high-degree SH coefficients due to the already strong presence of the systematic errors above degree 40, which had to be expected according to Fig. 9.10 due to the longer acceleration intervals. As a matter of fact, an approximately 4 times longer series of orbital positions would already be sufficient to lower the random errors to a level which is comparable to the systematic errors displayed in Fig. 9.19. Therefore, we conclude that even HRD orbit positions based on 60 s piecewise constant accelerations are not suited to derive unbiased gravity field information, at least not in the high-frequency part above degree 40.

Figure 9.19 demonstrates that an even stronger statement has to be made for the solution (N+A) based on HRD 60 s pulse orbits. As in Fig. 9.17, the recovered SH coefficients are strongly influenced by the systematic errors of the a priori gravity field model over almost the entire range of frequencies. It is thus no surprise that the difference degree amplitudes of this solution may partly exceed the kinematic solution already with only four days of analyzed data, which is just one more argument against using

HRD orbits based on pulses for the purpose of gravity field recovery.

Finally, Fig. 9.19 illustrates that a dramatic increase in the propagation of the systematic a priori gravity field model errors into the recovered SH coefficients has to be observed if too long subintervals of the pseudo-stochastic parameters have been used to determine the underlying HRD orbits. The solution (N+A) based on HRD 120 s acceleration orbits is completely dominated by systematic errors over the entire range of frequencies, i.e., above and even below degree 20, where some a priori gravity field information was introduced. The difference degree amplitudes should therefore be understood as a warning to not make use of any conventional reduced-dynamic orbits for the purpose of gravity field recovery – even if random errors may be greatly reduced (see solution (N) in Fig. 9.19) due to the longer subintervals.

9.5.6 Comment on Applications using Real Observations

One of the main differences between simulated and real gravity field recoveries is the much more enhanced presence of the various types of systematic errors. Whereas the simulations discussed previously were confined to only include systematic errors in the static part of the a priori gravity field model, various other sources for systematic errors in the dynamical models must be considered in practice for gravity field recovery, e.g., omission errors due to the restriction to a finite number of coefficients in the SH expansion and non-gravitational model errors, to name only the two most important error sources. Moreover, one has to be aware that the systematic errors in the used pseudo-observations may be significant, as well, as it was illustrated by Fig. 9.5. This is either due to the limitations in the available GPS data, e.g., caused by a bad receiver performance (data outages, low quality measurements), or due to the limitations in the GPS data processing, e.g., due to bad or rapidly changing viewing geometries.

It is hard to predict the effect of such additional systematic errors on analogue simulations as performed in the previous sections (without actually simulating them), especially because a considerable amount of arc-specific parameters is usually estimated to reduce the propagation into the SH coefficients. Therefore, we emphasize that any interpretation of the simulation results should be performed in a careful "one-way direction" only: (1) bad gravity field recovery results in the simulation certainly indicate bad recovery results in a "real-world" application, as well, (2) good gravity field recovery results, however, do not necessarily imply good recovery results in a real-world application due to the various sources of errors not studied in the presented simulations.

In practice, data outages and low quality GPS measurements probably impose the most serious restrictions on the validity of the simulation results due to the generally weak determination of the many pseudo-stochastic parameters. It was mentioned in Sect. 9.3.1, e.g., that even for a maximum reduced-dynamic (MRD) orbit an influence of the a priori gravity field model could be observed at the neighboring epochs of data gaps, and sometimes even at other epochs than just the neighboring ones. It is hard to predict whether the use of similar "problematic" HRD positions would harm the recovery results more than the use of the corresponding kinematic positions, which suffer from data outages and low quality GPS observations, as well. One should keep in mind that such effects might considerably deteriorate optimistic expectations from simulations using synthetic data.

9.6 Summary and Comments

The results presented in this chapter show that pseudo-stochastic orbit modeling techniques are excellent to absorb deficiencies in the underlying dynamic models for orbit determination, which in turn can be

used to improve our knowledge on these models from the analysis of (highly) reduced-dynamic trajectories. The number of estimated pseudo-stochastic parameters allows for a smooth transition between using and compensating for information about LEO dynamics for orbit determination.

Section 9.1 showed that unconstrained piecewise constant and piecewise linear accelerations may be directly identified with the pointwise values of a once-per-revolution acceleration at a level of 4% and 0.07%, respectively, indicating that a direct interpretation of single estimates of piecewise constant accelerations may introduce comparably large model errors, such as observed in the combination study with accelerometer data in Sect. 7.8.4.

Section 9.2 showed that an analysis of orbital positions is well suited to replace a more complicated integrated analysis of all acceleration (or pulse) estimates to allow for a recovery of force model parameters. This is an attractive and simple way to separate the GPS processing from a further orbit analysis, e.g., for gravity field recovery. One has to keep in mind, however, that the correlations between the orbit positions are neglected by such a "two-step" approach. Sect. 9.2.3 showed that discretization errors introduced by pseudo-stochastic parameters are negligible if they are set up at a sufficient frequency.

Section 9.3 made full use of the developments of Chapter 6 to introduce so-called highly reduced-dynamic (HRD) orbits, reduced-dynamic orbits with pseudo-stochastic parameters set up at a frequency close to the GPS observation sampling rate. It could be shown that the HRD orbit positions are equivalent to the kinematic positions at the subinterval boundaries, provided that data gaps do not occur and that a set of 3 pseudo-stochastic parameters is set up at the highest possible frequency (MRD orbits). Kinematic orbits are well established for a subsequent recovery of parameters describing the Earth's gravity field, which makes it interesting to analyze HRD orbits for this purpose.

In Sect. 9.4 we analyzed different HRD orbits with varying subinterval lengths and different types of pseudo-stochastic parameters. Spectral analysis revealed that the reduction of the high-frequency part of the position noise goes hand-in-hand with the introduction of dependencies on the underlying force models such as the a priori gravity field model. In essence, orbit signals with periods shorter than twice the subinterval length of the estimated pseudo-stochastic parameters are caused by the underlying force models: they do not contain independent information on the actual force field. It could be shown that significant differences exist between different types of pseudo-stochastic parameters to keep the impact of the dynamic models small. Piecewise constant accelerations are much better suited than pulses, as they act over an entire subinterval length and not only at a certain discrete epoch. We concluded in Sect. 9.4 that too long subintervals have to be avoided if not too much a priori information shall be introduced into the orbit determination process. The same statement holds for a priori constraints, as well.

Section 9.5 confirmed the findings of Sect. 9.4. In order to be competitive with gravity field recovery results from 30 s kinematic positions, a subinterval length of 30 s is necessary for piecewise constant accelerations, as well. This implies that the GPS data have to be processed at a higher sampling rate for orbit determination in order to benefit from the reduced-dynamic filtering of the trajectory. A most reliable estimation of the parameters may be expected if the GPS data sampling rate is much smaller than the subinterval length. It could be shown that recoveries from long series of HRD 30 s acceleration orbits based on 10 s GPS sampling are at least as good – if not even slightly better – than the recoveries obtained from the corresponding kinematic orbits.

The upcoming GOCE mission will be well suited to further validate this approach due to the provided 1 Hz GPS data. Preliminary studies are foreseen together with the Institute of Navigation and Satellite Geodesy of the Graz University of Technology in the context of the bridging phase of the High-level

Processing Facility of GOCE. In the same context, reduced-kinematic orbits will be assessed for gravity field recovery, as well. Reduced-kinematic orbits are kinematic orbits with adjacent position differences constrained to position differences of a conventional reduced-dynamic orbit in order to reduce the noise [*Švehla and Rothacher,* 2005b].

10. Summary, Conclusions, and Outlook

The new generation of dedicated gravity field missions equipped with onboard dual-frequency GPS receivers like CHAMP and GRACE provide the unique opportunity to derive highly accurate satellite orbits, Earth gravity field parameters, and information about the Earth's atmosphere. In our analysis we studied the problems dealing with the extraction of precise orbital information using dual-frequency GPS data.

Since October 1, 2002, we analyze spaceborne GPS data from CHAMP and GRACE in the context of this work, which is part of the LEO activities at the Astronomical Institute of the University of Bern (AIUB). To derive very precise orbits in the post-processing mode, we have to analyze the ionosphere-free linear combination of undifferenced or doubly differenced carrier phase measurements from the spaceborne GPS receivers. The double difference solutions do not only include the spaceborne measurements but also the carrier phase measurements from the tracking network of the International GNSS Service (IGS). The terrestrial data are also processed at the Center for Orbit Determination in Europe (CODE) to derive the core products for the IGS. Unnecessary to say that we made full use of the CODE final products to establish LEO orbits in a well-defined reference frame.

Our LEO orbits are represented by six initial conditions, a few dynamic parameters, and a usually large number of pseudo-stochastic parameters referring to a local orbital frame, because perturbing forces are best characterized in such frames. After having implemented more refined pseudo-stochastic representations based on acceleration parameters, longer series of CHAMP and GRACE data were analyzed.

A first comparison with CHAMP orbits from other LEO analysis centers in the context of the CHAMP orbit comparison campaign showed that our orbits are competitive with solutions based on other processing strategies and software packages. The AIUB "zero difference" orbits yielded the best quality for the eleven days of the orbit comparison campaign with a 1-D accuracy of about 3 cm. The good ranking of the "zero difference" orbits confirmed the applicability of our pseudo-stochastic orbit modeling techniques and demonstrated the quality of the CODE high-rate clock corrections used in our analysis.

A computation of CHAMP orbits for 200 days based on undifferenced tracking data confirmed, in essence, the experience gained from the CHAMP orbit comparison campaign in terms of accuracy. Even in the complete absence of non-gravitational force models, pseudo-stochastic orbit modeling enables a very precise restitution of a satellite's trajectory. The correlation of the estimated accelerations from GPS data with the accelerations measured by the onboard STAR accelerometer proved to be very high. We observed that the piecewise constant or piecewise linear accelerations follow the pronounced along-track perturbations induced by atmospheric drag without problems, but we also identified weaknesses in the recovery of short-term perturbations by single acceleration estimates. We conclude that precise orbit determination is certainly the most important application for pseudo-stochastic orbit modeling based on acceleration parameters, but do not rule out that the estimates of the unmodeled perturbations might be an interesting low-cost alternative to measurements from onboard accelerometers – provided that mission requirements are not extremely high and state-of-the-art gravity field models are available.

More experience concerning "zero difference" orbit determination was gained from the 2003 data set of the first GRACE data release. We analyzed eleven month of undifferenced GPS data with (one of) the state-of-the-art gravity field model(s) of that time. The validation with Satellite Laser Ranging data revealed that both GRACE orbits may be determined with a 1-D accuracy of about 2.5 cm. A period of about eight weeks could be identified, where the GPS tracking performance of the GRACE receivers was of exceptional quality, which even allowed us to demonstrate a 1-D orbit accuracy for GRACE B below 2 cm. This accuracy requirement will have to be met in the near future for the upcoming GOCE mission. The GOCE precise science orbit product will be based on the same baseline procedure and will be derived in the context of the High-level Processing Facility of the European GOCE Gravity Consortium at AIUB.

We compared the GRACE A and B "zero difference" orbits with the ultra-precise observations from the microwave K-band link between the two GRACE satellites. This validation allowed us to continuously monitor the 1-D precision of the relative position between GRACE A and B, which was found to be about 1.25 cm. Weaknesses in the pseudo-stochastic modeling could be identified in the context of K-band validation for time intervals where no GPS data are available. Due to the fact that we did not take any models of non-gravitational perturbations into account, our orbits are not well predictable across extended data gaps, which may be a disadvantage if the receiver frequently looses track to all GPS satellites for long time spans. It is of course no problem to take additional model information into account – the pseudo-stochastic parameters are then simply estimated on top of the introduced a priori values.

In addition to the processing of undifferenced GPS GRACE data, experience was gained on the optimal processing of doubly differenced GPS data from the flying baseline between GRACE A and B, and on the exploitation of the interferometric nature of the GPS system by resolving the doubly differenced carrier phase ambiguities to their integer values.

A comparison of the reduced-dynamic estimates of the flying baseline from doubly differenced GPS data with independent observations indicates that the processing of the differenced observables "alone" is beneficial in terms of precision and accuracy. Relative a priori constraints between the pseudo-stochastic parameters of GRACE A and B were found to further improve the baseline estimates as both satellites experience similar perturbations due to their separation of 220 km, which only corresponds to 30 s in time. The reconstruction of the baseline with "ultimate" precision, however, requires the resolution of the doubly differenced ambiguities. An eight-week comparison of reduced-dynamic estimates of the flying baseline with the ultra-precise K-band observations demonstrated that (sub)-mm precision is feasible, if about ninety percent of the doubly differenced space baseline ambiguities are correctly resolved to integer values. We found evidence that the radial and cross-track components are determined with a similar precision as well. Such a precise knowledge of the inter-satellite vector will be of interest in the near future for the upcoming SAR mission TerraSAR-X.

In addition, the positive impact of ambiguity resolution on the space-ground baselines could be demonstrated. Based on our validation studies we recognized a significant improvement in the relative GRACE orbit solutions by comparing them with the K-band observations, but so far we could not demonstrate an improvement in the SLR residuals for the two GRACE satellites in an absolute sense. The low success-rates of less than 50% percent of resolved space-ground baseline ambiguities may be mainly responsible for this. Many receivers of the ground network did not provide P-code measurements of good quality, which is a prerequisite for a successful resolution of the wide-lane ambiguities with the Melbourne-Wübbena linear combination. A refined selection of IGS receiver sites tailored to the quality of the code measurements might further improve the situation for ambiguity resolution on space-ground baselines.

Based on a performance analysis concerning CPU times for different types of reduced-dynamic orbit determination problems we concluded that the normal equation handling is sub-optimal in terms of efficiency if large numbers of pseudo-stochastic parameters are estimated. We described in detail how pseudo-stochastic parameters may be solved for efficiently by making full use of the underlying mathematical structures, e.g., by a filter-like approach where only "currently" active parameters are kept in the system of normal equations. Such methods are essential for an efficient determination of orbits from doubly differenced GPS data formed between the LEO receiver and a large number of GPS ground stations, or for an efficient determination of large numbers of pseudo-stochastic parameters.

Efficient methods are prerequisite when striving for the highest resolution of pseudo-stochastic parameters. We could demonstrate that so-called highly reduced-dynamic orbit positions are identical at the GPS observation epochs with kinematic orbit positions obtained from a precise point positioning, provided a set of three pseudo-stochastic orbit parameters is set up at every GPS observation epoch and that no gaps are present in the GPS data. It is thus possible to achieve the "kinematic limit" also by pseudo-stochastic orbit modeling.

Based on a spectral analysis of orbit positions derived from simulated GPS data we concluded that high-frequency noise in the orbit positions may be suppressed by a pseudo-stochastic modeling of the orbits. At the same time, we pointed out that one cannot avoid the introduction of a dependency of the resulting positions on the dynamic a priori models used for orbit determination, if pseudo-stochastic parameters are not set up at every observation epoch. We found evidence for a trade-off between the two competing effects in a simulation study when pseudo-stochastic parameters are solved for at rates very close to the GPS sampling rate.

An extensive simulation study was conducted to clarify the usefulness of highly reduced-dynamic orbit positions for the purpose of gravity field determination. We analyzed recovered gravity field parameters up to degree 90 with respect to their noise and their signal content from models used for orbit determination. The comparison with the recovery results from 30 s kinematic positions clearly revealed that pseudo-stochastic parameters have to be solved for at least every 30 s to ensure an unbiased recovery of the gravity field coefficients. Orbits based on pseudo-stochastic parameters set up less frequently, e.g., at 60 s or even longer subintervals, are detrimental for the recovery. Such "smoothed orbits" are better in terms of noise, but strongly biased with respect to the underlying models used for orbit determination, which maps into the estimated gravity field parameters. As a consequence, only highly reduced-dynamic orbit positions based 30 s subintervals may be used, which are identical to 30 s kinematic orbits if GPS data are processed at 30 s intervals.

Let us mention that the situation is different if full-rate GPS data from the spaceborne receivers is used to estimate pseudo-stochastic parameters every 30 s, e.g., 10 s GPS data from CHAMP and GRACE or 1 s GPS data from the upcoming GOCE mission. We noticed a small advantage in the recovery of the high-degree terms of the Earth gravity field in terms of noise when using highly reduced-dynamic orbit positions based on 10 s GPS data instead of 10 s or 30 s kinematic positions, and would expect an even better recovery with 1 s GPS data. Based on our simulation studies we favor the reduced-dynamic orbits based on piecewise constant accelerations. It is a substantial advantage of this parametrization to account for the gravity signals during the entire subintervals, as opposed, e.g., to pulses, which only accommodate the orbits at discrete time epochs.

We intend to further study highly reduced-dynamic orbit determination with real data in the context of the High-level Processing Facility for the upcoming GOCE mission. Preliminary studies are foreseen for the bridging phase before the planned start of the satellite in March, 2008.

In our analysis we uniquely studied gravity field recovery from kinematic or highly reduced-dynamic orbit positions. It may be expected, however, that the inclusion of the precisely determined ambiguity-fixed kinematic or highly reduced-dynamic GRACE baseline will further improve the recovery – even without using the K-band observations. It will in particular be possible to obtain more reliable estimates for the SH coefficients of higher degrees, i.e., for the degrees where we noticed small advantages when using highly reduced-dynamic instead of kinematic orbit positions.

Bibliography

Abshire, J.B., X. Sun, H. Riris, J.M. Sirota, J.F. McGarry, S. Palm, D. Yi, and P. Liiva (2005), Geoscience Laser Altimeter System (GLAS) on the ICESat Mission: On-orbit measurement performance, *Geophysical Research Letters*, 32, L21S02, doi:10.1029/2005GL024028.

American Institute of Aeronautics and Astronautics (1999), MEO/LEO Constellations: U.S. Laws, Policies, and Regulations on Orbital Debris Mitigation, Special Report, 16(2).

Angermann, D., G. Baustert, and R. Galas (1997), EPOS.P.V3 (Earth Parameter & Orbit System): Software User Manual for GPS Data Processing, Scientific Technical Report, 97/14, GFZ Potsdam, Germany, September 1997.

Bertiger, W.I., Y.E. Bar-Sever, E.J. Christensen, E.S. Davis, J.R. Guinn, B.J. Haines, R.W. Ibanez-Meier, J.R. Jee, S.M. Lichten, W.G. Melbourne, R.J. Muellerschoen, T.N. Munson, Y. Vigue, S.C. Wu, T.P. Yunck, B.E. Schutz, P.A.M. Abusali, H.J. Rim, M.M Watkins, and P. Willis (1994), GPS precise tracking of TOPEX/POSEIDON: results and implication, *Journal of Geophysical Research*, 99(C12), 24449–24464, 10.1029/94JC01171.

Beutler, G., E. Brockmann, W. Gurtner, U. Hugentobler, L. Mervart, M. Rothacher, and A. Verdun (1994a), Extended orbit modeling techniques at the CODE processing center of the international GPS service for geodynamics (IGS): theory and initial results, *Manuscripta Geodaetica*, 19, 367–386.

Beutler, G., I.I. Mueller, and R.E. Neilan (1994b), The International GPS Service for Geodynamics (IGS): Development and Start of Official Service on 1 January 1994, *Manuscripta Geodaetica*, 68, 43–51.

Beutler, G., R. Weber, U. Hugentobler, M. Rothacher, and A. Verdun (1998), GPS Satellite Orbits, in *GPS for Geodesy*, edited by P.J.G. Teunissen and A. Kleusberg, pp. 43–109, Springer, ISBN 3-540-63661-7.

Beutler, G. (2005), *Methods of Celestial Mechanics*, Springer, ISBN 3-540-40749-9, 3-540-40750-2.

Beutler, G., A. Jäggi, U. Hugentobler, and L. Mervart (2006), Efficient satellite orbit modelling using pseudo-stochastic parameters, *Journal of Geodesy*, 80(7), 353–372.

Biancale, R., G. Balmino, J.-M. Lemoine, J.-C. Marty, B. Moynot, F. Barlier, P. Exertier, O. Laurain, P. Gegout, P. Schwintzer, C. Reigber, A. Bode, R. König, F.-H. Massmann, J.-C. Raimondo, R. Schmidt, and S.Y. Zhu (2000), A new global Earth's gravity field model from satellite orbit perturbations: GRIM5-S1, *Geophysical Research Letters*, 27(22), 3611–3614, 10.1029/2000GL011721.

Biancale, R., S. Bruinsma, J.-M. Lemoine, S. Loyer, F. Perosanz, G. Balmino, F. Flechtner, R. Schmidt, and U. Meyer (2005), Traitement des données de GRACE: Mesures GPS et KBR, presented at the Journées "Gravimétrie spatiale", Paris, France, May 11–12 2005.

Birmingham, W.P., B.L. Miller, W.L. Stein (1983), Experimental Results of Using the GPS for Landsat 4 Onboard Navigation, *Navigation*, 30(3), 244–251.

Bock, R. and H. Lühr (2001), CHAMP Aberration Correction, Technical Note 2702, GFZ Potsdam, Germany, April 2001.

Bock, H. (2003), *Efficient Methods for Determining Precise Orbits of Low Earth Orbiters Using the Global Positioning System*, Vol. 65 of *Geodätisch-geophysikalische Arbeiten in der Schweiz*, Schweizerische Geodätische Kommission, ISBN 3-908440-08-4.

Bock, H., R. Dach, U. Hugentobler, S. Schaer, and G. Beutler (2004), CODE High-rate GPS Satellite Clock Corrections, presented at the IGS Workshop, Bern, Switzerland, March 1–5 2004.

Bock, H., A. Jäggi, D. Švehla, G. Beutler, U. Hugentobler, and P. Visser (2007), Precise Orbit Determination for the GOCE Satellite Using GPS, *Advances in Space Research*, 39(10), 1638–1647.

Boomkamp, H. (2001), Discussion on CHAMP slr results, IGS LEO Mail, No. 31.

Boomkamp, H. (2003), The CHAMP Orbit Comparison Campaign, in *First CHAMP Mission Results for Gravity, Magnetic and Atmospheric Studies*, edited by C. Reigber, H. Lühr, and P. Schwintzer, pp. 53–58, Springer, ISBN 3-540-00206-5.

Boomkamp, H. (2004), Update of the CHAMP Orbit Comparison Campaign, private communication.

Braasch, M.S. (1995), Multipath effects, in *Global Positioning System – Theory and Applications – Volume I*, edited by B.W. Parkinson and J.J. Spilker, pp. 547–568, American Institute for Aeronautics and Astronautics, ISBN 1-563-47106-1.

Bruinsma, S., S. Loyer, J.-M. Lemoine, F. Perosanz, and D. Tamagnan (2003), The impact of accelerometry on CHAMP orbit determination, *Journal of Geodesy*, 77(1-2), 86–93.

Bruinsma, S., D. Tamagnan, and R. Biancale (2004), Atmospheric densities from CHAMP/STAR accelerometer observations, *Planetary and Space Sciences*, 52, 297–312.

Case, K., G. Kruizinga, and S. Wu (2002), GRACE Level 1B Data Product User Handbook, D-22027, JPL Publication, Pasadena, California, USA.

Christensen, E.J., B.J. Haines, S.J. Keihm, C.S. Morris, R.A. Norman, G.H. Purcell, B.G. Williams, B.D. Wilson, G.H. Born, M.E. Parke, S.K. Gill, C.K. Shum, B.D. Tapley, R. Kolenkiewicz, and R.S. Nerem (1994), Calibration of TOPEX/POSEIDON at Platform Harvest, *Journal of Geophysical Research*, 99(C12), 24465–24486, 10.1029/94JC01641.

Dach, R., G. Beutler, U. Hugentobler, S. Schaer, T. Schildknecht, T. Springer, G. Dudle, and L. Prost (2003), Time transfer using GPS carrier phase: Error propagation and results, *Journal of Geodesy*, 77(1-2), 1–14.

Dach, R., U. Hugentobler, P. Fridez, and M. Meindl (eds.) (2007), *Bernese GPS Software Version 5.0*, Astronomical Institute, University of Bern, Switzerland.

Dilssner, F., G. Seeber, M. Schmitz, G. Wübbena, G. Toso, and D. Maeusli (2006), Characterization of GOCE SSTI Antennas, *Zeitschrift für Geodäsie, Geoinformation und Landmanagement*, Heft 2/2006, 61–71.

Ditmar, P. and A.A. van Eck van der Sluijs (2004), A technique for modeling the Earth's gravity field on the basis of satellite accelerations, *Journal of Geodesy*, 78(1-2), 12–33.

Ditmar, P., V. Kuznetsov, A.A. van Eck van der Sluijs, E. Schrama, and R. Klees (2006), 'DEOS_CHAMP-01C_70': a model of the Earth's gravity field computed from accelerations of the CHAMP satellite, *Journal of Geodesy*, 79(10-11), 586–601.

Dow, J.M., R.E. Neilan, and G. Gendt (2005), The International GPS Service: Celebrating the 10th anniversary and looking to the next decade, *Advances in Space Research*, 36(3), 320–326.

Dunn, C., W. Bertiger, Y. Bar-Sever, S. Desai, B. Haines, D. Kuang, G. Franklin, I. Harris, G. Kruizinga, T. Meehan, S. Nandi, D. Nguyen, T. Rogstad, J.B. Thomas, J. Tien, L. Romans, M. Watkins, S.-C. Wu, S. Bettadpur, and J. Kim (2003), Instrument of GRACE, *GPS World*, February 2003.

European Space Agency ESA (1997), The Hipparcos and Tycho Catalogues, ESA SP-1200, ESA Publication Division.

European Space Agency ESA (1999), The Four Candidate Earth Explorer Core Missions: Gravity Field and Steady-State Ocean Circulation Mission, ESA SP-1233(1), ESA Publication Division.

Földváry, L., D. Švehla, C. Gerlach, M. Wermuth, T. Gruber, R. Rummel, M. Rothacher, B. Frommknecht, T. Peters, and P. Steigenberger (2004), Gravity Model TUM-2Sp Based on the Energy Balance Approach and Kinematic CHAMP Orbits, in *Earth Observation with CHAMP – Results from Three Years in Orbit*, edited by C. Reigber, H. Lühr, P. Schwintzer, and J. Wickert, pp. 13–18, Springer, ISBN 3-540-22804-7.

Förste, C. and S. Choi (2004), CHAMP Accelerometer Preprocessing at GeoForschungsZentrum Potsdam, in *Earth Observation with CHAMP – Results from Three Years in Orbit*, edited by C. Reigber, H. Lühr, P. Schwintzer, and J. Wickert, pp. 169–174, Springer, ISBN 3-540-22804-7.

Förste, C., F. Flechtner, R. Schmidt, U. Meyer, R. Stubenvoll, F. Barthelmes, R. König, K.H. Neumayer, M. Rothacher, C. Reigber, R. Biancale, S. Bruinsma, J.-M. Lemoine, and J.C. Raimondo (2005), A New High Resolution Global Gravity Field Model Derived From Combination of GRACE and CHAMP Mission and Altimetry/Gravimetry Surface Gravity Data, in *Geophysical Research Abstracts*, Vol. 7, European Geosciences Union.

Förste, C., F. Flechtner, R. Schmidt, R. König, U. Meyer, R. Stubenvoll, M. Rothacher, F. Barthelmes, K.H. Neumayer, R. Biancale, S. Bruinsma, J.-M. Lemoine, and S. Loyer (2006), A Mean Global Gravity Field Model from the Combination of Satellite Mission and Altimetry/Gravimetry Surface Gravity Data – EIGEN-GL04C, in *Geophysical Research Abstracts*, Vol. 8, European Geosciences Union.

Fu, L., E.J. Christensen, C.A. Yamarone, M. Lefebvre, Y. Ménard, M. Dorrer, and P. Escudier (1994), TOPEX/POSEIDON mission overview, *Journal of Geophysical Research*, 99(C12), 24369–24381.

Gendt, G. (2006), IGS switch to absolute antenna model and ITRF2005, IGS Mail, No. 5438.

Gerlach, C., N. Sneeuw, P. Visser, and D. Švehla (2003a), CHAMP Gravity Field Recovery with the Energy Balance Approach: First Results, in *First CHAMP Mission Results for Gravity, Magnetic and Atmospheric Studies*, edited by C. Reigber, H. Lühr, and P. Schwintzer, pp. 134–139, Springer, ISBN 3-540-00206-5.

Gerlach, C., N. Sneeuw, P. Visser, and D. Švehla (2003b), CHAMP gravity field recovery using the energy balance approach, *Advances in Geosciences*, 1, 73–80.

Gerlach, C., L. Földváry, D. Švehla, T. Gruber, M. Wermuth, N. Sneeuw, B. Frommknecht, H. Oberndorfer, T. Peters, M. Rothacher, R. Rummel, and P. Steigenberger (2003c), A CHAMP-only gravity field model from kinematic orbits using the energy integral, *Geophysical Research Letters*, 30(20), 2037, doi:10.1029/2003GL018025.

Gruber, T., A. Bode, C. Reigber, P. Schwintzer, G. Balmino, R. Biancale, and J.-M. Lemoine (2000), GRIM5-C1: Combination solution of the global gravity field to degree and order 120, *Geophysical Research Letters*, 27(24), 4005–4008, 10.1029/2000GL011589.

Grunwaldt, L. and T. Meehan (2003), CHAMP Orbit and Gravity Instrument Status, in *First CHAMP Mission Results for Gravity, Magnetic and Atmospheric Studies*, edited by C. Reigber, H. Lühr, and P. Schwintzer, pp. 03–10, Springer, ISBN 3-540-00206-5.

Gurtner, W. (1994), RINEX: The Receiver-Independent Exchange Format, *GPS World*, 5(7), 48–52.

Haines, B., Y. Bar-Sever, W. Bertiger, S. Desai, and P. Willis (2004), One-Centimeter Orbit Determination for Jason-1: New GPS-Based Strategies, *Marine Geodesy*, 27(1-2), 299–318.

Haines, B., S. Desai, W. Bertiger, Y. Bar-Sever, S. Byun, and G. Hajj (2005), GPS satellite antenna phase center variations: new perspectives from the GRACE Mission, presented at the Dynamic Planet Joint Meeting of the IAG, IAPSO and IABO, Cairns, Australia, August 22–26 2005.

Hedin, A.E. (1987), The MSIS-86 Termospheric Model, *Journal of Geophysical Research*, 92(A5), 4649–4662.

Heiskanen, W.A. and H. Moritz (1967), *Physical Geodesy*, Freeman.

van Helleputte, T. (2004), User manual for the GHOST orbit determination software, FDS-SUM-3110, Deutsches Zentrum für Luft und Raumfahrt, Oberpfaffenhofen, Germany.

Heuberger, H. (1984), Performance of the GPS Package on Landsat5, in *Plans' 84 – Position Location and Navigation Symposium*, pp. 147–152, Institute of Electrical and Electronics Engineers.

Hoffman, E.J. and W.P. Birmingham (1978), GPSPAC: A Spaceborne GPS Navigation Set, in *Plans' 78 – Position Location and Navigation Symposium*, pp. 13–20, Institute of Electrical and Electronics Engineers.

Howe, E. and C.C. Tscherning (2003), Preliminary Analysis of CHAMP State Vector and Accelerometer Data for the Recovery of the Gravity Potential, in *First CHAMP Mission Results for Gravity, Magnetic and Atmospheric Studies*, edited by C. Reigber, H. Lühr, and P. Schwintzer, pp. 140–145, Springer, ISBN 3-540-00206-5.

Hugentobler, U. (2004a), CODE high rate clocks, IGS Mail, No. 4913.

Hugentobler, U., S. Schaer, G. Beutler, H. Bock, R. Dach, A. Jäggi, M. Meindl, C. Urschl, L. Mervart, M. Rothacher, U. Wild, A. Wiget, E. Brockmann, D. Ineichen, G. Weber, H. Habrich, and C. Boucher (2004b), CODE IGS Analysis Center Technical Report 2002, in *IGS – 2001-2002 Technical Reports*, edited by K. Gowey, R. Neilan, and A. Moore, pp. 43–52, JPL Publication 04-017.

Hugentobler, U., A. Jäggi, S. Schaer, and G. Beutler (2005a), Combined Processing of GPS Data from Ground Station and LEO Receivers in a Global Solution, in *A Window on the Future of Geodesy*, edited by F. Sansò, pp. 169–174, Springer, ISBN 3-540-24055-1.

Hugentobler, U., S. Schaer, R. Dach, C. Urschl, and G. Beutler (2005b), Relevance of GPS Geocenter for Precise Point Positioning, in *Geophysical Research Abstracts*, Vol. 7, European Geosciences Union.

Hwang, C. and Y.C. Kao (2003), Time-varying gravity research associated with ROCSAT-3/COSMIC mission: Gravity field variation due to oceanic mass redistribution, in *Proceedings of 2003 ROCSAT.3/COSMIC Workshop*, pp. 115–120.

van den IJssel, J., P. Visser, and E.P. Rodriguez (2003), Champ Precise Orbit Determination Using GPS Data, *Advances in Space Research*, 31(8), 1889–1895.

van den IJssel, J. and P. Visser (2005), Determination of non-conservative accelerations from GPS satellite-to-satellite tracking of CHAMP, *Advances in Space Research*, 36(3), 418–423.

van den IJssel, J. and P. Visser (2007), Performance of GPS-based accelerometry: CHAMP and GRACE, *Advances in Space Research*, 39(10), 1597–1603.

Ilk, K.H., J. Flury, R. Rummel, P. Schwintzer, W. Bosch, C. Haas, J. Schröter, D. Stammer, W. Zahel, H. Miller, R. Dietrich, P. Huybrechts, H. Schmeling, D. Wolf, H.J. Götze, J. Riegger, A. Bardossy, A. Günter, and T. Gruber (2005), Mass Transport and Mass Distribution in the Earth System: Contribution of the New Generation of Satellite Gravity and Altimetry Missions to Geosciences, Proposal for a German Priority Research Program, GOCE-Projektbüro Deutschland, Technische Universität München, GeoForschungsZentrum Potsdam, Germany, January 2005.

Jäggi, A., H. Bock, U. Hugentobler, and G. Beutler (2004), Comparison of Different Stochastic Orbit Modeling Techniques, in *Earth Observation with CHAMP – Results from Three Years in Orbit*, edited by C. Reigber, H. Lühr, P. Schwintzer, and J. Wickert, pp. 89–94, Springer, ISBN 3-540-22804-7.

Jäggi, A., G. Beutler, and U. Hugentobler (2005a), Reduced-dynamic orbit determination and the use of accelerometer data, *Advances in Space Research*, 36(3), 438–444.

Jäggi, A., U. Hugentobler, and G. Beutler (2005b), Efficient Stochastic Orbit Modeling Techniques using Least Squares Estimators, in *A Window on the Future of Geodesy*, edited by F. Sansò, pp. 175–180, Springer, ISBN 3-540-24055-1.

Jäggi, A., U. Hugentobler, and G. Beutler (2006a), Pseudo-stochastic orbit modeling techniques for low-Earth orbiters, *Journal of Geodesy*, 80(1), 47–60.

Jäggi, A., G. Beutler, and U. Hugentobler (2006b), Kinematic versus highly reduced-dynamic LEO orbits for global gravity field recovery, in *Geophysical Research Abstracts*, Vol. 8, European Geosciences Union.

Jäggi, A., H. Bock, U. Hugentobler, and G. Beutler (2006c), Orbit Determination of Low Earth Satellites at AIUB, presented at the IGS Workshop, Darmstadt, Germany, May 8–12 2006.

Jäggi, A., G. Beutler, H. Bock, and U. Hugentobler (2006d), Kinematic and highly reduced-dynamic LEO orbit determination for gravity field estimation, in *Dynamic Planet – Monitoring and Understanding a Dynamic Planet with Geodetic and Oceanographic Tools*, edited by C. Rizos and P. Tregoning, pp. 354–361, Springer, ISBN 3-540-49349-2.

Jäggi, A., U. Hugentobler, H. Bock, and G. Beutler (2007), Precise Orbit Determination for GRACE Using Undifferenced or Doubly Differenced GPS Data, *Advances in Space Research*, 39(10), 1612–1619.

Jazwinski, A.H. (1970), *Stochastic Processes and Filtering Theories*, Academic Press.

Johanessen, J., G. Balmino, C. LeProvost, R. Rummel, R. Sabadini, H. Sünkel, C.C. Tscherning, P. Visser, P. Woodworth, C. Hughes, P. LeGrand, N. Sneeuw, F. Perosanz, M. Aguirre-Martinez, H. Rebhan, and M. Drinkwater (2003), The European Gravity Field and steady-state Ocean Circulation Explorer satellite mission: Its impact on Geophysics, *Surveys in Geophysics*, 24, 339–386.

Jorgensen, J.L. (1999), In Orbit Performance of a fully Autonomous Star Tracker, in *Proceedings of the 4th ESA International Conference on Spacecraft Guidance, Navigation and Control Systems*, pp. 103–110.

Kang, Z., B. Tapley, S. Bettadpur, J. Ries, P. Nagel, and R. Pastor (2006), Precise orbit determination for the GRACE mission using only GPS data, *Journal of Geodesy*, 80(6), 322–331.

König, R., Z. Chen, C. Reigber, and P. Schwintzer (1999), Improvement in global gravity field recovery using GFZ-1 satellite laser tracking data, *Journal of Geodesy*, 73, 398–406.

König, R., G. Michalak, K.H. Neumayer, R. Schmidt, S.Y. Zhu, H. Meixner, and C. Reigber (2004), Recent developments in CHAMP orbit determination at GFZ, in *Earth Observation with CHAMP – Results from Three Years in Orbit*, edited by C. Reigber, H. Lühr, P. Schwintzer, and J. Wickert, pp. 65–70, Springer, ISBN 3-540-22804-7.

König, R., C. Reigber, S.Y. Zhu (2005), Dynamic model orbits and Earth system parameters from combined GPS and LEO data, *Advances in Space Research*, 36(3), 431–437.

Kroes, R. (2006), *Precise Relative Positioning of Formation Flying Spacecraft using GPS*, Vol. 61 of *Publications on Geodesy*, Nederlandse Commissie voor Geodesie, ISBN 90-6132-296-0.

Kuang, D., Y. Bar-Sever, W. Bertiger, S. Desai, B. Haines, B. Iijima, G. Kruizinga, T. Meehan, and L. Romans (2001), Precise Orbit Determination for CHAMP Using GPS Data from BlackJack Receiver, presented at the ION National Technical Meeting, Long Beach, California, USA, January 22–24.

Kursinski, E.R., G.A. Hajj, J.T. Schofield, R.P. Linfield, and K.R. Hardy (1997), Observing Earth's atmosphere with radio occultation measurements using the Global Positioning System, *Journal of Geophysical Research*, 102(D19), 23429–23466, 10.1029/97JD01569.

Lusignan, B., G. Modrell, A. Morrison, J. Pomalaza, and S.G. Ungar (1969), Sensing the Earth's Atmosphere with Occultation Satellites, in *Proceedings of the IEEE*, 57(4), 458–467.

Luthcke, S.B., N.P. Zelensky, D.D Rowlands, F.G. Lemoine, and T.A. Williams (2003), The 1-Centimeter Orbit: Jason-1 Precision Orbit Determination Using GPS, SLR, DORIS, and Altimeter Data, *Marine Geodesy*, 26(3-4), 399–421.

Marini, J.W. and C.W. Murray (1973), Correction of Laser Range Tracking Data for Atmospheric Refraction at Elevations Above 10 Degrees, X-591-73-351, NASA GSFC.

Mayer-Gürr, T., K.H. Ilk, A. Eicker, and M. Feuchtinger (2005), ITG-CHAMP01: a CHAMP gravity field model from short kinematic arcs over a one-year observation period, *Journal of Geodesy*, 78(7-8), 462–480.

Mayer-Gürr, T., A. Eicker, and K.H. Ilk (2006), ITG-GRACE02S: a GRACE gravity field derived from short arcs of the satellite's orbit, presented at the First Symposium of the International Gravity Field Service, Istanbul, Turkey, August 28 – September 01 2006.

McCarthy, D.D. (ed.) (1996), *IERS Conventions (1996)*, IERS Technical Note No. 21, Central Bureau of IERS, Observatoire de Paris, France.

McCarthy, D.D. and G. Petit (eds.) (2003), *IERS Conventions (2003)*, IERS Technical Note No. 32, Central Bureau of IERS, Observatoire de Paris, France.

Meindl, M. (ed.) (2005), *Celebrating a Decade of the International GPS Service – Workshop and Symposium 2004*, Astronomical Institute, University of Berne, Switzerland.

Melbourne, W.G. (1985), The Case for Ranging in GPS Based Geodetic Systems, in *Proceedings of the First International Symposium on Precise Positioning with the Global Positioning System*, Rockville, Maryland, USA.

Mervart, L. (1995), *Ambiguity Resolution Techniques in Geodetic and Geodynamic Applications of the Global Positioning System*, Vol. 53 of *Geodätisch-geophysikalische Arbeiten in der Schweiz*, Schweizerische Geodätische Kommission.

Montenbruck, O. and R. Kroes (2003), In-flight performance analysis of the CHAMP BlackJack GPS Receiver, *GPS Solutions*, 7(2), 74–86.

Montenbruck, O., E. Gill, and R. Kroes (2005), Rapid orbit determination of LEO satellites using IGS clock and ephemeris products, *GPS Solutions*, 9(3), 226–235.

Montenbruck, O., M. Kirschner, S. D'Amico, and S. Bettadpur (2006), E/i-vector separation for safe switching of the GRACE formation, *Aerospace Science and Technology*, 10(7), 628–635.

Moreira, A., G. Krieger, I. Hajnsek, D. Hounam, M. Werner, S. Riegger, and E. Settelmeyer (2004), TanDEM-X: A TerraSAR-X Add-On Satellite for Single-Pass SAR Interferometry, in *Proceedings of IGARSS '04*, Vol. 2, pp. 1000–1003.

Neubert, R., L. Grunwaldt, and J. Neubert (1998), The Retro-Reflector for the CHAMP Satellite: Final Design and Realization, presented at the ILRS Workshop, Deggendorf, Germany, September 21–25 1998.

O'Keefe, J.A. (1957), An application of Jacobi's integral to the motion of an Earth satellite, *Astronomical Journal*, 62(1252), 265–266.

Pearlman, M.R., J.J. Degnan, and J.M. Bosworth (2002), The International Laser Ranging Service, *Advances in Space Research*, 30(2), 135–143.

Perosanz, F., R. Biancale, S. Loyer, J.-M. Lemoine, A. Perret, P. Touboul, B. Foulon, G. Pradels, L. Grunwaldt, T. Fayard, N. Vales, and M. Sarrailh (2003), On Board Evaluation of the STAR Accelerometer, in *First CHAMP Mission Results for Gravity, Magnetic and Atmospheric Studies*, edited by C. Reigber, H. Lühr, and P. Schwintzer, pp. 11–18, Springer, ISBN 3-540-00206-5.

Perosanz, F., R. Biancale, J.-M. Lemoine, N. Vales, S. Loyer, and S. Bruinsma (2004), Evaluation of the CHAMP Accelerometer on two Years of Mission, in *Earth Observation with CHAMP – Results from Three Years in Orbit*, edited by C. Reigber, H. Lühr, P. Schwintzer, and J. Wickert, pp. 77–82, Springer, ISBN 3-540-22804-7.

Perosanz, F., J.-M. Lemoine, S. Bruinsma, S. Melachroinos, R. Biancale, and S. Loyer (2006), Grace accelerometers calibration, in *Geophysical Research Abstracts*, Vol. 8, European Geosciences Union.

Reigber, C., H. Lühr, and P. Schwintzer (1998), Status of the CHAMP Mission, in *Towards an Integrated Global Geodetic Observing System (IGGOS)*, edited by R. Rummel, H. Drewes, W. Bosch, and H. Hornik, pp. 63–65, Springer, ISBN 3-540-67079-3.

Reigber, C. (2001), First CHAMP Science Meeting, IGS LEO Mail, No. 2.

Reigber, C. (2002a), CHAMP Newsletter No. 10, `http://www.gfz-potsdam.de/champ/pb1/op/champ/more/newsletter_CHAMP_010.html`.

Reigber, C., G. Balmino, P. Schwintzer, R. Biancale, A. Bode, J.-M. Lemoine, R. König, S. Loyer, H. Neumayer, J.-C. Marty, F. Barthelmes, F. Perosanz, and S.Y. Zhu (2002b), A high quality global gravity field model from CHAMP GPS tracking data and accelerometry (EIGEN-1S), *Geophysical Research Letters*, 29(14), doi:10.1029/2002GL015064.

Reigber, C., G. Balmino, P. Schwintzer, R. Biancale, A. Bode, J.-M. Lemoine, R. König, S. Loyer, H. Neumayer, J.-C. Marty, F. Barthelmes, F. Perosanz, and S.Y. Zhu (2003a), Global Gravity Field Recovery Using Solely GPS Tracking and Accelerometer Data from CHAMP, *Space Science Reviews*, 29, 55–66.

Reigber, C., P. Schwintzer, K.-H. Neumayer, F. Barthelmes, R. König, C. Förste, G. Balmino, R. Biancale, J.-M. Lemoine, S. Loyer, S. Bruinsma, F. Perosanz, and T. Fayard (2003b), The CHAMP-only Earth Gravity Field Model EIGEN-2, *Advances in Space Research*, 31(8), 1883–1888.

Reigber, C. (2004a), First GRACE Data Release, private communication.

Reigber, C., H. Jochmann, J. Wünsch, S. Petrovic, P. Schwintzer, F. Barthelmes, K.-H. Neumayer, R. König, C. Förste, G. Balmino, R. Biancale, J.-M. Lemoine, S. Loyer, and F. Perosanz (2004b), Earth Gravity Field and Seasonal Variability from CHAMP, in *Earth Observation with CHAMP – Results from Three Years in Orbit*, edited by C. Reigber, H. Lühr, P. Schwintzer, and J. Wickert, pp. 25–30, Springer, ISBN 3-540-22804-7.

Reigber, C., R. Schmidt, F. Flechtner, R. König, U. Meyer, K.-H. Neumayer, P. Schwintzer, and S.Y. Zhu (2005), An Earth gravity field model complete to degree and order 150 from GRACE: EIGEN-GRACE02S, *Journal of Geodynamics*, 39(1), 1–10.

Reigber, C., P. Schwintzer, R. Stubenvoll, R. Schmidt, F. Flechtner, U. Meyer, R. König, K.H. Neumayer, C. Förste, F. Barthelmes, S.Y. Zhu, G. Balmino, R. Biancale, J.-M. Lemoine, H. Meixner, and J.C. Raimondo (2006), A High Resolution Global Gravity Field Model Combining CHAMP and GRACE Satellite Mission and Surface Gravity Data, Scientific Technical Report, GFZ Potsdam, Germany, in press.

Remondi, B.W. (1991), NGS second generation ASCII and binary orbit formats and associated interpolation studies, in *Proceedings of the 20th General Assembly of the International Union of Geodesy and Geophysics*, Vienna, Austria.

Rim, H., S. Yoon, B. Schutz, Z. Kang, P. Nagel, S. Bettadpur, B. Tapley, K. Choi, J. Ries, and M. Cheng (2002), CHAMP POD at CSR, presented at the First CHAMP Science Meeting, Potsdam, Germany, January 21–24 2002.

Rim, H.-J., S.-P. Yoon, Y. Kim, and B.E. Schutz (2005), ICESat precision orbit determination over solar storm period, in *Spaceflight Mechanics 2005*, edited by D.A. Vallado, M.J. Gabor, and P.N. Desai, Vol. 120, pp. 579–588, Univelt, ISBN 0-87-703520-2.

Rocken, C., R. Anthes, M. Exner, D. Hunt, S. Sokolovskiy, R. Ware, M. Gorbunov, W. Schreiner, D. Feng, B. Herman, Y.-H. Kuo, and X. Zou (1997), Analysis and validation of GPS/MET data in the neutral atmosphere, *Journal of Geophysical Research*, 102(D25), 29849–29866, 10.1029/97JD02400.

Rockwell International Corporation (1984), GPS Interface Control Document, ICD-GPS-200, Satellite Systems Division, September 1984.

Rothacher, M. (2001), Comparison of absolute and relative antenna phase center variations, *GPS Solutions*, 4(4), 55–60.

Rowlands, D.D., J.A. Marshall, J.J. McCarthy, S.C. Rowton, D. Moore, D.E. Pavlis, S.B. Luthcke, and L.S. Tsaoussi (1995), GEODYN II system description, Vol. 1-5, Contractor Report, Hughes STX Corporation, Greenbelt, Maryland, USA.

Rummel, R., G. Balmino, J. Johanessen, P. Visser, and R. Woodworth (2002), Dedicated Gravity Field Missions. Principles and Aims, *Journal of Geodynamics*, 33, 3–20.

Sansò, F. and R. Rummel (eds.) (1989), *Theory of Satellite Geodesy and Gravity Field Determination*, Springer, ISBN 3-540-51528-3.

Schaer, S. (1999), *Mapping and Predicting the Earth's Ionosphere Using the Global Positioning System*, Vol. 59 of *Geodätisch-geophysikalische Arbeiten in der Schweiz*, Schweizerische Geodätische Kommission, ISBN 3-908440-01-7.

Schaer, S., M. Meindl, and U. Hugentobler (2002), Determination and Use of Differential $P_1 - P_2$ and $P_1 - C_1$ Code Bias Values for Precise GPS Applications, private communication.

Schmid, R. and M. Rothacher (2003), Estimation of elevation-dependent satellite antenna phase center variations of GPS satellites, *Journal of Geodesy*, 77(7-8), 440–446.

Schmid, R., M. Rothacher, D. Thaller, and P. Steigenberger (2005a), Absolute phase center corrections of satellite and receiver antennas: Impact on global GPS solutions and estimation of azimuthal phase center variations of the satellite antenna, *GPS Solutions*, 9(4), 283–293.

Schmid, R., G. Mader, and T. Herring (2005b), From Relative to Absolute Antenna Phase Center Corrections, in *Celebrating a Decade of the International GPS Service – Workshop and Symposium 2004*, edited by M. Meindl, pp. 209–219, Astronomical Institute, University of Berne.

Schutz, B.E, H.J. Zwally, C.A. Shuman, D. Hancock, and J.P. DiMarzio (2005), Overview of the ICESat Mission, Transformations and Standards, *Geophysical Research Letters*, 32, L21S01, doi:10.1029/2005GL024009.

Schwintzer, P., H. Lühr, C. Reigber, L. Grunwaldt, and C. Förste (2002), CHAMP Reference Systems, Transformations and Standards, CH-GFZ-RS-002, GFZ Potsdam, Germany, April 2002.

Springer, T.A. (2000), *Modeling and Validating Orbits and Clocks Using the Global Positioning System*, Vol. 60 of *Geodätisch-geophysikalische Arbeiten in der Schweiz*, Schweizerische Geodätische Kommission, ISBN 3-908440-02-5.

Švehla, D. and M. Rothacher (2002), Kinematic Orbit Determination of LEOs Based on Zero or Double-difference Algorithms Using Simulated and Real SST GPS Data, in *Vistas for Geodesy in the New Millennium*, edited by J. Ádám and K.-P. Schwarz, pp. 322–328, Springer, ISBN 3-540-43454-2.

Švehla, D. and M. Rothacher (2003a), CHAMP Double-Difference Kinematic POD with Ambiguity Resolution, in *First CHAMP Mission Results for Gravity, Magnetic and Atmospheric Studies*, edited by C. Reigber, H. Lühr, and P. Schwintzer, pp. 70–77, Springer, ISBN 3-540-00206-5.

Švehla, D. and M. Rothacher (2003b), Kinematic and Reduced-Dynamic Precise Orbit Determination of Low Earth Orbiters, *Advances in Geosciences*, 1, 47–56.

Švehla, D. and M. Rothacher (2003c), Kinematic and reduced-dynamic precise orbit determination of CHAMP satellite over one year using zero-differences, in *Geophysical Research Abstracts*, Vol. 5, European Geosciences Union.

Švehla, D. and M. Rothacher (2004a), Two Years of CHAMP Kinematic Orbits for Geosciences, in *Geophysical Research Abstracts*, Vol. 6, European Geosciences Union.

Švehla, D. and M. Rothacher (2004b), CHAMP and GRACE in Tandem: POD with GPS and K-Band Measurements, presented at the Joint CHAMP/GRACE Science Meeting, Potsdam, Germany, July 6–8 2004.

Švehla, D. and M. Rothacher (2005a), Kinematic Precise Orbit Determination for Gravity Field Determination, in *A Window on the Future of Geodesy*, edited by F. Sansò, pp. 181–188, Springer, ISBN 3-540-24055-1.

Švehla, D. and M. Rothacher (2005b), Kinematic positioning of LEO and GPS satellites and IGS stations on the ground, *Advances in Space Research*, 36(3), 376–381.

Švehla, D. and M. Rothacher (2006), Impact of a LEO Formation and a LEO/GPS Dual Constellation on the IGS Products, presented at the IGS Workshop, Darmstadt, Germany, May 8–12 2006.

Tapley, B.D., D. Chambers, M. Cheng, M. Kim, S. Poole, and J.C. Ries (2000), The TEG-4 Gravity Field Model, presented at the EGS General Assembly, Nice, France, April 25–29 2000.

Tapley, B.D. and C. Reigber (2001), The GRACE Mission: Status and future plans, in *EOS, Transactions*, 82(47), American Geophysical Union.

Tapley, B.D., S. Bettadpur, M. Watkins, and C. Reigber (2004a), The gravity recovery and climate experiment: Mission overview and early results, *Geophysical Research Letters*, 31, L09607, doi:10.1029/2004GL019920.

Tapley, B.D., S. Bettadpur, J.C. Ries, P.F. Thompson, and M. Watkins (2004b), GRACE measurements of mass variability in the Earth system, *Science*, 305(5683), 503–505.

Tapley, B.D., B.E. Schutz, G.H. Born (2004c), *Statistical Orbit Determination*, Elsevier Academic Press, ISBN 0-12-683630-2.

Tapley, B., J. Ries, S. Bettadpur, D. Chambers, M. Cheng, F. Condi, B. Gunter, Z. Kang, P. Nagel, R. Pastor, T. Pekker, S. Poole, and F. Wang (2005), GGM02 - An Improved Earth Gravity Field Model from GRACE, *Journal of Geodesy*, 79(8), 467–478.

Teunissen, P.J.G. and A. Kleusberg (eds.) (1998a), *GPS for Geodesy*, Springer, ISBN 3-540-63661-7.

Teunissen, P.J.G. and A. Kleusberg (1998b), GPS Observation Equations and Positioning Concepts, in *GPS for Geodesy*, edited by P.J.G. Teunissen and A. Kleusberg, pp. 187–229, Springer, ISBN 3-540-63661-7.

Touboul, P., B. Foulon, and G.-M. Le Clerc (1998), STAR, the accelerometer of the geodesic mission CHAMP, in *Proceedings of the 49th IAF Congress*, IAF-98-B.3.07, Melbourne, Australia.

Touboul, P., E. Willemenot, B. Foulon, and V. Josselin (1999), Accelerometers for CHAMP, GRACE, and GOCE space missions: synergy and evolution, *Bollettino di Geofisica Teorica ed Applicata*, 40(3-4), 321–327.

Urschl, C., W. Gurtner, U. Hugentobler, S. Schaer, and G. Beutler (2005), Validation of GNSS Orbits Using SLR Observations, *Advances in Space Research*, 36(3), 412–417.

Visser, P.N.A.M., N. Sneeuw, and C. Gerlach (2003), Energy integral method for gravity field determination from satellite orbit coordinates, *Journal of Geodesy*, 77(3-4), 207–216.

Wermuth, M., D. Švehla, L. Földváry, C. Gerlach, T. Gruber, B. Frommknecht, T. Peters, M. Rothacher, R. Rummel, and P. Steigenberger (2004), A gravity field model from two years of CHAMP kinematic orbits using the energy balance approach, in *Geophysical Research Abstracts*, Vol. 6, European Geosciences Union.

Wolff, M. (1969), Direct Measurements of the Earth's Gravitational Potential Using a Satellite Pair, *Journal of Geophysical Research*, 74(22), 5295–5300.

Wu, J.T., S.C. Wu, G.A. Hajj, W.I. Bertiger, and S.M. Lichten (1993), Effects of antenna orientation on GPS carrier phase, *Manuscripta Geodaetica*, 18, 91–98.

Wu, S.C., T.P. Yunck, and C.L. Thornton (1991), Reduced-dynamic technique for precise orbit determination of low Earth satellites, *Journal of Guidance, Control, and Dynamics*, 14(1), 24–30.

Wu, B.-H., V. Chu, P. Chen, and T. Ting (2005), FORMOSAT-3/COSMIC science mission update, *GPS Solutions*, 9(2), 111–121.

Wübbena, G. (1985), Software Developments for Geodetic Positioning with GPS Using TI-4100 Code and Carrier Measurements, in *Proceedings of the First International Symposium on Precise Positioning with the Global Positioning System*, Rockville, Maryland, USA.

Yunck, T.P., S.C. Wu, J.T. Wu, and C.L. Thornton (1990), Precise tracking of remote sensing satellites with the Global Positioning System, in *IEEE Transactions on Geoscience and Remote Sensing*, 28(1), 108–116.

Zhu, S.Y., C. Reigber, and R. König (2004), Integrated adjustment of CHAMP, GRACE and GPS data, *Journal of Geodesy*, 78(1-2), 103–108.

Zieger, A.R., D.W. Hancock, G.S. Hayne, and C.L. Purdy (1991), NASA radar altimeter for the TOPEX/Poseidon project, in *Proceedings of the IEEE*, 79(6), 810–826.

Zin, A., S. Landenna, A. Conti, L. Marradi, and M.S. Di Raimondo (2006), ENEIDE: an Experiment of a Space-borne, L1/L2 Integrated GPS/WAAS/EGNOS Receiver, in *Proceedings of the European Navigation Conference*, Manchester, United Kingdom.

Zwally, H.J., B. Schutz, W. Abdalati, J. Abshire, C. Bentley, A. Brenner, J. Bufton, J. Dezio, D. Hancock, D. Harding, T. Herring, B. Minster, K. Quinn, S. Palm, J. Spinhirne, and R. Thomas (2002), ICESat's laser measurements of polar ice, atmosphere, ocean and land, *Journal of Geodynamics*, 34, 405–445.